Universidad de Oviedo

DOCTORAL THESIS

DESIGN, OPTIMIZATION AND ANALYSIS TECHNIQUES OF NON-LINEAR DEVICES BASED ON GRAPHENE OR HIGHLY ORDERED PYROLYTIC GRAPHITE FOR TERAHERTZ SYSTEM APPLICATIONS

ANDREEA IOANA HADARIG

Programa de Doctorado en Tecnologías de la Información y Comunicaciones en Redes Móviles

2017

Director: Samuel Ver Hoeye

Celor mai dragi persoane din viaţa mea:
tatălui meu Mircea, care s-a stins din
viaţă înainte de a putea vedea această
teză finalizată, mamei mele Nuţa, surorii
mele Ramona şi lui Andreas.

Mulţumiri

La încheierea procesului de elaborare a acestei Teze Doctorale, doresc să adresez mulţumiri tuturor celor care m-au îndrumat, mi-au împărtăşit cunoştinţele profesionale, m-au sprijinit moral şi au fost alături de mine în momentele dificile.

În primul rând, doresc să îmi exprim recunoştinţa faţă de Samuel Ver Hoeye în calitate de coordonator al lucrării mele de doctorat, pentru îndrumarea activităţii mele ştiinţifice, pentru ajutorul, sprijinul şi răbdarea de care a dat dovadă în formarea mea profesională precum şi pentru efortul depus de-a lungul anilor în a-mi explica conceptele ştiinţifice. Suportul necondiţionat oferit şi încurajarea activităţii desfăşurate au fost esenţiale în îndeplinirea obiectivelor acestei Teze.

Aş dori, de asemenea, să îi adresez mulţumiri lui Fernando Las Heras, în calitate de şef al departamentului, pentru oportunitatea oferită de a face parte din cadrul ariei "Teoría de la Señal y Comunicaciones".

Îmi exprim sincera recunoştinţă şi apreciere faţă de Sergey Mikhailov, pentru acceptul de a mă primi, în calitate de invitat colaborator, pentru o scurtă şedere, la Institutul de Fizică, Catedra de Fizică Teoretică II din cadrul Universităţii din Augsburg, Germania. Înţelepciunea lui, profesionalismul şi sfaturile oferite în timpul colaborării noastre au fost foarte apreciate. Îi mulţumesc foarte mult pentru oportunitatea de a cunoaşte o altă perspectivă a muncii de cercetare. Adresez mulţumiri speciale catre Nadezda Savostiyanova pentru ideile şi discuţiile valoroase pe care le-am avut in Augsburg cu privire la munca mea de cercetare. De asemenea, îi mulţumesc domnului Prof. Ulrich Eckern, şeful catedrei TP II, pentru multiplele invitaţii la seminariile de grup organizate, precum şi la diverse evenimente sociale. Le mulţumesc lui Andreas, Marion, Liviu, Ruijing, Johannes, Marcelo, Sebastian, Fabiana, Katharina şi mulţi alţii pentru că m-au făcut să mă simt bine în Augsburg.

Sunt foarte recunoscătoare tuturor profesorilor mei de la Universitatea Tehnică din Cluj-Napoca, România. Adresez mulţumiri speciale doamnei Prof. Marina Ţopa şi domnului Prof. Tudor Palade pentru discuţiile avute de-a lungul anilor de studenţie.

Aş dori să le mulţumesc domnului Prof. Ladislau Matekovits, Universitatea

Tehnică din Torino, şi doamnei Prof. Marina Ţopa, Universitatea Tehnică din Cluj-Napoca, cei care au fost revizorii externi ai acestei teze de doctorat, pentru timpul dedicat şi analiza intensă a manuscrisului, care prin rigoare şi exigenţă au contribuit la finalizarea acestei teze.

Le mulţumesc tuturor membrilor tribunalului academic pentru acceptarea examinării tezei mele, pentru interesul lor în munca mea şi pentru rigoarea de care au dat dovadă.

Adresez mulţumiri speciale tuturor colegilor mei din laborator. Mulţumesc lui Carlos, Rene, Miguel şi George pentru ajutorul lor nepreţuit şi pentru cooperarea dezvoltată în multiplele proiecte la care am lucrat împreună. Fără sprijinul lor constant progresul acestei teze ar fi fost unul mai lent. De asemenea, îi mulţumesc lui Cebrian pentru prietenia lui şi pentru toate sfaturile de viaţă pe care mi le-a dat de-a lungul acestor ani. Mulţumiri tuturor celorlalţi membri din laborator.

Această teză nu s-ar fi putut realiza fără sprijinul familiei mele. Aş dori să le mulţumesc din suflet părinţilor mei care, întotdeauna au subliniat importanţa unei bune educaţii. Vreau să îi mulţumesc surorii mea Ramona, cea care în 2012 m-a îndrumat să urmez studiile de master la Universitatea din Oviedo, şi cea care mai apoi m-a încurajat să încep studiile doctorale. De asemenea, doresc să le mulţumesc cumnatului meu George şi bunicelor mele, pentru încurajarea şi ajutorul acordat pe parcursul acestor ani. Sunt profund recunoscătoare lui Andreas pentru importanţa avută în viaţa mea în ultimii ani. Nu există cuvinte suficiente care să poată exprima tot sprijinul primit din partea tuturor acestor persoane şi recunoştinţa ce le-o port pentru acest lucru.

Nu in ultimul rând doresc să mulţumesc tuturor celor care la un moment sau altul, de-a lungul acestor ani, au avut un impact pozitiv asupra vieţii mele.

Această Teză Doctorală a fost obţinută cu sprijinul Comisiei Europene prin proiectul cu numărul 600849, Guvernului Spaniei prin proiectele IPT-2011-0951-390000, TECNIGRAF, MINECO-17-TEC2016-80815-P, GMILLITECH, TEC2015-72110-EXP, TERAGRAPH, Guvernului Principatului Asturias (PCTI)/FEDER-FSE prin proiectele EQUIP08- 06, EQUIP10-31, GRUPIN14-114, IDI/2016/000373 şi bursei BP13034.

Acknowledgments

The work presented in this Thesis would not have been possible without the encouragement, support and inspiration that I received from many people throughout my Doctoral studies. I take this opportunity to extend my sincere gratitude and appreciation to all those who contributed to the development and completion of this Thesis.

First of all, I would like to express my sincere and foremost gratitude to my supervisor Samuel Ver Hoeye, for introducing me to this exciting engineering field, for his dedicated help, advice, guidance and great efforts to explain things as clearly and simply as possible. His encouragement and continuous support during all these years were essential in achieving the goals of this Thesis.

I would like also to thank Fernando Las Heras, the head of the department for giving me the opportunity to be part of the Área de Teoría de la Señal y Comunicaciones.

I express my sincere gratitude and appreciation to Sergey Mikhailov who accepted me, for a short stay, as a research guest at the Institute of Physics, Chair of Theoretical Physics II from University of Augsburg, Germany. His wisdom, professionalism and advices during our collaboration were much appreciated. I thank him for giving me the opportunity to work in a different research environment. Special thanks are also given to Nadezda Savostiyanova for valuable ideas and discussions regarding my research. Also, I thank Prof. Ulrich Eckern, the head of TP II Chair from University of Augsburg, for inviting me to every group seminar as well as leisure group events. A thank also Andreas, Marion, Liviu, Ruijing, Johannes, Marcelo, Sebastian, Fabiana, Katharina and many others for making me feel welcomed in Augsburg.

I am very grateful to all my professors from Technical University of Cluj-Napoca, Romania. Sincerely thanks especially to Prof. Marina Topa and Prof. Tudor Palade for useful discussions.

I take this chance to thank Prof. Ladislau Matekovits, Technical University of Torino, and Prof. Marina Topa, Technical University of Cluj Napoca, the reviewers

of my Doctoral Thesis for their time and intense analysis of the manuscript which by rigor and stringency, contributed to the completion of the Thesis.

I thank the entire academic jury for accepting the examination of my Thesis, for their interest in my work and for their rigor.

A special mention of thanks go to all my colleagues from the laboratory. I am grateful to Carlos, Rene, Miguel and George for their invaluable help and cooperation on the projects we worked together. Without their constant support the progress of this Thesis would have been slower. I thank also Cebrian for his friendship and all his life advices throughout these years. Thank to all the other members from the laboratory.

This Thesis would not have been possible without the support of my family. I would like to thank my parents who always stressed the importance of a good education. I want to thank my sister Ramona who determined me to pursue a Master's degree at the University of Oviedo, back in 2012, and who highly encouraged me to start my Doctoral studies. I also want to thank my brother-in-law George and my grandmothers, for their encouragement and help during these years. I am deeply grateful to Andreas for his important role in my life during the last years. No amount of words can express the immense support I have received from all of them.

And I thank everyone else who at one time or another, during these years, had a positive impact on my life.

The work presented in this Thesis has been supported by the European Commission under project number 600849, by the Gobierno de España under the projects IPT-2011-0951-390000, TECNIGRAF, MINECO-17-TEC2016-80815-P, GMILLITECH, TEC2015-72110-EXP, TERAGRAPH, by the Gobierno del Principado de Asturias (PCTI)/FEDER-FSE under projects EQUIP08- 06, EQUIP10-31, GRUPIN14-114, IDI/2016/000373 and by the grant BP13034.

Resumen

La presente Tesis Doctoral se ha dedicado a la investigación de técnicas de análisis y optimización de dispositivos no lineales, multiplicadores y mezcladores de frecuencia, basados en grafeno multicapa y monocapa y su integración en transmisores y receptores de señales de banda submilimétrica/terahercios. El efecto de multiplicación y mezclado de frecuencia de los dispositivos se ha logrado mediante el uso de la respuesta no lineal del grafeno que ofrece una alternativa atractiva a las soluciones actuales basadas en semiconductores tradicionales. Por tanto, los dispositivos propuestos tienen por objetivo superar la barrera tecnológica existente en la generación de señales de onda submilimétrica/terahercios. La limitación tecnológica está restringiendo seriamente la viabilidad comercial de múltiples aplicaciones en la banda de submilimétricas/terahercios en sectores industriales tan diversos como diagnóstico médico, sistemas de seguridad o comunicaciones.

La presente Tesis Doctoral está estructurada en cuatro capítulos. El Capítulo 1 contiene un análisis de la respuesta electromagnética del grafeno basada en su estructura de banda electrónica. Se analiza la respuesta lineal y no lineal de una capa de grafeno irradiada con un campo eléctrico externo y las expresiones de la conductividad del primer orden armónico y de armónicos de orden N, $N = 3$ a 7, que se estudian y se derivan de la densidad de corriente inducida. Además, se estudia la irradiación de una capa de grafeno con dos ondas polarizadas paralelamente a la superficie de la capa con el objetivo de verificar el efecto no lineal de mezclado de frecuencia. Los nuevos aportes científicos desarrollados comienzan con la derivación de una ecuación de densidad de corriente no lineal generalizada, que se produce al irradiar la capa de grafeno con campo eléctrico externo. La literatura proporciona información de hasta el tercer orden armónico generado en el grafeno. Por tanto, se han desarrollado varias ecuaciones considerando los dos efectos no lineales de multiplicación y mezclado de frecuencia con componente armónicos superiores, $N > 3$, producidos en una capa de grafeno. El análisis teórico desarrollado en el Capítulo 1 tiene una aplicación directa en los diseños que se han estudiado en capítulos posteriores.

En el Capítulo 2, se presenta una topología que es común para tres multiplicadores de frecuencia basados en Grafeno de orden armónico elevado y con la conversión de frecuencia realizada en una sola etapa de multiplicación. La dinámica no lineal de multiplicación de frecuencia de los dispositivos se obtiene mediante el uso de una estructura *microstrip* con una abertura cubierta por varias capas de grafeno. Los circuitos se han analizado en dos etapas, donde los subsistemas pasivos de entrada y salida han sido diseñados y optimizados individualmente para maximizar el ancho de banda operativo en las bandas de frecuencia correspondientes. La topología propuesta se ha validado experimentalmente mediante la fabricación y medición de los tres prototipos propuestos. Los resultados presentados en este capítulo representan la primera realización práctica de un multiplicador de frecuencia de orden armónico elevado, de $N = 5$ a 17, en el cual, en una sola etapa de multiplicación realiza la conversión de frecuencia de señales de entrada en banda K_a, a señales de salida en la banda de 140-500 GHz mediante el uso del comportamiento electromagnético no lineal de unas películas de grafeno multicapa.

En el Capítulo 3, se presenta una topología de un circuito mezclador de frecuencias. La topología ha sido realizada a partir de las consideraciones de diseño propuestas en el Capítulo 2. Por tanto, tres circuitos han sido diseñados y analizados como parte de un bloque principal para un sistema de transmisión y/o recepción de señales de onda submilimétrica/terahercios. Se ha estudiado la dinámica no lineal de estos circuitos, que realizan varias funciones, como la generación de la señal del oscilado local y la mezcla con armónicos de orden elevado. El comportamiento de los mezcladores subarmonicos de frecuencia basados en grafeno ha sido analizado mediante simulaciones electromagnéticas y posteriormente ha sido validado experimentalmente a través de la caracterización de la potencia de salida de los prototipos fabricados. El trabajo presentado en este capítulo representa la primera realización practica de mezcladores subarmonicos basados en una película de grafeno multicapa que operan como conversores superiores y conversores inferiores de frecuencia utilizando un orden armónico elevado, $M = 6$ a 18, de la señal del oscilador local en banda K_a, una señal de IF de 400 MHz y una señal de RF en banda de 140-500 GHz.

Finalmente, en el Capítulo 4 se propone un multiplicador de frecuencia de orden armónico siete basado en una cavidad resonante que integra una película de grafeno monocapa/multicapa. El enfoque de este capítulo se basa en el diseño de una novedosa topología, en la cual, se han colocado películas de grafeno en el interior de una cavidad resonante, para asegurar que estén expuestas a niveles del campo eléctrico altos. La generación eficiente de los componentes armónicos de orden elevado requiere un campo eléctrico incidente alto, por lo tanto, el enfoque propuesto

representa una solución eficaz al aumentar la eficiencia de conversión del sistema. Partiendo del diseño de un bloque principal de guía de onda con características resonantes, se han implementado varios componentes de grafeno monocapa y multicapa que se introducen en el interior de la cavidad resonante. El comportamiento de los circuitos se analiza empleando simulaciones electromagnéticas en las cuales se investiga la respuesta resonante del circuito y la radiación de la señal del armónico de orden 7 hacia la salida del circuito. Finalmente, los circuitos se caracterizan experimentalmente mediante la fabricación y medición de los prototipos.

Conclusiones

En la presente Tesis Doctoral se han estudiado y evaluado experimentalmente dispositivos pasivos con contenido armónico no lineal, en base al empleo de grafeno mono y multicapa, que operan en la banda submilimétrica/terahercios. Además, se ha investigado rigurosamente el comportamiento electromagnético no lineal del grafeno, debido a su estructura de banda electrónica, para la generación de los componentes armónicos elevados que dan lugar a los efectos de mezcla y multiplicación de frecuencias.

La primera topología que se ha presento ha sido utilizada en la implementación de tres circuitos multiplicadores de frecuencia de una sola etapa basados en grafeno. La principal aplicación de estos circuitos es la generación de señales de onda submilimétrica/terahercios para aplicaciones de *imaging*, como bloques fundamentales en sistemas de transmisión. Debido a que la señal de salida es un componente armónico elevado, de $N = 5$ a 17, de la señal de entrada en banda K_a generada en una película de grafeno multicapa, los circuitos han sido diseñados y optimizados para proporcionar una amplitud de la señal de salida elevada en la banda de frecuencia 140-500 GHz. Los diseños han sido validados experimentalmente mediante la fabricación y medición de tres prototipos. Componentes armónicos de orden par e impar se han observado a la salida de los prototipos medidos. La amplitud de los componentes armónicos de orden impar se encontró constantemente más alta y con una respuesta de frecuencia plana en comparación con el contenido de orden par. La potencia de salida máxima medida con esta topología ha sido de -34 dBm a 252 GHz. Este valor se obtiene con una potencia de entrada P_{in}= 24 dBm y se ha medido considerando el armónico séptimo del grafeno. La potencia obtenida se encuentra en el mismo rango que los hallados en estado del arte, donde las implementaciones con componentes armónicos similares generan señales con frecuencias de hasta 70 GHz.

A partir de la topología del multiplicador de frecuencia basado en grafeno, se ha diseñado y validado experimentalmente una topología de tres circuitos mezcladores de frecuencia. Los circuitos se han analizado teniendo en cuenta la potencia de salida de la conversión ascendente y descendente obtenida para diferentes órdenes

armónicos pares, de $M = 6$ a 18. La potencia máxima de la conversión inferior alcanzada, -44.1 dBm (ganancia de conversión de -56 dBm) y la potencia máxima de la conversión descendente alcanzada, -73.7 dBm (ganancia de conversión de -53 dBm), se han obtenido a 347 GHz y corresponden al octavo orden armónico, el séptimo producto de intermodulación de las dos señales de entrada con las que se irradia la película de grafeno multicapa. Efectos de mezcla de frecuencia se han observado a lo largo de toda la banda de frecuencia de 140 a 500 GHz, en la cual la respuesta para los diferentes órdenes armónicos ha sido limitada por las características de adaptación de impedancia de la señal del oscilador local en banda K_a.

Además, se ha implementado un sub-sistema de un transmisor-receptor que tienen la señal de radiofrecuencia generada por medio de un multiplicador o un mezclador de frecuencia (conversor superior) basado en grafeno en banda 140-220 GHz. Esta señal se detecta por medio de un mezclador de frecuencia basado en grafeno, conversor inferior. El receptor ha presentado un rango dinámico, según la configuración transmisor-receptor utilizada, entre 20 y 45 dB.

La última topología propuesta y analizada en la presente Tesis Doctoral es la de un multiplicador de frecuencia del orden armónico séptimo basado en una cavidad resonante que contiene capas de grafeno en su interior. La influencia de varios componentes de grafeno sobre la generación de la señal del orden armónico siete y la radiación de esta señal hacia la salida del multiplicador de frecuencia se ha analizado mediante simulaciones electromagnéticas y se ha demostrado experimentalmente a través de la medición de los prototipos.

El análisis ha revelado que los diseños con componentes de grafeno multicapa, diseñados a partir de un primer multiplicador de frecuencia que contenia un componente de grafeno monocapa, ha presentado una respuesta resonante superior a la del primer circuito y una conversión armónica en múltiples capas de grafeno, que han aumentado considerablemente la potencia de salida medida. En este contexto, la potencia de salida máxima obtenida con el multiplicador de frecuencia basado en grafeno monocapa ha sido P_{out} = - 93.5 dBm (potencia de entrada máxima aplicada P_{in} = 33 dBm) mientras que el valor ha incrementado en 60 dB (P_{out} = - 34 dBm - potencia de entrada máxima aplicada P_{in} = 30 dBm) en el multiplicador de frecuencia basado en grafeno multicapa.

Por lo tanto, los circuitos desarrollados representan una demonstración conceptual que confirma que el grafeno (monocapa/multicapa) puede usarse por sí mismo como generador y/o detector de señales, basado en la multiplicación o mezcla de frecuencias, en la banda submilimétrica/terahercios.

Abstract

The Doctoral Thesis has been devoted to the development of innovative concepts for the implementation of passive devices with non-linear harmonic content. These devices are based on frequency multiplication and frequency mixing on mono- and multi-layer graphene films which are used for the generation and/or detection of submillimeter wave/low THz band signals. The desired frequency multiplication and mixing performance of the proposed structures is obtained by taking advantage of the non-linear electromagnetic response of graphene which offers an attractive alternative to current solutions based on traditional semiconductors. In this context, the developed structures are set out to address the existing technological bottleneck in the cost-effective generation of submillimeter wave/THz band signals. The technological limitation is seriously restricting the commercial viability of a wide variety of applications, in industrial sectors as diverse as medical diagnostics, security, non-destructive testing or communications.

The document is organized in four chapters. Chapter 1 contains an analysis of the graphene electromagnetic behavior based on its electronic band structure. The linear and non-linear response of a graphene layer irradiated with an external uniform, parallel to the layer surface, electric field is discussed and the expression of the first order conductivity and N^{th} order conductivity, $N = 3$ to 7, are studied and derived from the induced current density. Furthermore, the irradiation of a graphene layer with two parallel polarized waves in the attempt of testing its frequency mixing capability is also studied. The novel scientific contributions developed by the author start with the derivation of a generalized non-linear current density equation, produced by irradiating the graphene layer with an external electric field. The literature provides information of up to 3^{rd} harmonic generation in graphene. Therefore, several equations have been developed considering both the multiplication effect and the mixing effect with high harmonic orders, $N > 3$, produced in a graphene layer. The theoretical analysis developed in Chapter 1 has a direct application on the designs that are developed in the later chapters.

In Chapter 2, a topology which is common for three Single Stage High Order

Submillimeter Wave/THz band Graphene based Frequency Multipliers is presented. The frequency multiplication performance of the devices is obtained using a non-linear component consisting of a microstrip line gap covered by several graphene layers. The operation of these circuits is established through a two step analysis in which the input and output passive sub-systems used are individually analyzed and optimized in terms of broad operational bandwidth in the corresponding frequency bands. The simulations are validated by experimental results obtained through the fabrication and measurement of the prototypes. The results presented in this chapter represent the first realization of a Single Stage High Order, $N = 5$ to 17, Frequency Multiplier in which the output signal in the $140 - 500$ GHz has been generated throughout frequency multiplication due to the non-linear electromagnetic behavior of a multi-layer graphene film.

Furthermore, in Chapter 3 a mixing topology has been developed starting from the design considerations proposed in Chapter 2. In this way, three circuits are intended as part of a front-end block for a submillimeter wave/THz band transmission and/or reception system. The non-linear dynamics of these circuits, that perform several functions, such as the generation of the local oscillator signal and the high order harmonic mixing are studied. Thus, the behavior of the considered High Order Subharmonic Graphene based Mixers is analyzed through electromagnetic simulations and further validated through the experimental characterization of the prototypes. The work presented in this chapter represents the first realization of Single Stage Subharmonic Mixers, based on a multi-layer graphene film, which are experimentally characterized in both up- and downconversion for the high harmonic orders between 6 and 18.

Finally, in Chapter 4 a 7^{th} Order Frequency Multiplier based on a Resonant Cavity which integrates a mono-/multi-layer graphene film is proposed. The approach is based on a novel single stage topology in which graphene sheets are placed inside a resonant cavity, to ensure that they are exposed to high electric field levels. The efficient excitation of high order harmonic components requires exciting the graphene sheet with relatively high electric field levels which makes the proposed approach an effective solution for increasing the efficiency of the whole system. Therefore, starting from the design of a main waveguide block structure with resonant features, several mono- and multi-layer graphene components are implemented and one at a time arranged inside it. The behavior of the circuits is analyzed through electromagnetic simulations and experimentally characterized through the fabrication and measurement of the prototypes.

Contents

List of Figures

List of Tables

Chapter 1

Analysis of Graphene behavior. Linear response. Non-linear response.

Contents

1.1 Introduction

Since the discovery of the one-atom thin single layer graphene sheet in 2004, an achievement for which A. Geim and K. Novoselov were awarded the Nobel price in 2010, many theoretical and experimental studies were conducted in order to investigate its properties. Their conclusions revealed that graphene has fascinating qualities that had never been noticed in any other material. For the first time, it was possible to isolate a two-dimensional sheet single atom thick. This is considered one of the thinnest material ever found. Prior to this discovery, the existence of 2-D crystals were doubted mainly due to the Mermin-Wagner theorem which states that a completely planar 2-D crystal looses its long-range order, and thus melts, at any small, non-zero temperature, due to thermal fluctuations [1],[2]. However, the discovery of graphene does not violate the Mermin-Wagner theorem since it was found that long range graphene has a rippled structure which causes it to curve. In other words, graphene becomes stable by slowly bending its structure in the third dimension on a scale of 100 Å [3] such that its fluctuations diverge at large length scale. An alternative point of view is that the 2-D crystal graphene was extracted from the highly stable 3-D graphitic stack and therefore it is packed in stable state.

Graphene is a monolayer of carbon atoms arranged together in a honeycomb lattice due to their sp^2 hybridization. Carbon can be found in nature under the form of 0-D fullerene, 1-D nanotubes, 3-D graphite or diamond. Some of its allotropes are presented in Figure 1.1.

During the last few years, graphene has become a popular research topic for experimental and theoretical researchers basically because of its unique properties such as high carrier mobility [5], mechanical strength [6], operation at high frequency [7], high thermal conductivity and generation of high order harmonic components [8]. These characteristics together with the possibility to scale the device which incorporates it down to nanometer-size (the thickness of monolayer graphene is 3.4Å) have made graphene a promising material which can be integrated in many electronics applications.

Graphene seems to be one of the materials which erased the gap between the engineering applications and basic theoretical research studies. Methods that enable the use of graphene in applications such as graphene-based transistors [9], graphene-based mixers [10] and multipliers [11] are developed simultaneously. Therefore, graphene may be considered the element for which the theoretical predictions are helpful in designing and analyzing experiments and new applications.

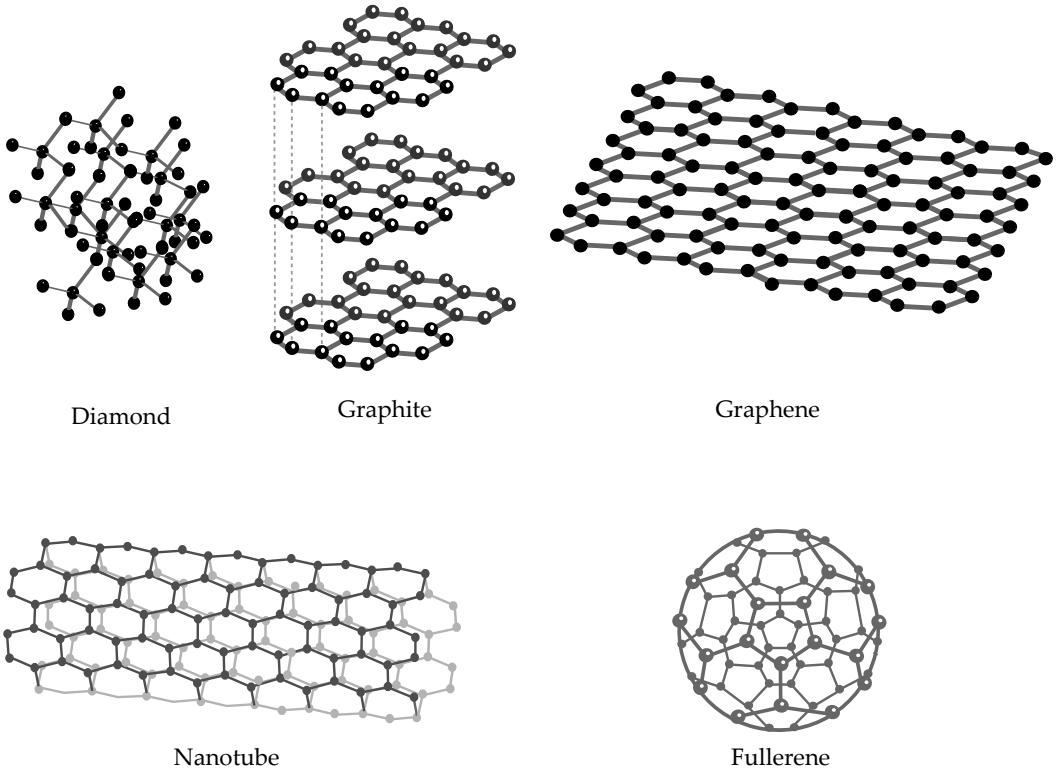

Figure 1.1: Some carbon allotropes. Graphite and Diamond are known since ancient times. Fullerenes were discovered in 1985 and nanotubes in 1991 [4]. Graphene was first isolated from graphite via mechanical exfoliation in 2004.

The purpose of this chapter is to present a theoretical analysis of the graphene band structure. All the important characteristics of graphene on which this Thesis is focused on, like the generation of harmonic components that enable the frequency mixing and multiplication operations, are a result of its exceptional electronic band structure. Therefore, Section 1.2 will describe the hybridization process of carbon atoms. The formation of σ and π bonds will be discussed, the last one being responsible for the electronic conduction of graphene electrons. In Section 1.3 the spectrum of the wave functions of graphene electrons in the tight-binding approximation is presented.

The linear response of a graphene layer irradiated with an external uniform electric field is introduced in Section 1.4. The expression of the first order conductivity is calculated using the Drude model for transport of electrons in the material. Section 1.5 contains a study of the non-linear electromagnetic response of graphene. The derivation of the third, fifth and seventh order harmonic components of graphene are being discussed. The non-linear conductivity of each of the previously mentioned harmonics is calculated. Graphene can generate only odd order harmonic components due to its central symmetry. When irradiated with two parallel polarized waves it can act as a frequency mixer with the inputs at the two applied waves. Section 1.6 introduces a study of the emitted power density for high order harmonic components of graphene.

Finally, the optimal number of graphene layers required to acquire maximum intensity of generation of the n^{th} order harmonic is being addressed in Section 1.8.

1.2 Hybridization of Carbon Atoms

Carbon, the fundamental component of graphene, has the atomic number $Z = 6$. The six electrons in the atomic ground state are in the configuration $1s^2 2s^2 2p^2$ ($1s^2 2s^2 2p_x^1 2p_y^1 2p_z^0$) which means that two electrons fill the inner energy level and four occupy the outer energy level of $2s$ and $2p$ orbitals [12]. According to this configuration, carbon has two half-filled orbitals and it should be bivalent.

The $2p$ orbitals are 4 eV higher than the $2s$ orbitals which means that it is energetically favorable to place two electrons on the $2s$ orbital and the remaining two on the $2p$ orbital as in Figure 1.2. However, when carbon enters in contact with other atoms (H, O or other C atoms) and they share electrons to form covalent bonds it is favorable to excite one electron from the $2s$ to the $2p$ orbital in order to form more covalent bonds. The energy gain produced from the covalent bond is generally bigger than the 4 eV required to produce the electron jump. Thus, in

the excited state carbon needs four electrons from other atoms to acquire a stable configuration and hence this explains the tetravalency of it [12].

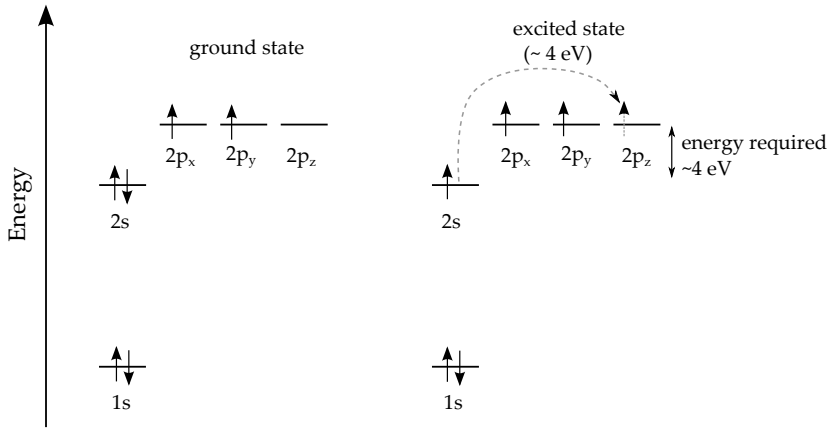

Figure 1.2: Ground state electronic configuration of Carbon (left), when there is no interaction between electrons, and in the excited state, when the electrons interact (right).

The electronic configuration in the excited state may be written as $1s^2 2s^1 2p^3$ ($1s^2 2s^1 2p_x^1 2p_y^1 2p_z^1$). The s and p orbitals have different energy and shape and therefore the carbon atoms form two types of bonds. Three bonds are formed with three electrons from the $2p$ orbitals and one bond is formed with the electron from the $2s$ orbitals. The superposition of the one $2s$ orbital with a number n of $2p$ orbitals is called sp^n hybridization and this concept is essential in the covalent carbon bond.

1.2.1 sp^2 hybridization

The sp^2 hybridization is the combination of one $2s$ orbital with two $2p$ orbitals, mainly the $2p_x$ and $2p_y$ states while leaving one $2p$ orbital ($2p_z$) untouched. The result is a set of three sp^2 hybrid orbitals of equal energy arranged in a trigonal planar configuration (Figure 1.3). The characteristic angle between the hybrid orbitals is 120° and they are linked by a σ bond. The remaining $2p_z$ orbital is perpendicular to the sp^2 hybrid orbitals and form a π bond [13].

A classical example of a sp^2 hybridized structure, where carbon layers are disposed in parallel one with respect to the other, is multi-layered graphene (graphite). The π orbitals produce weak van der Waals interactions between the layers of graphite and as a result they can be exfoliated easily.

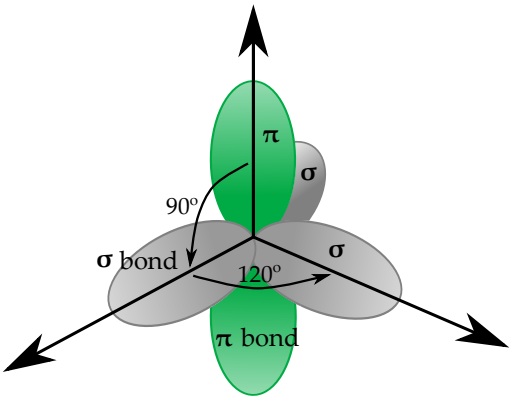

Figure 1.3: Schematic view of the sp^2 hybridization.

1.3 Energy band structure of graphene

The majority of the graphene properties are a result of the special band structure at the Fermi level. Wallace [14] first described in 1947 the band structure of graphite using the tight binding model. He reported that the conduction and the valence band of a single graphite layer are not separated by a gap and at the same time they do not overlap. In reality they have conical shape and they intersect in two of the high symmetry points, denoted by K and K' also called Dirac points in the Brillouin zone. Near these points the energy varies linearly with the magnitude of momentum. Because the conduction and the valence band intersect, graphene is described as a zero gap semiconductor, or a semimetal. The Fermi level for graphene is situated at the Dirac points. The Dirac point is the crossing point of the linear energy dispersion from the Dirac equation.

The linear dispersion of the electronic band structure near the K-point in graphene has charge carriers with zero effective mass. Its value is:

$$E = \pm \hbar v_F |\overrightarrow{k}| = \pm \hbar v_F \sqrt{k_x^2 + k_y^2} \tag{1.1}$$

where $\hbar$ is the reduced Plank constant, v_F is the Fermi velocity and $\overrightarrow{k}$ is the electron wave vector. This equation is similar to that of photons, $E = \pm \hbar c |\overrightarrow{k}|$, with the difference that the velocity of light c is changed by the Fermi velocity, v_F. The measured value of the Fermi velocity is v_F=$10^6 m/s$ which is about 300 times slower than the speed of light. Thus, particles inside graphene propagate at much slower speed than speed of light and so they are characterized by a non-relativistic quantum theory.

This linear approximation of the band structure near Fermi level is also called the Dirac approximation. Because of this linear approximation, near the Dirac points, graphene exhibits properties distinct to those noticed in traditional materials, which have non-zero effective mass m and are characterized by a parabolic energy dispersion $E = \pm\hbar^2 k^2/2m$.

The band structure of graphene will be discussed more in detail in a subsequent subsection.

1.3.1 Graphene lattice

The carbon atom from the honeycomb lattice forms three σ bonds with three nearest neighboring carbon atoms. These covalent C-C bonds are almost similar to the bonds holding diamond together and as a result the mechanical and thermal properties of graphene are very much alike to those of diamond. The last valence electron occupies the p_z orbital which is perpendicular to the graphene layer and it overlaps with the π orbital of its nearest neighbor. As a consequence a half filled π bond is formed and it is responsible for the electron conduction in the graphene layer. The σ electronic bands are entirely occupied and have a considerable separation in energy from the π bands and therefore they do not contribute to the electrical properties of graphene [15].

The graphene structure can be described by two sublattices A and B. Both sublattices are considered triangular Bravais lattices and therefore the honeycomb lattice can be seen as triangular Bravais lattice with a two atom nucleus A and B (Figure 1.4) [16]. For the two triangular Bravais lattices, all points within A and B sublattice are equivalent and any vector connecting lattice points are considered lattice vectors. The dashed lines from the Figure 1.4 shows the boundaries of the elementary unit cell.

The two lattice vectors of the hexagonal/triangular Bravais lattice take the form:

$$\begin{aligned} \overrightarrow{a_1} &= a\sin 30^\circ\ \overrightarrow{x} + a\cos 30^\circ\ \overrightarrow{y} = a(\frac{1}{2}, \frac{\sqrt{3}}{2}) \\ \overrightarrow{a_2} &= -\,a\cos 30^\circ\ \overrightarrow{x} + a\cos 30^\circ\ \overrightarrow{y} = a(-\frac{1}{2}, \frac{\sqrt{3}}{2}) \end{aligned} \tag{1.2}$$

with $|\overrightarrow{a_1}|=|\overrightarrow{a_2}|=a$, where a is the lattice constant which according to measurements, equals $a = 2.46$ Å.

The three vectors which link one point from the first sublattice with a nearest neighbor from the second sublattice are given by the expressions:

$$\begin{aligned}
\overrightarrow{b_1} &= \frac{a}{\sqrt{3}}\overrightarrow{y} = a(0, \frac{1}{\sqrt{3}}) \\
\overrightarrow{b_2} &= -\overrightarrow{a_2} + \overrightarrow{b_1} = \frac{a}{2}\overrightarrow{x} - \frac{a}{2\sqrt{3}}\overrightarrow{y} = a(\frac{1}{2}, -\frac{1}{2\sqrt{3}}) \\
\overrightarrow{b_3} &= -\overrightarrow{a_1} + \overrightarrow{b_1} = -\frac{a}{2}\overrightarrow{x} - \frac{a}{2\sqrt{3}}\overrightarrow{y} = a(-\frac{1}{2}, -\frac{1}{2\sqrt{3}})
\end{aligned} \tag{1.3}$$

with $|\overrightarrow{b_1}|=|\overrightarrow{b_2}|=|\overrightarrow{b_3}|=\frac{a}{\sqrt{3}}$=1.42 Å.

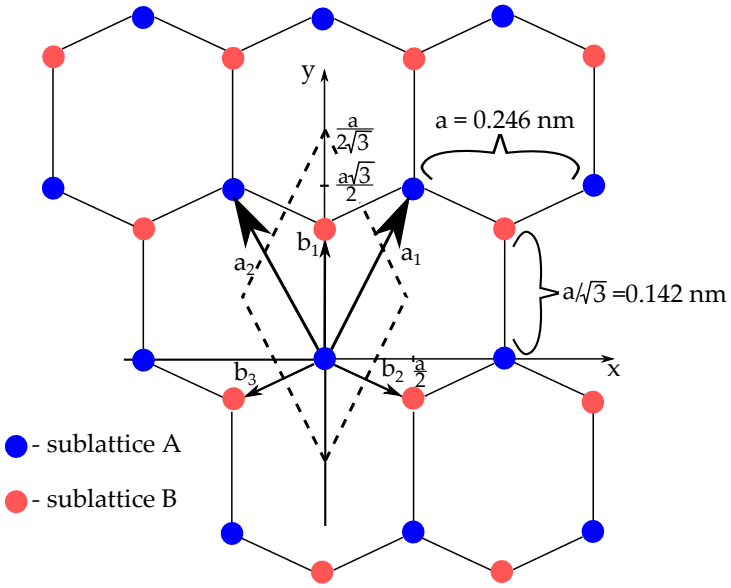

Figure 1.4: Honeycomb lattice of graphene. The elementary unit cell is the dashed region with a basis of two atoms A and B, the angle between the two lattice vectors $\overrightarrow{a_1}$ and $\overrightarrow{a_2}$ is 60°.

Both sublattices are filled with carbon atoms, so that graphene has two atoms per elementary cell. The area of the elementary unit cell is given by the formula:

$$A_{cell} = a^2\frac{\sqrt{3}}{2} = 0.0524nm^2. \tag{1.4}$$

The total density of carbon atoms in the graphene lattice is:

$$N_{Catoms} = \frac{2}{A_{cell}} = 38nm^{-2} = 3.8 \times 10^{15} cm^{-2}. \tag{1.5}$$

The honeycomb lattice has one π electron per carbon atom that is not participating in the covalent σ bond and therefore the density of these electrons is equal to that of the carbon atoms [15].

The reciprocal lattice, described relative to the triangular Bravais lattice, is represented in Figure 1.5 . The reciprocal vectors a_1^* and a_2^* defined by the condition $a_i \cdot a_j^* = 2\pi\delta_{ij}$ are:

$$a_1^* = \frac{2\pi}{a}(1, \frac{1}{\sqrt{3}}), \quad a_2^* = \frac{2\pi}{a}(-1, \frac{1}{\sqrt{3}}). \tag{1.6}$$

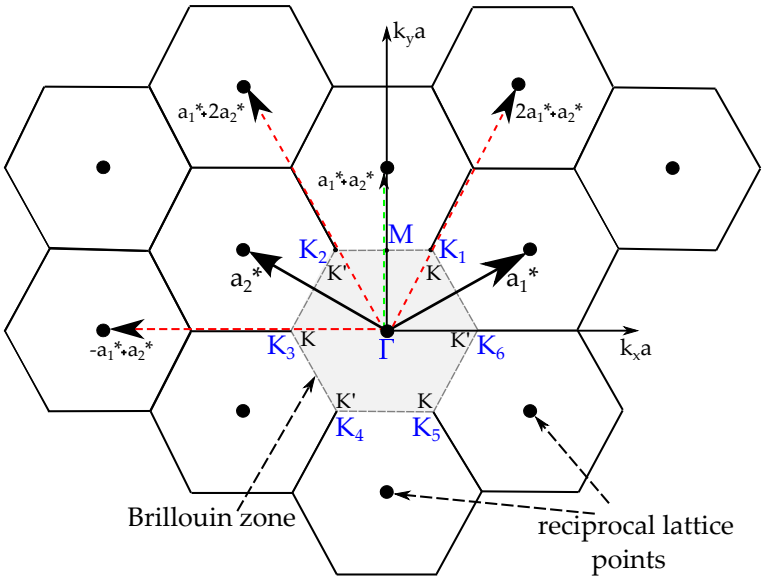

Figure 1.5: Reciprocal lattice of graphene with its primitive lattice vectors a_1^* and a_2^*. The gray dashed region represents the Brillouin zone with its high symmetry points Γ, M and K (K'). The green dashed arrow and the red dashed arrows represent how ΓM vector respectively ΓK ($\Gamma K'$) vector can be calculated using the two reciprocal vectors a_1^* and a_2^*. The odd numbered corners of the Brillouin zone are considered the $K - points$ while the even numbered corners the $K' - points$.

The 2-D reciprocal lattice is spanned by the two primitive vectors a_1^* and a_2^* of length $\beta = \frac{4\pi}{a\sqrt{3}}$. The Brillouin zone of graphene has hexagonal form as the original

honeycomb lattice and it is bounded by the planes which divide into two the vectors connecting the nearest neighbor points of the reciprocal lattice. This is why the Brillouin zone is rotated with respect to the original honeycomb lattice by $\pi/2$.

There are three main locations of high symmetry in the Brillouin zone. These locations are its center, the $\Gamma - point$, the middle of its edges, the $M - points$, and its corners, the $K - points$ [15]. The vectors indicating the position of the $M - point$ and $K - point$ with respect to the center of the Brillouin zone are:

$$\Gamma M = \frac{1}{2}(\vec{a_1}* + \vec{a_2}*) = \frac{2\pi}{a\sqrt{3}}k_y = \frac{2\pi}{a}(0, \frac{1}{\sqrt{3}}) \tag{1.7}$$

$$\begin{aligned}
\Gamma K_1 =& \frac{1}{3}(2 \cdot \vec{a_1}* + \vec{a_2}*) = \frac{2\pi}{3a}k_x + \frac{2\pi}{a\sqrt{3}}k_y = \frac{2\pi}{a}(\frac{1}{3}, \frac{1}{\sqrt{3}}) \\
\Gamma K_2 =& \frac{1}{3}(\vec{a_1}* + 2 \cdot \vec{a_2}*) = -\frac{2\pi}{3a}k_x + \frac{2\pi}{a\sqrt{3}}k_y = \frac{2\pi}{a}(-\frac{1}{3}, \frac{1}{\sqrt{3}}) \\
\Gamma K_3 =& \frac{1}{3}(-\vec{a_1}* + \vec{a_2}*) = -\frac{4\pi}{3a}k_x = \frac{2\pi}{a}(-\frac{2}{3}, 0) \\
\Gamma K_4 =& -\Gamma K_1 = -\frac{2\pi}{a}(\frac{1}{3}, \frac{1}{\sqrt{3}}) \\
\Gamma K_5 =& -\Gamma K_2 = -\frac{2\pi}{a}(-\frac{1}{3}, \frac{1}{\sqrt{3}}) \\
\Gamma K_6 =& -\Gamma K_3 = -\frac{2\pi}{a}(-\frac{2}{3}, 0)
\end{aligned} \tag{1.8}$$

The Brillouin zone has six $K - points$ and six $M - points$. Every second corner of the Brillouin zone is equivalent since they are connected by reciprocal lattice vectors (they differ only by addition or subtraction operations of the reciprocal basis vectors) [17]. Therefore only two corners K and K' should be considered in the Brillouin zone as points where the conduction band intersects the valence band, and they are called Dirac points.

1.3.2 Electronic configuration

The electronic band structure of graphene is directly associated with the unhybridized p_z orbital which overlaps with the nearest neighbors to form π bonds. The π electrons are responsible for the electronic properties of graphene close to the Dirac points mainly at low energies.

The band structure of graphene can be determined using a tight-binding model approximation [14]. In order to find the band structure of graphene (E-k depen-

dence) the eigenvalues of the Dirac equation in the non-relativistic approximation and at low energies (Schrödinger equation) are to be calculated:

$$H\xi = E\xi \tag{1.9}$$

where H is the Hamiltonian of π graphene electrons, ξ is the total wavefunction and E is the electron energy in the π orbital of graphene [18].

As the elementary unit cell of graphene has two carbon atoms, A and B, the total wavefunction ξ can be written as a linear combination of two Bloch functions Φ_A and Φ_B:

$$\xi(\overrightarrow{k}, \overrightarrow{r}) = \Psi_A\Phi_A(\overrightarrow{k}, \overrightarrow{r}) + \Psi_B\Phi_B(\overrightarrow{k}, \overrightarrow{r}). \tag{1.10}$$

The wavefunctions Φ_A and Φ_B are given by:

$$\Phi_{A(B)}(\overrightarrow{k}, \overrightarrow{r}) = \frac{1}{\sqrt{N}} \sum_{A(B)}^{N} e^{i\overrightarrow{k}\cdot\vec{r}_{A(B)}} X(\overrightarrow{r} - \vec{r}_{A(B)}) \tag{1.11}$$

where this sum is taken over all the A(B) carbon atoms in the lattice, $X(\overrightarrow{r})$ is the π orbital wave function for an isolated carbon atom, $\vec{r}_{A(B)}$ denotes the position of the A(B) atom and N is the number of unit cells in the honeycomb lattice. The factor $\frac{1}{\sqrt{N}}$ ensures that the Bloch wavefunctions are normalized and $e^{i\vec{k}\cdot\vec{r}_{A(B)}}$ contains the periodicity of the lattice [18].

In order to obtain the energy eigenvalues, the total wavefunction from Eq. 1.10 is substituted in the Schrödinger Eq. 1.9, it is multiplied by the complex conjugate Φ_A^* and integrated over the whole 2-D space [15]. The procedure is repeated for Φ_B^* resulting in a system of two equations as follows:

$$\begin{aligned}
\int_\Omega \Phi_A^* H(\Psi_A\Phi_A + \Psi_B\Phi_B)dr &= \int_\Omega \Phi_A^* E(\Psi_A\Phi_A + \Psi_B\Phi_B)dr \\
\int_\Omega \Phi_B^* H(\Psi_A\Phi_A + \Psi_B\Phi_B)dr &= \int_\Omega \Phi_B^* E(\Psi_A\Phi_A + \Psi_B\Phi_B)dr
\end{aligned} \tag{1.12}$$

Ψ_A and Ψ_B are not dependent on r so they can be dragged in front of the integral. The matrix elements H_{ij} and S_{ij} are described as:

$$H_{ij} = \int_{\Omega} \Phi_i^* H \Phi_j dr \;\; with \;\; i,j \in \{A,B\}$$
$$S_{ij} = \int_{\Omega} \Phi_i^* \Phi_j dr \;\; with \;\; i,j \in \{A,B\} \tag{1.13}$$

H_{ij} is the transfer integral matrix element or the Hamiltonian of the matrix elements. S_{ij} is the overlap integral matrix element between Bloch functions. It defines the overlap strength of the π orbitals on different carbon atoms.

The Schrödinger equation can be written in the matrix form as:

$$\begin{pmatrix} H_{AA} & H_{AB} \\ H_{BA} & H_{BB} \end{pmatrix} \begin{pmatrix} \Psi_A \\ \Psi_B \end{pmatrix} = E \begin{pmatrix} S_{AA} & S_{AB} \\ S_{BA} & S_{BB} \end{pmatrix} \begin{pmatrix} \Psi_A \\ \Psi_B \end{pmatrix}. \tag{1.14}$$

The A sub-lattice is equivalent to the B sub-lattice so $H_{AA} = H_{BB}$ and $S_{AA} = S_{BB}$. In graphene lattice the nearest neighbors of an A atom are all atoms of the B sub-lattice. Further it is considered that the overlapping between two nearest neighbor atoms is neglected $S_{AB} = S_{BA} = 0$ [19].

The overlap integral equation between two identical A atoms can be easily calculated from Eq. 1.13:

$$S_{AA} = \int_{\Omega} \Phi_A^* \Phi_A dr. \tag{1.15}$$

Inserting the Bloch function Φ_A, it is obtained:

$$S_{AA'} = \frac{1}{N} \sum_{A,A'}^{N} e^{-i\vec{k}\cdot(\vec{r}_A - \vec{r}_{A'})} \int X^*(\vec{r} - \vec{r}_A) \cdot X(\vec{r} - \vec{r}_{A'}) d^3r \tag{1.16}$$

where $r_A = r_{A'} \rightarrow S_{AA} = 1$. But it was assumed that sub-lattice A is equivalent to sub-lattice B thus $S_{AA} = S_{BB} = 1$.

The determinant of the Schrödinger equation gives the total energy of the π orbitals.

$$\begin{vmatrix} H_{AA} - E & H_{AB} \\ H_{BA} & H_{BB} - E \end{vmatrix} = 0 \tag{1.17}$$

The solution:

$$E = H_{AA} \pm \sqrt{H_{AB} \cdot H_{BA}} \tag{1.18}$$

is the relation of the energy eigenvalues in terms of the Hamiltonian.

The diagonal elements H_{AA} and H_{BB} can be calculated from Eq. 1.13 as:

$$H_{AA} = \int_{\Omega} \Phi_A^* H \Phi_A dr. \tag{1.19}$$

Inserting the Bloch function Φ_A , it is obtained:

$$H_{AA} = \frac{1}{N} \sum_{A,A'}^{N} e^{-i\vec{k}\cdot(\vec{r}_A - \vec{r}_{A'})} \int X^*(\vec{r} - \vec{r}_A) \cdot H \cdot X(\vec{r} - \vec{r}_{A'}) d^3r \tag{1.20}$$

where $r_A = r_{A'}$, so:

$$H_{AA} = \int X^*(\vec{r} - \vec{r}_A) \cdot H \cdot X(\vec{r} - \vec{r}_A) d^3r = E_0 \tag{1.21}$$

where E_0 is a constant energy shift between $A(B)$ carbon atoms [19].

The off-diagonal elements H_{AB} and H_{BA} can be calculated from Eq. 1.13 as:

$$H_{AB} = \int_{\Omega} \Phi_A^* H \Phi_B dr \tag{1.22}$$

where $H_{BA} = H_{AB}^*$.

After inserting the Bloch functions Φ_A and Φ_B the definition becomes:

$$H_{AB} = \frac{1}{N} \sum_{A,B}^{N} e^{-i\vec{k}\cdot(\vec{r}_A - \vec{r}_B)} \int X^*(\vec{r} - \vec{r}_A) \cdot H \cdot X(\vec{r} - \vec{r}_B) d^3r. \tag{1.23}$$

As it was mentioned before, the A carbon atom in graphene has three nearest neighbor B atoms. The vectors describing the bonds are defined by $\vec{r}_A - \vec{r}_B = \vec{b}_j$, where $\vec{b}_j$ was computed in Eq. 1.3. The matrix element can be rewritten in the form:

$$\begin{aligned} H_{AB} =& \frac{1}{N}\sum_{j} e^{-i\vec{k}\cdot\vec{b}_j}\int X^*(\vec{r})\cdot H\cdot X(\vec{r}-\vec{b}_j)d^3r \\ =& (e^{-i\vec{k}\cdot\vec{b}_1}+e^{-i\vec{k}\cdot\vec{b}_2}+e^{-i\vec{k}\cdot\vec{b}_3})\int X^*(\vec{r})\cdot H\cdot X(\vec{r}-\vec{b}_j)d^3r. \end{aligned} \tag{1.24}$$

The interaction between nearest neighbor atoms is defined as in [19]:

$$\int X^*(\vec{r})\cdot H\cdot X(\vec{r}-\vec{b}_j)d^3r = \gamma_0. \tag{1.25}$$

Substituting the values of the vector points b_j from Eq. 1.3 into the off-diagonal element H_{AB} from Eq. 1.25 leads to the following expression:

$$\begin{aligned} H_{AB} =& (e^{-i\vec{k}\cdot\vec{b}_1}+e^{-i\vec{k}\cdot\vec{b}_2}+e^{-i\vec{k}\cdot\vec{b}_3})\gamma_0 \\ =& (e^{-i\frac{a}{\sqrt{3}}k_y}+e^{-i\frac{a}{2}k_x}\cdot e^{i\frac{a}{2\sqrt{3}}k_y}+e^{i\frac{a}{2}k_x}\cdot e^{i\frac{a}{2\sqrt{3}}k_y})\gamma_0 \\ =& (e^{-i\frac{a}{\sqrt{3}}k_y}+e^{i\frac{a}{2\sqrt{3}}k_y}\cdot 2\cos(\frac{a}{2}k_x))\gamma_0 \end{aligned} \tag{1.26}$$

The off-diagonal element $H_{BA} = H^*_{AB}$ can be calculated using the same principle.

$$H^*_{AB} = (e^{i\frac{a}{\sqrt{3}}k_y}+e^{-i\frac{a}{2\sqrt{3}}k_y}\cdot 2\cos(\frac{a}{2}k_x))\gamma_0. \tag{1.27}$$

The equation of the total energy, Eq. 1.18, is then recalculated and the following formula is obtained:

$$E = E_0 \pm \gamma_0\left[1+4\cos(\frac{a}{2}k_x)\cos(\frac{a\sqrt{3}}{2}k_y)+4\cos^2(\frac{a}{2}k_x)\right]^{\frac{1}{2}} \tag{1.28}$$

where the negative sign refers to the valence band and the positive sign to the conduction band respectively.

From this equation, it results that the total energy E, depends on the energy E_0, which is a constant energy shift and for simplicity it was assumed zero, and the interaction between nearest neighbor atoms γ_0 [18].

As already stated, graphene has three main locations of high symmetry, the $\Gamma - point$, the $M - point$ and the $K - point$. At the $K - point$ the total energy

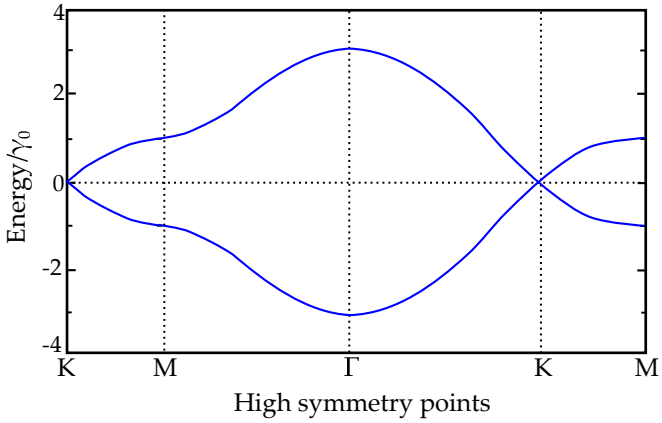

Figure 1.6: Energy dispersion of the π electrons in graphene along the $\Gamma - point$, $M - point$ and $K - point$.

calculated from Eq. 1.28, when the energy shift $E_0 = 0$ is zero. This indicates that the valence and the conduction bands touch each other at the so called Dirac points K. For this reason graphene is considered a semimetal or a zero gap semiconductor. Figure 1.6 displays the representation of the energy dispersion plotted along the high symmetry points $\Gamma - K - M$.

The six corners of the Brillouin zone, the $K - points$ and $K' - points$, have a special importance in graphene as the total energy, calculated in Eq. 1.28, is zero when the Fermi energy is assumed at the intersection point between the valence and conduction band. Since each carbon atom has one π electron responsible for electronic properties, at $T = 0$ the valence band is completely filled, while the conduction band is completely empty. Thus graphene can be seen as a half-filled system. The energy width of each bands is assumed ~ 9 eV. Figure 1.7 presents the energy band structure of graphene for the first Brillouin zone calculated from Eq. 1.28.

Further, it is important to study the shape of the graphene band structure around Dirac points K and K'. As previously indicated, the energy dispersion close to these points is expected to have a conical shape. With this purpose a low energy expansion around the high symmetry points K respectively K' is conducted in the following subsection for small variations of the wave vector. The band structure of graphene from Figure 1.7 is analyzed. It results that the energy dispersion, when the Fermi energy varies in small intervals close to the intersection point between the energy bands, is linear at the six corners of the Brillouin zone [20]. The Fermi energy is assumed to have small variations basically because of the low energy needed to move

the electrons within the two bands in the linear energy regime. As stated earlier, a large energy of ~ 9 eV is required for an electron from the valence band to reach the highest state in the conduction band.

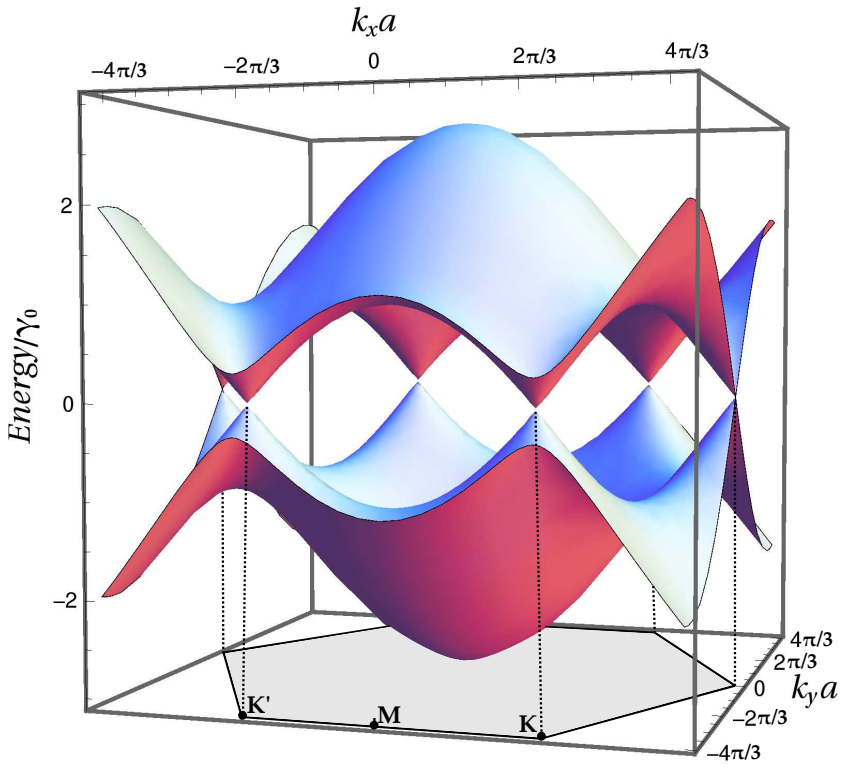

Figure 1.7: Band structure of the graphene electrons calculated using a tight-binding model approximation for the first Brillouin zone.

1.3.2.1 Conical shape of the energy dispersion

Consider that the wave vector $\vec{k}$ varies with a small vector $\vec{q}$ at the corners of the Brillouin zone as:

$$\vec{k} = \vec{K} + \vec{q} \; and \; \vec{k} = \vec{K'} + \vec{q} \tag{1.29}$$

where $q \ll K$ and $q \ll K$'. The two Dirac points K and K' are assumed to have the value $(k_x, k_y) = (\pm\frac{4\pi}{3a}, 0)$. The expansion can be conducted for any value of the six Dirac points calculated in Eq. 1.8.

In order to calculate the band structure of graphene at low energy, the expression of the Hamiltonian H_{AB} calculated in Eq. 1.26 is needed where the wave vector $\vec{k}$ is replaced with the assumption from Eq. 1.29 [21]. For simplicity it is taken $H_{AB} = h(k)$.

$$h(k) = h(K+q) = h(K'+q) = \gamma_0 \cdot \sum_j e^{-i(K+q)b_j} \approx \gamma_0 \cdot \sum_j e^{-iKb_j}(1 - iqb_j). \tag{1.30}$$

In this equation, the identity:

$$\gamma_0 \sum_j e^{-iKb_j} = 0 \tag{1.31}$$

at the Dirac point $(k_x, k_y) = (\pm\frac{4\pi}{3a}, 0)$ and where the vector points b_j are the three nearest neighbor vectors of an isolated carbon atom calculated in Eq. 1.3.

So, the expression of the Hamiltonian H_{AB} is reduced to:

$$h(k) = -i\gamma_0 \sum_j e^{-iKb_j} \cdot qb_j. \tag{1.32}$$

After some calculations, described in Appendix A, the definition of $h(k)$ becomes:

$$\begin{aligned} h(k) = &- i\gamma_0 \left[\frac{a}{\sqrt{3}} q_y e^{-i\frac{a}{\sqrt{3}}K_y} - 2i \sin\left(\frac{a}{2}K_x\right) \frac{a}{2} q_x e^{i\frac{a}{2\sqrt{3}}K_y} \right. \\ &\left. -2\cos(\frac{a}{2}K_x)\frac{a}{2\sqrt{3}} q_y e^{i\frac{a}{2\sqrt{3}}K_y} \right]. \end{aligned} \tag{1.33}$$

The shape of the dispersion relation of graphene near the Dirac points K can be determined by expanding $h(K+q)$ to the first order around Dirac points of value $(k_x, k_y) = \left(-\frac{4\pi}{3a}, 0\right)$.

$$h(k) = -\frac{a\sqrt{3}}{2}\gamma_0(-q_x + iq_y) \tag{1.34}$$

Similar calculations are performed by expanding $h(K'+q)$ around K' points of value $(k_x, k_y) = \left(\frac{4\pi}{3a}, 0\right)$ which gives:

$$h(k) = -\frac{a\sqrt{3}}{2}\gamma_0(q_x + iq_y). \tag{1.35}$$

The results of $h(k)$ vary only by one sign. This variation is also called valley index, so the expression of the Hamiltonian can be written like $H_{AB}=-\frac{a\sqrt{3}}{2}\gamma_0(\pm q_x + iq_y)$ [21]. From this equation it results that graphene has two valleys, the K valley which corresponds to -1 index and K' valley for +1 index.

Assuming the Fermi energy is very close to the intersection point between the valence and conduction band so it can be considered zero, the total energy equation can be written as:

$$E = \pm\sqrt{H_{AB} \cdot H_{AB}^*}. \tag{1.36}$$

So the resulting energy dispersion is:

$$E = \pm\frac{a\sqrt{3}}{2}\gamma_0\sqrt{q_x^2 + q_y^2} = \pm\frac{a\sqrt{3}}{2}\gamma_0|q|. \tag{1.37}$$

This proves that the energy band structure of graphene is symmetrical in relation to $x-y$ plane at low energy and for small variations of the wave vector k. Moreover, the linear dispersion near K points can be approximated to the Fermi velocity of electrons v_F as:

$$\frac{dE}{dk}\Big\|_K = \frac{a\sqrt{3}}{2}\gamma_0 = \hbar v_F \ ; \ \frac{dE}{dp}\Big\|_K = v_F \tag{1.38}$$

$$p = \hbar k \tag{1.39}$$

Figure 1.8 presents the conical shape of the dispersion relation calculated from Eq. 1.37 for $E_0 = 0$ and in the vicinity of the Dirac points K and K'.

The velocity of electrons v_F in graphene has a constant value, $\approx 10^6 m/s$, for any carrier concentration.

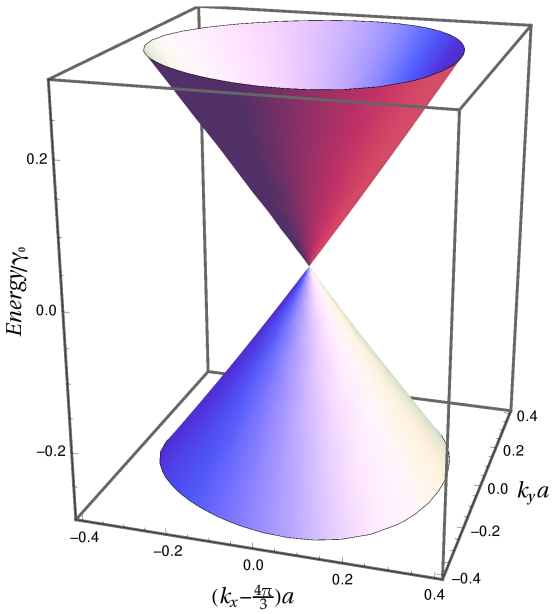

Figure 1.8: Linear energy dispersion of graphene around Dirac point $K' = K_6$. At low energies the conical structure is visible.

Thus, the total energy dispersion of π electrons in graphene near the Dirac points is:

$$E = \pm \hbar v_F \sqrt{q_x^2 + q_y^2}. \tag{1.40}$$

This is similar to the dispersion relation calculated using the Dirac equation from relativistic theory:

$$\frac{E^2}{c^2} - p^2 = m^2 c^2 \tag{1.41}$$

$$E = \pm\sqrt{(m^2c^4 + c^2p^2)} \tag{1.42}$$

with zero effective mass $m = 0$ and the speed of light c replaced by the Fermi velocity, v_F.

1.4 Linear response of Graphene

In order to calculate the graphene conductivity, the transport of electrons in the material, a monolayer graphene sheet is irradiated with an external uniform electric field. The layer is lying in the $x - y$ plane. For a better calculation of the graphene conductivity it is necessary to first investigate the charge carrier density for a particle placed in the 2-D $x - y$ system. For this it is assumed that the Fermi energy ϵ_F lies close to the intersection point between the conduction and the valence band and the temperature T tends to zero so $T \ll \epsilon_F$ [8]. The external electromagnetic radiation is linearly polarized in the $x-$ direction, and has the form $E_x(t) = E_0 \cos \omega t$. As previously stated, graphene is considered to have a central symmetry and thus identical results are expected when the external electromagnetic radiation is linearly polarized in $x-$ direction as well as in $y-$ direction.

Further, it is considered that the particles are placed in an electron-impurity system, a system of free electrons with distributed impurities. The momentum distribution function of electrons $f_p(t)$ can be calculated by solving the Boltzmann kinetic equation. The variation in the distribution function $f_p(t)$ can be produced by the force acting on the electrons in the 2-D momentum space and by collisions. The general form of the Boltzmann equation is:

$$\frac{\partial f_p(t)}{\partial t} + \frac{\partial f_p(t)}{\partial t}\bigg|_{force} = \frac{\partial f_p(t)}{\partial t}\bigg|_{collision}. \tag{1.43}$$

Newton's second law of motion states that:

$$F_E = \frac{\partial p}{\partial t} \tag{1.44}$$

where F_E is the electrical force which takes the value $F_E = -e \cdot E\,(t)$.

The force expression from Eq. 1.43 produced by the electrical force F_E which acts on the electron particles is:

$$\left.\frac{\partial f_p(t)}{\partial t}\right|_{force} = \frac{\partial p}{\partial t} \cdot \frac{\partial f_p(t)}{\partial p} = -eE_x(t) \cdot \frac{\partial f_p(t)}{\partial p_x}. \tag{1.45}$$

Thus, the kinetic Boltzmann equation where the collisions of electrons with impurities inside the lattice structure have been neglected is:

$$\frac{\partial f_p(t)}{\partial t} - eE_x(t) \cdot \frac{\partial f_p(t)}{\partial p_x} = 0. \tag{1.46}$$

The solution of the Eq. 1.46 is:

$$f_p(t) = F_0(p_x - p_0(t), p_y) \tag{1.47}$$

where

$$F_0(p_x, p_y) = \left[1 + exp\left(\frac{v_F\sqrt{p_x^2 + p_y^2} - \epsilon_F}{T}\right)\right]^{-1} \tag{1.48}$$

is the Fermi-Dirac distribution function or the electronic distribution function, and in Eq. 1.47, $p_0(t) = -e\int_{-\infty}^{t} E_x(t)dt$ is the solution of the single particle equation of motion [8].

Knowing this, the charge carrier density can be written as:

$$n_s = \frac{g_s g_v}{S}\sum_p f_p(t) \tag{1.49}$$

where S is the area of the sample and $g_s = g_v = 2$ are the spin and valley degeneracies in graphene.

At absolute zero temperature, $T = 0$, the Fermi-Dirac distribution function becomes the Heaviside Step Function:

$$F_0(p_x - p_0(t), p_y) = \theta\left[p_F^2 - (p_x - p_0(t))^2 - p_y^2\right]. \tag{1.50}$$

Working with polar coordinates, the expression of the charge carrier density:

$$n_s = \frac{g_s g_v}{S} \cdot \frac{S}{(2\pi\hbar)^2} \iint dp_x dp_y f_p(t) \tag{1.51}$$

becomes:

$$n_s = \frac{g_s g_v}{(2\pi\hbar)^2} \int_{-p_F}^{p_F} dp_y \int_{p_0-\sqrt{p_F^2-p_y^2}}^{p_0+\sqrt{p_F^2-p_y^2}} dp_x, \tag{1.52}$$

where p_F is the Fermi momentum of charge particles in graphene which have Fermi energy [8].

After performing some transformations on Eq. 1.52, which are presented in some detail in Appendix B, the general formula of the charge carrier density becomes:

$$n_s = \frac{g_s g_v p_F^2}{4\pi\hbar^2}. \tag{1.53}$$

1.4.1 First order Conductivity

The Drude model for transport of electrons in materials is used for the calculation of the linear graphene conductivity. First, the case of a simple parabolic energy band model normally used in traditional materials will be considered. The linear conductivity of such materials will be determined followed by an expansion of this interpretation for graphene particles with zero rest mass.

The Drude model uses the presumption that electrons in metals can move about freely, with straight trajectories, from atom to atom according to Newton's laws until they are scattered by ions or other lattice impurities. No forces act on them during the travel time before collision. After an electron has been scattered its momentum is completely random. By applying an external uniform linearly polarized electromagnetic radiation $E_x(t)$ the electron motion, on average, can be determined by using a differential equation which represents the effect of the total forces acting on one charge carrier with negative charge $-e$.

Consider that the momentum of an electron at any time t is known and it has the expression $p_x(t)$. On the next time interval, $t + dt$, the electron can suffer a collision. The probability of collision in short time intervals dt is $P_c = dt/\tau$, where τ is the average time an electron travels before suffering collision or it can be interpreted also as relaxation time, the time between two collisions. The expression

of the momentum in this case is $p_c\left(t+dt\right) = F_x\left(t\right)dt$. The other event which can happen is that the electron suffers no collision. The probability of no collision is $P_{nc} = \left(1 - dt/\tau\right)$ basically because $P_c + P_{nc} = 1$. Under the circumstance of no scattering, the electron can evolve normally according to Newton's laws. The expression of the momentum is then $p_{nc}(t+dt) = p_x(t) + F_x(t)dt$ [23].

Thus, the new momentum is:

$$\begin{aligned} p_x\left(t+dt\right) =& P_c \cdot p_c\left(t+dt\right) + P_{nc} \cdot p_{nc}\left(t+dt\right) \\ =& \frac{dt}{\tau} F_x\left(t\right) dt + \left(1 - \frac{dt}{\tau}\right)\left[p_x\left(t\right) + F_x\left(t\right) dt\right] \\ =& p_x\left(t\right) - \frac{dt}{\tau} p_x\left(t\right) + F_x\left(t\right) dt. \end{aligned} \tag{1.54}$$

So, the Drude equation of motion can be written as:

$$\frac{dp_x(t)}{dt} = -\frac{p_x(t)}{\tau} - eE_x(t). \tag{1.55}$$

The external electric field applied, $E_x(t) = \Re\left[E_x\left(\omega\right) e^{-i\omega t}\right]$, has a periodic behavior and is assumed to be time-dependent with frequency ω . Therefore, the solution of the differential Eq. 1.55 has to take the form $p_x(t) = \Re\left[p_x\left(\omega\right) e^{-i\omega t}\right]$, so:

$$-i\omega p_x(\omega) = -\frac{p_x\left(\omega\right)}{\tau} - eE_x\left(\omega\right). \tag{1.56}$$

After some calculations, the solution of Eq. 1.56 becomes:

$$p_x(\omega) = \frac{-e\tau}{1 - i\omega\tau} E_x\left(\omega\right). \tag{1.57}$$

The current density of electrons which move with velocity $\overrightarrow{v} = \frac{\overrightarrow{p}}{m}$ inside a traditional parabolic material is $\overrightarrow{j} = -en_s\overrightarrow{v}$, where n_s is the charge carrier density of electrons and m the effective electron mass. Inserting Eq. 1.57 into the definition of the electron current density leads to the expression of the current $\overrightarrow{j}$ [23]:

$$j_x(\omega) = \frac{n_s e^2 \tau}{m(1 - i\omega\tau)} E_x(\omega). \tag{1.58}$$

From Ohm's law $\overrightarrow{j} = \sigma \overrightarrow{E}$, the AC electrical conductivity of a traditional semiconductor can be written as:

$$\sigma(\omega) = \frac{\sigma_0}{1 - i\omega\tau}. \tag{1.59}$$

In this equation σ_0 is the DC conductivity. It's value is:

$$\sigma_0 = \frac{n_s e^2 \tau}{m}. \tag{1.60}$$

It is advantageous to insert into the equation of the AC electrical conductivity the reciprocal value of the relaxation time τ, called scattering rate, $\gamma = 1/\tau$. By inserting this value, the conductivity becomes independent of τ:

$$\sigma(\omega) = \frac{i n_s e^2}{m(\omega + i\gamma)}. \tag{1.61}$$

In graphene, near K points in the electronic band structure, the rest mass of an electron is zero. The Fermi momentum of charge particles in graphene having Fermi energy is $p_F = \frac{\epsilon_F}{v_F}$. In [24]-[26] it was assumed that the effective mass of graphene takes the value:

$$m = \frac{\epsilon_F}{v_F^2}. \tag{1.62}$$

Replacing the above consideration of the graphene effective mass into Eq. 1.61, one can obtain the general form of the 2-D linear graphene conductivity (Drude conductivity) [17]:

$$\sigma_{2D}(\omega) = \frac{e^2 v_F}{\hbar} \sqrt{\frac{n_s}{\pi}} \frac{i}{\omega + i/\tau}. \tag{1.63}$$

Consider a $3-D$ finite sample of an ordinary material, their linear response should be described by a conductivity equal to:

$$\sigma_{3D} = \frac{\sigma_{2D}}{d}. \tag{1.64}$$

In the above equation, d is the thickness of the material taken as model. This thickness has to be significantly smaller than the skin depth in order to have a uniform electric field distribution along the considered sample [27]. Under this assumption, the current density is directly proportional to the electric field and the electrical conductivity is the coefficient of proportionality, thus the Ohm's law: $j_\omega = \sigma \cdot E_\omega$ is being fulfilled.

Consider the sample analyzed is irradiated with an external electromagnetic wave, the amplitude of such a wave will decrease exponentially when passing through the sample. The interval at which the intensity of radiation has decreased to about 37% of the incident value is defined as the skin depth or penetration depth δ, which can be expressed as:

$$\delta = \frac{c}{\sqrt{2\pi\sigma_{3D}\omega\mu}} \tag{1.65}$$

where ω is the angular frequency, c is the speed of light and μ is the permeability of the material [28].

However, when the skin depth becomes comparable to the sample thickness d, the carriers can no longer be assumed to move under the effect of a constant field, and the current at any point can be influenced by values of the electric field from any position along the sample.

When working with finite $3-D$ multiple layered graphene (graphite), the linear response of the whole assembly should be express as: $N \cdot \sigma_{3D}$, where N is the number of graphene layers and σ_{3D} is the $3-D$ anisotropic conductivity with finite thickness which can be calculated as in Eq. 1.64.

1.5 Non-linear electromagnetic response of graphene

In order to demonstrate the non-linear behavior of graphene, a $2-D$ particle with negative charge $-e$ and energy spectrum $E = \hbar v_F \sqrt{k_x^2 + k_y^2}$ is being considered. The particle is accelerated with an external electric field of the form $E_x(t) = E_0 \cos\omega t$, as represented in Figure 1.9(a), similar with the work presented

in Ref [29]. Note that all the available calculations found in the state of the art literature analyzed the non-linearity of graphene up to the third order. The higher order non-linear calculations presented in this chapter are completely new and they have been developed for the purpose of this thesis.

According to Newton's second law of motion shown in Eq. 1.44, the momentum equation of the mentioned particles can be written as:

$$p_x(t) = -e\frac{E_0}{\omega}\sin\omega t. \tag{1.66}$$

Figure 1.9(b) shows the momentum behavior of the particle.

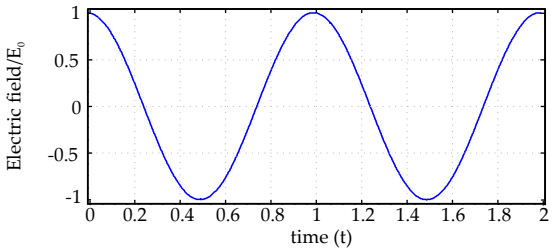

(a) Electric field as a function of time.

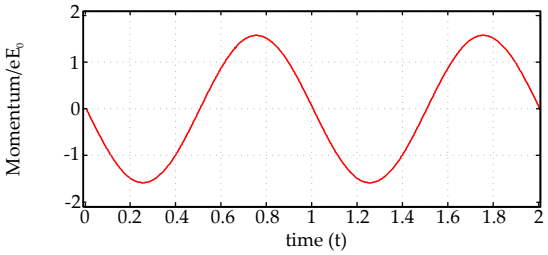

(b) Momentum as a function of time.

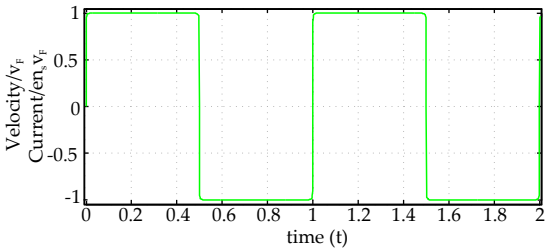

(c) Velocity and current density as a function of time.

Figure 1.9: Behavior of a particle with energy spectrum $E = v_F\sqrt{p_x^2 + p_y^2}$.

As demonstrated earlier, in conventional semiconductors which have parabolic energy dispersion, $E = p^2/2m$, the charge carrier velocity $v = \partial E/\partial p = p/m$, as well as the current density $j = -en_s v$, are proportional to momentum p. So considering the same external electric field, $E_x(t)$, the system response is a linear one as it responds always to the same frequency ω.

On the contrary, in graphene the charge carrier velocity takes the form:

$$v_x = \frac{\partial E}{\partial p_x} = v_F \frac{p_x}{\sqrt{p_x^2 + p_y^2}}. \tag{1.67}$$

Now if p_y is considered zero, $v_x = v_F \cdot p_x / |p_x|$ which is a non-linear function dependent on p_x. This demonstrates the graphene non-linear behavior [8]. The expression of graphene charge carrier velocity is then:

$$v_x(t) = v_F \cdot sgn(\sin \omega t) \tag{1.68}$$

while the expression of the graphene current density is:

$$\begin{aligned} j_x(t) =& en_s v_F \cdot sgn(\sin \omega t) \\ =& en_s v_F \frac{4}{\pi}\left(\sin \omega t + \frac{1}{3}\sin 3\omega t + \frac{1}{5}\sin 5\omega t + ...\right) \end{aligned} \tag{1.69}$$

The current density from Eq. 1.69 (plotted in Figure 1.9(c)) consists of only odd Fourier harmonics. The amplitude of each Fourier harmonic gives the amplitude of its corresponding current density. As an important remark, the value of the current density, j_n, where n is the harmonic number, decreases with the inverse of the harmonic number n [8]. Thus, a single layer of graphene sheet can act as a non-linear material generating high order harmonic components when excited with an external uniform linearly polarized electric field $E_x(t) = E_0 \cos \omega t$.

Moreover, the electric field is not present in the expression of the current density calculated in Eq. 1.69. This indicates that the above expansion is not entirely accurate. As stated in Ref [8] and Ref [29] the above analysis is not taking into account the Fermi distribution of charge carriers (electrons and holes) over the quantum states in the energy bands of graphene. To overcome this problem the solution proposed in Ref [8] and Ref [29] is to first compute the momentum distribution function of electrons by solving the kinetic Boltzmann equation presented in Eq. 1.46, and

then calculate the current density of electrons inside the material using the formula: $\overrightarrow{j} = -en_s\overrightarrow{v}$. The charge carrier density of electrons n_s under this assumption was already computed in Eq. 1.49 and thus, the current density of electrons can be written as:

$$j\left(t\right) = -e \cdot \frac{g_s g_v}{S} \sum_p v \cdot f_p\left(t\right). \tag{1.70}$$

At absolute zero temperature, the Fermi-Dirac distribution function, calculated in Eq. 1.47 becomes the Heaviside Step Function (see Eq. 1.50). Polar coordinates are used to integrate the Fermi-Dirac distribution function over the entire 2-D space and so the expression of the current density becomes:

$$j_x\left(t\right) = -e\frac{g_s g_v v_F}{\left(2\pi\hbar\right)^2}\int\int dp_x dp_y \frac{p_x}{\sqrt{p_x^2+p_y^2}} \cdot f_p\left(t\right) \tag{1.71}$$

where $g_s = g_v = 2$ are the spin and valley degeneracies in graphene and S is the area of the sample.

Likewise in Eq. 1.52, using the definition of the Heaviside Step Function, the current density of electrons can be written as:

$$j_x\left(t\right) = -e\frac{g_s g_v v_F}{\left(2\pi\hbar\right)^2}\int_{-p_F}^{p_F} dp_y \int_{p_0-\sqrt{p_F^2-p_y^2}}^{p_0+\sqrt{p_F^2-p_y^2}} dp_x \frac{p_x}{\sqrt{p_x^2+p_y^2}}. \tag{1.72}$$

After performing some transformations and the integration over the y space, Eq. 1.72 is rewritten as:

$$j_x = -\frac{2ev_F}{\left(\pi\hbar\right)^2}\int_0^{\pi/2} p_F^2\cos x\, dx \cdot \sqrt{Q^2+1}\left(\sqrt{1-\frac{2Q}{Q^2+1}\cos x}\right.$$
$$\left. - \sqrt{1+\frac{2Q}{Q^2+1}\cos x}\right) \tag{1.73}$$

where similar to Ref [8] the parameter $Q = -\frac{p_0(t)}{p_F} = \frac{eE_0 v_F}{\omega\varepsilon_F}\sin\omega t = Q_0\sin\omega t$ is used which is assumed to be proportional to the electric field $E_x\left(t\right)$.

Under the condition $\left|\frac{2Q}{Q^2+1}\right| < 1, \forall Q$, $\sqrt{1-\frac{2Q}{Q^2+1}\cos x}$ and $\sqrt{1+\frac{2Q}{Q^2+1}\cos x}$ are expanded up to the seventh order. After some extended transformations (detailed calculation in Appendix C) and replacing the value of the charge carrier density n_s calculated in Eq. 1.53, for $Q_0 < 1$ the expression of the current density becomes:

$$j_x(t) = en_s v_F \left(Q_0 \sin\omega t - \frac{4}{2^5} Q_0^3 \sin^3\omega t - \frac{1}{2^6} Q_0^5 \sin^5\omega t - \frac{5}{2^{10}} Q_0^7 \sin^7\omega t \right). \quad (1.74)$$

From the above equation the contribution of the 1^{st}, 3^{rd}, 5^{th} and 7^{th} harmonic components to the current density are needed. Thus the current density of electrons from Eq. 1.74 where $Q_0 < 1$ can be written in the final form as:

$$\begin{aligned} j_x(t) =& en_s v_F \left\{ \sin\omega t \left[Q_0 - \frac{3}{2^5} Q_0^3 - \frac{10}{2^{10}} Q_0^5 - \frac{175}{2^{16}} Q_0^7 \right] \right. \\ &+ \sin 3\omega t \left[\frac{1}{2^5} Q_0^3 + \frac{5}{2^{10}} Q_0^5 + \frac{105}{2^{16}} Q_0^7 \right] \\ &+ \sin 5\omega t \left[-\frac{1}{2^{10}} Q_0^5 - \frac{35}{2^{16}} Q_0^7 \right] \\ &\left. + \sin 7\omega t \frac{5}{2^{16}} Q_0^7 \right\} \end{aligned} \quad (1.75)$$

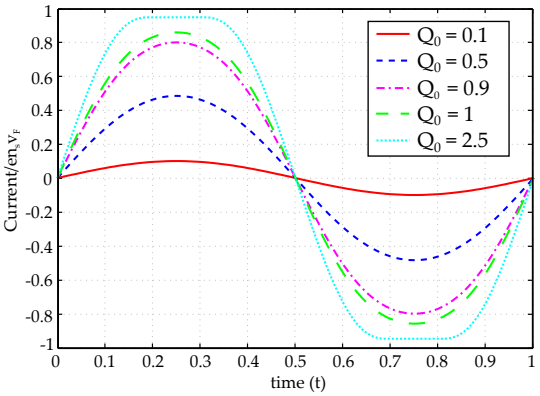

Figure 1.10: Current density of electrons calculated while taking into account the Fermi distribution of charge carriers over the quantum states in the energy band structure of graphene.

Figure 1.10 presents the total current density of electrons calculated in Eq. 1.73 for different values of the field parameter Q_0. For high value of the field parameter Q_0 the time dependence of the current density becomes similar with the one calculated

in Eq. 1.69 (see Figure 1.9(c)). All the calculations of the high harmonic current density and conductivity developed further on are under condition $Q_0 < 1$.

$$Q_0 = \frac{eE_0 v_F}{\omega \varepsilon_F} < 1 \tag{1.76}$$

Thus, the low-field condition 1.76 is fulfilled for an electric field:

$$E_0 < \frac{\omega \varepsilon_F}{e v_F} = \frac{\omega \hbar \sqrt{\pi n_s}}{e}. \tag{1.77}$$

At $f \simeq 40$ GHz and $n_s \simeq 10^{12}$ cm^{-2}, the inequality 1.77 is satisfied for $E_0 \lesssim 300$ V cm^{-1}.

Eq. 1.75 provides the amplitude of the 1^{st}, 3^{rd}, 5^{th} and 7^{th} order current harmonic without taking into account the scattering of the electrons inside the lattice structure. Figure 1.11 displays the representation of the amplitudes. The Fourier component of each current amplitudes, as demonstrated in [31], is the product between the corresponding n^{th} order non-linear conductivity, $\sigma^{n\omega}$, and the Fourier component of the electric field E_ω :

$$j_{n\omega} = \sigma^{n\omega} \cdot (E_\omega)^n \tag{1.78}$$

where $E_x(t) = E_0 \cos \omega t = \frac{E_0}{2}\left(e^{i\omega t} + e^{-i\omega t}\right) = E_\omega \left(e^{i\omega t} + e^{-i\omega t}\right)$.

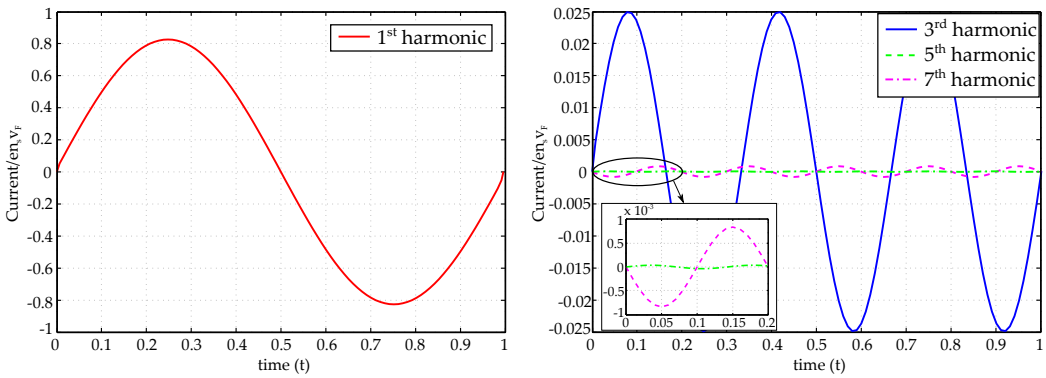

Figure 1.11: Representation of the current density amplitudes for the 1^{st}, 3^{rd}, 5^{th} and 7^{th} order harmonics when the field parameter $Q_0 = 0.9$.

1.5.1 3^{rd} order Harmonic Component

The third order current density due to the contribution of the third harmonic component generated in the graphene layer has the form:

$$j_x(t) = en_s v_F \cdot \frac{1}{2^5} Q_0^3 \sin 3\omega t. \tag{1.79}$$

where as $Q_0 < 1$, the other terms corresponding to the third harmonic in Eq. 1.75 can be neglected.

One can transform the above equation from the time domain to the frequency domain using Fourier transformation which gives the following third order frequency domain current density:

$$j_{3\omega} = -ien_s v_F \frac{Q_0^3}{64}. \tag{1.80}$$

The field parameter $Q_0 = \frac{eE_0 v_F}{\omega \varepsilon_F}$ thus, the current density from Eq. 1.80 becomes:

$$j_{3\omega} = -ien_s v_F \frac{e^3 v_F^3}{8\omega^3 \varepsilon_F^3} E_\omega^3. \tag{1.81}$$

From Eq. 1.81, the amplitude of the third order harmonic current can be interpreted as the product between the third order conductivity multiplied by the electric field cubed of the fundamental harmonic, taken from the linear response of graphene.

The third order non-linear conductivity, assuming that the electrons travel freely inside the lattice structure and they are not scattered by ions or other impurities, is:

$$\sigma^{3\omega} = -\frac{ie^4 v_F}{8\pi \hbar^3 \sqrt{\pi n_s}} \cdot \frac{1}{\omega^3}. \tag{1.82}$$

For more precise results the equation of the third harmonic component has to be derived in the presence of electron collisions. Likewise in the case of graphene linear response (Drude model) the relaxation time τ is considered, as the time between two collisions, and this parameter is introduced in the equation of the non-linear conductivity:

$$\sigma^{3\omega} = -\frac{1}{4}\frac{e^4 v_F}{\pi\hbar^3\sqrt{\pi n_s}} \cdot \frac{3i}{(3\omega + i/\tau)(2\omega + i/\tau)(\omega + i/\tau)}. \tag{1.83}$$

1.5.2 5^{th} order Harmonic Component

From the general equation of the current density of electrons in the collisionless approximation, expressed in Eq. 1.75, one can extract the fifth order graphene current density:

$$j_x(t) = -en_s v_F \cdot \frac{1}{2^{10}} Q_0^5 \sin 5\omega t. \tag{1.84}$$

The above equation is written in the time domain. For the calculation of the fifth order conductivity it is necessary to determine the frequency domain current by applying the Fourier transformation to Eq. 1.84. Thus, the fifth order frequency domain current density is:

$$j_{5\omega} = ien_s v_F \frac{Q_0^5}{2^{11}}. \tag{1.85}$$

Inserting the value of the field parameter Q_0, the current from Eq. 1.85 becomes:

$$j_{5\omega} = ien_s v_F \frac{e^5 v_F^5}{2^6 \omega^5 \varepsilon_F^5} E_\omega^5. \tag{1.86}$$

The fifth order non-linear conductivity in the collisionless approximation, knowing that $j_{5\omega} = \sigma^{5\omega} \cdot (E_\omega)^5$ from Eq. 1.78, is:

$$\sigma^{5\omega} = \frac{ie^6 v_F}{2^6 \hbar^5 \pi^2 n_s \sqrt{\pi n_s}} \cdot \frac{1}{\omega^5}. \tag{1.87}$$

The above equation considers that the electrons suffer no collisions. For more accurate results it is required to take into account scattering. Under this assumption, the fifth order conductivity can be written as:

$$\sigma^{5\omega} = \frac{3}{8}\frac{e^6 v_F}{\hbar^5 \pi^2 n_s \sqrt{\pi n_s}} \cdot \frac{5i}{(5\omega + i/\tau)(4\omega + i/\tau)(3\omega + i/\tau)} \cdot \frac{1}{(2\omega + i/\tau)(\omega + i/\tau)} \tag{1.88}$$

1.5.3 7^{th} order Harmonic Component

The seventh order current density of a monolayer graphene sheet calculated taking into account the Fermi distribution of charge carriers over the energy states in the graphene band structure is:

$$j_x(t) = e n_s v_F \cdot \frac{5}{2^{16}} Q_0^7 \sin 7\omega t. \tag{1.89}$$

The frequency domain seventh order current density calculated from Eq. 1.89 assumes the form:

$$j_{7\omega} = -ie n_s v_F \cdot \frac{5}{2^{17}} \left(\frac{e \cdot 2E_\omega v_F}{\omega \varepsilon_F}\right)^7. \tag{1.90}$$

Then the seventh order non-linear conductivity calculated under the assumption of no scattering inside the lattice structure is:

$$\sigma^{7\omega} = -\frac{5ie^8 v_F}{2^{10}\pi\hbar^7 (\pi n_s)^2 \sqrt{\pi n_s}} \cdot \frac{1}{\omega^7}. \tag{1.91}$$

The above equation is not entirely accurate as it is not taking into account collisions between electrons. To get a more precise description of the problem, the relaxation time τ, the average time an electron travels before suffering a collision, is introduced so that:

$$\sigma^{7\omega} = \frac{5^2 \cdot 3^2}{2^6}\frac{e^8 v_F}{\pi\hbar^7 (\pi n_s)^2 \sqrt{\pi n_s}} \cdot \frac{-7i}{(7\omega + i/\tau)(6\omega + i/\tau)(5\omega + i/\tau)(4\omega + i/\tau)} \cdot \frac{1}{(3\omega + i/\tau)(2\omega + i/\tau)(\omega + i/\tau)} \tag{1.92}$$

1.6 Frequency mixing effect in graphene

Consider a graphene layer which is irradiated by an external uniform electric field of the form:

$$E_x(t) = E_1 \cos \omega_1 t + E_2 \cos \omega_2 t \tag{1.93}$$

where E_1 and E_2 are incident parallel polarized waves [30].

As in the previous section, the momentum distribution function of electrons is computed by solving the Boltzmann equation 1.46, and then the current density of electrons flowing inside the material is calculated ($\overrightarrow{j} = -en_s \overrightarrow{v}$).

According to Newton's second law of motion from Eq. 1.44, the electrical force F_E under the action of the external electric field as expressed in Eq. 1.93 is:

$$F_E = \frac{\partial p_x}{\partial t} = -e\left(E_1 \cos \omega_1 t + E_2 \cos \omega_2 t\right). \tag{1.94}$$

The momentum equation of electrons accelerated with an external electromagnetic radiation polarized in the x- direction is then:

$$p_x(t) = -\frac{eE_1}{\omega_1} \sin \omega_1 t - \frac{eE_2}{\omega_2} \sin \omega_2 t. \tag{1.95}$$

The current density of electrons indicated in Eq. 1.70, solved under the assumption of an external uniform electric field with two incident parallel polarized waves is:

$$j_x(t) = en_s v_F \left(Q_x(t) - \frac{4}{2^5} Q_x^3(t) - \frac{1}{2^6} Q_x^5(t) - \frac{5}{2^{10}} Q_x^7(t)\right) \tag{1.96}$$

where $Q_x(t)$ is a field parameter, $Q_x(t) = -\frac{p_0(t)}{p_F} = \frac{eE_1 v_F}{\omega_1 \varepsilon_F} \sin \omega_1 t + \frac{eE_2 v_F}{\omega_2 \varepsilon_F} \sin \omega_2 t$.

Similar to the previous section, the equation of the current density was expanded up to the seventh order, so in Eq. 1.96 there are the contributions of the 1^{st}, 3^{rd}, 5^{th}, and 7^{th} harmonic components of the current.

The Fourier components of such a current contain the following terms:

⋆ first order harmonics: ω_1, ω_2

- ⋆ third order harmonics: $3\omega_1, 3\omega_2, 2\omega_1 \pm \omega_2, 2\omega_2 \pm \omega_1$
- ⋆ fifth order harmonics: $5\omega_1, 5\omega_2, 4\omega_1 \pm \omega_2, 4\omega_2 \pm \omega_1, 3\omega_1 \pm 2\omega_2, 3\omega_2 \pm 2\omega_1$
- ⋆ seventh order harmonics: $7\omega_1, 7\omega_2, 6\omega_1 \pm \omega_2, 6\omega_2 \pm \omega_1, 4\omega_1 \pm 3\omega_2, 4\omega_2 \pm 3\omega_1, 2\omega_1 \pm 5\omega_2, 2\omega_2 \pm 5\omega_1$

1.6.1 3^{rd}, 5^{th} and 7^{th} order Current

Considering the emission at the frequency $\omega_{e1} = 2\omega_1 - \omega_2$. The third order current generated at the mentioned frequency ω_{e1} in the graphene layer has the form:

$$j_x(t) = en_s v_F \cdot \frac{3}{2^5} Q_1^2 Q_2 \sin(2\omega_1 - \omega_2)\, t. \tag{1.97}$$

One can transform the above equation from time domain to frequency domain using the Fourier transformation, therefore:

$$j_{3\omega} = -ien_s v_F \frac{3}{64} Q_1^2 Q_2 \tag{1.98}$$

where the field parameter $Q_1 = \frac{eE_1 v_F}{\omega_1 \varepsilon_F}$ and $Q_2 = \frac{eE_2 v_F}{\omega_2 \varepsilon_F}$.

The third-order current density due to the contribution of two parallel polarized waves from Eq. 1.98, is three times bigger than the third-order current density due to the contribution of one linearly polarized wave, obtained in Eq. 1.80 when $E_1 = E_2 = E_0$.

Next, the emission at the randomly chosen frequency $\omega_{e2} = 4\omega_1 - \omega_2$ is studied. The fifth-order current generated at the frequency ω_{e2} in the graphene particles has the form:

$$j_x(t) = -en_s v_F \cdot \frac{5}{2^{10}} Q_1^4 Q_2 \sin(4\omega_1 - \omega_2)\, t. \tag{1.99}$$

The Fourier transformation of the above current is:

$$j_{5\omega} = en_s v_F \cdot \frac{5}{2^{11}} Q_1^4 Q_2. \tag{1.100}$$

Eq. 1.100 was obtained in the presence of two parallel polarized waves, E_1 and E_2. Under the assumption that $E_1 = E_2 = E_0$, the fifth-order current density previously calculated is five times bigger than the current density from Eq. 1.85 which considers the contribution of a monochromatic linearly polarized wave.

Furthermore, owing to the contribution of the same two parallel polarized waves, E_1 and E_2, at the frequency $\omega_{e3} = 6\omega_1 - \omega_2$ the generation of the seventh-order harmonic is considered. The seventh-order current density calculated from Eq. 1.96 at this frequency is:

$$j_x(t) = en_s v_F \cdot \frac{5 \cdot 7}{2^{16}} Q_1^6 Q_2 \sin(6\omega_1 - \omega_2)\, t. \tag{1.101}$$

Applying the Fourier transformation to Eq. 1.101 one obtains:

$$j_{7\omega} = en_s v_F \cdot \frac{5 \cdot 7}{2^{17}} Q_1^6 Q_2. \tag{1.102}$$

Eq. 1.102 is seven times bigger than its corresponding Eq. 1.100 which discusses the case of a single linearly polarized wave, E_0.

Thus, after the above analysis, one can conclude that the n^{th} order harmonic of the graphene current density increases with the harmonic number n when two incident parallel polarized waves are applied from an external source.

1.7 Emitted power density of the n^{th} order harmonics

The case of a single layer graphene sheet lying on a dielectric substrate of thickness d and refractive index $n_1 = \sqrt{\varepsilon_1}$, similar with work done in Ref [31], is studied. The graphene particles are accelerated by an external uniform linearly polarized electromagnetic radiation $E_x(t) = E_0 \cos \omega t$. This radiation has periodic behavior, is time-dependent with a frequency ω and has the power density I_ω. The aim of this analysis is to examine the influence of a dielectric material on the graphene efficiency of generating high order harmonic components. With this purpose two situations will be studied.

The first situation consist in analyzing a configuration type graphene - dielectric slab (Figure 1.12(a)). In such a configuration, when $n_1 = 1$ (air propagation of the electromagnetic radiation) one can evaluate the case of a suspended (isolated) graphene.

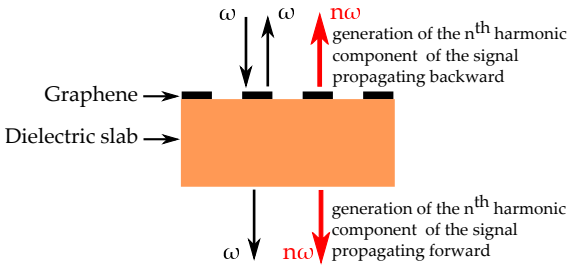

(a) Graphene - dielectric slab configuration

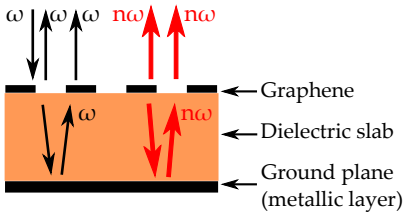

(b) Graphene - dielectric slab - metallic ground configuration

Figure 1.12: Analysis of n^{th} order graphene emitted power density.

The second situation consist in analyzing a structure type graphene - dielectric slab - metallic layer (Figure 1.12(b)). When the thickness of the metallic layer d_{Metal} is sufficiently large it could become opaque to any harmonic radiation. Therefore, it is predicted that the high order harmonic signal generated in the forward direction will be reflected by the metallic layer. This signal is mixed with the corresponding high order harmonic signal generated in the backward direction and thus the total intensity is expected to increase.

In the real case the metallic layer can both absorb and reflect the high order harmonic signal. In this work it is assumed that the absorption is minimum such that the intensity of the high order signal generated forward and reflected by the metallic layer $I_{n\omega-forwards}$ is similar to the high order signal generated backward ($I_{n\omega-backwards} \approx I_{n\omega-forwards}$). Thus, the intensity of the high order emitted signal in both (forward and backward) directions, when they are in phase, equals $2I_{n\omega}$, where $I_{n\omega} = I_{n\omega-backwards} = I_{n\omega-forwards}$.

The intensity of the emitted radiation in one direction (forward or backward) as stated in Ref [30] and Ref [16] can be determined by the Poynting theorem. Thus, the energy density of a monochromatic propagating wave ($E_x(t)$) is:

$$u = \frac{1}{2 \cdot 2\pi} |E_\omega|^2 . \tag{1.103}$$

The intensity, I_ω, is obtained multiplying the above expression by the wave velocity which propagates in free space, c :

$$I_\omega = \frac{c}{4\pi} |E_\omega|^2 \propto |E_\omega|^2 . \tag{1.104}$$

According to Eq. 1.78, the Fourier component of the n^{th} order non-linear harmonic of the current density in the case of an isolated graphene layer has the form: $j_{n\omega} = \sigma^{n\omega} \cdot (E_\omega)^n = \sigma^{n\omega} \cdot (E_0/2)^n$. Moreover, the Fourier amplitude of the electric and magnetic field of such harmonic is proportional to the corresponding non-linear current (from Maxwell's equations):

$$E_{n\omega} \propto H_{n\omega} \propto j_{n\omega} = \sigma^{n\omega} \cdot (E_\omega)^n \tag{1.105}$$

Thus, the intensity of the emitted n^{th} order radiation, $I_{n\omega}$, for an isolated graphene layer is:

$$I_{n\omega} = \frac{c}{4\pi} |E_{n\omega}|^2 \propto |E_{n\omega}|^2 \propto |\sigma^{n\omega}|^2 I_\omega^n \tag{1.106}$$

In Ref [31] it is shown that the third-order intensity $I_{3\omega-diel}$ emitted from a graphene layer placed on a dielectric substrate, similar with the case previously analyzed (Figure 1.12(a)), is an oscillating function dependent on the thickness of the dielectric d. The authors have proved that in the points of maxima the values of the third-order intensity generated on the graphene layer are identical to the case of isolated graphene (Eq. 1.106). On such points of maxima the dielectric thickness equal to integer numbers of half-wavelengths ($\lambda_{3\omega}/\sqrt{\varepsilon_1}$) :

$$d = \frac{\lambda_{3\omega}}{2\sqrt{\varepsilon_1}} \cdot m,\ m = 0, 1, 2... \tag{1.107}$$

Their study can be extended to the case of n^{th} harmonic generation examined in this work.

In Ref [31] the case of a graphene layer placed on a dielectric slab with the bottom side metalized, similar with the second case previously analyzed (Figure 1.12(b)), is also investigated. The bottom metallic layer of thickness d_{Metal} acts as a mirror reflecting back the third-order emitted signal. In the corresponding geometry due to the boundary conditions, the tangential electric field at the plane containing the metallic layer should be zero ($E_{\omega\perp-Metal} = 0$). It was assumed that the intensity is an oscillating function dependent on the thickness d of the dielectric layer. With the new boundary condition defined, the maximum intensity of the third order signal is reached when the dielectric thickness d equals to integer numbers of quarter-wavelengths:

$$d = \frac{\lambda_{n\omega}}{2\sqrt{\varepsilon_1}}(m + \frac{1}{2}), \;\; m = 0, 1, 2... \tag{1.108}$$

On the points of maxima, the third order intensity $I_{3\omega-Metal}$ generated on the graphene layer (backward and forward) placed on a dielectric slab metalized on the back side has similar value to $I_{3\omega}$ from the case of isolated graphene (Eq. 1.106). On such points the total third order harmonic intensity emitted by the graphene layer in both forward and backward directions equals $2I_{3\omega}$.

The work done in Ref [31] refers to the third-harmonic case while a more general analysis for the n^{th} harmonic component is being studied further on.

The total n^{th} harmonic power generated on the surface of the graphene layer, in the presence of a dielectric slab metalized on the back side (Figure 1.12(b)), and emitted in both backward and forward directions can be written using Eq. 1.106 as:

$$I_{n\omega-Metal} \approx 2\left|E_{n\omega-Metal}\right|^2. \tag{1.109}$$

Moreover, the electric field of the fundamental harmonic generated on the graphene layer $E_{\omega-Metal}$ is two times bigger than the incident electromagnetic radiation E_ω due to the reflection of the forward generated wave on the metallic wall. Under this condition, the n^{th} order current can be written as:

$$j_{n\omega-Metal} \approx \sigma^{n\omega}\left(2E_\omega\right)^n. \tag{1.110}$$

The Fourier amplitude of the electric and magnetic field of the n^{th} order harmonic is proportional to the corresponding non-linear current. Since the n^{th} order wave is reflected back from the metallic wall:

$$E_{n\omega-Metal} \propto H_{n\omega-Metal} \propto 2j_{n\omega-Metal} = 2^{n+1}\sigma^{n\omega}\cdot\left(E_\omega\right)^n. \tag{1.111}$$

Thus, the total emitted n^{th} order power (both directions) is:

$$I_{n\omega-Metal} \approx 2^{2n+3}\left|\sigma^{n\omega}\cdot\left(E_\omega\right)^n\right|^2. \tag{1.112}$$

Comparing the n^{th} order emitted power in the presence of the metalized dielectric

slab (Figure 1.12(b)) and in the absence of it (Figure 1.12(a)) one can conclude that the total emitted power (backward and forward) increases with a factor of $2^{2(n+1)}$ when the metallic wall acts as a mirror reflecting the forward generated signal. For an even higher increase of the n^{th} order emitted power the structure type graphene - dielectric slab - metallic layer can be placed inside a resonant cavity with a high quality factor.

1.8 Optimal number of graphene layers

When calculating the optimal number of graphene layers the absorption phenomena is one of the most important aspect which should be taken into account. The electromagnetic radiation absorbed by each layer of graphene in the microwave range is about $20-25\%$ of the incident radiation [32]. The absorption of electromagnetic radiation inside a material is defined as the transfer of energy from the incoming wave to the material as the wave passes through it. The absorption is highly dependent on the radiating frequency of the incident wave [33]. As the wave passes through the material its amplitude will decrease exponentially because part of it is absorbed by the material and part is reflected. From the energy conservation law, the total absorption inside a n layered structure, as the case of n layered graphene, can be defined as: $A = 1 - T - R$, where T is the total transmitted signal and R the total reflected signal by n layered graphene structure [32].

Furthermore, absorption means that the permittivity ε of the material must be seen as a complex variable which has an imaginary part [34]. This imaginary part of the complex permittivity indicates that the material is able to store energy inside it.

Consider an electromagnetic wave which interacts with a graphene layer producing moving charges and electric heat. The Maxwell's equation describing the generation of electric currents, also known as Ampere's law of induction, is:

$$\begin{aligned} \nabla \times \overrightarrow{H} &= \frac{4\pi}{c}\overrightarrow{j} + \frac{1}{c}\frac{\partial \overrightarrow{D}}{\partial t} \\ &= \frac{4\pi}{c}\sigma \overrightarrow{E} + \frac{\varepsilon}{c}\frac{\partial \overrightarrow{E}}{\partial t} \end{aligned} \tag{1.113}$$

where $\overrightarrow{H}$ is the magnetic field and $\overrightarrow{D}$ is the electric displacement field which equals the electric field multiplied by the permittivity $\overrightarrow{D} = \varepsilon \overrightarrow{E}$. The linear conductivity, as calculated in Eq. 1.59 is a complex function therefore, $\sigma = \sigma' + i\sigma''$.

Take the electric field as: $E(x,t) = E_x(\omega)\, e^{i(kx-\omega t)}$. The time derivative of this field is: $\partial E(x,t)/\partial t = -i\omega E(x,t)$. Inserting the time derivative of the electric field into Eq. 1.113 it is obtained that:

$$\nabla \times \overrightarrow{H} = \frac{1}{c}\left[i\frac{4\pi}{\omega}\left(\sigma' + i\sigma''\right) + \varepsilon\right]\frac{\partial \overrightarrow{E}}{\partial t} = \frac{\varepsilon(\omega)}{c}\frac{\partial \overrightarrow{E}}{\partial t}. \tag{1.114}$$

This equation describes that graphene can have complex permittivity with value:

$$\varepsilon(\omega) = \varepsilon - \frac{4\pi\sigma''}{\omega} + i\frac{4\pi\sigma'}{\omega}. \tag{1.115}$$

Because the permittivity is a complex function $\varepsilon(\omega)$, the refraction index $n_{complex}$ is also complex:

$$n_{complex} = n_{ref} + ik_e = \sqrt{\varepsilon(\omega)} \tag{1.116}$$

thus:

$$n_{complex}^2 = \left(n_{ref} + ik_e\right)^2 = \varepsilon(\omega). \tag{1.117}$$

In the above equation, n_{ref} is the real part of the refraction index and k_e is called extinction coefficient and it describes the attenuation of an electromagnetic wave in the considered material. Inserting the equation of the complex permittivity Eq. 1.115 into the equation of the complex refraction index Eq. 1.117 it is obtained that:

$$n_{ref}^2 - k_e^2 + i \cdot 2n_{ref}k_e = \varepsilon - \frac{4\pi\sigma''}{\omega} + i\frac{4\pi\sigma'}{\omega}, \tag{1.118}$$

therefore:

$$2n_{ref}k_e = \frac{4\pi\sigma'}{\omega}. \tag{1.119}$$

Since it was assumed that the refraction index is a complex value and can be written as in Eq. 1.116, one can rewrite the electric field as:

$$\begin{aligned} E(x,t) =& E_x(\omega)e^{i(kx-\omega t)} \\ =& E_x(\omega)e^{i(\frac{2\pi n_{complex}}{\lambda_0}x-\omega t)} \\ =& E_x(\omega)e^{i(\frac{2\pi}{\lambda_0}(n_{ref}+ik_e)x-\omega t)} \end{aligned} \tag{1.120}$$

where the angular wavenumber $k = \frac{2\pi}{\lambda}$. For a given frequency, the wavelength of an electromagnetic wave is affected by the material in which it is propagating. The vacuum wavelength has the form $\lambda_0 = \frac{2\pi c}{\omega}$. The refraction index is the ratio between the wavelength propagating in the material and the vacuum wavelength $n_{ref} = \frac{\lambda}{\lambda_0}$.

After some calculations, the electric field from Eq. 1.120 can be written as:

$$E\left(x,t\right) = e^{-\frac{2\pi k_e}{\lambda_0}x} E_x\left(\omega\right) e^{i(kx-\omega t)}. \tag{1.121}$$

The intensity of the wave propagating inside the material can be calculated using the Poynting theorem which was discussed in a previous section. According to Eq. 1.104 it can be approximated to:

$$I_x \propto \left|E\left(x,t\right)\right|^2 \propto e^{-\frac{4\pi k_e}{\lambda_0}x} \left|E_x\left(\omega\right)\right|^2 \tag{1.122}$$

The absorption of an electromagnetic radiation inside a material is strongly connected with the intensity of radiation I of the wave passing through the material. According to the Beer-Lambert law [35], the intensity of an electromagnetic wave inside a one layered material can be written as:

$$I_x = I_0 e^{-\alpha x} \tag{1.123}$$

where α is the absorption coefficient of the material making up the layer.

Inserting Eq. 1.122 into Eq. 1.123, one obtains that the value of the absorption coefficient for the single layer is:

$$\alpha = \frac{4\pi k_e}{\lambda_0} = \frac{2k_e\omega}{c}. \tag{1.124}$$

From Eq. 1.119, $2k_e\omega = \frac{4\pi\sigma'}{n_{ref}}$, thus:

$$\alpha = \frac{4\pi\sigma'}{n_{ref}c}. \tag{1.125}$$

The intensity of the non-linear high order harmonic signal is strongly related to the numbers of graphene layers used. In order to calculate the maximum intensity of the n^{th} order non-linear signal, first the electric field amplitude inside the N-layered graphene structure E_N is computed:

$$E_N = \frac{E_0}{1 + N\frac{4\pi\sigma_{2D}}{n_{ref}c}} \tag{1.126}$$

where E_0 is the electric field amplitude of the incident electromagnetic wave and $N\frac{4\pi\sigma_{2D}}{n_{ref}c}$ is a dimensionless sheet conductance parameter [30].

For more precise results, the transmission T, reflection R, and absorption A coefficients of the incident electromagnetic wave passing through the N-layered graphene structure are calculated using Fresnel formulas [32]. These formulas describe the behavior of a plane wave interacting with two dielectric media which have a very thin conducting layer between them. From these formulas:

$$T = \frac{4n_1n_2}{|n_1 + n_2 + N\frac{4\pi\sigma_{2D}}{n_{ref}c}|^2}, \quad A = \frac{4n_1N\frac{4\pi\sigma'}{n_{ref}c}}{|n_1 + n_2 + N\frac{4\pi\sigma_{2D}}{n_{ref}c}|^2}, \quad R = \frac{|n_1 - n_2 - N\frac{4\pi\sigma_{2D}}{n_{ref}c}|^2}{|n_1 + n_2 + N\frac{4\pi\sigma_{2D}}{n_{ref}c}|^2}. \tag{1.127}$$

Assume $n_1 = n_2 = 1$, for a suspended (isolated) N-layered graphene:

$$T = \frac{1}{|1 + N\frac{2\pi\sigma_{2D}}{n_{ref}c}|^2}, \quad A = \frac{N\frac{4\pi\sigma'}{n_{ref}c}}{|1 + N\frac{2\pi\sigma_{2D}}{n_{ref}c}|^2}, \quad R = \frac{\left|N\frac{2\pi\sigma_{2D}}{n_{ref}c}\right|^2}{|1 + N\frac{2\pi\sigma_{2D}}{n_{ref}c}|^2}. \tag{1.128}$$

These formulas are represented in Figure 1.13 for an arbitrary value of the first order conductivity $\sigma' = 4 \cdot 10^7$Siemens/m and $n_{ref} = 1$.

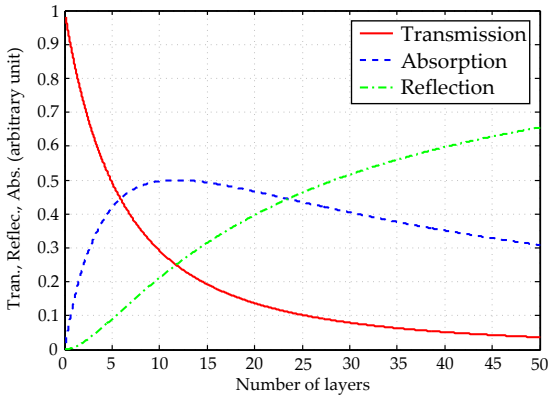

Figure 1.13: The Transmission, Absorption and Reflection coefficients of a suspended (isolated) N-layered graphene.

The n^{th} order current produced in the N-layered graphene structure is then:

$$j_{n\omega} = \sigma^{n\omega} \cdot (E_N)^n = \frac{\sigma^{n\omega} \cdot (E_0)^n}{\left(1 + N\frac{4\pi\sigma_{2D}}{n_{ref}c}\right)^n}. \tag{1.129}$$

As discussed in Ref [36], the high order generated current is gradually added in each of the graphene layers. The high order electric field emitted by each layer is:

$$E_{n\omega} \propto j_{n\omega} \cdot \frac{N}{1 + N\frac{4\pi\sigma_{2D}}{n_{ref}c}}. \tag{1.130}$$

The intensity of the emitted n^{th} order radiation from the graphene layer can be approximated to the square of the electric field at the mentioned harmonic, thus:

$$I_{n\omega} \propto |E_{n\omega}|^2 = \frac{\left(\sigma^{n\omega}\right)^2 \cdot I_\omega^n N^2}{\left(1 + N\frac{4\pi\sigma_{2D}}{n_{ref}c}\right)^{2(n+1)}}. \tag{1.131}$$

The intensity of the emitted high order radiation has a maximum value corresponding to the ideal number of graphene layers which are optimal to work with (see Figure 1.14). As was discussed in the first part of this section, a single layer of graphene is able to absorb around $\alpha \approx 20 - 25\%$ of the incident electromagnetic wave. Thus, the optimal value of graphene layers is $N_{opt} = \frac{n_{ref}c}{4\pi\sigma'} = \frac{1}{\alpha} \approx 5 - 6$ layers. The intensity of the n^{th} order harmonic grows with the number of graphene

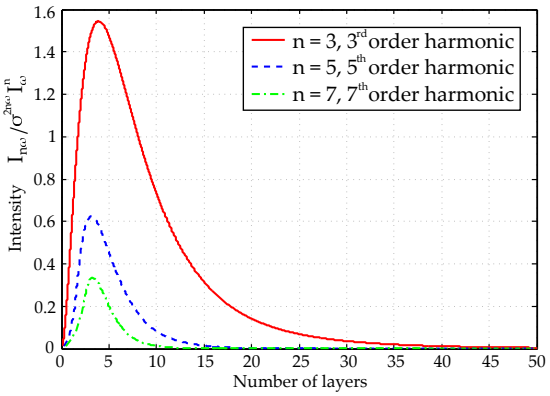

Figure 1.14: Intensity of the emitted n^{th} order harmonic.

layers until it reaches its maximum value corresponding to N_{opt}. As presented in Figure 1.13, above N_{opt} the reflection of the incident wave increases and therefore the probability of high order harmonics generation diminish [30]. Moreover as the absorption rises with the number of layers used, when working with multi-layered structures it is very probable that the non-linear signal generated inside the structures is reabsorbed.

Bibliography

[1] A. K. Geim, K. S. Novoselov, "The rise of graphene, " Nature Materials, vol. 6, pp. 183 -191, March 2007.

[2] J. N. Fuchs and M. O. Goerbig, "Introduction to the Physical Properties of Graphene," Lecture Notes, pp. 1-62, 2008.

[3] A. Fasolino, J. H. Los, M. I. Katsnelson, "Intrinsic ripples in graphene, " Nature Materials, vol. 6, pp. 858 - 861, September 2007.

[4] Sekhar Chandra Ray, "Applications of graphene and graphene-oxide based nanomaterials," Micro and Nano Technologies Series, Elsevier Inc. 2015.

[5] E. L. Wolf, "Applications of Graphene: An Overview, " Springer, ISSN 2192-1091, 2014

[6] Joseph Scott Bunch, "Mechanical and electrical properties of graphene sheets, " Ph. D. thesis, Cornell University 2008.

[7] F. Bonaccorso, Z. Sun, T. Hasan, A. C. Ferrari, "Graphene photonics and optoelectronics, " Nature Photonics, vol. 4, pp. 611 - 622, August 2010.

[8] S. A. Mikhailov, "Non-linear electromagnetic response of graphene, " Europhys. Lett. 79, 27002 (2007).

[9] B. K. Sharma, Jong-Hyun Ahn, "Graphene based field effect transistors: Efforts made towards flexible electronics, " Solid-State Electronics, vol. 89, pp. 177 - 188, November 2013.

[10] C. Vazquez, A. Hadarig, S. Ver Hoeye, M. Fernandez, R. Camblor, G. Hotopan, F. Las Heras, "High-Order Subharmonic Millimeter-Wave Mixer Based on Few-Layer Graphene, " IEEE Transactions on Microwave Theory and Techniques, vol. 63, Issue 4, pp. 1361 - 1369, February 2015.

[11] A. I. Hadarig, C. Vázquez, M. Fernández , S. Ver Hoeye, G. R. Hotopan, R. Camblor, F. Las Heras, "Experimental analysis of the high-order harmonic components generation in few-layer graphene, " Applied Physics A, vol. 118, Issue 1, pp. 82 - 89, January 2015.

[12] M. O. Goerbig, "Electronic properties of graphene in a strong magnetic field, " Reviews of Modern Physics, vol. 83, pp. 1193 - 1243, December 2011.

[13] Luis E. F. Foa Torres, Stephan Roche and Jean-Christophe Charlier, "Graphene - Based Nanomaterials: From Electronic Structure to Quantum Transport, " Cambridge University Press, 2014.

[14] P. R. Wallace, "The band theory of graphite, " Physical Review, vol. 71, no. 9, pp. 622 - 634, May 1947.

[15] H. S. Philip Wong, Deji Akinwande, "Carbon Nanotube and Graphene Device Physics, " Cambridge University Press, 2011

[16] S. A. Mikhailov, "Quantum theory of the third-order nonlinear electrodynamic effects of graphene, " Physical Review B 93, 085403 (2016).

[17] S. A. Mikhailov, "Frequency Mixing Effects in Graphene: Physics and Applications of Graphene - Theory, " ISBN: 978-953-307-152-7, edited by Sergey Mikhailov (InTech, Rijeka, Croatia); chapter 25, pp. 519 - 534, 2011.

[18] Ji-Yong Park, "Carbon Nanotube Electronics, " edited by Ali Javey and Jing Kong, Springer, pp. 1 - 42, 2009.

[19] Edward McCann, "Electronic properties of monolayer and bilayer graphene, " Cond. Mat. Mes., Mesoscale and Nanoscale Physics, Springer-Verlag Berlin Heidelberg, vol. 1205, pp. 237 - 275, May 2012.

[20] R. Saito, G. Dresselhaus, M. S. Dresselhaus, "Physical Properties of Carbon Nanotubes, " Imperial College Press, London, 1998.

[21] Petra Dietl, "Numerical Studies of electronic transport through graphene nanoribbons with disorder, " Thesis, Universitat Karlsruhe, January 2009.

[22] Shigeji Fujita and Kei Ito, "Quantum Theory of Conducting Matter: Newtonian Equations of Motion for a Bloch Electron, " Springer, ISBN 978-0-387-74102-4, 2007.

[23] John Singleton, "Band Theory and Electronic Properties of Solids, " Oxford Master Series in Physics, August 2001.

[24] G. Carpintero, L. E. G. Muñoz, H. L. Hartnagel, S. Preu, A. V. Räisänen, "Terahertz Technology Deviced and Systems at Room Temperature Operation," John Wiley & Sons Ltd, 2015.

[25] A. A. Toropov, T. V. Shubina, "Plasmonic Effects in Metal-Semiconductor Nanostructures, " Oxford University Press, 2015.

[26] Bahram Nabet, "Photodetectors Materials, Devices and Applications, " Woodhead Publishing, First edition, 2015.

[27] L. Hao, J. Gallop, S. Goniszewski, A. Gregory, O. Shaforost, N. Klein and R. Yakimova, "Non-contact method for measurement of the microwave conductivity of graphene, " Appl. Phys. Lett. 103, 123103 (2013).

[28] N. P. Singh and T. Mogi, "Effective skin depth of the EM fields due to large circular loop and electronic dipole sources, " Earth Planets and Space, Springer, vol. 55, Issue 6, pp. 301 - 313, June 2014.

[29] S. A. Mikhailov and K. Ziegler, "Nonlinear electromagnetic response of graphene: frequency multiplication and the self-consistent-field effects, " J. Phys.: Condens. Matter 20 (2008) 384204.

[30] S. A. Mikhailov, "Theory of the nonlinear optical frequency mixing effect in graphene, " Physica E, vol. 44, pp. 924 - 927, 2012

[31] N. A. Savostianova and S. A. Mikhailov, "Giant enhancement of the third harmonic in graphene integrated in a layered structure, " Appl. Phys. Lett. 107, 181104 (2015).

[32] K. Batrakov , P. Kuzhir, S. Maksimenko, A. Paddubskaya, S. Voronovich, Ph Lambin, T. Kaplas, Yu Svirko, "Flexible transparent graphene/polymer multilayers for efficient electromagnetic field absorption, " Nature, Scientific Reports, vol. 4 : 7191, November 2014.

[33] M. Born, E. Wolf, "Principles of Optics: Electromagnetic theory of propagation, interference and diffraction of light, " Cambridge University Press, 1980.

[34] B. Yao, Y. Wu, Z. Wang, Y. Cheng, Y. Rao, Y. Gong, Y. Chen, Y. Li, "Demonstration of complex refractive index of graphene waveguide by microfiber-based Mach-Zehnder interferometer, " Optics Express, vol. 21, No. 24, pp. 29818 - 29826, December 2013.

[35] David W. Ball, “Field Guide to Spectroscopy, ” Spie Press, Bellingham, WA 2006.

[36] E., P. J. Hale, J. Moger, A. K. Savchenko, S. A. Mikhailov, “Coherent Nonlinear Optical Response of Graphene, ” Phys. Rev. Lett. 105, 097401 (2010).

Chapter 2

Graphene based Frequency Multiplier

Contents

2.1 Introduction

In this chapter, the design and analysis of Single Stage High Order Submillimeter Wave/THz band Graphene Based Frequency Multipliers are carried out. The desired frequency multiplication performance is obtained by taking advantage of the non-linear behavior of graphene sheets under excitation with an incident electromagnetic field. The performance of the frequency multipliers is studied for an input signal provided through a WR28 standard waveguide section which operates in the K_a frequency band (26.5 to 40 GHz). The non-linear electromagnetic response of graphene is exploited to efficiently generate high order harmonic content. Therefore three frequency multipliers are implemented in which the output signal in the 140 to 220 GHz, 220 to 330 GHz and 330 to 500 GHz is obtained as a high order harmonic component of the input signal in the K_a frequency band.

In related scientific work, a considerable number of non-linear phenomena, including second [1]-[6] and third [7]-[11] harmonic generation in the graphene charge carriers have been theoretically predicted and experimentally demonstrated. The theoretical work presented in [5]-[6] and [12]-[15] studies the case of the oblique and normal incidence of the electromagnetic wave radiating on a uniform graphene layer giving rise to even and odd harmonic content. Second and third harmonic generation with high efficiency has been reached in single-layer graphene based transistors, from low frequencies up to the millimeter wave frequency band [16, 17]. Up to third

harmonic generation has also been experimentally observed in multi-layer graphene sheets [4, 9, 18, 19].

The Submillimeter wave/THz band can be reached from the microwave region through the integration of ultra-fast devices, such as Schottky diodes or Field-Effect Transistors (FETs) in waveguide topologies [20, 21]. Signals in the desired frequency bands can be generated with frequency multipliers that provide a harmonic component of an input signal at a lower frequency band by taking advantage of the non-linearity of the used device. High orders of multiplication are normally obtained by cascading several low order multiplication stages ended with intermediate amplifiers in a complex and expensive structure. Moreover, the bandwidth of the multiplier when using traditional semiconductors depends on the intrinsic cutoff frequency of the non-linear device used.

High order frequency multipliers are usually passive circuits with non-linear harmonic content and relatively low conversion efficiencies. This means that only a lower portion of the input power is efficiently converted into usable output power in the required frequency band. The unused power can be either dissipated or converted into a series of spurious frequency components [24], which must be afterward filtered out of the device so they do not alter the output signal.

When working with broadband frequency devices, a common problem which sometimes arises is the inability of the non-linear device to absorb all the incident power which is thus reflected back to the previous stage [25]. In order not to damage the circuitry corresponding to such a stage this requires the addition of isolators which might increase the overall losses. The topology of the Single Stage High Order Graphene based Frequency Multipliers, proposed in this chapter, has been developed as a solution in order to overcome the above mentioned issues.

The content of this chapter is discussed as follows. It commences with the description of the general topology which is common for all tree frequency multipliers. Subsequently, each frequency multiplier is discussed separately. The design and optimization process of the transitions involved are described. For the design of the frequency multipliers, the device topology is iteratively modified until a suitable compromise is achieved between the efficiency and bandwidth. Once each frequency multiplier is characterized through electromagnetic simulations, the fabrication process of the manufactured prototypes will be explained. The performance at room temperature for both even and odd harmonic orders will be investigated. The focus is set on the general operation of the blocks as independent subsystems, with regard to the power generated at their output. Moreover, the difference between the even and odd order harmonic components is being addressed. In addition, it will

be shown that the developed assemblies represent a proof of concept which confirms that graphene can be used in a single stage as submillimeter/THz signal source based on frequency multiplication.

2.2 Device Topology

This chapter presents a different and promising approach for the realization of cost-effective submillimeter/THz signal sources, based on the use of multi-layer graphene as an alternative for THz signal generators implemented with traditional semiconductor components. The topology of the proposed Single Stage High Order Submillimeter Wave/THz band Graphene Based Frequency Multipliers is illustrated in Figure 2.1. The devices are composed by a waveguide block and a microstrip structure containing a section with a multi-layer graphene film. The three frequency multipliers share the same topology and they are provided with the same input signal at the K_a band (26.5 to 40 GHz). This signal is guided to the microstrip structure containing the multi-layer graphene through a WR28 metallic waveguide section. The output signal, which is a harmonic component of the input signal generated in the graphene film, is extracted using another rectangular metallic waveguide section:

- WR3 standard waveguide (220 to 330 GHz) for the first frequency multiplier
- WR2.2 standard waveguide (330 to 500 GHz) for the second frequency multiplier
- WR5 standard waveguide (140 to 220 GHz) for the third frequency multiplier

In order to achieve a good impedance matching at the input port over the whole K_a frequency band a path is provided for the input signal through the microstrip structure towards a second WR28 waveguide section terminated in a waveguide matching load.

The graphene film integrated in the microstrip structure is prepared by mechanical exfoliation of Highly Ordered Pyrolytic Graphite (HOPG). Gold contacts, as presented in Figure 2.2, are deposited on top of the graphene film leaving a small gap of 100 μm uncovered. The dielectric substrate employed for the microstrip line is polyimide (Kapton). The properties of this material are summarized in Table 2.1. The microstrip line is composed by three waveguide to microstrip transitions connected through a high impedance transmission line. This structure has to be suitable to deal with both input and output signals of the multipliers. The orientation of the microstrip structure is parallel to the electric field of the fundamental

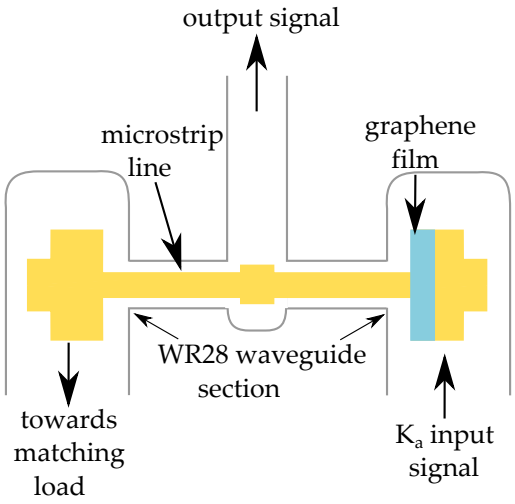

Figure 2.1: Topology of the proposed Single Stage High Order Submillimeter Wave/THz band Graphene Based Frequency Multiplier.

TE_{10} waveguide sections mode [22]. The excitation of the non-linear component is determined by the electric field distribution on the microstrip gap. Given the relatively low conductivity of the multi-layer graphene film, with regard to the rest of the microstrip line which is composed out of gold, a significant electric field contribution tangential to the graphene film will be produced. This electric field contribution, which is analogous to the case of the normal incidence of the electromagnetic wave, studied in Chapter 1, gives rise to odd order harmonic components in the induced current.

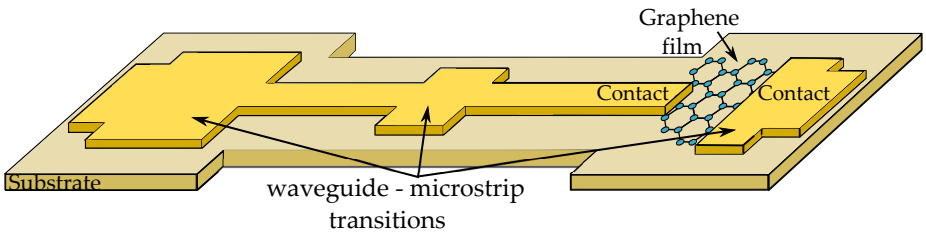

Figure 2.2: Schematic diagram of the microstrip structure integrating the graphene non-linear device.

However, substantial field contributions in the transverse direction are simultaneously present which may give rise to harmonic generation of unconstrained order. Therefore, it is expected that the harmonic content generated in the multi-layer graphene device contains both odd and even order components.

Symbol	Parameter	Value	Unit
ε_r	Relative Permittivity	3.5	
$\tan(\delta)$	Loss Tangent	0.008	
h	Thickness	25 or 50	μm

Table 2.1: Datasheet specification of the polyimide substrate used.

2.3 220 to 330 GHz band Frequency Multiplier

This section is dedicated to the implementation of a single stage graphene based frequency multiplier operating in the 220 to 330 GHz band (WR3 standard frequency band). The multiplier device uses the harmonic components from order 6 to 11 of a K_a band (26.5 to 40 GHz) input signal.

2.3.1 Design and optimization of the frequency multiplier

The main waveguide blocks involved in the topology of the proposed 220 to 330 GHz band frequency multiplier are the WR28 and WR3 waveguide sections. The dimensions and the frequency limits in which the waveguides operate are presented in Table 2.2.

WR-28 waveguide		WR3 waveguide	
Frequency limits [GHz]	Dimensions [mm]	Frequency limits [GHz]	Dimensions [mm]
26.5 - 40	7.112 x 3.556	220 - 330	0.864 x 0.432

Table 2.2: Dimensions of the WR28 and WR3 waveguide sections.

The graphene based frequency multiplier has been designed and evaluated using the tree-dimensional electromagnetic simulator Ansoft HFSS [26]. The optimization process of the multiplier's input and output passive blocks is presented in the following two subsections.

2.3.1.1 Optimization in the 220 to 330 GHz band

In order to maximize the power transfer of the high frequency signal from the microstrip structure to the output WR3 rectangular waveguide section, a microstrip to waveguide transition has to be carefully designed. The transition has been designed and optimized separately from the rest of the multiplier, using the topology shown in Figure 2.3. To improve the impedance matching in the desired frequency band, the dimensions of the WR3 rectangular waveguide section in the proximity of the

microstrip line, the location of the backshort, and the shape of the microstrip transition were optimized. The microstrip circuit is inserted in a rectangular metallic channel which is connected at both sides of the WR3 waveguide.

An analysis was conducted to evaluate the dimensions of the channel cross section. As presented in Table 2.3, it was deduced that its height has to be at least two times bigger than the thickness of the substrate and its width at least three times bigger than the width of the microstrip line it surrounds. By choosing these values it prevents the existence of propagative waveguide modes in the 220 to 330 GHz band and it restricts the transmission of the submillimeter wave signals to the microstrip line.

Furthermore, in order to have a good signal transmission, with low losses from the microstrip line to the WR3 waveguide section, the microstrip line transition placed inside the WR3 waveguide section was arranged approximately at a quarter wavelength from the waveguide backshort.

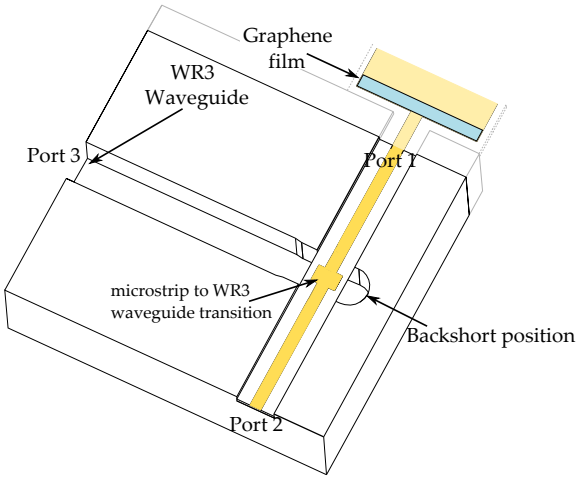

Figure 2.3: Topology of the microstrip to the WR3 waveguide transition.

The proper ports assignment along the structures and the meshing around the microstrip circuit are critical to get accurate results [23]. The design of the output passive block, which includes the WR3 waveguide section and the microstrip structure confined into the metallic channel, was fed through one of its three waveports. As presented in Figure 2.3, these waveports are placed two of them at each end of the channel cross section surrounding the microstrip structure (Port 1 and Port 2) and one at the extreme end of the WR3 waveguide section (Port 3). A solution frequency at $f_c = 275$ GHz, the central frequency of the 220 to 330 GHz band, is set in the HFSS circuital optimizer and this value is used in the generation of the

tetrahedral type adaptive mesh [27, 28] along the structure. The designs are usually optimized for a given input power. In this particular case, the design was optimized for 1 Watt time-average power.

Channel height [mm]	Substrate thickness [mm]	Channel width [mm]	Transmission line width [mm]
0.120	0.05	0.410	0.120

Table 2.3: Dimension assignment of the channel cross section - 220 to 330 GHz band frequency multiplier.

Various optimizations were performed in order to enhance the response of the circuit in the 220 to 330 GHz band. The optimizations evaluate the waveguide transition and the microstrip line parameters. Due to fabrication restrictions, the minimum waveguide height and the minimum corner diameter have been limited to 0.410 mm. A parameter sweep is performed on the microstrip structure with the results being presented in Figure 2.4. Only one parameter is changed at each time during the analysis. The microstrip line width W_{ML} controls the frequency bandwidth in which the transition is well-matched (decreasing W_{ML} the impedance of the line increases, the bandwidth is wider and the matching is improved). The matching between the microstrip line and the WR3 waveguide section improves when the width W_{MLtran} of the rectangular stub placed inside the WR3 waveguide increases and the length L_{MLtran} decreases. At the same time, the conversion of the propagating mode from TEM, the microstrip line mode, to TE_{10}, the fundamental waveguide mode, is enhanced and therefore more energy is transferred towards the output WR3 waveguide. The red line in each analyzed case illustrates the optimal value of the corresponding parameter chosen in the overall structure. The dimensions of the waveguide transition close to the WR3 backshort are depicted in Figure 2.4(d).

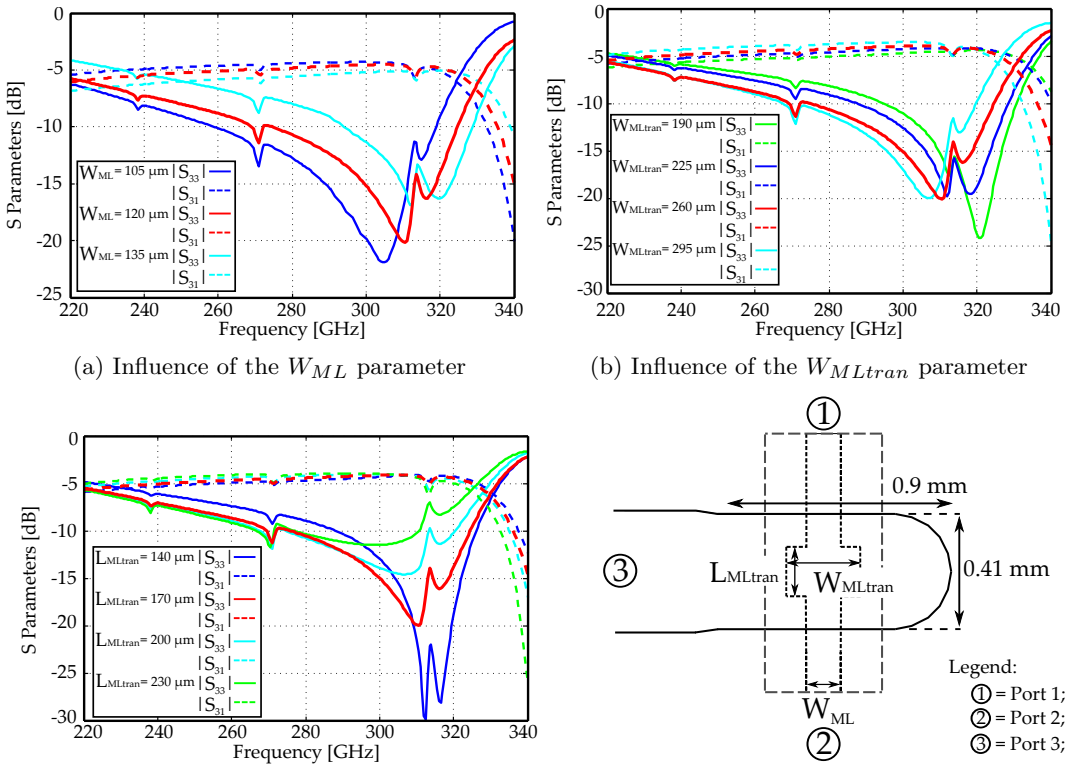

(a) Influence of the W_{ML} parameter

(b) Influence of the W_{MLtran} parameter

(c) Influence of the L_{MLtran} parameter

(d) Schematic of the waveguide transition and the microstrip structure

Figure 2.4: Simulated reflection coefficient at Port 3 and transmission coefficient between Port 1 and Port 3 when varying the microstrip structure parameters of the microstrip to WR3 waveguide transition.

Figure 2.5 illustrates the electric field distribution in the microstrip to WR3 waveguide transition. The design was fed through Port 1, the port placed the closest to the graphene layer in the complete frequency multiplier structure. The electric field distribution across the structure is plotted at 310 GHz frequency and at 235 GHz. These frequency points were chosen as they provide the best and the poorest response in terms of scattering parameters.

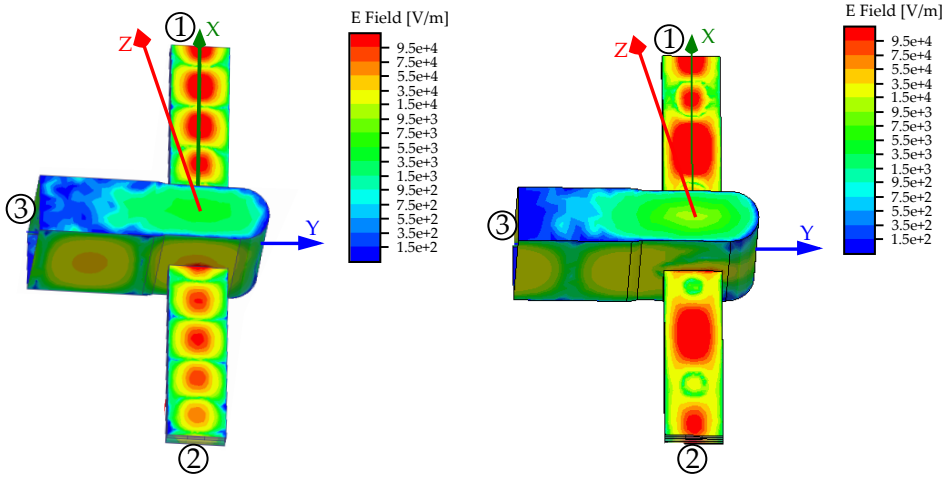

(a) E-field at 310 GHz.

(b) E-field at 235 GHz.

Figure 2.5: Electric field distribution along the microstrip to WR3 waveguide transition. Circuit fed through Port 1.

From this comparison one can notice that the electric field inside the WR3 waveguide section drops around one order of magnitude when the transition discussed is well matched against the case when it is mismatched. Also for the 235 GHz case, the propagating mode along the microstrip line is no longer a perfect TEM but a combination between the TEM and some other parasitic mode.

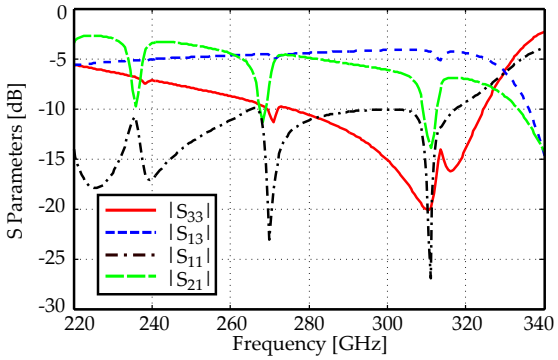

Figure 2.6: Frequency response of the microstrip to WR3 waveguide transition - Scattering parameters.

Moreover, the frequency response of the final optimized transition is presented in Figure 2.6. Good impedance matching with a reflection coefficient $|S_{11}| < -10$ dB in the entire 220 to 330 GHz band and $|S_{33}| < -10$ dB from approximately 260 to 330 GHz was obtained. The insertion loss between the input Port 1 and the output

Port 3 is approximately 5 dB.

2.3.1.2 Optimization in the K_a band

In a second design step, the complete frequency multiplier design is optimized in the K_a band. For this, the output passive block, which was previously optimized, is inserted and left unmodified in the complete frequency multiplier design. As presented in Figure 2.7, the topology used to analyze the frequency multiplier in the K_a band has two WR28 waveguide structures and two microstrip elements connected at the microstrip to WR3 waveguide transition. The complete microstrip line is terminated in two WR28 to microstrip transitions and a multi-layer graphene strip which is part of one of the microstrip elements. These elements are composed by some stubs which radiate at different frequencies together with several microstrip sections of low and high impedance. The aim of this structure is to couple the input K_a signal from the WR28 waveguide section to the microstrip line and transfer it to the graphene component. Further the input K_a signal is transmitted to the second WR28 waveguide. The total length of the microstrip structure is 9 mm and the width of its substrate in the interior of the WR28 waveguide section is 2.9 mm. The multi-layer graphene strip has a length of 150 μm and a width of 1.2 mm which is the same as the width of the microstrip line in its vicinity.

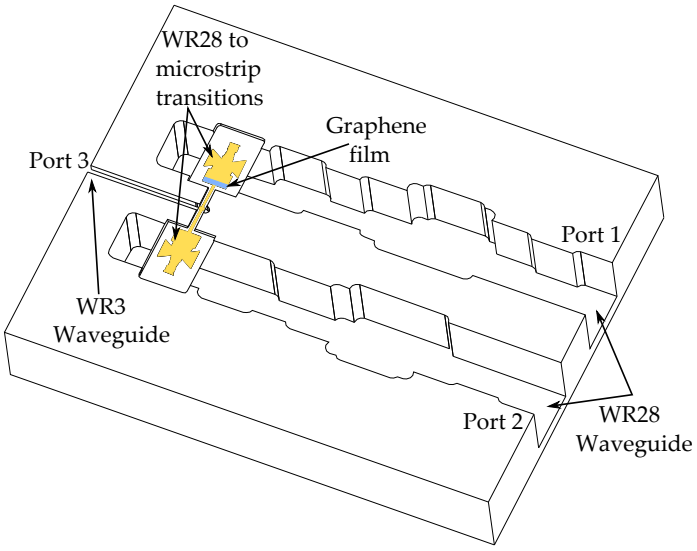

Figure 2.7: Topology of the frequency multiplier used in the optimization of the K_a band.

In order to improve the impedance matching in the K_a band, the standard WR28

waveguides have been modified with a sequence of several sections of high and low impedance. By proper choosing the dimensions of this structure the frequency response of the input WR28 waveguide was broadened. The geometrical restrictions imposed by the manufacturing process were taken into account and so the corners of the mentioned sections were rounded with a minimum 0.4 mm radius. The two WR28 waveguide sections have no impact on the output matching. The final optimized WR28 waveguides have a total length, from the input to their backshort, of approximately 24 mm.

In the simulation, the microstrip line, with the exception of the multi-layer graphene strip, is modeled as a gold layer. For the conductivity of the multi-layer graphene strip, the values specified by the HOPG sample provider were used. i.e., $\sigma_{\parallel} = 2.1 \cdot 10^6$ S/m parallel and $\sigma_{\perp} = 500$ S/m perpendicular to the layer surface.

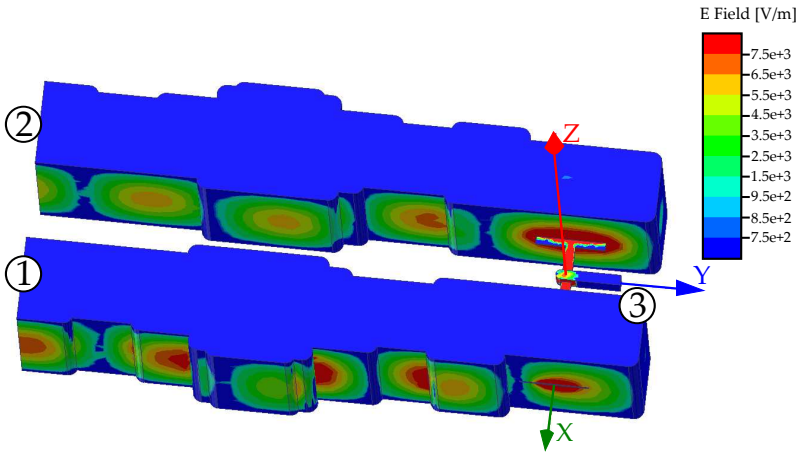

Figure 2.8: Electric field distribution at 34 GHz plotted along the frequency multiplier. Circuit fed through Port 1.

Figure 2.8 presents the electric field distribution inside the frequency multiplier at 34 GHz. The incident radiation, incoming from Port 1, is transferred throughout the microstrip line to the second WR28 waveguide section. By doing so the frequency multiplier input remains protected from unwanted reflections. Moreover, this enables a maximum power coupling into the microstrip line and a wide-band impedance matching over the K_a band at Port 1. No signal is coupled to the WR3 output waveguide since the K_a band lays below its cut-off frequency.

The electric field distribution on the microstrip line is illustrated in Figure 2.9. As one can observe, the electric field is more confined on the border between the microstrip structure placed inside the WR28 waveguide and the channel cross sec-

tion, precisely where the multi-layer graphene component is positioned. Therefore the input signal is efficiently converted into a high harmonic signal in a point of maximum input electric field.

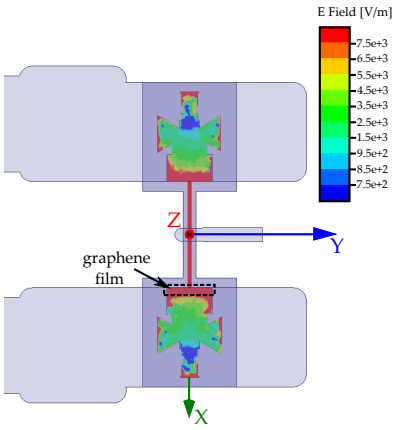

Figure 2.9: Electric field distribution at 34 GHz plotted along the complete microstrip line structure.

The simulated scattering parameters of the optimized transition are shown in Figure 2.10. A good impedance matching was obtained at the input Port 1 with a reflection coefficient lower than -10 dB in the 28 to 40 GHz frequency band. Note that between 26 to 27.7 GHz the transition is shorted while, about 40 GHz, higher order modes start to propagate leading to a reduced signal propagation under the desired fundamental TE_{10} mode. The power loss between the two ports placed at each WR28 waveguide extreme (Port 1 and Port 2) is below 4 dB.

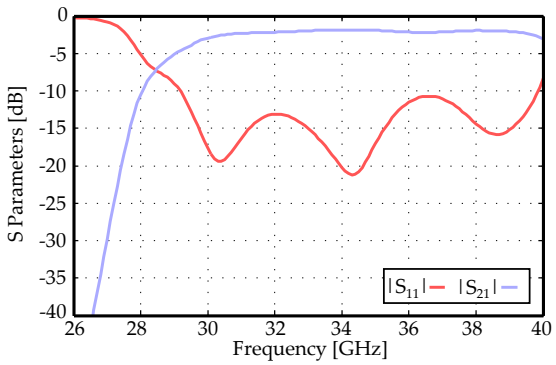

Figure 2.10: Scattering parameters of the frequency multiplier in the K_a band.

2.3.2 Prototype fabrication and experimental characterization

2.3.2.1 Prototype Implementation

For the evaluation of the graphene based frequency multiplier behavior, a prototype of the complete structure has been manufactured and experimentally characterized. The purpose of this thesis is to develop a first proof of concept prototype rather than a complete optimized design for a specific harmonic component. Therefore, the ability to manufacture it in-house, with existing resources, has been preferred which minimized the fabrication costs.

The waveguide structure, including the input WR28 and output WR3 waveguide sections, and the channel between them, was split into eight brass sheets each of 1 mm thickness. Each brass sheet has been sequentially micromachined using a 2.5 axis milling machine with limited travel distance in the direction perpendicular to the milling plane. Due to the final dimensions of the waveguides and rectangular channel cross sections as well as the restrictions imposed on the corner radius of these sections a 0.8 mm end mill tool for the WR28 waveguides and a 0.4 mm end mill tool for the WR3 waveguide and channel parts have been used. Standard WR28 (type $UG-599/U$) and WR3 (type $UG-387/UM$) interface flanges, required to connect the frequency multiplier with the vector network analyzer, have been manufactured using the same process. The standard flanges are soldered each to a structure composed by three precisely aligned micromachined brass layers as shown in figure 2.11. The two inner brass layers are left free to ease the assembling process of the microstrip structure.

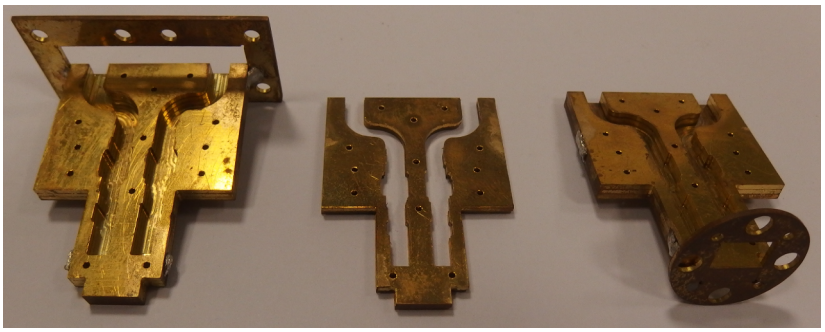

Figure 2.11: Manufactured brass sheets.

After depositing the multi-layer graphene sheet (exfoliated from HOPG) on top of the polyimide substrate, a mask aimed to cover the corresponding graphene area is prepared. The mask will secure the graphene layers when gold atoms are deposited along the polyimide dielectric throughout a sputtering process. The gold

layer obtained and the graphene component are then provided with the desired shape through a laser ablation process. The microstrip line before the final laser cutting process, of its polyimide substrate, is shown in Figure 2.12.

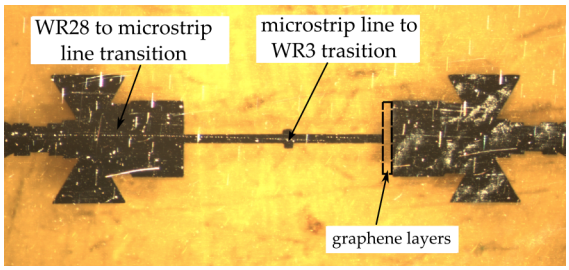

Figure 2.12: Prototype of the microstrip line structure.

The laser prototyping equipment used provides a cutting accuracy of ±2 μm, with a focused beam width of 25 μm. During this process, in the vicinity of the structure edges very high temperatures are achieved. This effect becomes especially critical when narrow metal lines are implemented in the design, in which case the metallic layer may be completely lifted from the substrate. In simulations, these considerations were taken into account. Therefore, the dimensions of the optimized frequency multiplier were carefully chosen so they could facilitate the fabrication of the prototype.

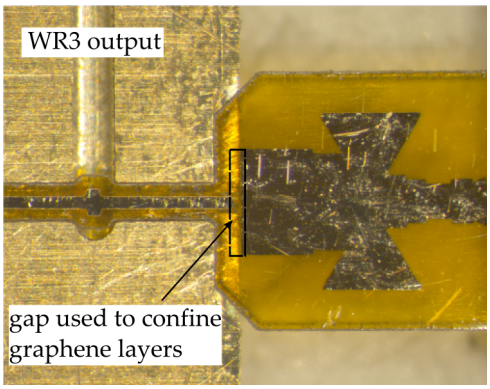

Figure 2.13: Image of the microstrip structure mounted into the channel cross section.

Further, taking advantage of a high precision pick and place system the microstrip structure is mounted on and secured into the channel. An internal view with focus on the microstrip structure is presented in Figure 2.13. The eight micromachined layers have been assembled and precisely aligned together with several

1 mm diameter and 8 mm length screws, tightened against the holes of the outer brass layer as it can be seen in Figure 2.14.

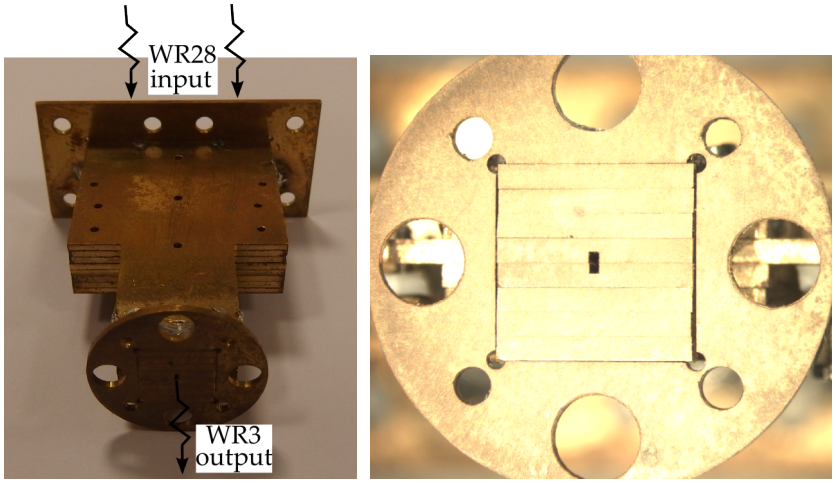

(a) Assembled prototype.

(b) WR3 waveguide terminated with its corresponding flange.

Figure 2.14: Prototype of the 220 to 330 GHz band graphene based frequency multiplier.

2.3.2.2 Measurement of the impedance matching and insertion loss in the K_a band

The schematic diagram used for the measurement of the impedance matching and insertion loss in the K_a band is presented in Figure 2.15. Two commercial coaxial to waveguide adapters from Agilent ($R281A$ and $R281B$) are each connected at one WR28 frequency multiplier port. The behavior of the frequency multiplier is characterized by connecting it to the vector network analyzer.

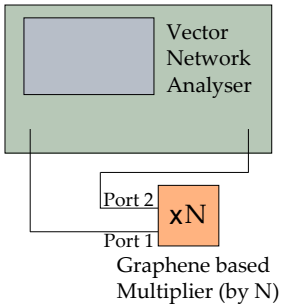

Figure 2.15: Schematic diagram of the S parameters measurement in the K_a band.

The measured scattering parameters are shown together with the simulated results in Figure 2.16. The small deviations between the two results might have appeared due to errors in the manufactured process or mismatches in the physical properties of the materials used. Nonetheless, good impedance matching with a reflection coefficient lower than -10 dB ($S_{11} < -10$ dB) between approximately 28.8 to 40.2 GHz frequency band was obtained in both simulated and measured data. The insertion loss remains slightly over 4 dB throughout most of the K_a band, although it gradually increases when approaching the lower end. Note that when considering the losses induced by the input of the frequency multiplier their value is half the value of the insertion losses presented in Figure 2.16 as the output WR3 waveguide section is placed halfway between the WR28 to WR28 waveguide transition.

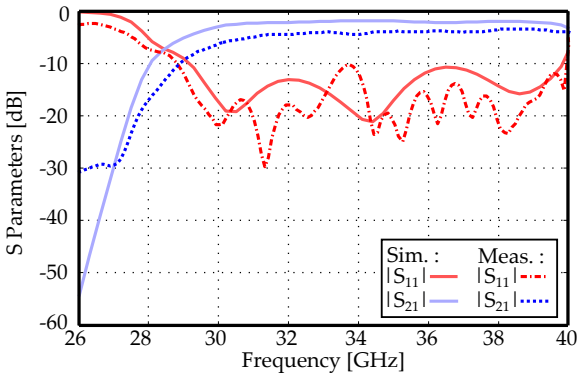

Figure 2.16: Simulated and measured performance of the frequency multiplier in the K_a band.

2.3.2.3 Measurement of the impedance matching in the 220 to 330 GHz band

The schematic diagram used for the measurement of the impedance matching in the 220 to 330 GHz band is depicted in Figure 2.15. The behavior of the frequency multiplier has been characterized using a *Virginia Diodes Inc.* frequency range extender module, connected to the $PNA - X$.

The measured reflection coefficient at the WR3 waveguide port in the 220 to 330 GHz band is shown together with the simulated result in Figure 2.18. This port will be connected to the measurement setup and is used to extract the output generated signal from the frequency multiplier. Therefore, good impedance matching is required in order to obtain accurate results.

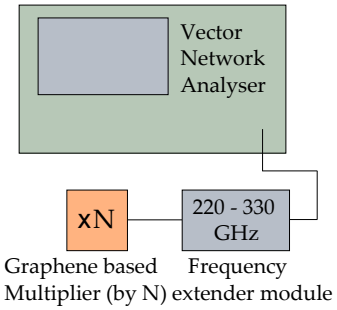

Figure 2.17: Schematic diagram of the impedance matching measurement in the 220 to 330 GHz band.

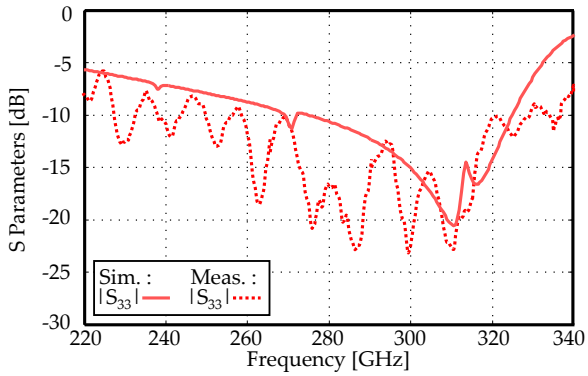

Figure 2.18: Simulated and measured reflection coefficient at Port 3 in the 220 to 330 GHz band.

2.3.2.4 Multiplier performance - output power

The schematic diagram of the measurement setup employed for the experimental characterization of the frequency multiplier performance is presented in Figure 2.19. The input signal, in the K_a band, is generated with an Agilent $N5247A$ $PNA-X$ vector network analyzer and it is amplified up to the desired power level with a 30 dB gain power amplifier with bandwidth between 20 to 45 GHz. By using a commercial Agilent $R281A$ coaxial to waveguide adapter, the signal generated from the $PNA-X$ vector network analyzer is delivered to the input of the graphene based frequency multiplier through the WR28 waveguide section which is closer to the graphene component. On the other WR28 waveguide port an Agilent $R281B$ coaxial to waveguide adapter terminated with a 50 Ω load is connected. The output signal, generated through frequency multiplication due to the non-linear electromagnetic

behavior of graphene, is measured at room temperature using a *Virginia Diodes Inc.* frequency range extender (receiver) module, connected to the $PNA-X$.

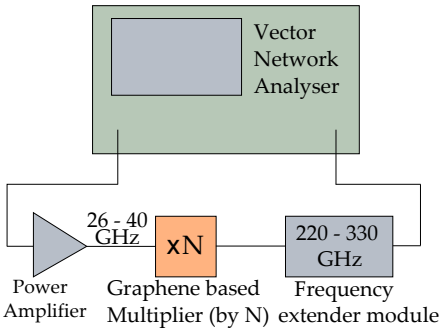

Figure 2.19: Schematic diagram of the measurement setup.

In order to verify if the $PNA-X$ and Power Amplifier generate harmonic content that is coupled to the output WR3 waveguide, a test has been performed using the same microstrip structure implemented completely in gold, i.e. replacing the graphene strip by a gold strip. For the same input parameters no multiplied signal was detected at the output of the device even for the maximum sensitivity settings of the $PNA-X$, for which the noise floor was about -130 dBm. The measurement results presented in the upcoming sections have been obtained for a noise floor of about -120 dBm, confirming that the frequency multiplication is entirely achieved in the graphene component.

The input and output of the frequency multiplier work under the desired fundamental TE_{10} waveguide mode in the frequency ranges from 28 to 40 GHz and from 220 to 330 GHz respectively. For this reason the order of the harmonic components generated in the multi-layer graphene can vary from order $N = 6$ to $N = 11$. The output operation band of the frequency multiplier is limited between 220 to 330 GHz and it should correspond to the following transformation: $28 \times N$ to $40 \times N$ GHz.

Odd order harmonic components

The behavior of the graphene based frequency multiplier in terms of output converted power at different odd order harmonic components is characterized in the 220 to 330 GHz band. For each studied multiplication order, the generated output power has been evaluated versus the frequency when the input power was varied from $P_{in} = 8$ to 20 dBm in 2 dB steps. Higher input power levels have been found to be unreliable, giving rise to anomalous behavior, instantly followed by the substrate dilatation and the device burnout. The measured data obtained for

odd order harmonic components is represented in Figure 2.20. The results at each harmonic have been seen only at specific frequencies within the output operating band. The nominal operation bands were calculated for each harmonic N, according to the frequency areas where the input and the output signals propagate under the fundamental TE_{10} mode. These areas are indicated in Figure 2.20 as shadowed areas.

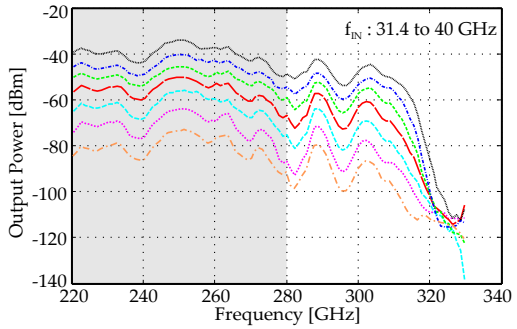

(a) Multiplication by 7.

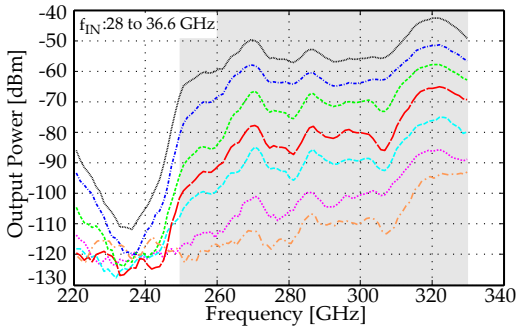

(b) Multiplication by 9.

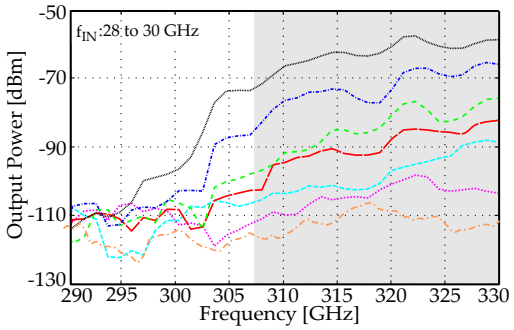

(c) Multiplication by 11.

Figure 2.20: Output power of the 220 to 330 GHz band frequency multiplier when odd harmonic components are used. Input power considered from 8 to 20 dBm varied in 2 dB steps.

In this way, only the seventh, ninth and eleventh harmonic component should be taken into account. For these multiplication orders, the input and output nominal operation bands are calculated as specified in Table 2.4.

As one can observe from Figure 2.20, the maximum power level achieved is around -34 dBm and corresponds to the case of the seventh order harmonic. Nonetheless increasing the harmonic order the conversion efficiency is reduced meaning that a smaller portion of the input delivered power is transformed into output power in the 220 to 330 GHz band. In this way, a maximum power level of -41.67 dBm in

the case of the ninth order harmonic and -60.9 dBm in the case of the eleventh harmonic order were observed.

Order N	Input signal range f_{in}	Output signal range $N \times f_{in}$
7^{th}	31.5 GHz to 40 GHz	220 GHz to 280 GHz
9^{th}	28 GHz to 36.6 GHz	252 GHz to 330 GHz
11^{th}	28 GHz to 30 GHz	308 GHz to 330 GHz

Table 2.4: Nominal operation bands for odd order harmonic components - 220 to 330 GHz band frequency multiplier.

The output power of the frequency multiplier when analyzing the odd order harmonic components is relatively flat throughout the considered frequency range, as theory predicted [7]. No sign of proper saturation is observed in the nominal operation bands used. As it can be seen in the graphics, the output power is relatively noisy for increased harmonic orders and for low values of the input power as the output power values decline towards the noise floor. In any case, the frequency multiplication phenomena due to the graphene strip is observed along the entire considered frequency band. Furthermore, as the input signal of the frequency multiplier propagates under multimode regime above 40 GHz and the upper limit of the power amplifier providing 30 dB gain is 45 GHz, a reduction of the power level is registered in the case of the seventh harmonic order from $40 \times N = 280$ GHz to $45 \times N = 315$ GHz.

Even order harmonic components

Assuming the same theoretical predictions, of normal incidence on the graphene sample (theoretically discussed in Chapter 1), the even order harmonic components are identically zero. These results consider an ideal infinite two-dimensional graphene sample with anisotropic perpendicular conductivity $\sigma_\perp = 0$. The conductivity values of the finite multi-layer graphene strip used in simulations, $\sigma_\perp = 500$ S/m and $\sigma_\parallel = 2.1 \cdot 10^6$ S/m, were estimated from the values given by the HOPG sample provider. The graphene sheet is placed on top of a polyimide substrate which could influence the behavior of its charge carriers as it may change the concentration of electrons at Fermi level. Moreover, the graphene component is placed on a point of maximum input electric field. The incident radiation exciting the graphene component is composed of tangential and perpendicular/oblique field contributions. For all the above reasons, the waveform of the graphene current density of electrons may

take a slightly different form as the one theoretically calculated in Chapter 1 (Eq. 1.75) and thus this may allow the generation of even order harmonic components.

The output power variation of the even order harmonic components, from order $N = 6$ to $N = 10$, has been represented in Figure 2.21. The shaded areas correspond to a propagation of both input and output signals under the fundamental TE_{10} mode. Table 2.5 indicates the nominal operation bands of the frequency multiplier for each harmonic component.

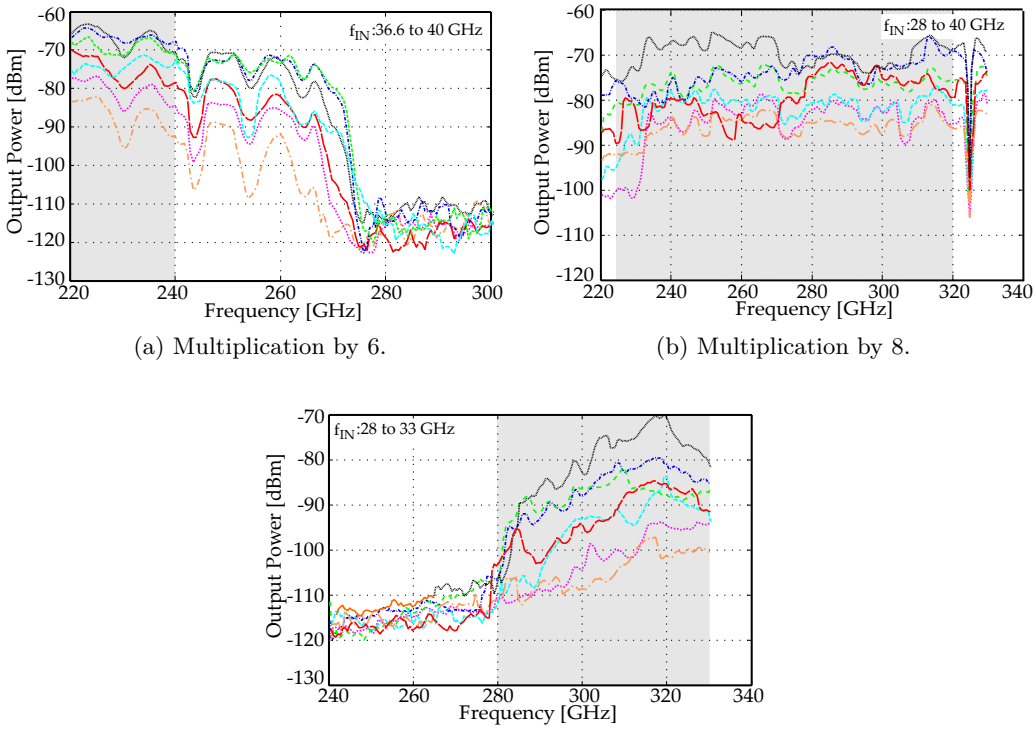

(a) Multiplication by 6.

(b) Multiplication by 8.

(c) Multiplication by 10.

Figure 2.21: Output power of the 220 to 330 GHz band frequency multiplier when even harmonic components are used. Input power considered from 8 to 20 dBm varied in 2 dB steps.

As in the previous case, the power of the input signal is varied in 2 dB steps, from 8 to 20 dBm. For the same value of the input power, the measured output power is considerably lower than the one obtained when evaluating the odd order harmonic components. Therefore, the maximum power level achieved is around -62 dBm in the case of the sixth harmonic component, -68 dBm in the case of the eighth harmonic and -71 dBm in the case of the tenth harmonic component. Analogously to the previous analyzed situation, some values of the output power

Order N	Input signal range f_{in}	Output signal range $N \times f_{in}$
6^{th}	36.6 GHz to 40 GHz	220 GHz to 240 GHz
8^{th}	28 GHz to 40 GHz	224 GHz to 320 GHz
10^{th}	28 GHz to 33 GHz	208 GHz to 330 GHz

Table 2.5: Nominal operation bands for even order harmonic components - 220 to 330 GHz band frequency multiplier.

outside the nominal operation bands (the case where the input signal propagates under multimode regime) are obtained for the sixth harmonic from $40 \times N = 240$ GHz to $45 \times N = 270$ GHz and also from 320 GHz to 330 GHz for the eighth harmonic component but should not be considered.

The output power response of even order harmonics is less regular as compared to the output power response of the odd order harmonics.

2.3.2.5 Variation of the output electric field versus the input electric field

The measured harmonic content generated at the output of the 220 to 330 GHz band graphene based frequency multiplier, when odd order harmonic components are considered, is compared with the theoretical estimations presented in Chapter 1. The input electric field versus the output electric field are analyzed in both the measurements and the theoretical estimations for each harmonic component.

The input power in all cases varies from $P_{in} = 8$ to 20 dBm in 2 dB steps. For the calculation of the input electric field, $E_{n\omega}$, the power formula $E_{n\omega} \propto \sqrt{P_{in}}$ has been used. The output seventh order power $P_{7\omega}$ is examined at the arbitrary frequency 270 GHz. The corresponding input frequency of this chosen value is $270/7 = 38.5$ GHz. This frequency point is situated in the flat region of the input nominal operation band. In the same way, the output ninth order power $P_{9\omega}$ is analyzed at 310 GHz and the output eleventh order power $P_{11\omega}$ at 330 GHz.

For the calculation of the theoretical n^{th} order output electric field, $E_{n\omega}$, the estimation: $E_{n\omega} \propto \sigma^{n\omega} \cdot (E_{\omega})^n \propto (E_{\omega})^n$, presented in Section 1.7, was employed. The results obtained for both the experimental and the theoretical calculations are represented in Figure 2.22.

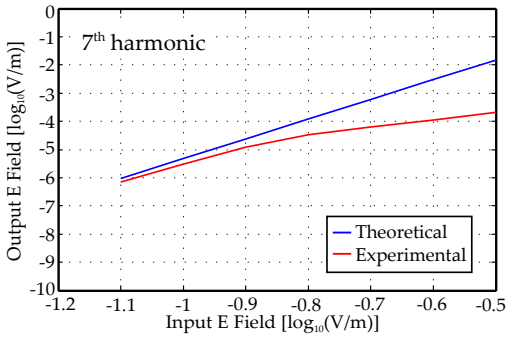

(a) 7^{th} harmonic component

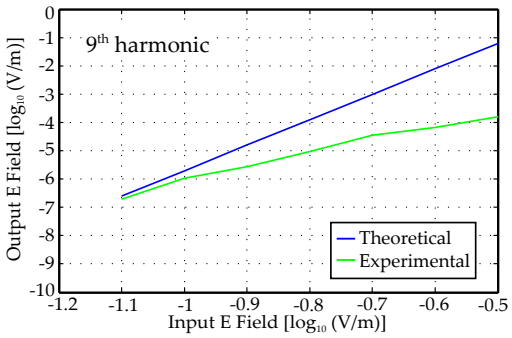

(b) 9^{th} harmonic component

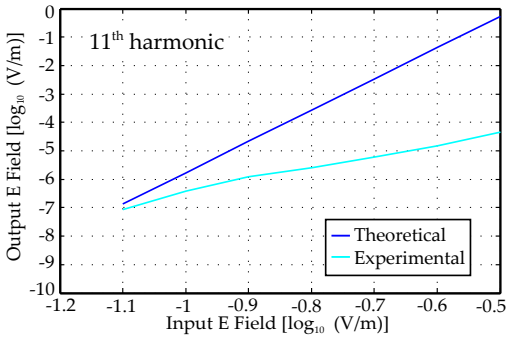

(c) 11^{th} harmonic component

Figure 2.22: Output versus input electric field for different odd order harmonic components.

Good agreement was observed in all analyzed cases at low values of the input field. This fact is in accordance with the low-field condition theory developed in Chapter 1.

2.3.2.6 Output electric field versus the harmonic order

The theoretical analysis developed in Chapter 1 shows that the amplitude of the odd order harmonic components generated when the ideal graphene layer is excited with an external uniform electric field tangential to the graphene sample decreases according to Eq. 1.67. Moreover, the mentioned calculations of the graphene current density are expanded up to the seventh order while higher order harmonic components are being evaluated at the output of the proposed 220 to 330 GHz band frequency multiplier. Therefore Eq. 1.67 has to be rewritten in order to contain all the elements up to the considered harmonic order. Performing the calculations described in Appendix C the formula of the graphene current density of electrons

due to the contribution of the 1^{st}, 3^{rd}, 5^{th}, 7^{th}, 9^{th}, and 11^{th} component, under low-field condition ($Q_0 < 1$), becomes:

$$\begin{aligned} j_x(t) =& en_s v_F \left[\sin\omega t \left(Q_0 - \frac{3}{2^5}Q_0^3 - \frac{10}{2^{10}}Q_0^5 - \frac{175}{2^{16}}Q_0^7 - \frac{2205}{2^{21}}Q_0^9 - \frac{33957}{2^{26}}Q_0^{11} \right) \right. \\ &+ \sin 3\omega t \left(\frac{1}{2^5}Q_0^3 + \frac{5}{2^{10}}Q_0^5 + \frac{105}{2^{16}}Q_0^7 + \frac{735}{2^{20}}Q_0^9 + \frac{24255}{2^{26}}Q_0^{11} \right) \\ &+ \sin 5\omega t \left(-\frac{1}{2^{10}}Q_0^5 - \frac{35}{2^{16}}Q_0^7 - \frac{315}{2^{20}}Q_0^9 - \frac{24255}{2^{27}}Q_0^{11} \right) \\ &+ \sin 7\omega t \left(\frac{5}{2^{16}}Q_0^7 + \frac{315}{2^{22}}Q_0^9 + \frac{8085}{2^{27}}Q_0^{11} \right) \\ &+ \sin 9\omega t \left(-\frac{35}{2^{22}}Q_0^9 - \frac{1617}{2^{27}}Q_0^{11} \right) \\ &\left. + \sin 11\omega t \frac{147}{2^{27}}Q_0^{11} \right] \end{aligned} \tag{2.1}$$

From this equation the harmonic components which are of interest in this section are seventh, ninth and eleventh order. The most relevant term which sets the current amplitude of each harmonic component is the term having the field parameter (Q_0) at the lowest power. All the other terms are quickly decreasing, as $Q_0 < 1$, and thus their influence on the response is insignificant. Therefore the values which are used in the analysis are:

$$\begin{aligned} j_{7\omega} =& en_s v_F \frac{5}{2^{16}}Q_0^7 \\ j_{9\omega} =& en_s v_F \frac{35}{2^{22}}Q_0^9 \\ j_{11\omega} =& en_s v_F \frac{147}{2^{27}}Q_0^{11} \end{aligned} \tag{2.2}$$

Considering the measured output power of the odd order harmonic components represented in Figure 2.20, the electric field amplitude related to each line has been calculated both experimentally and theoretically ($E_{n\omega} \propto \sqrt{P_{oddOrder}}$). The output nominal operation band of the odd order harmonics evaluated is different for each component (see Table 2.4). There is no common frequency point for all harmonic elements but instead each two were found to share a narrow bandwidth. Therefore, this analysis was conducted in two steps at two different frequencies. The output power when considering the seventh and ninth harmonic is evaluated at 270 GHz frequency and for the ninth and eleventh harmonic at 330 GHz. The input signal needed in the multiplication process in order to obtain these frequencies is situated

in the flat region of the multiplier input response. The experiment was conducted for an input power variation from 8 to 16 dBm in 2 dB steps. In the theoretical calculations the seventh order electric field at 270 GHz was taken from the experimental estimations and using the formula of the current density from Equation 2.2 the value of the field parameter Q_0 was computed. Each obtained Q_0 was introduced into the expression of the ninth order current density and using the approximation $E_{n\omega} \propto j_{n\omega}$ the value of the electric field at 270 GHz was determined. Analogously at 330 GHz the theoretical value of the ninth order electric field was taken from the experimental calculations and the eleventh order electric field was theoretically computed.

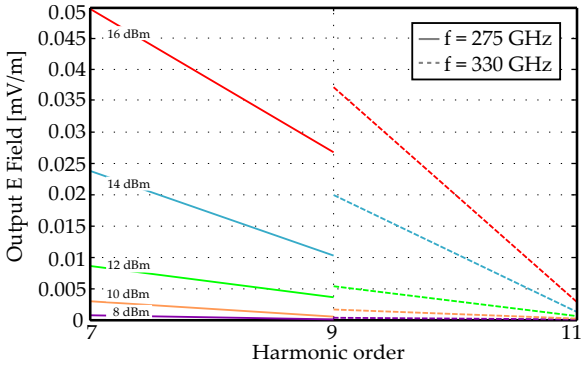

Figure 2.23: Experimental output electric field variation with the harmonic order for fixed values of the input power. The considered output frequency is 270 GHz for 7^{th} and 9^{th} harmonic (solid line) and 330 GHz for 9^{th} and 11^{th} harmonic (dashed line).

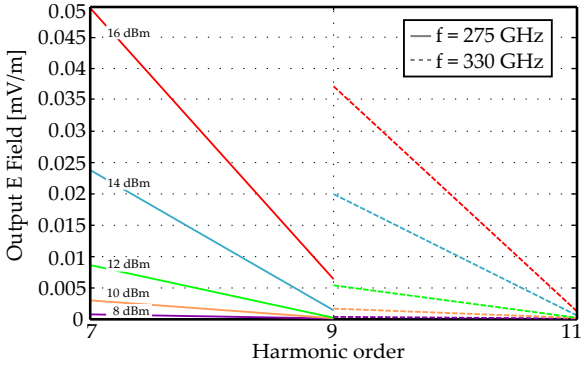

Figure 2.24: Theoretical output electric field variation with the harmonic order for fixed values of the input power. The considered output frequency is 270 GHz for 7^{th} and 9^{th} harmonic (solid line) and 330 GHz for 9^{th} and 11^{th} harmonic (dashed line).

The result of the experimental prediction is presented in Figure 2.23 while the theoretical calculations are illustrated in Figure 2.24. As one can appreciate, the experimental electric field of the examined high harmonic components is slightly higher than the theoretical calculations which considered an ideal isolated graphene layer.

Additionally, the maximum electric field of the different odd and even harmonic components generated at the output of the evaluated frequency multiplier are represented in Figure 2.25 versus the theoretical values. As already mentioned, a different way to calculate the output theoretical electric field is to take the value of the input electric field and raise it to the power of the considered harmonic. Note that the output theoretical electric field is computed only for odd order harmonics. To be consistent to the previously developed analysis, an input power at $P_{in} = 16$ dBm is considered.

The odd order harmonic components decrease analogously with the theoretical curve. On the contrary, in the case of the even order harmonics the decreasing tendency seems to obey a different trend.

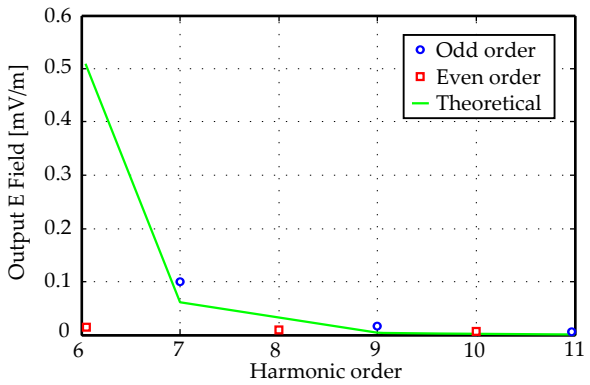

Figure 2.25: Maximum output electric field for different harmonic orders, compared to the theoretical curve.

The experimental results presented in this section demonstrate that graphene has a flat frequency response throughout the whole studied WR3 standard band as no sign of signal saturation was registered except the burnout of the sample. For high value of the input power it is assumed that part of the output power internally generated is converted into heat and thus it is not efficiently transformed into useful signal in the 220 to 330 GHz band. It is expected that for a substrate with a higher melting point the graphene sample can endure higher input power values which should lead to the generation of higher output power levels increasing the efficiency

of the overall device. Therefore, as the electromagnetic behavior of graphene is predicted to be flat from low frequencies to THz band it can be concluded that the frequency bandwidth in which the presented multiplier performs its operation is influenced by the input WR28 waveguide section, the output WR3 waveguide section and the microstrip line structure. Since the only restrictions in terms of operating bandwidth are the supplementary linear parts, the frequency multiplier design can be extended to higher or lower frequency bands, as will be presented in the subsequent sections.

2.4 330 to 500 GHz band Frequency Multiplier

The concept behind the implementation of the proposed 330 to 500 GHz band frequency multiplier is comparable to the previous evaluated 220 to 330 GHz band frequency multiplier based on a microstrip line device containing a gap with multi-layer graphene. The behavior of several harmonic components from order 9 to 17 generated in the multi-layer graphene component are examined while evaluating the output power and frequency response of the considered multiplier device.

2.4.1 Design and optimization of the frequency multiplier

The main waveguide blocks involved in the topology of the proposed frequency multiplier are the WR28 and WR2.2 waveguide sections. The new element introduced, the WR2.2 rectangular waveguide, has the dimensions and the frequency limits presented in Table 2.6:

WR2.2 waveguide	
Frequency limits [GHz]	Dimensions [mm]
330 - 500	0.57 x 0.285

Table 2.6: Characterization of the WR2.2 waveguide section.

The multiplier input and output matching transitions are synthesized using a three-dimensional electromagnetic simulator to calculate their S-parameters in an iterative procedure. The following two design steps are used in the optimization process.

2.4.1.1 Optimization in the 330 to 500 GHz and K_a band

The design process is started with the optimization of the submillimeter wave section composed by the microstrip to WR2.2 rectangular waveguide transition, the feeding microstrip line, and the output WR2.2 rectangular waveguide as presented schematically in Figure 2.26. In the same way as the previously analyzed (220 to 330 GHz band) frequency multiplier, the microstrip line structure is mounted into a metallic channel with rectangular cross section. The height of the channel placed on both sides of the WR2.2 waveguide section is 50 µm. From the bottom wall the first 25 µm are the microstrip substrate and the rest of the channel is filled with air. It has been sized to avoid the propagation of the waveguide modes around the microstrip circuit and the shorting of the microstrip circuit with the top wall. The dimensions of the rectangular channel and the microstrip line section which lies across it are displayed in Table 2.7.

Channel height [µm]	Substrate thickness [µm]	Channel width [mm]	Transmission line width [mm]
50	25	0.28	0.08

Table 2.7: Dimension assignment of the rectangular channel - 330 to 500 GHz band frequency multiplier.

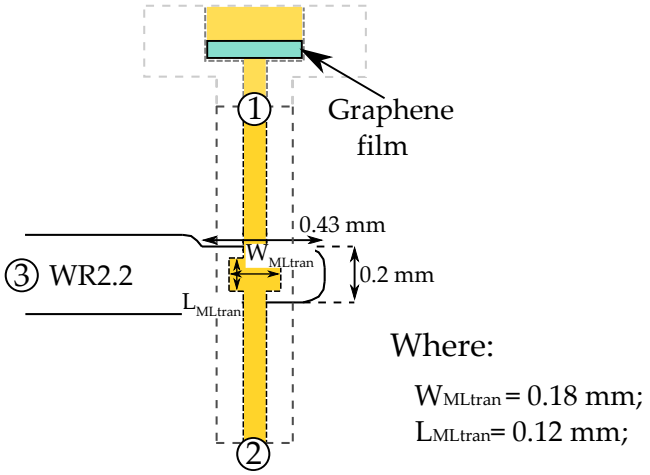

Figure 2.26: WR2.2 waveguide to microstrip line transition.

For the simulation of the electromagnetic behavior inside the proposed topology, the circuit was fed through one of the three waveports placed along its structure.

The position of each waveport as well as the dimensions of the optimized transition are presented in Figure 2.26.

The simulated scattering parameters are shown in Figure 2.28(a). The power loss between the output Port 3 and the input Port 1 is about 5 dB. The reflection coefficient at both the input and output port is below -10 dB in the 320 to 500 GHz respectively 320 to 440 GHz band, assuring a good impedance matching.

The microstrip to WR2.2 rectangular waveguide transition is the inner part of the topology used to propagate the input signal, in the K_a band, to the microstrip line structure and to the multi-layer graphene component. The topology of this transition is introduced in Figure 2.27. Therefore, in a second design step, two WR28 waveguide sections are arranged in a configuration with E-plane alignment and are interconnected by a microstrip line structure. The two WR28 rectangular waveguide sections are optimized together with the two microstrip elements placed inside them for a good signal transmission from Port 1 to Port 2 in the K_a band.

The relevant S parameters of the optimized transition are shown in Figure 2.28(b). Good impedance matching at the input Port 1 with a reflection coefficient lower than -10 dB ($S_{11} < -10$) in the 27.5 to 40 GHz frequency band was obtained. The insertion loss between Port 1 and Port 2 in the same frequency band is below 4 dB. Note that the frequency range from 27.5 to 40 GHz is the input optimum operation band of the frequency multiplier which will condition the output bandwidth of the different harmonic orders generated in the graphene component.

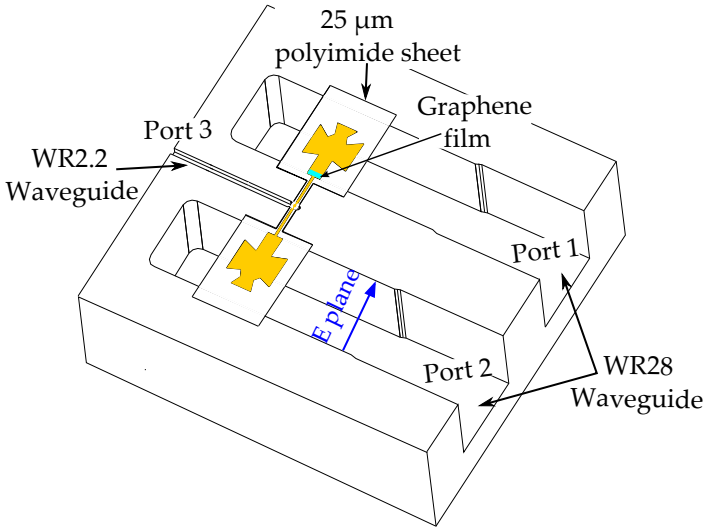

Figure 2.27: Topology of the 330 to 500 GHz band frequency multiplier used in the optimization of the K_a band.

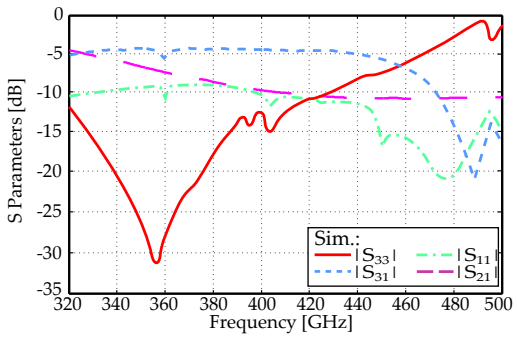

(a) Relevant S parameters of the high frequency section.

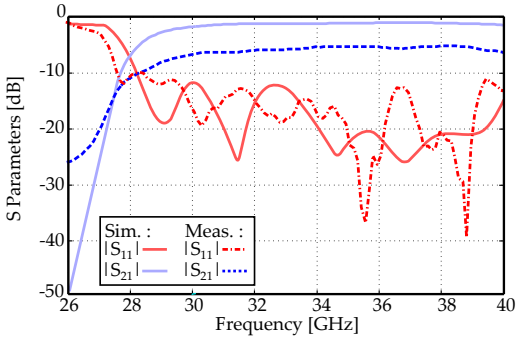

(b) Relevant S parameters of the low frequency section.

Figure 2.28: S parameters of the overall frequency multiplier assembly.

2.4.2 Prototype fabrication and experimental characterization

2.4.2.1 Prototype Implementation and Measurement setup

For the experimental validation of the 330 to 500 GHz band frequency multiplier a prototype has been manufactured and the test results are analyzed in terms of output power further on. The complete waveguide structure was divided into eight brass metal sheets, as shown in Figure 2.29(a), which were micromachined separately using the 2.5 axis milling machine used in the manufacture of the 220 to 330 GHz band frequency multiplier presented in Section 2.2. A 0.8 mm end mill tool for the WR28 waveguides and a 0.15 mm end mill tool for the WR2.2 waveguide and rectangular channel were used in the fabrication process of the prototype. Standard interface flanges for both WR28 and WR2.2 waveguides have been manufactured separately with the same aforementioned end milling tools and they were soldered to the assembled waveguide block. Figure 2.29(b) presents the assembled prototype terminated with its corresponding flanges while Figure 2.29(c) illustrates the output WR2.2 waveguide. The final microstrip structure prototype with focus on the graphene gap and the gold contacts, built on a 25 μm polyimide substrate in a single sputtering deposition process, is depicted in Figure 2.30.

The measurement setup employed for the experimental validation of the 330 to 500 GHz band graphene based frequency multiplier is similar with the schematic diagram presented in Figure 2.19 with the exception of the frequency extender module. The $PNA-X$ vector network analyzer is equipped with a *Virginia Diodes Inc.* frequency extender (receiver) module which is used to measure the power of the output signal in the 330 to 500 GHz frequency range, generated through frequency multiplication due to the non-linear electromagnetic behavior of the graphene.

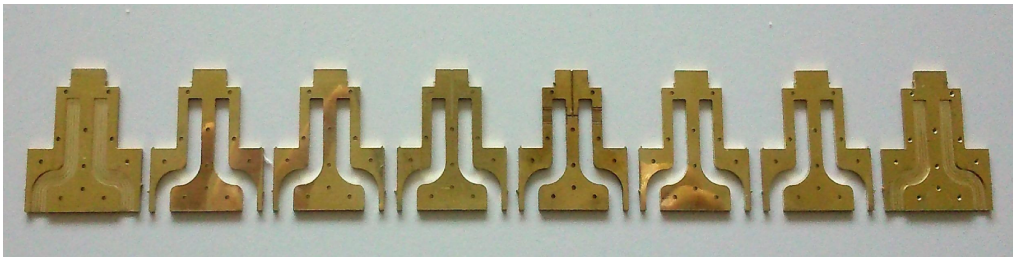

(a) Individual brass sheets.

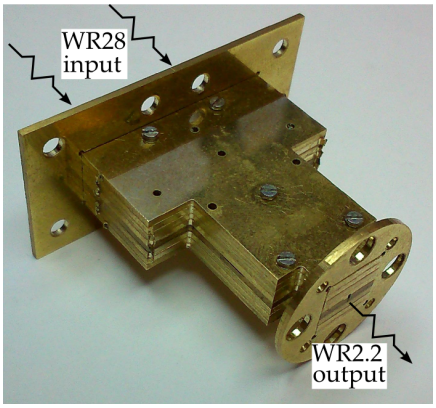

(b) Assembled prototype.

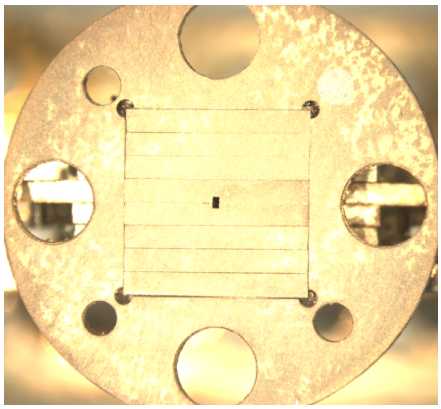

(c) WR2.2 waveguide with its corresponding flange.

Figure 2.29: Prototype of the 330 to 500 GHz band frequency multiplier.

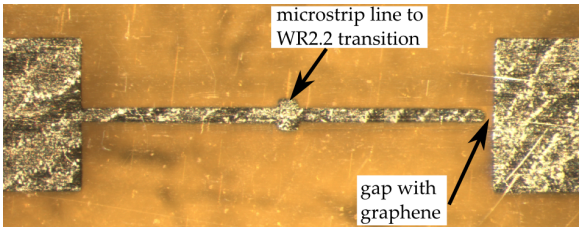

Figure 2.30: Image of the microstrip structure prototype which accentuates the graphene gap and the WR2.2 transition.

The input and output signals are limited by the bandwidth in which the corresponding waveguides operate under the fundamental TE_{10} mode and by the bandwidth of the measurement equipment. Since the input waveguide section works in the frequency band from 26 to 40 GHz, the harmonic components which provide an output signal in the 330 to 500 GHz frequency range can vary from $N = 9$ to $N = 17$. The whole output frequency range should be given by the expression: $26 \times N$ to $40 \times N$. The output waveguide section and the measurement system limit the frequency range in which one can evaluate the output multiplied signal. Therefore, for almost every value of N, the input and output operation bands should be calculated independently as they are only a portion of the K_a signal respectively 330 to 500 GHz signal.

2.4.2.2 Output power

Odd order harmonic components

The evolution of the output power of the odd order harmonic components, from order $N = 9$ to $N = 17$, has been represented in Figure 2.31. The output power of the selected harmonic components has been evaluated considering different values of the input power, which vary from $P_{in} = 10$ to 24 dBm in 2 dB steps. Higher input power values led to the melting of the substrate and burnout through the graphene device. The nominal operation bands for each harmonic number N have been calculated as stated in Table 2.8. These ranges have been marked as shadowed areas in the discussed graphics.

Order N	Input signal range f_{in}	Output signal range $N \times f_{in}$
9^{th}	36.6 GHz to 40 GHz	330 GHz to 360 GHz
11^{th}	30 GHz to 40 GHz	330 GHz to 440 GHz
13^{th}	26 GHz to 38.4 GHz	338 GHz to 500 GHz
15^{th}	26 GHz to 33.4 GHz	390 GHz to 500 GHz
17^{th}	26 GHz to 29.4 GHz	440 GHz to 500 GHz

Table 2.8: Nominal operation bands for odd order harmonic components - 330 to 500 GHz band frequency multiplier.

As one can observe from Figure 2.31, the maximum reached power in the case of the ninth order harmonic is around -36 dBm. This value is considerably higher than the maximum output power level of the ninth order harmonic in the case of the 220 to 330 GHz band frequency multiplier from Section 2.2. The mentioned value was around -41 dBm. Note that the maximum input power delivered to the

current frequency multiplier is 24 dBm while in the previous case (220 to 330 GHz band) it was 4 dB lower.

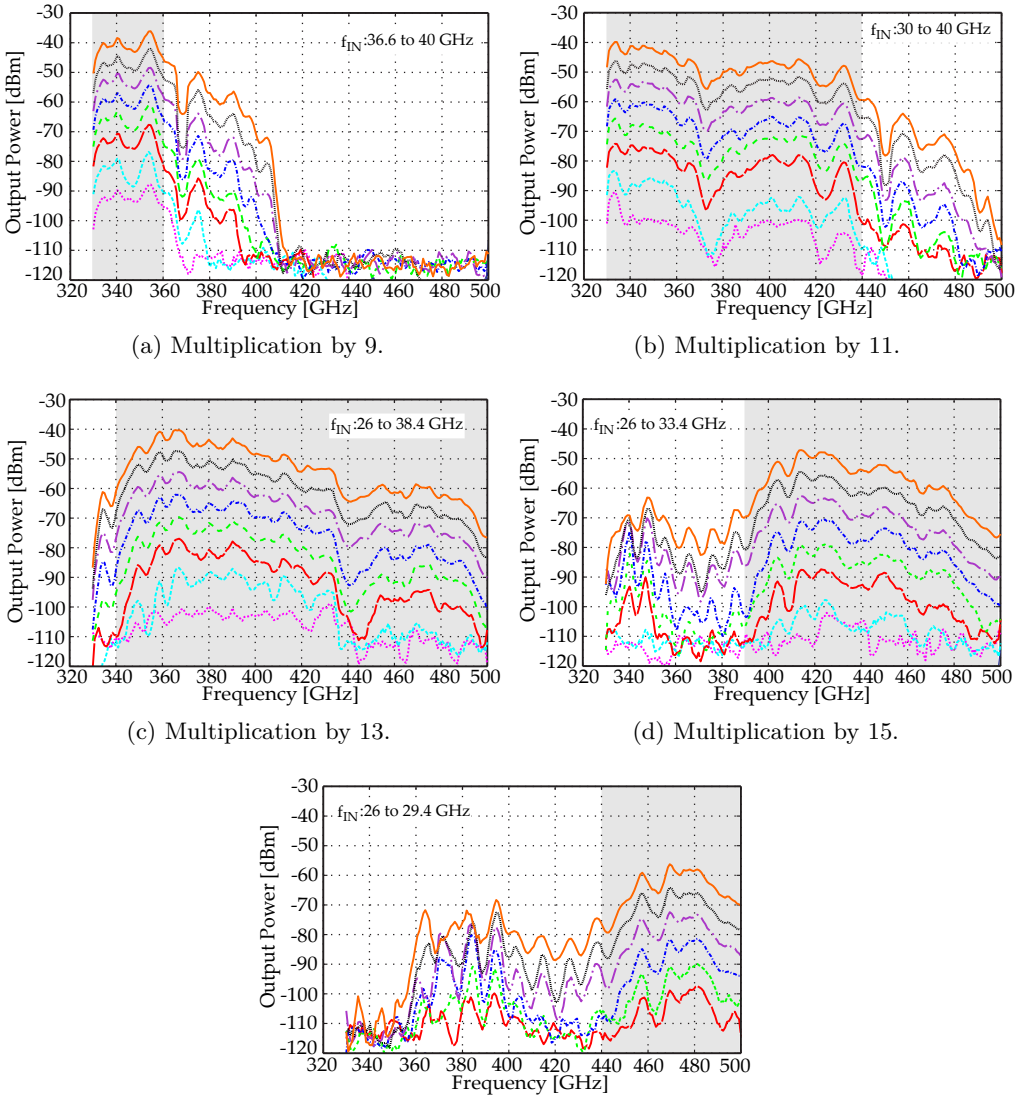

(a) Multiplication by 9.

(b) Multiplication by 11.

(c) Multiplication by 13.

(d) Multiplication by 15.

(e) Multiplication by 17.

Figure 2.31: Output power of the 330 to 500 GHz band frequency multiplier when odd harmonic components are used. Input power considered from 10 to 24 dBm varied in 2 dB steps.

Increasing the harmonic order the power levels measured at the output of the multiplier device are reduced. In this way, a maximum output power of around

−39 dBm in the case of the eleventh order harmonic, −41 dBm in the case of the thirteenth order harmonic, −47 dBm in the case of the fifteenth order harmonic and −57 dBm in the case of the seventeenth harmonic order were detected. Although the theory predicts nearly flat frequency response from low frequency to THz band, a rippled level is sometimes obtained. This can be due to possible impedance mismatching between the elements of the measurement setup.

Furthermore, the reason why an output power reduction is observed for frequency values greater than 450 GHz is because the S_{31} parameter represented in Figure 2.28(a) worsens from this frequency point. This means that a low portion of the signal generated in the 450 to 500 GHz frequency range is coupled to the output waveguide. A similar effect appears in the low frequency region for the harmonic components thirteen, fifteen and seventeen represented in Figure 2.31. In this case, since the input port is not well matched from 26 to 27.5 GHz (see S_{21} parameter in Figure 2.28(b)), the output power of the thirteen harmonic component under $13 \times 27.5 = 357.5$ GHz, the fifteen harmonic component under $15 \times 27.5 = 412.5$ GHz and the seventeen harmonic component under $17 \times 27.5 = 467.5$ GHz, is lower than expected. In any case, the bandwidth in which the frequency multiplication effect is obtained is only limited by the additional necessary circuitry and the measurement system, but not by the graphene sheet itself.

Even order harmonic components

The variation of the output power of the even order harmonic components, from order $N = 10$ to $N = 16$, has been represented in Figure 2.32. As in the case of odd order harmonic components, the power of the input signal varies in 2 dB steps, from 10 to 24 dBm. Table 2.9 illustrates the corresponding nominal frequency ranges in which the input and output waveguide sections work under the fundamental TE_{10} mode.

Order N	Input signal range f_{in}	Output signal range $N \times f_{in}$
10^{th}	33 GHz to 40 GHz	330 GHz to 400 GHz
12^{th}	27.5 GHz to 40 GHz	330 GHz to 480 GHz
14^{th}	26 GHz to 35.7 GHz	364 GHz to 500 GHz
16^{th}	26 GHz to 31.3 GHz	416 GHz to 500 GHz

Table 2.9: Nominal operation bands for even order harmonic components - 330 to 500 GHz band frequency multiplier.

The maximum power level produced is around −67.5 dBm and it corresponds

to the case of the tenth harmonic. Moreover, the maximum power achieved in the case of the twelfth harmonic is around −68.5 dBm, in the case of the fourteenth around −69.5 dBm and sixteenth around−88.5 dBm. For the same value of the input power, the measured output power is considerably lower than the one obtained when evaluating the odd harmonic case.

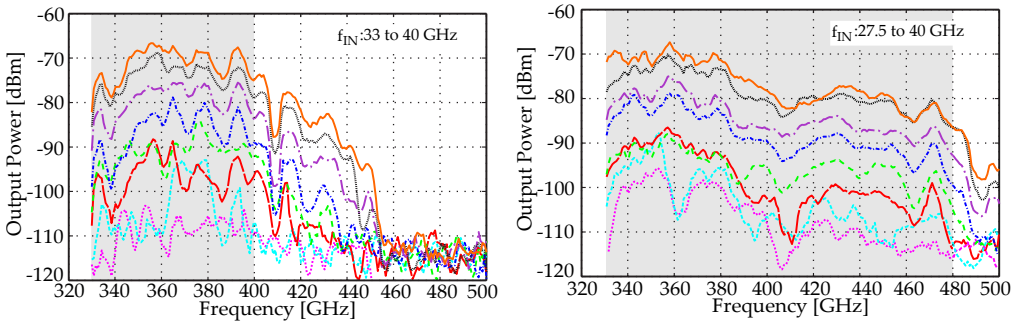

(a) Multiplication by 10.

(b) Multiplication by 12.

(c) Multiplication by 14.

(d) Multiplication by 16.

Figure 2.32: Output power of the 330 to 500 GHz band frequency multiplier when even harmonic components are used. Input power considered from 10 to 24 dBm varied in 2 dB steps.

2.4.2.3 Variation of the output electric field versus the input electric field

This subsection presents a comparison between the theoretical evaluation from Chapter 1 and the odd order harmonic content generated from the 330 to 500 GHz band graphene based frequency multiplier. The concept behind the current analysis is identical with Subsection 2.2.2.5. The input electric field and experimental output electric field were calculated using the power formula $E_{n\omega} \propto \sqrt{P_{in/out}}$, where n is the order of the considered harmonic. The output power of each examined harmonic

component is computed at a certain frequency point chosen carefully so the input signal which led to such a frequency value is within the flat region of the input nominal frequency range.

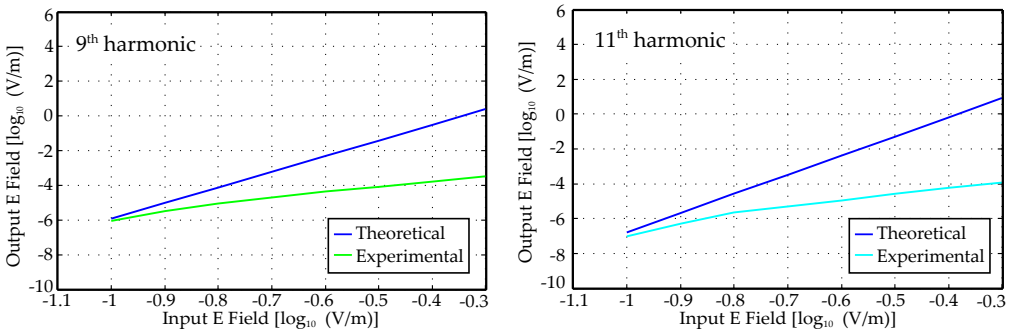

(a) 9^{th} harmonic component

(b) 11^{th} harmonic component

(c) 13^{th} harmonic component

(d) 15^{th} harmonic component

Figure 2.33: Experimental and theoretical comparison of the output versus the input electric field for different odd order harmonic components.

Therefore, the output ninth order power is examined at $f_{9\omega_{out}} = 350$ GHz ($f_{9\omega_{in}} = 39$ GHz), the eleventh order power at $f_{11\omega_{out}} = 380$ GHz ($f_{11\omega_{in}} = 34.5$ GHz), the thirteenth order power at $f_{13\omega_{out}} = 435$ GHz ($f_{11\omega_{in}} = 33.5$ GHz) and the fifteenth order power at $f_{15\omega_{out}} = 450$ GHz ($f_{15\omega_{in}} = 30.5$ GHz). For the seventeenth order component, the input signal needed to generate an output signal in the frequency range $f_{17\omega_{out}} = 440$ to 500 GHz is situated in a region of very high reflections (see $f_{17\omega_{in}} = 26$ to 29.4 GHz region from Figure 2.28(b)). For this reason, it was assumed that the results of the experimental output power generated for the mentioned harmonic component are not accurate and they should not be considered. Therefore they were excluded from Figure 2.33. In this way, only ninth, eleventh, thirteenth and fifteenth harmonic components are being represented fur-

ther on. The blue line from each figure represents the theoretical calculation of the n^{th} order electric field determined as the input electric field at the power of the considered harmonic ($E_{n\omega} \propto (E_{\omega})^n$).

At low values of the input electric field a good agreement between the theoretical and experimental results is noticed. Although when increasing the input power delivered to the multiplier device, the calculated theoretical data and measured experimental data seem not to follow the same tendency. This is in conformity with the low-field condition imposed on the calculations developed in Chapter 1.

2.4.2.4 Output electric field versus the harmonic order

This subsection discusses the case of the output electric field evaluated against the harmonic order for certain selected frequency points. The concept is similar with the analysis from Subsection 2.2.2.6. The formula of the graphene current density of electrons from Equation 2.1 was expanded in order to contain the contribution of the harmonic content from the ninth order up to the fifteenth order. Therefore, the current density values of the components which are important in the conducted analysis are:

$$\begin{aligned} j_{9\omega} &= en_s v_F \frac{35}{2^{22}} Q_0^9 \\ j_{11\omega} &= en_s v_F \frac{147}{2^{27}} Q_0^{11} \\ j_{13\omega} &= en_s v_F \frac{693}{2^{32}} Q_0^{13} \\ j_{15\omega} &= en_s v_F \frac{14157}{2^{39}} Q_0^{15} \end{aligned} \tag{2.3}$$

As in the case of the 220 to 330 GHz band graphene based frequency multiplier, the graphics of the output power when considering the odd order harmonic generation (see Figure 2.31) are analyzed at particular frequencies. There is no frequency point within the nominal operation bands of the proposed multiplier device common to all odd harmonic components. For this reason, a fixed frequency point was chosen for every two/three harmonics and the experimental value of the electric field was computed using the power formula. Therefore, the ninth and eleventh order electric field were examined at 350 GHz and the eleventh, thirteenth and fifteenth at 435 GHz. From the estimated experimental electric field considering the approximation $E_{n\omega} \propto j_{n\omega}$, the current corresponding to each harmonic component was computed. These values were introduced into Equation 2.3 and the value of the field parameter Q_0 was calculated. The experiment was conducted for an input power variation from

10 to 14 dBm in 2 dB steps. Replacing the value of Q_0, calculated for the ninth harmonic at 350 GHz, into the equation of the eleventh order current density one is able to compute the theoretical value of the eleventh order electric field. Likewise, using the value of Q_0 calculated for the eleventh harmonic at 435 GHz and replacing this value into the equation of the thirteenth and fifteenth harmonic current density, one is able to calculate the output theoretical thirteenth and fifteenth electric field.

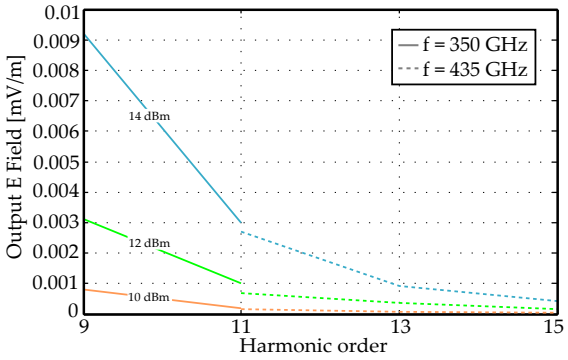

Figure 2.34: Experimental output electric field variation with the harmonic order for fixed values of the input power. The output frequency of the power considered is 350 GHz for 9^{th} and 11^{th} harmonic (solid line) and 435 GHz for 11^{th}, 13^{th} and 15^{th} harmonic (dashed line).

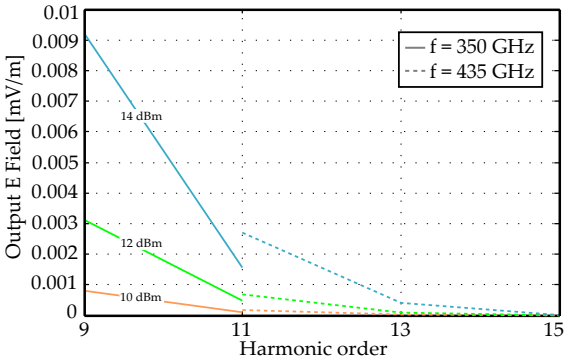

Figure 2.35: Theoretical output electric field variation with the harmonic order for fixed values of the input power. The output frequency of the power considered is 350 GHz for 9^{th} and 11^{th} harmonic (solid line) and 435 GHz for 11^{th},13^{th} and 15^{th} harmonic (dashed line).

The results of the experimental and theoretical predictions are represented in Figure 2.34 and Figure 2.35. As already observed from the analysis presented in Subsection 2.3.2.6, the electric field obtained from the measurements of the different

high harmonic components is generated with higher values than the corresponding calculated theoretical one.

Additionally, for the visualization of both even and odd harmonic components generated at the output of the considered frequency multiplier, the maximum electric field for a given input power is represented versus the theoretical values in Figure 2.36. The output theoretical electric field of each odd order examined harmonic was calculated using the value of the electric field incident on the multi-layer graphene raised at the power of the considered component ($E_{n\omega} \propto (E_{\omega})^n$). In order to maintain consistency with the previous analysis presented in this subsection, a $P_{in} =$ 14 dBm input power is considered. The output theoretical electric field is computed only for odd order harmonic components. The results for the harmonic orders 16 and 17 are not included in the representation as the theoretical curve decreases several orders of magnitude faster than the experimental content. As can be seen, the odd order harmonic components decrease analogously with the theoretical results. On the contrary, the even order components seem to follow a smoother decreasing trend.

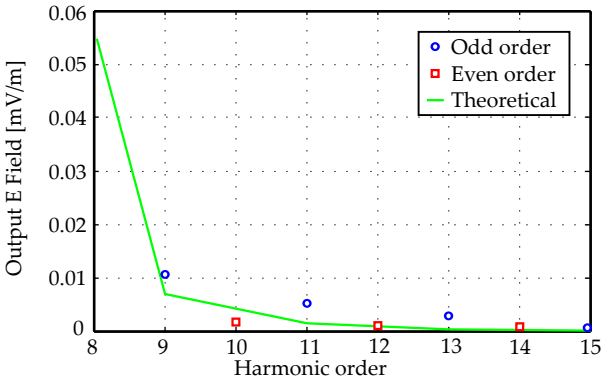

Figure 2.36: Maximum output electric field for different harmonic orders, compared to the theoretical defined curve.

2.5 140 to 220 GHz band Frequency Multiplier

In order to demonstrate the broad frequency response of graphene a third single stage high order frequency multiplier with the output response in the 140 to 220 GHz (WR5 standard frequency) band is being discussed herein. The behavior of the frequency multiplier is analyzed when different harmonic components from order 5 to 8 are being generated in a graphene strip placed along a microstrip line structure.

2.5.1 Design and optimization of the frequency multiplier

The main waveguide blocks involved in the topology of the proposed 140 to 220 GHz band frequency multiplier are the WR28 and WR5 waveguide sections. The dimensions of the WR5 waveguide section, are shown in Table 2.10.

WR5 waveguide	
Frequency limits [GHz]	Dimensions [mm]
140 - 220	1.295 x 0.648

Table 2.10: Characterization of the WR5 waveguide section.

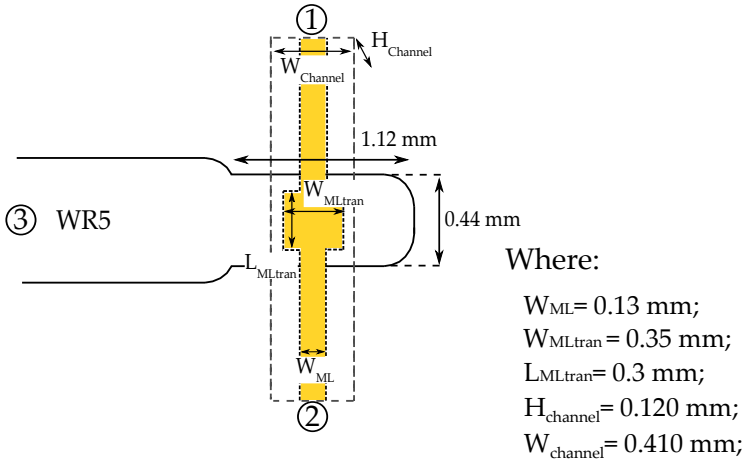

Figure 2.37: Topology of the microstrip to WR5 waveguide transition.

The electromagnetic fields inside the frequency multiplier structure are calculated using three-dimensional electromagnetic simulation software (Ansoft HFSS). As already indicated, the scope of the current thesis is to demonstrate the practical implementation of multi-layer graphene into a configuration which reproduces the electromagnetic behavior of theoretically isolated graphene, in terms of high harmonic generation in the frequency band from 140 to 500 GHz. Therefore the main difference of the current implementation with respect to the previous two analyzed frequency multipliers is the design of the microstrip to WR5 transition. This transition couples and transfers to the output of the complete device the high harmonic multiplied signal, in the 140 to 220 GHz band. The topology of the transition with the adequate dimensions is presented in Figure 2.37.

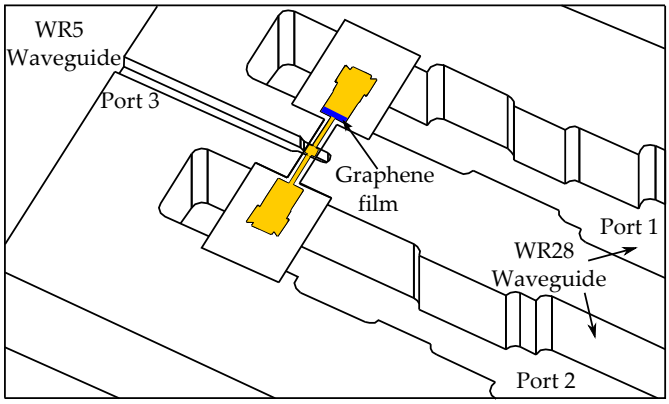

Figure 2.38: 140 to 220 GHz band band Frequency Multiplier topology.

For the propagation of the input signal, in the K_a band, towards the graphene component, a WR28 waveguide to microstrip line transition is designed. As presented in Figure 2.38, the microstrip terminal of the transition is connected to the optimized microstrip to WR5 rectangular waveguide transition. The high harmonic multiplied signal is transferred through the WR5 waveguide section at the output of the frequency multiplier while the untransferred input signal is transmitted to a second WR28 waveguide section.

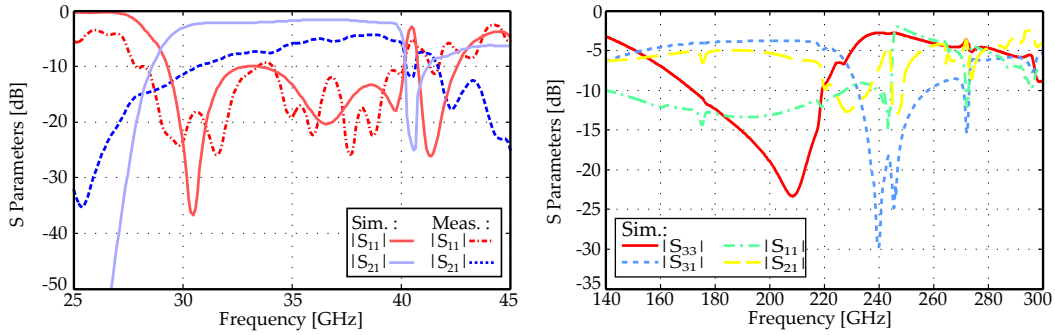

(a) Input frequency response.

(b) Output frequency response.

Figure 2.39: 140 to 220 GHz band frequency multiplier - Scattering parameters.

The input signal performance in terms of the scattering parameters is presented in Figure 2.39(a). The reflection coefficient at the input port is $S_{11} < -10$ dB in the frequency range from around 28 to 40 GHz, assuring a good input impedance matching. The transmission coefficient between Port 1 and Port 2 in the same band is below -4 dB. Moreover, the output signal performance in the 140 to 220 GHz band in terms of the scattering parameters is presented in Figure 2.39(b). The output

insertion loss from Port 1 to Port 3 is under 5 dB.

2.5.2 Prototype fabrication and experimental characterization

2.5.2.1 Prototype Implementation and Measurement setup

Once the transitions that compose the 140 to 220 GHz band frequency multiplier have been designed, analyzed and experimentally validated, they are put together in a prototype of the complete system. This subsection is focused on the development of the prototype and on the obtainment of experimental results to evaluate the practical performance of multi-layer graphene in the generation of harmonic content with frequency response in the WR5 standard band.

In the manufactured process, due to the size of the WR28 input waveguide section which has a width of 7.112 mm, the complete frequency multiplier structure was divided, as in the earlier described 220 to 330 GHz and 330 to 500 GHz band frequency multipliers, in eight brass sheets of 1 mm thickness each. These blocks are individually micromachined. The assembled block, back side and front side, together with the corresponding interface flanges soldered on it are presented in Figure 2.40.

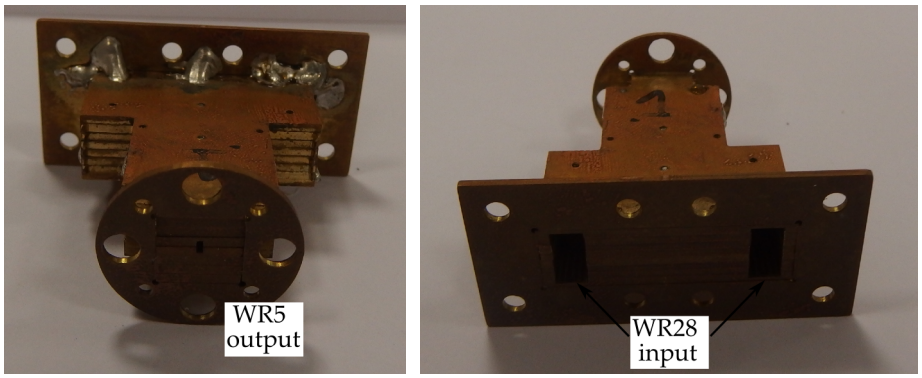

(a) Assembled prototype front view. (b) Assembled prototype back view.

Figure 2.40: Prototype of the 140 to 220 GHz band graphene based frequency multiplier.

The prototype of the microstrip structure composed of a pair of WR28 waveguide to microstrip line transitions and a microstrip line to WR5 waveguide transition as well as the gap filled with multi-layer graphene is displayed in Figure 2.41.

The frequency multiplier is pumped with an input signal in the K_a band, generated by an Agilent $N5247A$ $PNA-X$ vector network analyzer and amplified to a maximum power lever of 24 dBm with a 30 dB gain power amplifier, as depicted in the schematic diagram from Figure 2.19. The output submillimeter wave signal

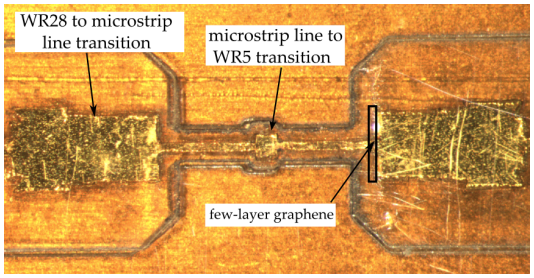

Figure 2.41: Microstrip structure prototype after the final laser cutting process.

is measured with a receiving extender head in the adjacent WR3 standard band (220 to 330 GHz) due to the absence of a WR5 band extender head. Although the used extender head is only guaranteed to consistently detect submillimeter wave radiation in the WR3 band, above 220 GHz, it has been verified to receive several decaying peaks under that frequency. For this reason, the output power generated from the proposed frequency multiplier has been represented down to 170 GHz. The measurements under 220 GHz have been marked with an arrow which delimits the WR5 standard band. A complete frequency response in the WR5 standard band is going to be measured in the next chapter through the implementation of a sixth and eight order subharmonic graphene based mixer which receives the RF radiation from the current WR5 band graphene based frequency multiplier and downconverts it to an IF signal by using a subharmonic LO signal in the K_a band.

2.5.2.2 Output power

The output power, corresponding to an electric field incident on the multi-layer graphene in both tangential and perpendicular direction, has been measured as a function of frequency for an input power level which varies from $P_{in} = 12$ to 24 dBm in 2 dB steps. The harmonic content detected at the output of the graphene based frequency multiplier varies from order $N = 5$ to $N = 8$ including odd and even order harmonics.

Odd order harmonic components

The input and output frequency range of the 5^{th} and 7^{th} order harmonic component are calculated and displayed in Table 2.11. These data are represented in Figure 2.42 as shadowed areas.

For the harmonic order 5, as the input signal from 41 to 45 GHz is not totally coupled to the microstrip line but it is partially reflected back (check scattering parameters from Figure 2.39(a)) a reduction of the output power is noticed from

Order N	Input signal range f_{in}	Output signal range $N \times f_{in}$
5^{th}	39 to 40 GHz	195 to 200 GHz
7^{th}	28 to 40 GHz	195 to 280 GHz

Table 2.11: Nominal operation bands for odd order harmonic components - 140 to 220 GHz band frequency multiplier.

205 to 230 GHz. After that, the multiplied power drops to the noise floor level, which is around −120 dBm, whereas the seventh component can still be used. This phenomena of power level reduction is also noticed for the harmonic order 7 from $40 \times N$ to $44 \times N$ which is comparable to an output signal in the frequency band 280 GHz to 310 GHz. The measurements in the 140 to 220 GHz band have been marked with an arrow in Figure 2.42, since they are distorted by the out-of-band performance of the receiving extender head. However, the signal level observed at some particular frequencies in the upper end of the WR5 standard band are similar to those from the beginning of the WR3 standard band, which indicates the proper operation of the circuit.

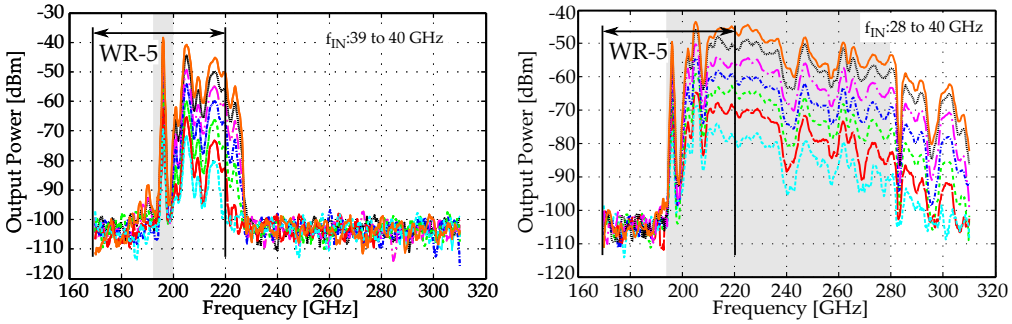

(a) Multiplication by 5.

(b) Multiplication by 7.

Figure 2.42: Output power of the 140 to 220 GHz band frequency multiplier when odd harmonic components are used. Input power considered from 12 to 24 dBm varied in 2 dB steps.

Even order components

The output power, when considering the 6^{th} and 8^{th} even order harmonic components generated in the graphene sample, is displayed in Figure 2.43. The power of the input signal varies in 2 dB steps, with a maximum value of 24 dBm, as in the previous case. The nominal frequency ranges of the input and output signal

flowing through the WR28 respectively WR5 waveguide section are determined in Table 2.12 and are shaded in Figure 2.43.

Order N	Input signal range f_{in}	Output signal range $N \times f_{in}$
6^{th}	32.5 to 40 GHz	195 to 240 GHz
8^{th}	28 to 40 GHz	224 to 320 GHz

Table 2.12: Nominal operation bands for even order harmonic components - 140 to 220 GHz band frequency multiplier.

Note that although outside the nominal ranges some values of the output power can still be noticed, for example in the case of the harmonic order 6 from 240 to 250 which corresponds to a signal transformation $40 \times N$ to $41.6 \times N$, these values were not considered part of the nominal operation bands. The insertion loss is substantially low outside the nominal ranges (see relevant S parameters from Figure 2.39(a)).

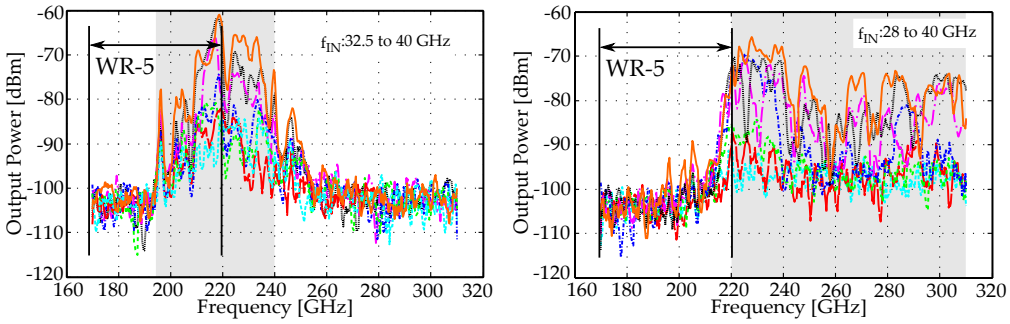

(a) Multiplication by 6.

(b) Multiplication by 8.

Figure 2.43: Output power of the 140 to 220 GHz band frequency multiplier when odd harmonic components are used.

2.5.2.3 Variation of the output electric field versus the input electric field

The output versus the input electric field variation is evaluated both experimentally and theoretically, using the power content generated at the output of the 140 to 220 GHz band frequency multiplier and the consideration from Chapter 1. Applying the power formula, $E_{n\omega} \propto \sqrt{P_{in/out}}$, the input electric field and experimental output electric field are each computed.

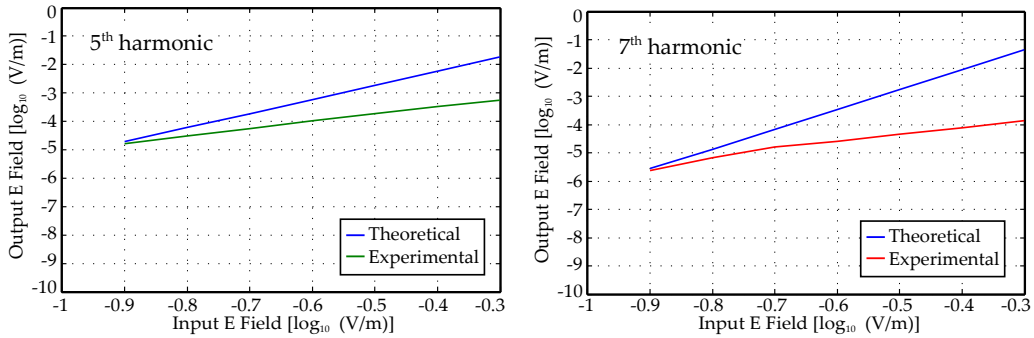

(a) 5^{th} harmonic component

(b) 7^{th} harmonic component

Figure 2.44: Experimental and theoretical comparison of the output versus input electric field dependency for different odd order harmonic components.

Since the frequency response of the different harmonic components is not completely flat throughout all the output nominal operation bands, the output power of each harmonic component has to be analyzed at particular frequency points within their nominal range. Therefore, the output fifth order power is investigated at $f_{5\omega_{out}} = 195$ GHz and the output seventh order power at $f_{7\omega_{out}} = 220$ GHz. The theoretical output electric field is computed using the assumption that this value equals the input electric field at the power of the examined harmonic ($E_{n\omega} \propto (E_{\omega})^n$). The results are illustrated in Figure 2.44.

2.5.2.4 Output electric field versus the harmonic order

Figure 2.45 presents a comparison between the theoretical results, calculated for an input power $P_{in} = 16$ dBm, and the maximum output electric field for the different odd and even order harmonic components generated in the multi-layer graphene sheet.

As an important remark, the experimental values measured at the output of the frequency multiplier could have been altered by the out of band performance of the used receiving extender head. For this reason it is supposed that, in some cases, the amplitude of the generated high order components is slightly different than the measured values. This can be the main reason why the theoretical curve from Figure 2.45 is not precisely consistent with the odd order experimental values. Moreover, the even orders 6 and 8 have almost the same value and their amplitudes are considerably lower than the theoretical results.

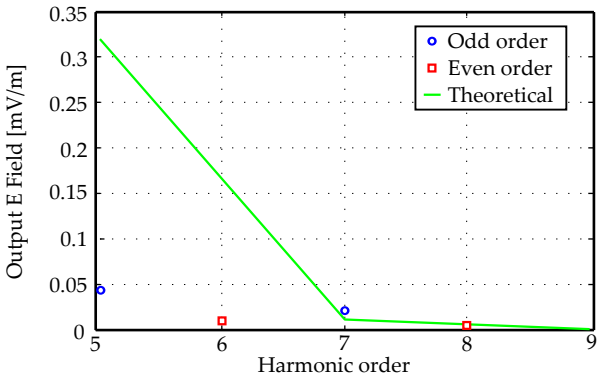

Figure 2.45: Maximum output electric field for different harmonic orders, compared to the theoretical curve

2.6 Comparison with other frequency multipliers

The performance of the graphene based frequency multipliers that have been proposed is compared with other graphene based implementations presented in the literature in Table 2.13. In [29] and [30] the frequency doublers are implemented using graphene based FET transistors while [10] presents a frequency tripler based on a microstrip gap with a multi-layer graphene sheet. In [1] the frequency multiplication effect is experimentally demonstrated on a metallic coplanar line waveguide (CPW) device deposited directly on a graphene monolayer which is further DC biased. Different harmonic components of the input applied signal from order $n = 2$ to $n = 7$ have been directly analyzed at the output of the CPW device.

Conversion efficiency values substantially higher than those presented in this thesis have been found in the literature, corresponding to lower harmonic implementations, operating at output frequencies up to 70 GHz. Nevertheless, for similar high order harmonic components the values become nearly comparable.

Furthermore, Table 2.14 presents a comparison between the work herein and other recently published scientific works regarding waveguide frequency multipliers, implemented with traditional semiconductors and operating in the low THz frequency range. A frequency doubler integrating two MMIC (monolithic microwave integrated circuit) chips with six GaAs Schottky diodes each has been demonstrated in [31]. Moreover, two frequency triplers implemented using a GaAs varactor diode chip are designed and experimentally analyzed in [32]. A single stage frequency quintupler for 474 GHz has been demonstrated in [33] using a silicon integrated Heterostructure Barrier Varactor (HBV). For increased harmonic orders, the direct conversion with conventional semiconductors, in the low THz band, is absent in the

literature. A common method used to obtain high orders of multiplication is by chaining a set of cascading low order frequency multipliers. This approach is considered in [34] where the performance of a 2×3×3 frequency multiplier chain to the 1.7-1.9 THz band is demonstrated using GaAs Schottky diodes.

Ref.	Input frequency f_{in} [GHz]	Output frequency f_{out} [GHz]	Harmonic order N	Conversion efficiency [dB]	Maximum output power [dBm]
[29]	0.7	1.4	2	-30 to -45	-24
[30]	3	6	2	-28 to -40	-23
[10]	2.5-5	7.5-15	3	-26 to -55	-6
[1]	1-10	2-70	2	< -32	-38
			3	< -34	-44
			4	< -36	-49
			5	< -43	-53
			6	< -45	-58
			7	< -48	-63
This work	26.5-40	140-220	5	< -60.75	-36.75
			6	< -84.2	-60.2
			7	< -67.75	-43.75
			8	< -89	-65
		220-330	6	< -82.36	-62.36
			7	< -54.3	-34.3
			8	< -88.34	-68.34
			9	< -61.67	-41.67
			10	< -90.95	-70.95
			11	< -80.9	-60.9
		330-500	9	< -60.12	-36.12
			10	< -91.36	-67.36
			11	< -62.94	-38.94
			12	< -92.4	-68.4
			13	< -64.75	-40.75
			14	< -93.26	-69.26
			15	< -71.14	-47.14
			16	< -94.48	-70.48
			17	< -80.29	-56.29

Table 2.13: Comparison of graphene based frequency multipliers.

As the graphene based frequency multipliers, developed in this thesis, were not optimized for a specific harmonic order but they were developed essentially to prove the direct high harmonic generation of multi-layer graphene, the efficiency of the proposed devices is considerably lower than the state of the art waveguide frequency multipliers implemented with traditional semiconductors. It is believed that this performance can be improved by further optimizing the transitions involved.

Ref.	Input frequency f_{in} [GHz]	Output frequency f_{out} [GHz]	Harmonic order N	No of stages	Efficiency [%]	Maximum output power [dBm]
[31]	88-102	176-204	2	1	9	8.57
[32]	70-76	210-228	3	1	16	13
	140-150	420-450	3		12	9.54
[33]	92-96	460-480	5	1	0.75	4.47
[34]	92-106	184-212	2	1	9 to 29	14.62
	92-106	560-640	2×3	2	0.75 to 2.9	4.62
	92-106	1680-1920	2×3×3	3	1.5e-2	-18.24
This work	26.5-40	140-220	5	1	8.5e-5	-36.75
			6		3.9e-7	-60.2
			7		1.65e-5	-43.75
			8		1.27e-7	-65
		220-330	6	1	5.8e-9	-62.36
			7		3.72e-4	-34.3
			8		1.5e-7	-68.34
			9		6.8e-5	-41.67
			10		8e-8	-70.95
			11		8.13e-7	-60.9
		330-500	9	1	9.8e-5	-36.12
			10		7.35e-8	-67.36
			11		5.1e-5	-38.94
			12		5.78e-8	-68.4
			13		3.36e-5	-40.75
			14		4.74e-8	-69.26
			15		7.73e-6	-47.14
			16		3.58e-8	-70.48
			17		9.4e-7	-56.29

Table 2.14: Comparison of waveguide frequency multipliers.

2.7 Conclusions

This chapter presents the design procedure, analysis and the experimental validation of three Single Stage High Order Submillimeter Wave/THz band Graphene Based Frequency Multipliers. First of all, the general topology which is common for all frequency multipliers has been given. Secondly, each circuit is being discussed separately and the differences with respect to each other are introduced. For each single stage high order graphene based frequency multiplier a prototype has been implemented and experimentally characterized at room temperature. The evolution of the output power as a function of frequency has been analyzed for different values of the input signal and for different harmonic components. Both even and odd order harmonic components have been generated at the output of the multiplier devices. Assuming the theoretical predictions of normal incidence on a graphene sample, the even order harmonic elements are equally zero. However, due to many differences between the multi-layer graphene sample used in this thesis and the isolated graphene layer theoretically analyzed, harmonic components of unconstrained order are also generated in the induced current. The amplitude of the even order harmonic components was substantially lower than the amplitude of odd order harmonic content. The experimental results obtained with the three prototypes of the frequency multipliers have shown that graphene has flat frequency response from 140 GHz to 500 GHz frequency band as no sign of signal saturation was noticed. The maximum input power delivered to the frequency multipliers was limited to $P_{in} = 24$ dBm. High values of the input power led to the melting of the substrate used and burnout through the graphene device. A peak output power value around -34 dBm corresponding to the seventh harmonic component has been obtained when analyzing the multiplier devices.

Further, the obtained results when evaluating the odd order harmonic components have been compared with the theoretical analysis developed in Chapter 1. The output experimental and theoretical electric field was evaluated against the input electric field. The results agree at low values of the input field. This fact is in consonance with the low-field condition imposed on the theoretical developed calculations.

Therefore, although the experimental results have been obtained from a finite multi-layer graphene device placed on top of a dielectric substrate, they are in agreement with the previously reported theoretical studies which consider ideal infinite two-dimensional graphene samples. In conclusion the described devices represent a proof of concept which experimentally validate that graphene can be used by itself as signal generator in the submillimeter/low THz band.

Bibliography

[1] M. Dragoman, D. Neculoiu, G. Deligeorgis, G. Konstantinidis, D. Dragoman, A. Cismaru, A. A. Muller, and R. Plana, "Millimeter-wave generation via frequency multiplication in graphene," Appl. Phys. Lett. 97, 093101, 2010.

[2] M. Dragoman, A. Cismaru, A. Dinescu, D. Dragoman, G. Stavrinidis, and G. Konstantinidis, "Enhancement of higher harmonics in graphene-based coupled coplanar line microwave multipliers," J. Appl. Phys. Lett., 114, 154304, 2013.

[3] J. J. Dean, H. M. van Driel, "Second harmonic generation from graphene and graphitic films," Phys. Lett. 95, 261910, 2009.

[4] J. J. Dean, H. M. van Driel, "Graphene and few-layer graphite probed by second-harmonic generation: Theory and experiment, " Phys. Rev. B 82, 125411, 2010.

[5] S. A. Mikhailov, "Theory of the giant plasmon-enhanced second-harmonic generation in graphene and semiconductor two-dimensional electron system," Phys. Rev. B 84, 045432, 2011.

[6] M. Glazov, "Second Harmonic Generation in Graphene," JETP Letters 93 (7), 366 (2011).

[7] S. A. Mikhailov, "Non-linear electromagnetic response of graphene, " EPL 79, 27002-pl, 2007.

[8] E. Hendry, P. J. Hale, J. Moger, and A. K. Savchenko, and S. A. Mikhailov, "Coherent Nonlinear Optical Response of Graphene," Phys. Rev. Lett. 105, 097401, 2010.

[9] N. Kumar, J. Kumar, C. Gerstenkorn, R. Wang, H. Y. Chiu, A. L. Smirl, and H. Zhao, "Third harmonic generation in graphene and few-layer graphite films," Phys. Rev. B 87, 121406, 2013.

[10] R. Camblor, S. V. Hoeye, G. Hotopan, C. Vazquez, M. Fernandez, F. L. Heras, P. Alvarez, R. Menendez, "Microwave frequency tripler based on a microstrip gap with graphene, " Journal of Electromagnetic Waves and Applications, vol. 25, no. 14-15, pp. 1921-1929, 2011.

[11] S. Y. Hong, J. I Dadap, N. Petrone, P. C. Yeh, J. Hone, and R. M. Osgood Jr., "Optical Third-Harmonic Generation in Graphene," Phys. Rev. X 3, 021014, 2013.

[12] S. A. Mikhailov and K. Ziegler, "Non-linear electromagnetic response of graphene: Frequency multiplication and the self-conistent-field effects," J. Phys. Condens. Matter 20, 384204, 2008.

[13] F. J. Lopez-Rodriguez and G. G. Naumis, "Analytic solution for electrons and holes in graphene under electromagnetic wave Gap appearance and nonlinear effects, " Phys. Rev. B 78, 201406(R), 2008.

[14] S. A. Mikhailov, "Non-linear graphene optics for terahertz applications, " Microelectron. J. 40, 715, 2009.

[15] K.L. Ishikawa, "Nonlinear optical response of graphene in time domain, " Rhys. Rev. B 82, 201402, 2010.

[16] H. Wang, D. Nezich, J. Kong, and T. Palacios, "Graphene frequency multipliers," IEEE Electron Device Letters, Vol. 30, No. 5, May 2009.

[17] Z. Wang, Z. Zhang, H. Xu, L. Ding, S. Wang, and L. M. Peng, "A high-performance top-gate graphene field-effect transistor based frequency doubler," Appl. Phys. Lett. 96, 173104, 2010.

[18] G. Hotopan, S. Ver Hoeye, C. Vazquez, R. Camblor, M. Fernandez, F. Las Heras, P. Alvarez, and R. Menendez, "Millimeter wave microstrip mixer based on graphene," Prog. Electromagn. Res., Vol. 118, 57-69, 2011.

[19] G. Hotopan, S. Ver Hoeye, C. Vazquez, A. I. Hadarig, R. Camblor, M. Fernandez, and F. Las Heras, "Millimeter wave subharmonic mixer implementation using graphene film coating," Prog. Electromagn. Res., Vol. 140, 781-794, 2013.

[20] A. Maestrini, B. Thomas, H. Wang, C. Jung, J. Treuttel, Y. Jin, G. Chattopadhyay, I. Mehdi, G. Beaudin, "Schottky diodes based terahertz frequency multipliers and mixers," C. R. Physique 11, 480-495, 2010.

[21] A. Tessmann, I. Kallfass, A. Leuther, H. Massler, M. Kuri, M. Riessle, M. Zink, R. Sommer, A. Wahlen, H. Essen, V. Hurm, M. Schlechtweg, and O. Ambacher, "Metamorphic HEMT MMICs and modules for use in high-bandwidth 210 GHz radar," IEEE Journal of solid-state circuits, Vol 43, No 10, 2008.

[22] D. M. Polzar, "Microwave Engineering 2nd Edition, ", John Wiley & Sons, New York, 1998.

[23] A. Maestrini, J. Ward, J. Gill , H. Javadi, E. Schlecht, C. Tripon-Canseliet, G. Chattopadhyay, and I. Mehdi, "A 540-640 GHz High Efficiency Four-Anode Frequency Tripler, " IEEE Transactions on Microwave Theory and Techniques, Vol. 53, No. 9, 2835-2841, 2005.

[24] C. Vazquez, A. Hadarig, S. Ver Hoeye, M. Garcia, R. Camblor, G. Hotopan, and F. Las Heras, "High Order Subharmonic Millimeter Wave Mixer based on Few Layer Graphene," IEEE Transactions on Microwave Theory and Techniques, Vol. 63, Issue 4, 1361-1369, 2015.

[25] A. Maestrini, J. Ward, H. Javadi, C. Tripon-Canseliet, J. Gill, G. Chattopadhyay, E. Schlecht, and I. Mehdi, "Local oscillator chain for 1.55 to 1.75 thz with 100 muW peak power," IEEE Microwave and Wireless Components Letters, Vol. 15, Issue 12, 871-873, 2015.

[26] Ansoft HFSS. High Frequency Structure Simulator 12.0 Documentation. 2012.

[27] J. M. Jin, "The Finite Element Method in Electromagnetics, " second edition, John Willey and Sons, Inc., New York, 2002.

[28] J. L. Lolakis, A. Chatterjee and L. C. Kempel, "Finite element method for electromagnetics, " IEEE Press, Oxford University Press, 1997.

[29] H. Wang, A. Hsu, Ki K. Kim, J. Kong, T. Palacios, "Gigahertz Ambipolar Frequency Multiplier based on CVD Graphene, " 2010 IEEE International Electron Devices Meeting (IEDM), 23.6.1-23.6.4, Dec 2010.

[30] Lv Hongming, Wu Huaqiang, Liu Jinbiao, Can Huang, Li Junfeng, Yu Jiahan, Niu Jiebin, Xu Qiuxia, Yua Zhiping, and He Qian, "Inverted process for graphene integrated circuits fabrication," Nanoscale, 2014,6, 5826-5830.

[31] J. V. Siles, A. Maestrini, B. Alderman, S. Davies, H. Wang, J. Treuttel, E. Leclerc, T. Narhi and C. Goldstein, "A Single-Waveguide In-Phase Power-Combined Frequency Doubler at 190 GHz," IEEE Microwave and Wireless Components Letters, Vol. 21, Issue 6, 332-334, 2011.

[32] D. W. Porterfield, "High-Efficiency Terahertz Frequency Triplers," IEEE/MTT-S International Microwave Symposium, DOI: 10.1109/MWSYM.2007.380439, 2007.

[33] A. Malko, T. Bryllert, J. Vukusic and J. Stake, "A 474 GHz HBV Frequency Quintupler Integrated on a 20 µm Thick Silicon Substrate," IEEE Transactions on Terahertz Science and Technology, Vol. 5, Issue 1, 85-91, 2015.

[34] A. Maestrini, J. Ward, J. Gill, H. Javadi, E. Schlecht, G. Chattopadhyay, F. Maiwald, N. R. Erickson and I. Mehdi, "A 1.7-1.9 THz Local Oscillator Source," IEEE Microwave and Wireless Components Letters, Vol. 14, Issue 6, 253-255, 2004.

Chapter 3

Graphene based Subharmonic Mixer

Contents

3.1 Introduction

This chapter presents the design and analysis of Single Stage High Order Submillimeter Wave/low THz band Subharmonic Mixers. The frequency mixer module is one of the fundamental block in any modern system. Subharmonic mixers normally use a local oscillator signal (LO) corresponding to an integer fraction $1/m$ of the frequency that would be required with a fundamental-mode mixer [1]. The main advantage of the subharmonic mixers is that their local oscillator signal is much easier to generate, using a non-linear component, due to the decreased frequency. The reduction in the LO frequency can potentially simplify the LO design and can improve the phase noise performance of the oscillator, which can ultimately improve the overall system performance. At millimeter and THz frequencies in particular, there is a lack of compact sources providing sufficient power [2]. This is why it may be difficult to design an LO with the required output power and phase noise [3], which makes the subharmonic mixing technique attractive.

As mentioned, increasing the frequency, the direct generation of the local oscillator signal becomes more complex. In order to overcome this limitation, a common solution is to examine the effects of a non-linearity of a given order $m+1$, considering the sum of two signals with different frequencies ω_1 and ω_2 given by:

$$\begin{aligned}(\sin(\omega_1 t) + \sin(\omega_2 t))^{m+1} = \ldots + [&\sin((m\omega_1 - \omega_2)\, t) + \\ &- \sin((m\omega_1 + \omega_2)\, t)] + \ldots \end{aligned} \tag{3.1}$$

From this expression, the non-linearity of order $m+1$ produces the intermodulation products at the frequencies $m\omega \pm \omega_2$ and simultaneously at $\omega_1 \pm m\omega$ [4]. Therefore, direct frequency translations can thus be obtained by modeling a non-linear element with two incident signals of different frequencies.

The non-linear element used to provide the mixing operation of the proposed devices is multi-layer graphene. A quantum theory of the non-linear frequency mixing

effect in an isolated graphene layer has been recently developed in the theoretical work [5] assuming its irradiation with two monochromatic waves at different frequencies. This theory is generalized for the m^{th} harmonic order ($m+1$ intermodulation order of the two signals applied) in Chapter 1 and it is experimentally validated through the implementation of three subharmonic mixers presented further on. Moreover, the characterization of fundamental and subharmonic mixers using novel graphene based field effect transistors have been reported in [6] and in [9, 10]. On the other hand, the capability of graphene sheets covering a gap in a microstrip structure to directly generate high order harmonic components have been experimentally demonstrated in [7] and [4, 8] at millimeter wave frequency bands for both transmission and reception.

The content of this chapter is organized as follows. Firstly, the general topology which is shared by all three proposed devices is discussed followed by the particular implementation of each transition involved. Secondly, the similarities with the graphene based frequency multipliers developed in Chapter 2 are indicated. The design and optimization process of the LO, RF and IF terminals are then described. The performance at room temperature is studied for both upconversion and downconversion operations. The conversion gain of the devices used as submillimeter wave/THz band transmitters/receivers is investigated for different high intermodulation orders of both even and odd parity. Additionally, a transmitter-receiver sub-system is assembled using the frequency multipliers and the mixing devices developed in this thesis. The sub-system behavior with regard to the achieved dynamic range is evaluated.

3.2 Device Topology

The topology of the proposed High Order Subharmonic Submillimeter Wave/THz band Mixers is presented in Figure 3.1. The direct generation of the high order harmonic content at the output of the three mixing devices which share the same LO signal in the K_a band (26.5 to 40 GHz) is studied. The LO signal is guided to a microstrip structure, placed parallel to the E-plane of the corresponding waveguide and at a distance of quarter wavelength from the waveguide backshort. A graphene strip is introduced along the microstrip structure. The m^{th} harmonic component of the subharmonic LO signal is internally generated in the graphene charge carriers and at the same time mixed with the RF signal (downconversion performance) or IF signal (upconversion performance). The subharmonic LO signal which was not converted in the mixing process is collected through the second identical mirrored WR28 standard waveguide. A millimeter wave absorber is mounted at the end of

the second WR28 waveguide in order to absorb the unused subharmonic LO signal power. Thanks to the transport of the unused power towards the second WR28 waveguide and its absorption in the waveguide termination, it is possible to achieve a good impedance matching at the input WR28 port. The RF signal is inserted or extracted, depending on the frequency mixing operation, using another rectangular metallic waveguide section:

- WR3 standard waveguide (220 to 330 GHz) for the first subharmonic mixer
- WR2.2 standard waveguide (330 to 500 GHz) for the second subharmonic mixer
- WR5 standard waveguide (140 to 220 GHz) for the third subharmonic mixer

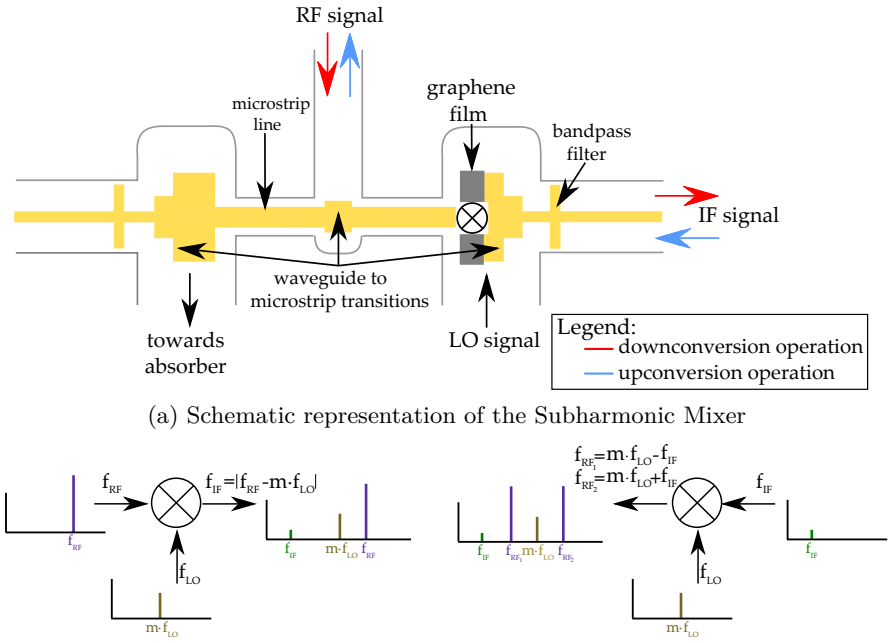

(a) Schematic representation of the Subharmonic Mixer

(b) Downconverting mixing scheme

(c) Upconverting mixing scheme

Figure 3.1: Proposed High Order Subharmonic Submillimeter Wave/THz band Mixer based on multi-layer graphene.

The three waveguides involved in the configuration of the subharmonic mixers are designed in a configuration with E-plane alignment. They are interconnected by a perpendicular channel with rectangular cross-section. The rectangular channel is the host of the microstrip structure which integrates the graphene component together with three waveguide to microstrip transitions. At the input/output port of the IF

terminal, a corresponding bandpass structure is designed. The filter prevents the subharmonic LO signal from leaking into the IF power supply.

The thin film of graphite (multi-layer graphene sheet), integrated in the microstrip structure, is obtained through a mechanical exfoliation technique and it is transferred on a polyimide substrate with dielectric constant $\varepsilon_r = 3.5$ and $\tan\delta = 0.008$. Using a laser ablation process the graphene film is shaped in the desired form. Gold contacts with 1 μm thickness are subsequently deposited over the graphene film by means of a sputtering process. The process of the microstrip structure design containing the waveguide to microstrip transitions was already described in Section 2.2 where a similar microstrip structure was used in the configuration of the Graphene Based Frequency Multipliers. Therefore the energy flow along the microstrip structure and the feeding technique of the graphene strip are not being described in this section as they have already been mentioned in the previous Chapter.

In particular, compared to Chapter 2, the current microstrip structure has two bandpass filters designed at each IF microstrip terminal. The filters lie into a $3 \times 4.5 \times 0.11$ mm^3 rectangular channel cross-section and are composed of metallic triangular shaped radial stubs structured on the same polyimide substrate. The filters were designed to operate at the central frequency $f_{IF} = 400$ MHz while rejecting any millimeter wave signal.

3.3 220 to 330 GHz band subharmonic Mixer

The graphene based high order subharmonic mixer proposed in this section performs the up-/downconversion of a signal to/from $220 - 330$ GHz band (WR3 standard frequency band), by using a subharmonic local oscillator signal, in the K_a band (26.5 to 40 GHz). An IF signal at $f_{IF} = 400$ MHz is used in the mixing operation. Different harmonic components from order 6 to 14 are examined while evaluating the behavior of the subharmonic mixer.

3.3.1 Design and optimization of the subharmonic mixer

The graphene based subharmonic mixer consists in a combined rectangular waveguide to microstrip and microstrip to waveguide structure which is designed and optimized using the three-dimensional electromagnetic simulator Ansoft HFSS. The whole circuit was divided into two blocks: the first block contains the inner part of the subharmonic mixer which includes the RF circuitry, while the LO circuitry and IF circuitry form part of the second block. The optimization process of these blocks is presented in the upcoming subsections.

3.3.1.1 Optimization in the 220 to 330 GHz band

The process of designing and optimizing the central WR3 waveguide to microstrip transition has already been presented in Subsection 2.3.1.1 of the previous chapter where an almost identical transition was implemented for the extraction of the output multiplied signal from the evaluated frequency multiplier. The dimensions of the waveguide block and rectangular channel are kept equal to the dimensions used in the mentioned subsection. As presented in Figure 3.2, the microstrip line substrate in the interior of the WR3 waveguide was 100 μm widened on both sides so it could be easier to align the WR3 waveguide to microstrip transition exactly in a point where the electric field along the rectangular waveguide has a maxima. Also for the ease of fabrication, the final dimension of the microstrip structure in the interior of the waveguide is 0.25×0.22 mm^2. The width of the microstrip transmission line which connects the central E-plane rectangularly shaped microstrip to waveguide transition is 0.12 mm and the substrate thickness is 50 μm.

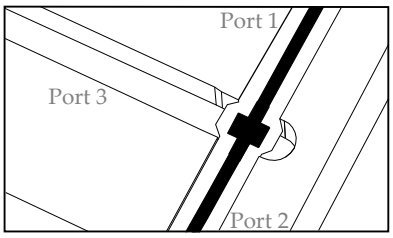

Figure 3.2: Close-up view on the RF circuitry.

The simulated results of the optimized three ports network are presented in Figure 3.3. The transition is symmetrical with respect to its vertical plane, so identical response is achieved on both microstrip ports (Port 1 and Port 2). It can be seen that the frequency response of the transition is well behaved, presenting a good impedance matching at the output Port 3 and low power loss between the input Port 1 and the output Port 3 ($S_{13} > -5$ dB).

3.3.1.2 Optimization in the K_a band

After optimizing the first block, it is placed in the middle of the complete design (as presented in Figure 3.4). In this way, the microstrip line from the rectangular channel is continued with a series of partially overlapped triangular shaped stubs of different lengths and widths, spread across most of the WR28 waveguide height.

The shape of the microstrip to WR28 waveguide transition is carefully optimized in order to obtain maximum coupling of the LO subharmonic signal to the microstrip

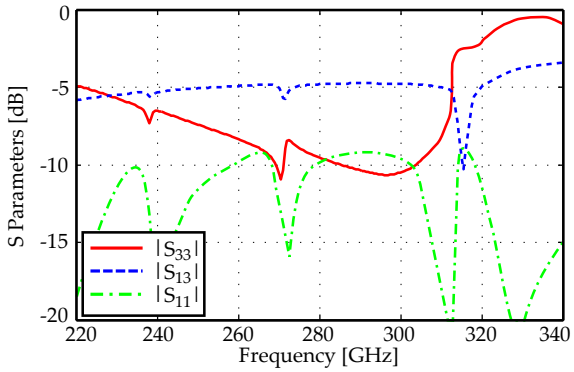

Figure 3.3: Frequency response of the RF circuitry in the 220 to 330 GHz band.

line. Towards the IF port, the microstrip line is continued with a high impedance microstrip line section and two pairs of triangular shaped stubs placed perpendicular one with respect to the other. This structure was optimized in order to provide a bandpass filter behavior, blocking the subharmonic LO radiation while having a central frequency at $f_{IF} = 400$ MHz. The total length of the microstrip structure from one IF port until the other extreme is 30 mm while the distance from one IF bandpass filter until the opposite one is 13 mm. The width of the high impedance microstrip line structure is 0.15 mm while the length until it meets the bandpass filter is 0.6 mm. Further, the two triangular shaped stubs have a length of 1.2 mm respectively 0.8 mm while theirs width is 2.1 mm respectively 0.45 mm.

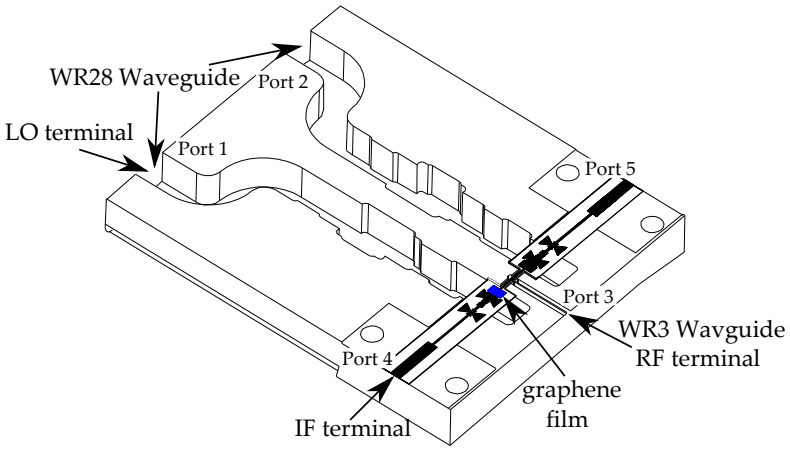

Figure 3.4: Topology of the subharmonic mixer used in the optimization of the K_a band.

The rectangular shape of the WR28 waveguide sections was modified by adding a sequence of several waveguide cavities with increased or reduced height in order to obtain a good impedance matching over the 26 to 40 GHz band. Moreover, as one can appreciate from the topology presented in Figure 3.4, at the end of the WR28 waveguides a rectangular waveguide section two times 90° curved was designed. The length of the waveguides is not a critical design parameter so it can be chosen any multiple wavelength as it will not influence the impedance matching. Therefore, the aim of the two extension elements was to separate the WR28 waveguides from each other for measurement purposes. Since these elements have no electromagnetic influence upon the subharmonic mixer design, in the simulation process they have not been taken into account.

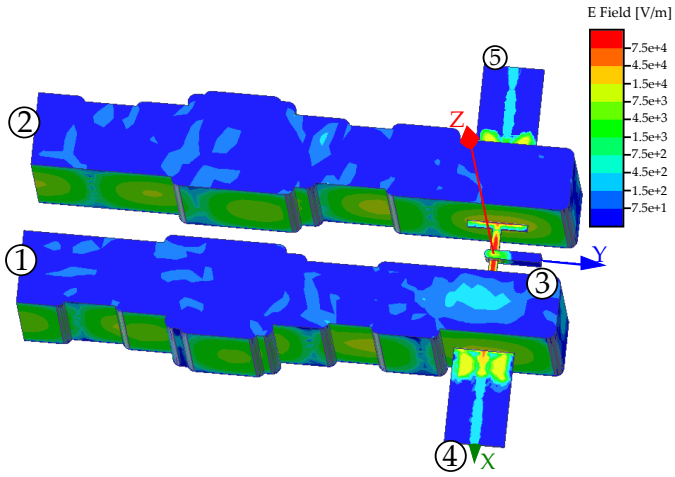

Figure 3.5: Electric field distribution at 34 GHz plotted along the subharmonic mixer. Circuit fed through the LO port (Port 1).

In Figure 3.5, the electric field distribution of the electromagnetic wave propagating from the LO port is studied. The input subharmonic LO signal is coupled to the microstrip structure situated in the interior of the WR28 waveguide and it is transmitted to the graphene strip. Part of the input LO subharmonic signal attempts to flow towards the IF port but it is blocked by the IF bandpass filter. Moreover, due to the dimension restrictions of its wavelength, the input LO subharmonic signal can not reach the RF port placed at the extreme of the WR3 waveguide.

In Figure 3.6, the electric field distribution of the electromagnetic wave incoming from the IF port is studied. The input IF signal is restricted to the propagation towards the microstrip line.

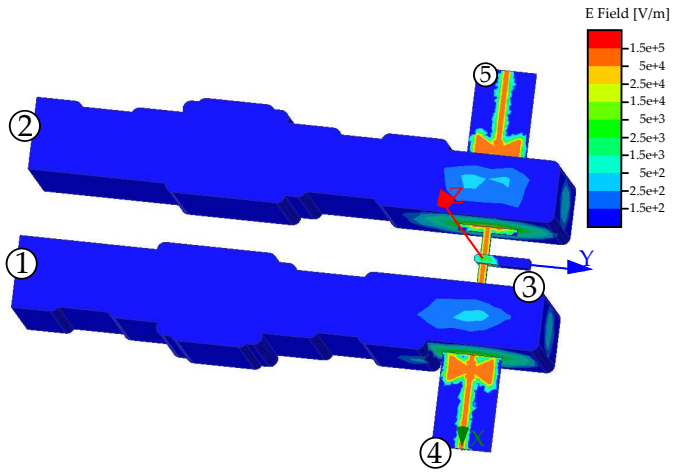

Figure 3.6: Electric field distribution at 400 MHz plotted along the subharmonic mixer. Circuit fed through the IF port (Port 4).

The results in terms of the scattering parameters are represented in Figure 3.7. Impedance matching ($|S_{11}| < -10$ dB) has been achieved approximately between 29 and 40 GHz. The insertion loss, $|S_{21}|$, in the same band is relatively flat and around 4 dB. Moreover, as outlined earlier, the WR3 waveguide to microstrip transition, placed in the middle of the channel, has no influence in the WR28 standard frequency band. Through a proper design of the bandpass structure at the IF port, considerably high attenuation levels were observed in the whole bandwidth ($|S_{14}| < -20$ dB), reaching a maximum of about 45 dB in the central of the band (at 36 GHz).

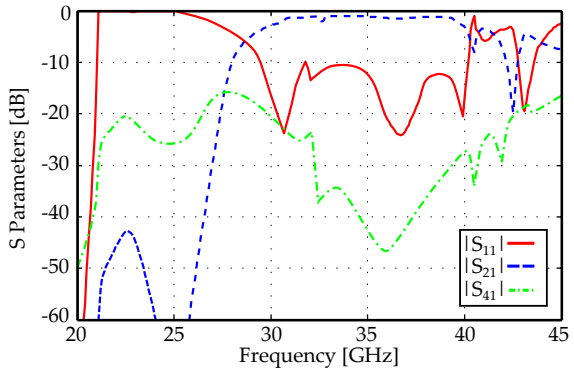

Figure 3.7: Scattering parameters of the LO and IF circuitry in the K_a band.

3.3.2 Prototype fabrication and experimental characterization

3.3.2.1 Prototype Implementation

For the experimental validation of the subharmonic mixer design a prototype has been manufactured and experimentally characterized. The purpose of this thesis is to develop a first proof of concept graphene based mixing device, therefore as in the previous chapter, the capability to manufacture it with existing facilities has been preferred.

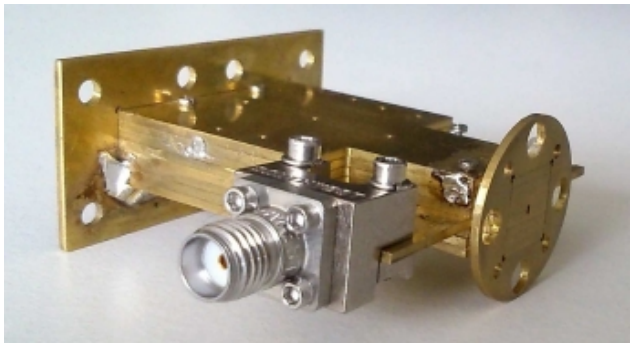

Figure 3.8: 220 to 330 GHz band subharmonic mixer - prototype overview.

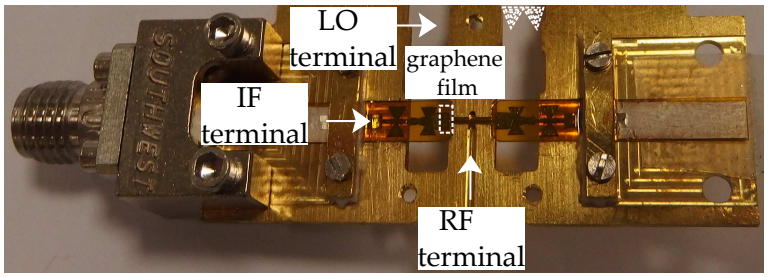

Figure 3.9: Image of the microstrip structure mounted on its corresponding channel.

The RF and LO waveguides are placed in the same plane. In the milling process this fact reduces the number of mechanical elements to be assembled. Therefore, the waveguide block, as outlined in Figure 3.8, has been milled out of eight brass sheets, which have subsequently been assembled together. The waveguide ports have been terminated with standard interface flanges. A coaxial SouthWest Microwave 2.4 mm SMI end launch connector has been placed at the IF port. An image of the microstrip structure assembled in its corresponding channel can be seen in Figure 3.9.

3.3.2.2 Measurement of the impedance matching and insertion loss in the K_a band

For the measurement of the impedance matching and insertion loss in the K_a band the schematic diagram presented in Figure 3.10(a) has been used. The measured scattering parameters are shown together with the simulated results in Figure 3.10(b).

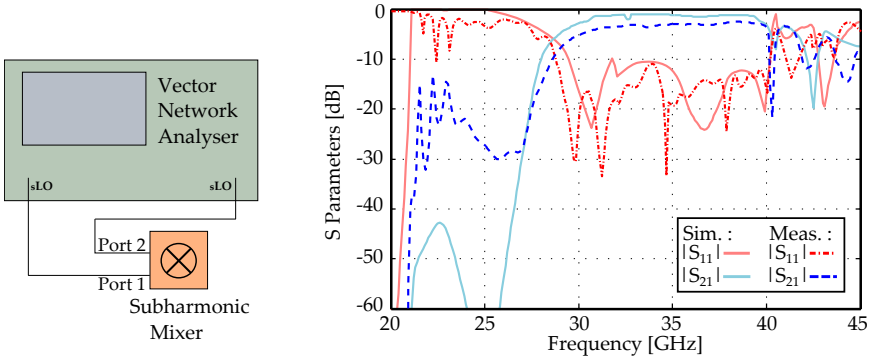

(a) Schematic diagram (b) S parameters

Figure 3.10: Simulated and measured data of the subharmonic LO input signal in the K_a band.

The subharmonic LO input signal presents a return loss, $|S_{11}|$, greater than 10 dB from 28 to 40 GHz. The insertion loss, $|S_{21}|$, in the same band is under 5 dB although its value starts to slightly increase for lower frequencies. Furthermore, relatively low values of the insertion loss are also noticed in the frequency band from 40 to 45 GHz and at some specific points along the 20 to 25 GHz. For this reason, the subharmonic LO input signal which is transmitted to the graphene strip is broader than expected. As one can appreciate, a relatively good agreement between the simulations and measurements was obtained.

3.3.2.3 Measurement of the impedance matching in the 220 to 330 GHz band

For the measurement of the impedance matching in the 220 to 330 GHz band the schematic diagram presented in Figure 3.11(a) has been used. Likewise in Subsection 2.3.2.3 from chapter 2, the behavior of the RF terminal of the subharmonic mixer has been characterized using a *Virginia Diodes Inc.* frequency range extender module which was connected to the $PNA-X$. The RF port, in the 220 to 330 GHz requires good impedance matching in order to receive/transmit accurate data

through the WR3 waveguide. The simulated and measured impedance matching of the RF terminal is illustrated in Figure 3.11(b).

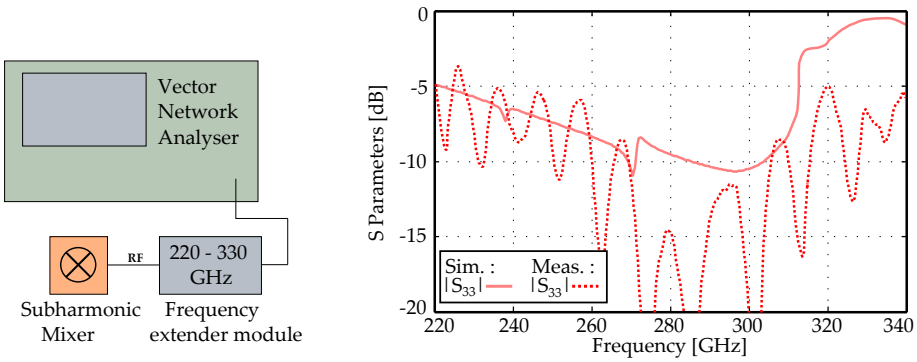

(a) Schematic diagram (b) S parameters

Figure 3.11: Simulated and measured data of the RF input/output signal in the WR3 band.

3.3.2.4 Mixing performance - output power

The mixing operation of the prototype has been evaluated using the two measurement setup diagrams presented in Figure 3.12.

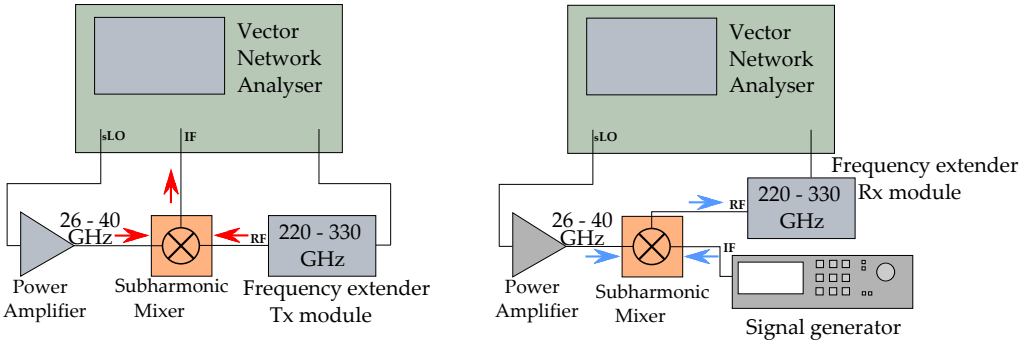

(a) Downconverting operation (b) Upconverting operation

Figure 3.12: Schematic diagram of the measurement setup.

The input LO signal, in the K_a band, needed to drive the mixing performance of the subharmonic mixer is generated with an Agilent N5247A PNA-X vector network analyzer and amplified up to a maximum power level $P_{sLO_{max}} = 22$ dBm with a 30 dB gain power amplifier. Through an Agilent $R281B$ coaxial to waveguide adapter, this signal generated in the PNA-X is sent to the WR28 input waveguide which is

the closest to the graphene strip. On the other WR28 waveguide a millimeter wave absorber is mounted and mechanically secured against the holes of its corresponding interface flange.

The submillimeter wave radiation in the 220 to 330 GHz band, is either measured for the downconversion operation, or generated for the upconversion operation through a frequency extender Virginia Diodes Tx/Rx head connected to the PNA-X.

The intermediate frequency is set at $f_{IF} = 400$ MHz. This signal is collected by the PNA-X in the downconversion operation and provided by a Rohde&Schwarz SMV03 vector signal generator in the upconversion operation.

For the measurement of the different harmonic orders, generated in the multilayer graphene sample of the subharmonic mixer, a noise floor level of around -120 dBm was fixed in the PNA-X settings.

The behavior of the subharmonic mixer has been experimentally evaluated in both downconversion and upconversion operations when different harmonic components from order 6 to 14 are generated in the multi-layer graphene sample.

Downconversion Performance

In the downconversion operation, the graphene sample generates the m^{th} harmonic component of the input subharmonic LO signal f_{sLO}, in the K_a band, and the generated signal is mixed with the input RF signal f_{RF}, in the 220 to 330 GHz band, according to the formula:

$$f_{IF} = f_{RF} - m \cdot f_{sLO}. \tag{3.2}$$

The input RF signal of the subharmonic mixer is generated through a frequency multiplier implemented inside the frequency extender transmitter head from Virginia Diodes. For this reason, the power of the signal is not constant but varies through the 220 to 330 GHz band according to its frequency response. The RF power has been characterized as a function of frequency with an Eriksson PM4 calorimeter based power meter and it was found that its response varies from -21 to -12 dBm.

The harmonic content from order 6 to 14 generated in the multi-layer graphene strip is evaluated as a function of the conversion gain versus the frequency. The obtained data is represented in Figure 3.13. The subharmonic LO input power used is varied in 2 dB steps, with a 22 dBm maximum level. The value of the conversion gain, G_c, was calculated according to the formula:

$$G_c\,[dB] = P_{IF}\,[dB] - P_{RF}\,[dB]. \tag{3.3}$$

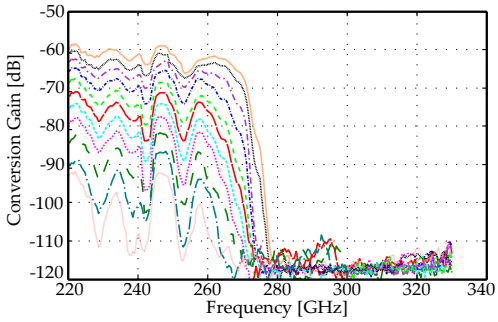

(a) Harmonic order 6.

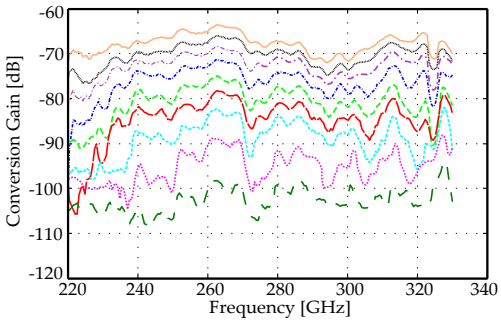

(b) Harmonic order 8.

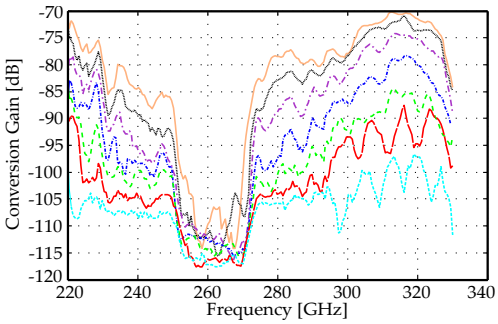

(c) Harmonic order 10.

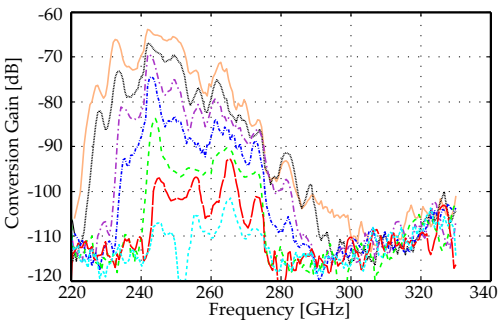

(d) Harmonic order 12.

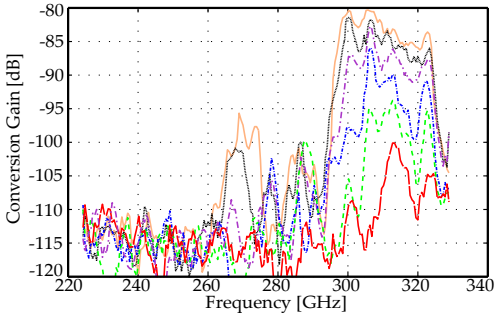

(e) Harmonic order 14.

Figure 3.13: Conversion gain of the subharmonic mixer in the downconversion operation versus frequency, for different harmonic orders. Input LO power varied in 2 dB steps with a maximum level of 22 dBm.

The data obtained for the odd harmonic orders was not represented as it either

did not exceed the noise floor or the behavior was irregular along the analyzed frequency band. Furthermore, considering the impedance matching at the WR28 input port, the harmonic order 8 is the only transformation possible to cover the whole 220 to 330 GHz band. For this, the LO subharmonic input signal required in the conversion varies from 27.5 to 41.25 GHz. Therefore, the output response of the different harmonic orders is strongly limited by the impedance matching of the input LO subharmonic signal.

As theoretically described in Section 1.6 and also presented in Eq. 3.1, in the mixing operation of two signals, the odd order intermodulation product corresponds to even harmonic orders. Furthermore, a flat frequency response with a slowly decaying amplitude trend can be appreciated in the mixing operation with even harmonic orders, as predicted in [11] and [12].

Upconversion Performance

In the upconversion operation, the graphene sample generates the m^{th} harmonic component of the input subharmonic LO signal f_{sLO}, in the K_a band, and the generated signal is mixed with the input IF signal f_{IF} at 400 MHz. The RF signal obtained, in the 220 to 330 GHz band, is given by the formula:

$$f_{RF} = f_{IF} + m \cdot f_{sLO} \tag{3.4}$$

In the particular case of the upconversion operation, the input IF signal at 400 MHz is set to the desired power level from the signal generator used. The mixing performance of the subharmonic mixer in terms of the conversion gain is presented in Figure 3.14. The power of the subharmonic LO signal is varied in 2 dB steps with a maximum value of 22 dBm while the IF power is set to 13 dBm. The value of the conversion gain, G_c, was computed according to the formula:

$$G_c\,[dB] = P_{RF}\,[dB] - P_{IF}\,[dB] \tag{3.5}$$

As one can appreciate, the results are similar to those corresponding with the downconversion operation from Figure 3.13. Only the even harmonic orders are not represented. The input IF power used is higher than the input RF power from the downconversion operation. For this reason the output power generated in the upconversion operation is substantially higher than the output power from the downconversion operation. Therefore, the upconverted signals can be detected for lower

values of the subharmonic power.

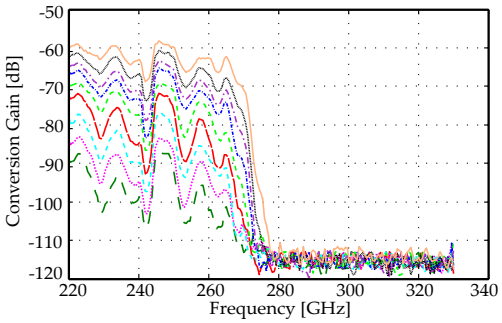

(a) Harmonic order 6.

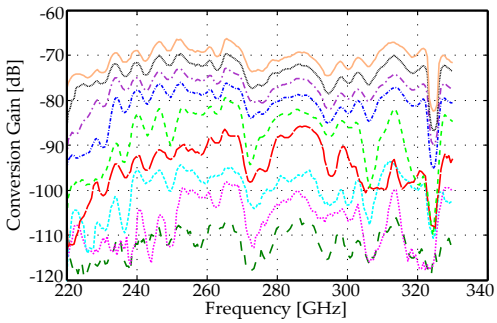

(b) Harmonic order 8.

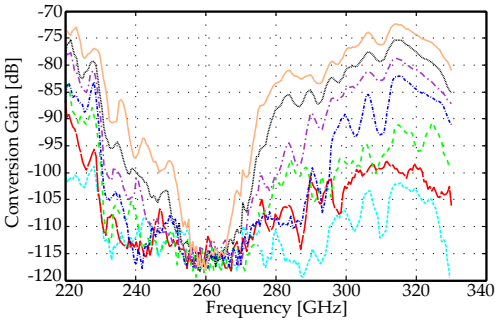

(c) Harmonic order 10.

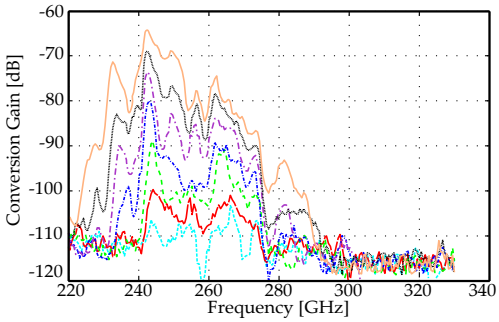

(d) Harmonic order 12.

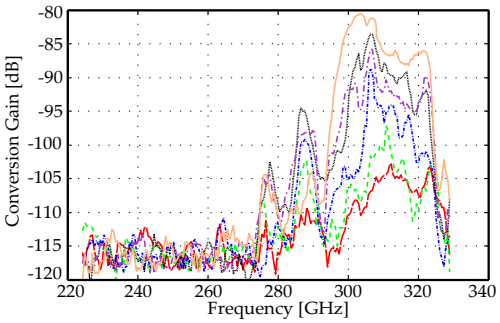

(e) Harmonic order 14.

Figure 3.14: Conversion gain of the subharmonic mixer in the upconversion operation versus frequency, for different harmonic orders. Input LO power varied in 2 dBm steps with a maximum value of 22 dB.

The influence of the IF power on the conversion gain of the subharmonic mixer was evaluated by sweeping P_{IF} from -15 to 13 dBm. The conversion gain for different even harmonic orders from 6 to 14 is represented in Figure 3.15. The

power of the subharmonic LO input was set to $P_{sLO} = 20$ dBm. As can be noticed, the response is relatively flat, although it becomes noisy for increased harmonic order and in regions close to the system noise floor.

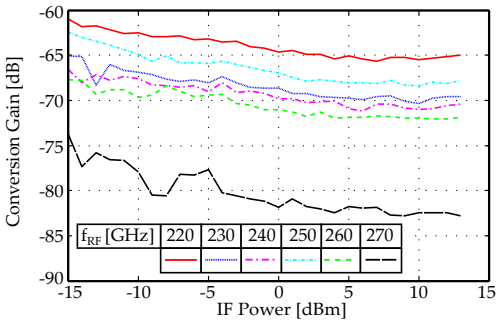

(a) Harmonic order 6.

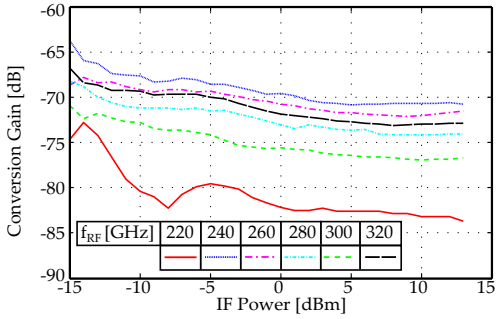

(b) Harmonic order 8.

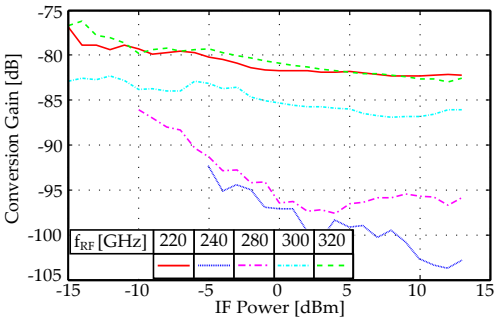

(c) Harmonic order 10.

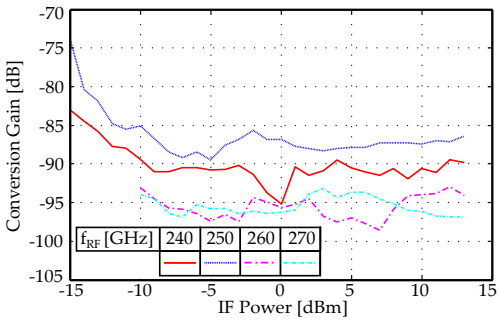

(d) Harmonic order 12.

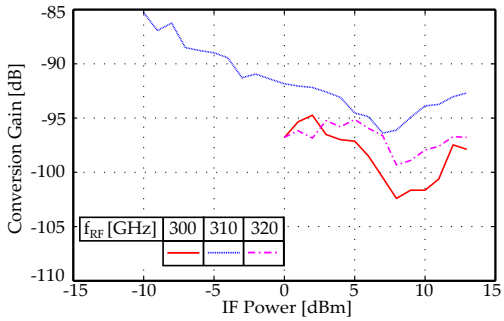

(e) Harmonic order 14.

Figure 3.15: Conversion gain as a function of the input IF power for different harmonic orders. The data is measured at specific frequency points within the corresponding operating band of the upconverted signals.

3.3.2.5 Variation of the output electric field versus the input electric field

The experimental content generated in the upconversion operation is examined against the theoretical data calculated using the estimations discussed in Chapter 1. The maximum upconverted electric field levels have been calculated at different specific frequency points considering the 7^{th}, 9^{th} and 11^{th} intermodulation orders. Therefore, the 6^{th} harmonic order was analyzed at f_{subh_6} = 248.1 GHz, the 8^{th} harmonic order at f_{subh_8} = 265.1 GHz and 10^{th} harmonic order at $f_{subh_{10}}$ = 317.4 GHz. The input subharmonic LO signal needed in the transformation process of the mentioned orders is within the frequency band where the return loss is relatively flat and under 5 dB (see Figure 3.10(b)).

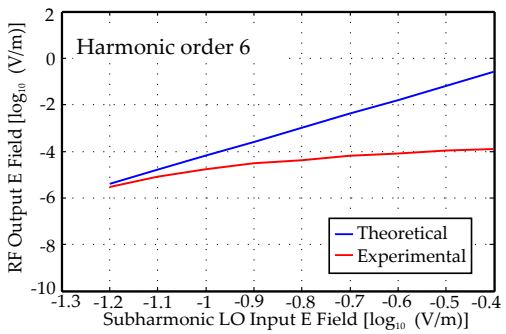

(a) Intermodulation Order 7

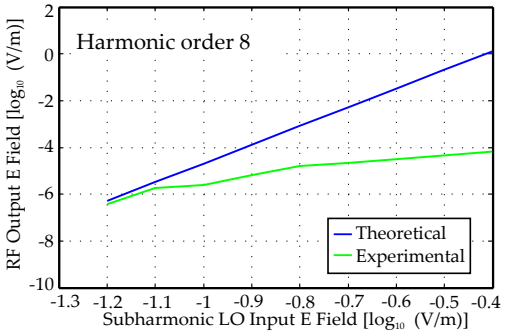

(b) Intermodulation Order 9

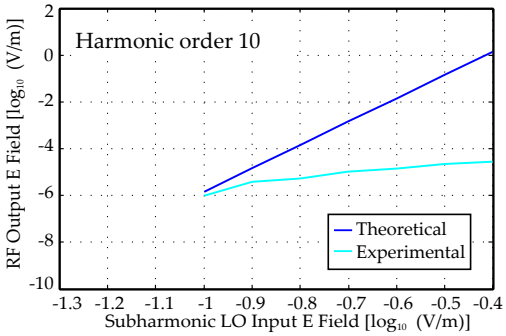

(c) Intermodulation Order 11

Figure 3.16: RF upconverted electric field versus subharmonic LO input for different intermodulation orders.

The RF output experimental electric field was represented in Figure 3.16 together with the theoretical values. The formula used for the computation of the theoretical data is:

$$E_{(m+1)\omega} \propto (E_{in1})^m \cdot (E_{in2}) \tag{3.6}$$

where $E_{(m+1)\omega}$ represents the output electric field of the intermodulation order $nm+1$, E_{in1} represents the electric field of the subharmonic LO signal and E_{in2} represents the electric field of the IF signal.

The input power of the subharmonic LO signal was varied from $P_{sLO} = 6$ to 22 dBm in 2 dB steps for the 7^{th} and 9^{th} intermodulation order and from $P_{sLO} = 10$ to 22 dBm for the 11^{th} intermodulation order while keeping fixed the input IF power at $P_{IF} = 13$ dBm. The behavior of the studied odd order intermodulation products is comparable to the theoretical predictions at low values of the input subharmonic electric field. This result is consistent with the low-field condition theory used in the development of the non-linear analysis from Chapter 1.

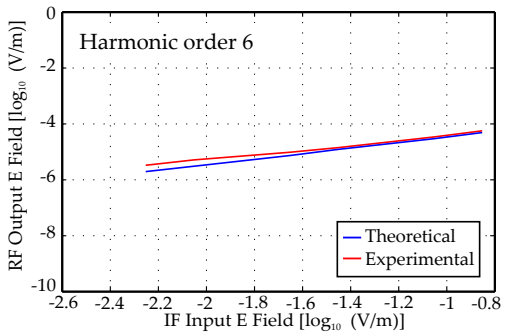

(a) Intermodulation Order 7

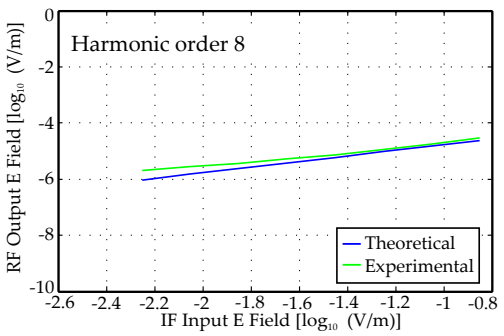

(b) Intermodulation Order 9

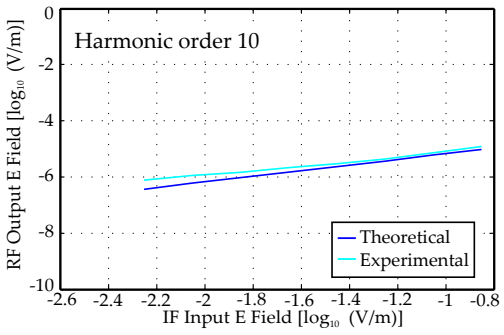

(c) Intermodulation Order 11

Figure 3.17: RF upconverted electric field versus IF input for different intermodulation orders.

Furthermore, the variation of the RF output electric field with respect to the

IF input is represented in Figure 3.17 for both experiment and theory. The IF power was varied from $P_{IF} = -15$ to 13 dBm in 4 dB steps while keeping fixed the subharmonic LO power at $P_{sLO} = 20$ dBm. The behavior of the experimental content is analogous with the theoretical data, although, for low values of the IF power as the upconverted RF signal approaches the noise floor a small deviation can be perceived.

3.3.2.6 Output electric field versus the harmonic order

Figure 3.18 presents the maximum upconverted electric field for different intermodulation orders $m+1$ plotted against the theoretical data, determined from Eq. 3.6. The power of the LO and IF signals are fixed at $P_{LO} = 16$ dBm respectively $P_{IF} = 13$ dBm. It can be verified that, except for the intermodulation order 13, the behavior of the odd order products is reciprocal to the theoretical values.

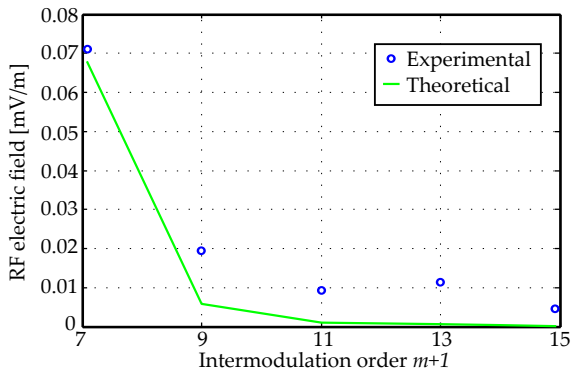

Figure 3.18: Maximum upconverted electric field for different intermodulation orders $m+1$, compared to the theoretical curve.

3.4 330 to 500 GHz band subharmonic Mixer

In this section a graphene based subharmonic mixer device which performs the up-/downconversion of a signal to/from $330-500$ GHz band (WR2.2 standard frequency band) is proposed. The considered local oscillator signal and IF signal are $26-40$ GHz (K_a band) respectively 400 MHz. The subharmonic mixer is characterized in terms of output power for different harmonic components from order 8 to 18.

3.4.1 Design and optimization of the subharmonic mixer

The topology of the 330 to 500 GHz band graphene based subharmonic mixer is schematically presented in Figure 3.19. This topology is based on the 330 to 500 GHz band graphene based frequency multiplier described in Section 2.4. Additionally the aforementioned frequency multiplier was complemented with the corresponding IF passive circuitry required by the mixer.

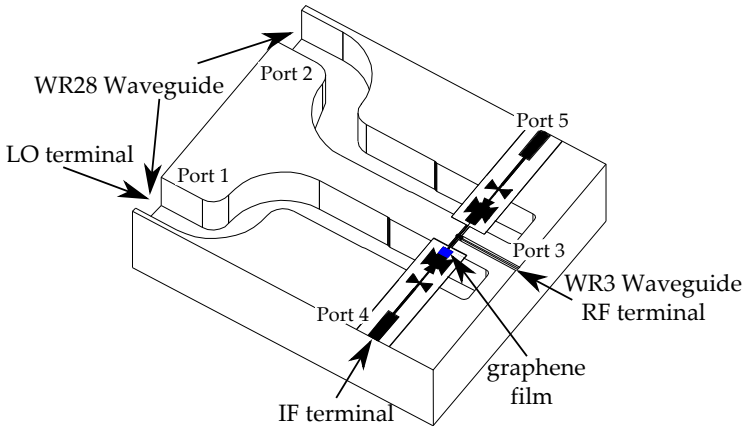

Figure 3.19: Proposed 330 to 500 GHz band subharmonic mixer.

The process of designing and optimizing the passive RF, LO and IF networks involved in the topology of the proposed device is similar with the process described in the previous section, where the RF signal was provided in the adjacent 220 to 330 GHz band. As already mentioned, the RF circuitry, in the 330 to 500 GHz band, and the LO circuitry, in the K_a band, were designed analogously with the circuit from Section 2.4.1. Furthermore, the IF circuitry has two pairs of perpendicular triangular shaped stubs of 1.4 mm length and 2.4 mm width respectively 0.7 mm length and 0.4 mm width placed on a microstrip line of 0.15 mm width. The two back to back WR28 waveguides and the IF network were optimized, with the RF circuitry placed between them. Good signal transmission between the two WR28 waveguides and high attenuation at the IF terminal was requested in the K_a band. The scattering parameters that describe the electromagnetic behavior of the optimized transitions are presented in Figure 3.20.

Note that a return loss greater than 10 dB has been obtained at the RF terminal ($|S_{33}| < -10$ dB and $|S_{11}| < -10$ dB) approximately from 330 to 550 GHz and at

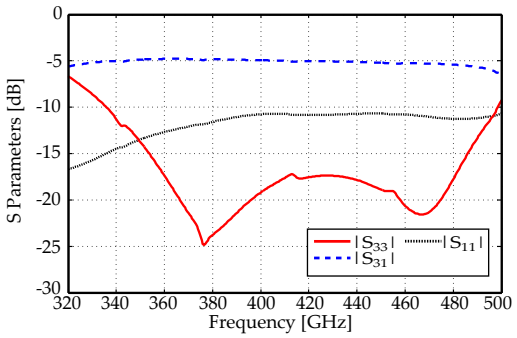

(a) Relevant S parameters of the RF circuitry.

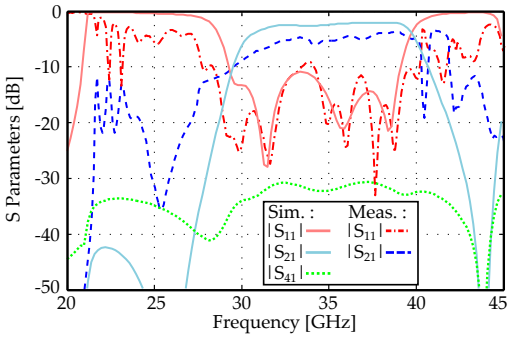

(b) Relevant S parameters of the LO and IF circuitry.

Figure 3.20: S parameters of the proposed 330 to 500 GHz band subharmonic mixer.

the LO terminal ($|S_{11}| < -10$ dB) from 29 to 41 GHz. The insertion loss in the K_a band, $|S_{21}|$, is relatively flat and lower than 6 dB. Moreover, due to a proper optimization of the bandpass structure at the IF port, a good attenuation with values higher than 30 dB ($|S_{41}| < -30$ dB) in the frequency band from 20 to 45 GHz was obtained. The impedance matching at the WR28 input terminal condition the frequency response of the different harmonic orders.

3.4.2 Prototype fabrication and experimental characterization

To evaluate the behavior of the graphene based subharmonic mixer a prototype of the complete structure has been manufactured and the results of the output converted signal are being investigated. The process of manufacturing is not introduced as it is similar with the process given in Subsection 3.3.2. The measurement setup used to evaluate the up-/downcoversion operation of the subharmonic mixer is almost identical to the setup presented in Figure 3.12 where the Tx/Rx extender head used in the current setup works in the adjacent 330 to 500 GHz band. As in the previous case, the low THz band signal from 330 to 500 GHz is internally generated through a frequency multiplier. Therefore, the power of this signal, P_{RF}, is not completely stable but varies throughout the band according to its frequency response. This power has been measured with an Eriksson PM4 calorimeter based power meter and exhibits a variation between -31 to -15 dBm.

In the downconversion operation, the output IF signal of the subharmonic mixer is generated as in Eq. 3.2, by mixing the input RF signal, in the 330 to 500 GHz band, with the m^{th} order harmonic of the LO signal, in the K_a band. The conversion

gain ($G_c = P_{IF} - P_{RF}$) is represented in Figure 3.21. Different even harmonic orders m from 8 to 18 are being analyzed when the input LO power increases in 2 dB steps from 10 to 24 dBm.

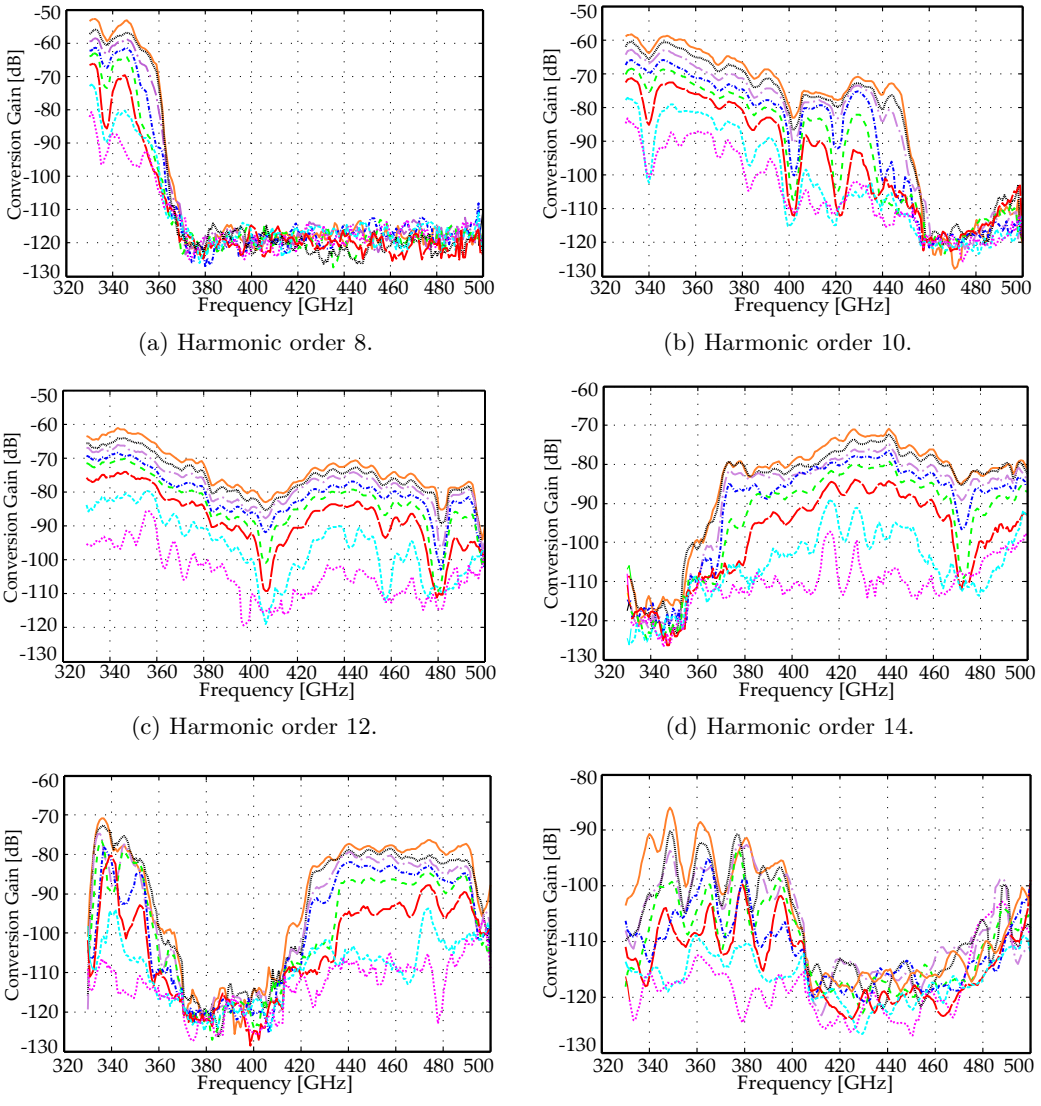

(a) Harmonic order 8.

(b) Harmonic order 10.

(c) Harmonic order 12.

(d) Harmonic order 14.

(e) Harmonic order 16.

(f) Harmonic order 18.

Figure 3.21: Conversion gain of the subharmonic mixer in the downconversion operation for different harmonic orders - P_{LO} varies from 10 to 24 dBm, in increments of 2 dB.

Furthermore, the output RF signal in the upconversion operation was generated according to Eq. 3.4, by mixing the IF signal with the m^{th} order harmonic of the

LO signal. For this, the conversion gain ($G_c = P_{RF} - P_{IF}$) is characterized as a function of frequency in Figure 3.22. The subharmonic LO signal was varied, as in the previous case, in increments of 2 dB with a maximum power level of 24 dBm while the IF power was fixed to 12 dBm.

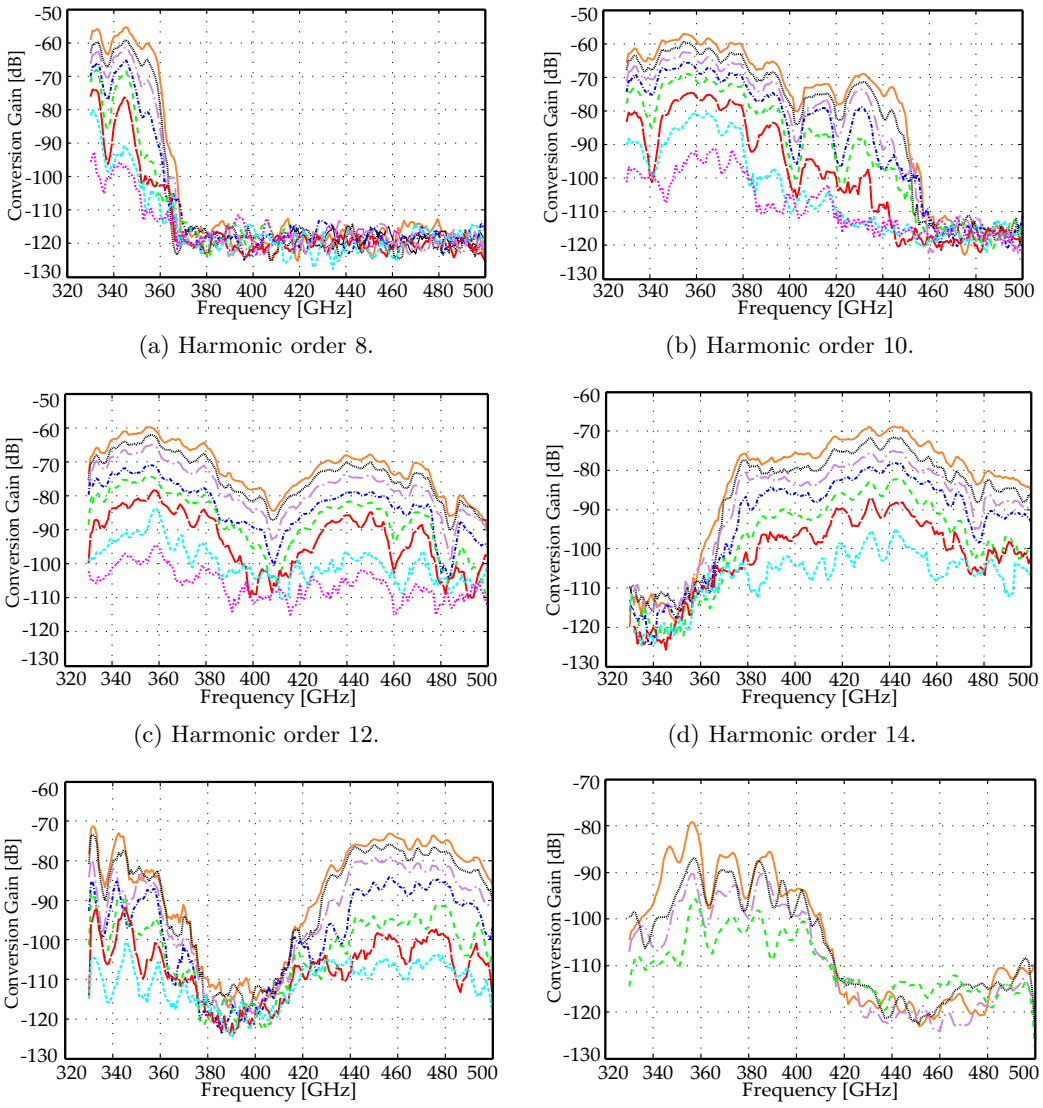

(a) Harmonic order 8.

(b) Harmonic order 10.

(c) Harmonic order 12.

(d) Harmonic order 14.

(e) Harmonic order 16.

(f) Harmonic order 18.

Figure 3.22: Conversion gain of the subharmonic mixer in the upconversion operation for different harmonic orders - P_{LO} varies in increments of 2 dB with a maximum level of 24 dBm.

The conversion gain obtained for the different harmonic orders in the upconver-

sion operation is slightly lower but still comparable to the results of the downconversion operation. A relatively flat frequency response has been obtained for the harmonic orders 8^{th}, 10^{th}, 12^{th} and 14^{th}. The input signal of these harmonic orders is placed in the frequency band from 28 to 36 GHz, where the insertion losses introduced by the WR28 input waveguide are linear and under 5 dB (see the measured data results from Figure 3.20(b)).

3.4.2.1 Variation of the output electric field versus the input electric field

This subsection is dedicated to the comparison of the measurement results obtained at the output of the graphene based subharmonic mixer, in the upconversion operation, and the theoretical data, calculated following the development from Section 1.6. For this, the maximum upconverted electric field of the even harmonic components from order 8 to 14 have been analyzed. Therefore, the 8^{th} harmonic order is analyzed at $f_{subH_8} = 345.3$ GHz, the 10^{th} harmonic order at $f_{subH_{10}} = 354.7$ GHz, the 12^{th} harmonic order at $f_{subH_{12}} = 356.4$ GHz and the 14^{th} harmonic order at $f_{subH_{14}} = 442.2$ GHz. The power of the LO input signal is swept between 12 to 24 dBm, in increments of 2 dB while the IF power is fixed at 12 dBm. The results of the analysis are represented in Figure 3.23 and Figure 3.24.

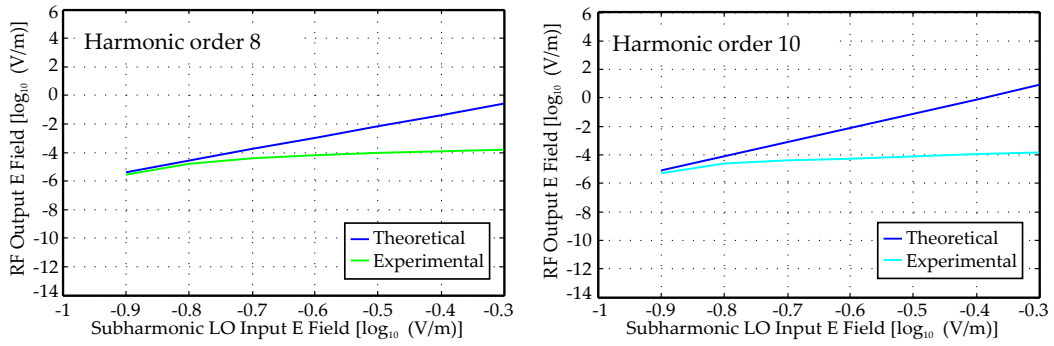

(a) Intermodulation Order 9^{th}

(b) Intermodulation Order 11^{th}

Figure 3.23: RF upconverted electric field versus subharmonic LO input for intermodulation order 9^{th} and 11^{th}.

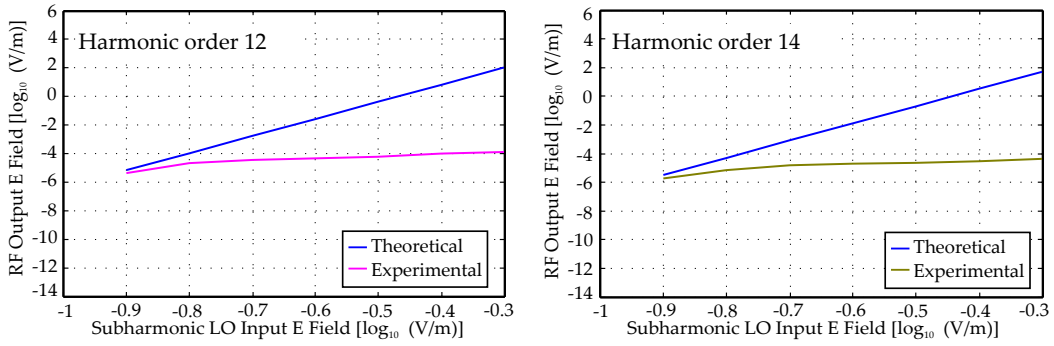

(a) Intermodulation Order 13^{th} (b) Intermodulation Order 15^{th}

Figure 3.24: RF upconverted electric field versus subharmonic LO input for intermodulation order 13^{th} and 15^{th}.

3.4.2.2 Output electric field versus the harmonic order

Figure 3.25 presents the maximum upconverted electric field for different intermodulation orders $m+1$ plotted against their theoretical values. The power of the two signals incident on the non-linear component is $P_{LO} = 18$ dBm respectively $P_{IF} = 12$ dBm.

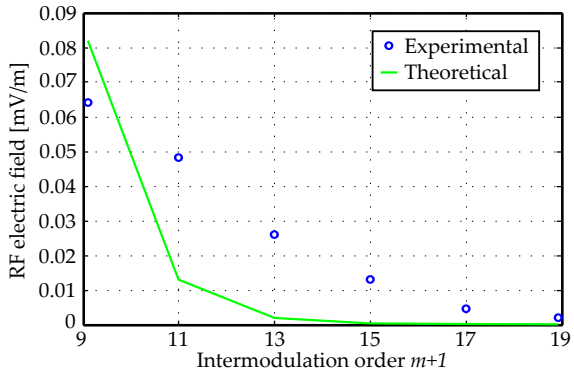

Figure 3.25: Maximum upconverted electric field for different intermodulation orders $m+1$, compared to the theoretical curve.

The results of the odd order intermodulation products decrease in magnitude steps relatively slower than the theoretical defined curve. This could be a consequence of the low-field condition violation as for increased harmonic order the input subharmonic power required in the conversion process is relatively high. The subharmonic power used in this analysis $P_{LO} = 18$ dBm could have been out of the

low-field condition range.

3.5 140 to 220 GHz band subharmonic Mixer

This section presents the implementation of a graphene based downconverting subharmonic mixer from an RF signal, in the 140 to 220 GHz band, to an IF signal at 400 MHz. The internally generated 6^{th} and 8^{th} harmonic components of an input signal in the K_a band, between 26.5 to 40 GHz, are used in the mixing operation. The RF signal of the subharmonic mixer is generated either through a 140 to 220 GHz band graphene based frequency multiplier or through an identical graphene based subharmonic mixer used in the upconversion operation.

3.5.1 Design, simulation and optimization process

The topology of the 140 to 220 GHz band graphene based subharmonic mixer is schematically presented in Figure 3.26. The design of the passive LO and RF circuitry is analogously with the design of the 140 to 220 GHz band graphene based frequency multiplier, discussed in Section 2.5. The IF circuitry is provided through a planar device consisting in a microstrip line section of 0.175 mm width and a bandpass filter. The filter is composed by two triangular shaped perpendicular stubs of 1 mm length and 1.8 mm width.

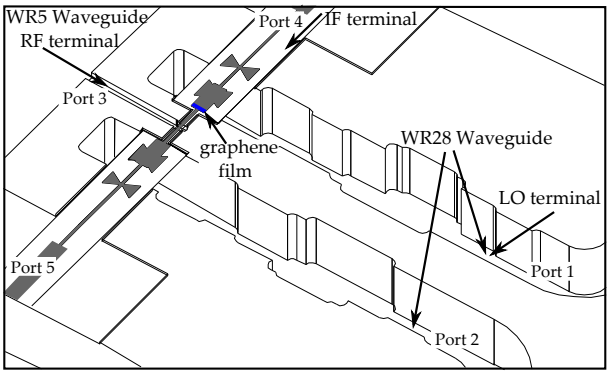

Figure 3.26: Proposed WR5 band subharmonic mixer.

First, the inner part of the design was optimized in the 140 to 220 GHz band for a good impedance matching and signal transmission through both the WR5 waveguide and microstrip line. Second, the whole circuit was optimized in the K_a band for a good transmission of the LO signal towards the graphene strip placed along the microstrip line and high attenuation at the IF port.

The simulated results of the optimized subharmonic mixer are presented in Figure 3.27. A good impedance matching with a reflection coefficient lower than −10 dB has been obtained at the RF terminal ($|S_{33}| < -10$ dB and $|S_{11}| < -10$ dB) in the frequency band from 160 to 220 GHz and at the LO terminal ($|S_{11}| < -10$ dB) from 28 to 40 GHz. The insertion loss, $|S_{31}|$ and $|S_{21}|$, in the same bands is lower than 3 dB. Moreover, the attenuation introduced by the IF filter in the 28 to 40 GHz band is under 20 dB ($|S_{41}| < -20$ dB) although it increases considerably when approaching the 25 GHz lower end.

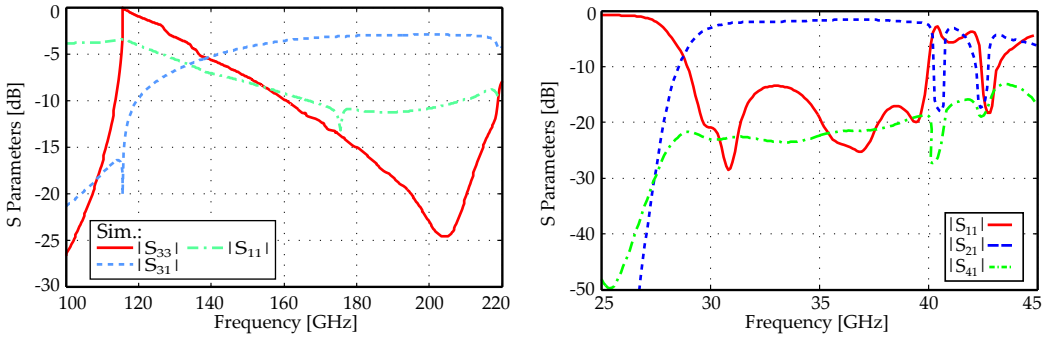

(a) Relevant S parameters of the RF circuitry.

(b) Relevant S parameters of the LO and IF circuitry.

Figure 3.27: S parameters of the proposed 140 to 220 GHz band subharmonic mixer.

3.5.2 Prototype fabrication and experimental characterization

The performance of the proposed 140 to 220 GHz band graphene based subharmonic mixer is experimentally characterized in the downconversion operation. For this, the circuit uses the 6^{th} and 8^{th} harmonic orders of an LO signal in the K_a band. The RF radiation, in the 140 to 220 GHz band, is internally generated through a high order graphene based frequency multiplier or an identical subharmonic mixer. Therefore two subharmonic mixer prototypes have been manufactured through mechanical and laser prototyping equipment. The manufacturing process is identical to the process explained in Subsection 3.3.2. The waveguide structures, as defined in Figure 3.26, have been divided into several brass sheets which were micromachined individually. A microstrip structure containing a graphene strip is inserted into each waveguide structure.

The measurement setup diagram used in order to evaluate the behavior of the receiving subharmonic mixer device is illustrated in Figure 3.28. First of all, the

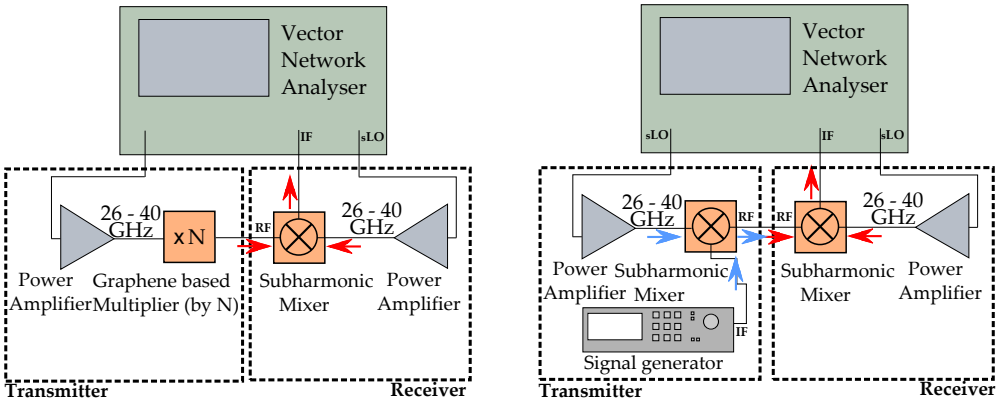

(a) Transmitter: frequency multiplier - Receiver: downconverting subharmonic mixer

(b) Transmitter: upconverting subharmonic mixer - Receiver: downconverting subharmonic mixer

Figure 3.28: Schematic diagram of the measurement setup.

device used to generate the submillimeter wave signal which is transmitted to the RF terminal of the subharmonic mixer is the 140 to 220 GHz band graphene based frequency multiplier presented in Section 2.5. The input signal of the transmitter, in the K_a band, is provided by the vector network analyzer. The power of this signal is amplified to a maximum level of 20 dBm. Further, this signal is multiplied with the harmonic component 5^{th} or 7^{th}, generated in a graphene non-linear component, and the resulting signal is transmitted to the subharmonic mixer (as indicated in Figure 3.28(a)). The LO input signal of the subharmonic mixer, in the K_a band, is provided by the same vector network analyzer and it is power amplified to a maximum level of 20 dBm. Using the internally generated 6^{th} or 8^{th} harmonic component of the input LO subharmonic signal, the receiver performs the downconversion operation of the 140 to 220 GHz RF signal to an IF signal at 400 MHz.

Second, in the configuration of the transmitter-receiver sub-system the transmitter is replaced with a graphene based subharmonic mixer (see Figure 3.28(b)). The subharmonic LO signal of this device, in the K_a band, is provided by the vector network analyzer and is amplified to a maximum level of 20 dBm. An IF signal at $f_{IF} = 400$ MHz is provided by a Rohde&Schwarz SMV03 vector signal generator and it is used to upconvert the LO signal to a 140 to 220 GHz band RF signal. A graphene non-linear device which generates the 6^{th} harmonic component of the LO signal is used in order to drive the mixing operation of the transmitter.

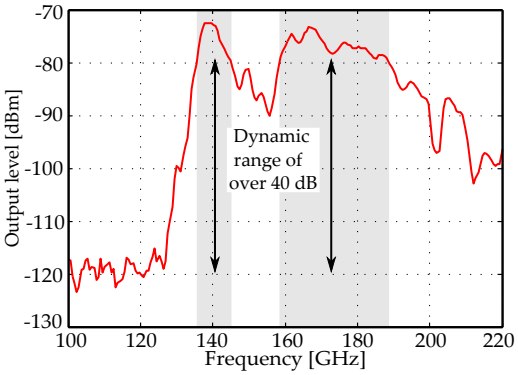

(a) Transmitter: 5^{th} order multiplier, Receiver: 6^{th} order subharmonic mixer

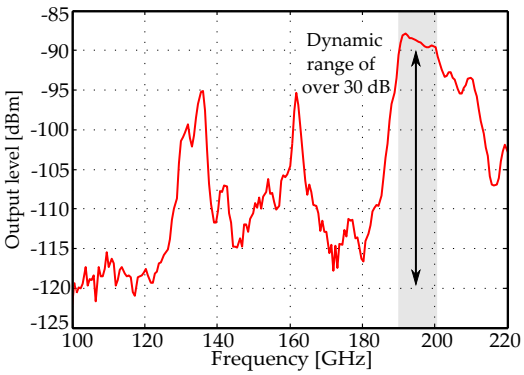

(b) Transmitter: 7^{th} order multiplier, Receiver: 6^{th} order subharmonic mixer

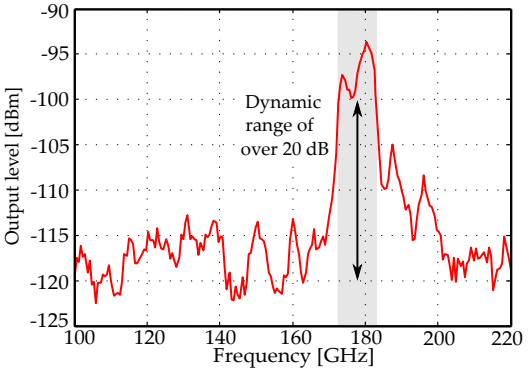

(c) Transmitter: 7^{th} order multiplier, Receiver: 8^{th} order subharmonic mixer

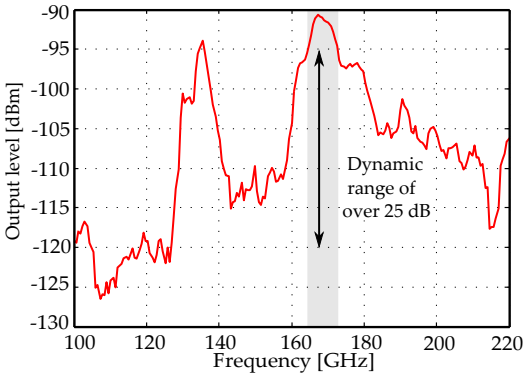

(d) Transmitter: 6^{th} order subharmonic mixer, Receiver: 6^{th} order subharmonic mixer

Figure 3.29: Downconverted IF power of the receiver measured in different transmitter-receiver configurations.

Figure 3.29 presents the receiver downconverted IF power considering different transmitter-receiver configurations. In the specific case of a 5^{th} order frequency multiplier device used as submillimeter wave transmitter and a 6^{th} order subharmonic downconverting mixer used as receiver, a dynamic range of over 40 dB has been measured in the frequency band from 135 to 145 GHz and also from 158 to 190 GHz (see Figure 3.29(a)). These areas are represented as shadowed regions. As the harmonic order of the frequency multiplier increases, the output power levels received by the subharmonic mixer decrease since less input signal is efficiently converted into usable output signal. Therefore, when analyzing the case of a 7^{th} order frequency multiplier device used as submillimeter wave transmitter and a 6^{th} order subharmonic downconverting mixer used as receiver, a dynamic range around 30 dB has been achieved in the frequency band from 190 to 200 GHz (see Figure 3.29(b)).

Moreover, a dynamic range of over 20 dB was measured from 172 to 182 GHz with a receiving 8^{th} order subharmonic mixer when its submillimeter wave radiation was transmitted with a 7^{th} order frequency multiplier (see Figure 3.29(c)). As a final transmitter-receiver configuration, two identical 6^{th} order subharmonic mixers were connected RF to RF terminal and the IF downconverted power of the receiver was analyzed. The achieved dynamic range between 165 to 173 GHz band was around 25 dB.

3.6 Comparison with other subharmonic mixers

The performance overview of the 140 to 220 GHz, 220 to 330 GHz respectively 330 to 500 GHz graphene based subharmonic mixers is presented in Table 3.1, comparing it with other graphene based implementations from the literature. Conversion gain values substantially higher than those presented in this chapter can be found in the literature, corresponding to fundamental, or at most, second-order subharmonic implementations, operating at RF frequencies up to 40 GHz.

Note that the conversion gain of the 140 to 220 GHz graphene based subharmonic mixer could not be accurately calculated and for this reason this data was not introduced into the comparison.

Additionally, Table 3.2 presents a comparison between the graphene based subharmonic mixers implemented in this thesis and other recently published scientific papers regarding waveguide mixers operating in the low THz frequency band.

Typically at high frequencies the LO signal needed in the mixing operation with traditional semiconductors is first generated, in one or multiple separate stages, using frequency multipliers [16, 17]. In doing so, the complexity of the non-linear mixing component is substantially reduced and the conversion efficiency of the device improved. Moreover, in applications which require high output power the most usual approach is to connect the output converted signal to a high power amplifier [15, 16, 17].

Ref.	Type	RF frequency [GHz]	Harmonic order M	Performance type	Conversion gain [dB]	Maximum output power [dBm]
[9]	GFET	0.0105	1	downconv.	-35	-43
[7]	GF	39.3	1	downconv.	-40	-30
[13]	GFET	30.1	2	downconv.	-19	-21
[8]	GF	39.75	2	downconv.	-29	-20
This work	GF	140-220	6	downconv.	–	-72.47
			8	downconv.	–	-93.61
		220-330	6	downconv.	-59.34	-74.33
				upconv.	-59.05	-46.05
			8	downconv.	-64.37	-77
				upconv.	-66.26	-53.26
			10	downconv.	-71.15	-86.80
				upconv.	-73	-60
			11	downconv.	-69.72	-84.44
				upconv.	-72.82	-59.82
			12	downconv.	-67.1	-90.58
				upconv.	-67.48	-54.48
			13	downconv.	-77.21	-91.28
				upconv.	-79.57	-66.57
			14	downconv.	-80.6	-95.19
				upconv.	-82.81	-69.81
		330-500	8	downconv.	-52.81	-73.76
				upconv.	-56.1	-44.1
			10	downconv.	-60.19	-79.98
				upconv.	-58.82	-46.82
			12	downconv.	-61.24	-82.56
				upconv.	-60.54	-48.54
			14	downconv.	-74.18	-91.88
				upconv.	-69.26	-57.26
			15	downconv.	-75.9	-95.94
				upconv.	-81	-69
			16	downconv.	-79.5	-98.53
				upconv.	-75.31	-63.31
			17	downconv.	-76.17	-94.39
				upconv.	-78.77	-66.77
			18	downconv.	-88.29	-106.6
				upconv.	-84.16	-72.16

Table 3.1: Comparison of graphene based mixers, where: GFET - graphene field effect transistor; GF - multi-layer graphene film.

Ref.	Type	RF frequency [GHz]	LO frequency [GHz]	Order M	No of stages	Performance type	Conversion gain [dB]
[14]	S.D.	165-200	91.5	2	1	downconv.	-14.8
		210-240	110				-14
[15]	S.D.	200-240	100-120	2	1	downconv.	-16
[16]	S.D.	300-360	$\times 2$ multip.	1	2	downconv.	-6.3
[17]	S.D.	520-590	$\times 2 \times 3$ multip.	1	3	downconv.	-10
This work	GF	220-330	26.5-40	6	1	downconv.	-59.34
						upconv.	-59.05
				8		downconv.	-64.37
						upconv.	-66.26
				10		downconv.	-71.15
						upconv.	-73
				11		downconv.	-69.72
						upconv.	-72.82
				12		downconv.	-67.1
						upconv.	-67.48
				13		downconv.	-77.21
						upconv.	-79.57
				14		downconv.	-80.6
						upconv.	-82.81
		330-500	26.5-40	8	1	downconv.	-52.81
						upconv.	-56.1
				10		downconv.	-60.19
						upconv.	-58.82
				12		downconv.	-61.24
						upconv.	-60.54
				14		downconv.	-74.18
						upconv.	-69.26
				15		downconv.	-75.9
						upconv.	-81
				16		downconv.	-79.5
						upconv.	-75.31
				17		downconv.	-76.17
						upconv.	-78.77
				18		downconv.	-88.29
						upconv.	-84.16

Table 3.2: Comparison of waveguide mixers, where: S.D. - GaAs Schottky diodes; GF - multi-layer graphene film.

3.7 Conclusions

In this chapter the design, analysis and experimental validation of three High Order Subharmonic Submillimeter Wave/THz band Graphene based Mixers have been presented. Using the non-linear behavior of graphene, the circuits have been conceived to perform the up-/downconversion of a signal to/from the submillimeter wave/THz band, by using a high harmonic component of the input LO signal in the K_a band. The conversion gain in the frequency band from 220 to 500 GHz has been analyzed for different high harmonic orders ($m = 6$ to 18). A maximum upconverted output power of -44.1 dBm corresponding to the eighth harmonic order and a maximum downconverted output power of -73.7 dBm corresponding to the same eighth harmonic order have been obtained while analyzing the mixing prototypes. The even harmonic orders, which correspond to odd intermodulation products, were found to have a relatively flat frequency response and they were consistently performed with a decaying amplitude trend.

Furthermore, a transmitter-receiver sub-system has been analyzed. The transmitter has been composed by a graphene based frequency multiplier or a subharmonic mixer. The generated radiation, in the WR5 standard band, was emitted to a second graphene based subharmonic mixer which downconverted it to an IF frequency. A dynamic range of over 40 dB in the frequency band from 135 to 145 and also from 158 to 190 GHz has been obtained taking advantage of the graphene non-linearity in both transmitter and receiver device.

Bibliography

[1] Bradley Richard Jackson, "Subharmonic Mixers in CMOS Microwave Integrated Circuits," Doctoral Thesis, Queen's University, Kingston, Ontario, Canada, March 2009.

[2] W. C. Tsai, "High Performance Electronics for Millimeter-Wave-to-Terahertz Plasma Diagnostics Instrumentation and High Power Devices, " Doctoral Thesis, University of California, Davis, ProQuest Dissertations Publishing, 2011.

[3] B. R. Jackson and C. E. Saavedra, "A CMOS Ku-Band 4x Subharmonic Mixer," IEEE Journal of Solid-State Circuits, Vol. 43, No. 6, June 2008.

[4] C. Vazquez, A. Hadarig, S. Ver Hoeye, M. Fernandez, R. Camblor, G. Hotopan, F. Las Heras, "High-Order Subharmonic Millimeter-Wave Mixer Based on Few-Layer Graphene, " IEEE Transactions on Microwave Theory and Technology, Vol. 63, No. 4, pp. 1361 - 1369, April 2015.

[5] S. A. Mikhailov, "Theory of the nonlinear optical frequency mixing effect in graphene," Physica E, Vol. 44, pp. 924-927, 2012.

[6] A. Montanaro, S. Mzali, J.-P. Mazellier, O. Bezencenet, C. Larat, S. Molin, P. Legagneux, D. Dolfi, B. Dlubak, P. Seneor, M.-B. Martin, S. Hofmann, J. Robertson, A. Centano, A. Zurutuza, "30 GHz optoelectronic mixing in CVD graphene," arXiv:1511.02791, 2015.

[7] G. R. Hotopan, S. Ver Hoeye, C. Vazquez, R. Camblor, M. Fernandez, F. Las Heras, P. Alvarez and R. Menendez, "Millimeter wave microstrip mixer based on graphene," Progress in Electromagnetics Research, Vol. 118, pp. 57-59, 2011.

[8] G. R. Hotopan, S. Ver Hoeye, C. Vazquez, A. Hadarig, R. Camblor, M. Fernandez, F. Las Heras, "Millimeter wave subharmonic mixer implemented using graphene film coating," Progress in Electromagnetics Research, Vol. 140, pp. 781-794, 2013.

[9] H. Wang, A. Hsu, J. Wu, J. Kong and T. Palacios, "Graphene-Based Ambipolar RF Mixer," IEEE Electron Device Letters, Vol. 31, No. 9, pp. 906–908, 2010.

[10] O. Habibpour, S. Cherednichenko, J. Vukusic, K. Yhland, J. Stake, "A subharmonic graphene FET mixer," IEEE Electron Device Letters, Vol. 33, No. 1, pp. 71-73, 2012.

[11] S. A. Mikhailov, "Non-linear electromagnetic response of graphene, " EPL 79, 27002-pl, 2007.

[12] S. A. Mikhailov and K. Ziegler, "Non-linear electromagnetic response of graphene: Frequency multiplication and the self-conistent-field effects," J. Phys. Condens. Matter 20, 384204, 2008.

[13] O. Habibpour, J. Vukusic, J. Stake, "A 30-GHz Integrated Subharmonic Mixer Based on a Multichannel Graphene FET, " IEEE Transactions on Microwave Theory and Techniques, Vol. 61, No. 2, pp. 841-847, February 2013.

[14] Yao Changfei, Zhou Ming, Luo Yunsheng, Wang Yigang and Xu Conghai, "Millimeter-wave fixed-tuned subharmonic mixers with planar Schottky diodes," Journal of Semiconductors, Volume 33, Number 11, 2012.

[15] T. Bryllert, V. Drakinskiy, K. B. Cooper, J. Stake, "Integrated 200–240-GHz FMCW Radar Transceiver Module," IEEE Transactions on Microwave Theory and Techniques, Vol. 61, Issue 10, 3808 - 3815, 2013.

[16] B. Thomas, A. Maestrini, Member and G. Beaudin, "A Low-Noise Fixed-Tuned 300–360-GHz Sub-Harmonic Mixer Using Planar Schottky Diodes," IEEE Microwave and Wireless Components Letters, Vol. 15, Issue 12, 865 - 867, 2005.

[17] E. T. Schlecht, J. J. Gill, R. H. Lin, R. J. Dengler, and I. Mehdi, "A 520–590 GHz Crossbar Balanced Fundamental Schottky Mixer," IEEE Microwave and Wireless Components Letters, Vol. 20, Issue 7, 387 - 389, 2010.

Chapter 4

Frequency Multiplier based on a Resonant Cavity Integrating Graphene layers

Contents

4.1 Introduction

This chapter presents a new approach for the implementation of a single stage high order frequency multiplier in which graphene sheets are placed inside a resonant cavity. As the resonant cavity concentrates the electric field [1]-[3], the graphene sheets are exposed to an electric field level several orders of magnitude higher than the one existing along a conventional waveguide structure. Taking advantage of this effect, the power efficiency of the whole system is expected to be greatly enhanced. Moreover, contributions of several coupling effects produced along the graphene sheets will be spatially combined with the electromagnetic response of the resonant cavity. In this way, the circuit resonant nature will be greatly intensified and so will be the generated output power.

In addition to the novel proposed concept of generating submillimeter wave signals by using the non-linear properties of graphene [4]-[6], novel manufacturing techniques of submillimeter wave devices based on high resolution 3D printing [7]-[9] will be developed as well. Hence, the chapter will present remarkable multidisciplinary

advantages in the state of the art, including contributions of the graphene patterning technologies and the design of submillimeter wave signal generators through frequency conversion.

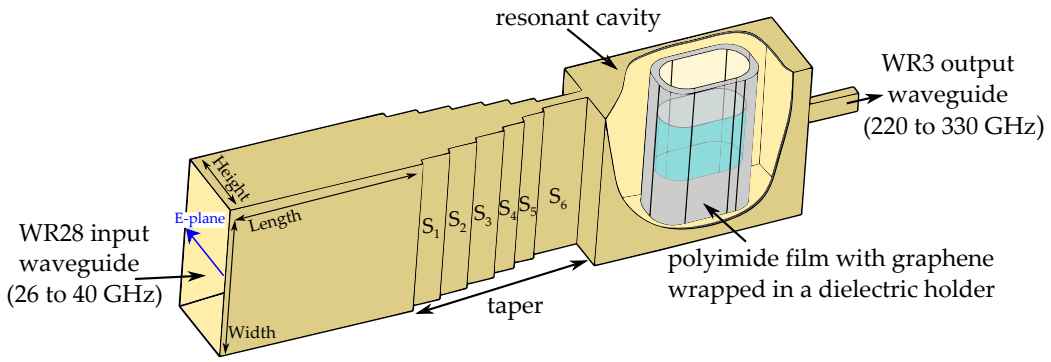

Figure 4.1: Starting topology of the proposed High Order Frequency Multiplier based on a Millimeter wave Resonant Cavity.

4.2 Device topology

The starting topology of the proposed high order frequency multiplier based on a millimeter wave resonant cavity is illustrated in Figure 4.1. The device is composed of a waveguide block and a few-layer/multi-layer graphene component. The waveguide block consists of a WR28 waveguide section which provides the input signal to a waveguide resonant cavity and a WR3 waveguide section which collects the resulted high harmonic multiplied signal. A waveguide taper is placed at the input of the frequency multiplier. This waveguide taper structure gradually reduces the height of the standard WR28 waveguide and thus increases the electric field levels injected into the rectangular cavity. The rectangular cavity is designed having two areas with high input electric fields. The electric fields vector on the two areas have opposite direction, therefore producing the current flow around the graphene component. The few-layer graphene component consists of a thin polyimide film covered with one respectively two graphene sheets. The sheets are inserted into a 3D printed acrylic resin holder with ring structure. The multi-layer graphene component has initially the same structure as the previous described few-layer graphene component. This structure has been gradually modified in order to enhance the resonant response of the rectangular cavity, which is needed for the generation of the high harmonic output content, and the radiation characteristics of the high harmonic multiplied signal.

4.3 Few-layer graphene based frequency multiplier

This section presents the implementation of a single stage frequency multiplier which contains a mono/bilayer graphene film inserted into a resonant cavity so it can be irradiated with high electric field levels. The proposed approach aims to demonstrate an innovative high frequency and power efficient graphene based frequency multiplier.

4.3.1 Design and optimization of the frequency multiplier

The frequency multiplier has been designed and optimized in the millimeter wave band (K_a band) using three-dimensional electromagnetic simulation software in which the behavior of the electromagnetic wave in terms of the scattering parameters and the numeric modeling of the electric field distribution inside the cavity and the waveguide sections are analyzed. Based on a set of numerical calculations, taken from the theoretical analysis provided in Chapter 1 (Eq. 1.75), the 7^{th} order current density along the few-layer graphene component is estimated. The resulting value is then inserted into the frequency multiplier design, as a current source defined around the graphene component, and it is used to excite the circuit in the submillimeter wave band (WR3 standard band). Therefore, a new set of simulations are performed in the 220 to 330 GHz band in which the behavior of the frequency multiplier is analyzed in terms of the converted 7^{th} order power levels received at the WR3 output waveguide.

4.3.1.1 Optimization in the millimeter wave band

This section presents the design and optimization process of the proposed single stage high order frequency multiplier. Firstly, for the generation of a primary suitable solution, the assembly composed only by the waveguide blocks is analyzed and optimized in the millimeter wave band. Secondly, a few-layer graphene component is placed inside a resonant cavity which is part of the optimized waveguide block. Finally, the complete design of the frequency multiplier is optimized in the millimeter wave band.

Waveguide block structure

The investigation of the waveguide block structure starts with the design of a standard WR28 waveguide section which is connected to a resonant cavity. Following the WR28 waveguide section, a taper with six stages is designed. Through this structure, the electric field levels inserted and stored in the resonant cavity are

expected to be higher than the propagating electric field levels along the input WR28 waveguide.

The waveguide cavity is designed to resonate at a frequency similar with the one from the input signal in the K_a band. For this its width and height are chosen equal to the standard dimensions of a WR28 rectangular waveguide, i.e. 7.112×3.556 mm^2. The length of the waveguide cavity is chosen one wavelength at its resonant frequency so that the second resonant mode of the rectangular cavity, which produces two areas with high input electric field levels in the cavity, is excited. The value of the wavelength can be theoretically calculated using the formula:

$$\lambda_{guide} = \frac{c}{f_r} \times \frac{1}{\sqrt{1 - \left(\frac{c}{2a \cdot f_r}\right)^2}} \tag{4.1}$$

where c is the speed of light, $c = 3 \cdot 10^8$ m/s, f_r is the cavity resonant frequency and a is the dimension of the broad wall, in this case $a = 7.112$ mm. Thus, for a chosen resonant frequency at $f_r = 39.1$ GHz, the length of the waveguide cavity should be equal to $\lambda_{guide} = 9.1$ mm.

Additionally, the waveguide cavity is continued with a standard WR3 rectangular waveguide section. All the elements of the discussed assembly are arranged in a configuration with E-plane alignment.

In order to simulate the waveguide based design, two waveports are assigned along its structure. One waveport is placed at the input of the WR28 waveguide section (Port 1) and the other waveport is placed at the output of the WR3 waveguide section (Port 2). In the millimeter wave band the circuit was fed through its WR28 input port with 1 Watt time-average power. The WR3 waveguide section in the K_a band acts as a short-circuit termination, reflecting the electromagnetic wave incoming from the WR28 input waveguide. There is no transmitted millimeter wave signal through the output WR3 waveguide section. Furthermore, the walls of the waveguide based design are modeled as 1 μm thickness gold layers.

The values of the optimized waveguide taper and resonant cavity are presented in Table 4.1. The response of the simulated return loss at the input Port 1 is illustrated in Figure 4.2. As one can notice, two resonant frequencies can be appreciated in the figure. The resonance at $f_{r1} = 26.8$ GHz corresponds to the first resonant cavity mode while the resonance at $f_{r2} = 39.1$ GHz corresponds to the second resonant cavity mode. The circuit has a 3-dB bandwidth at the first resonant mode of $BW_{3dB_1} = 20$ MHz and at the second resonant mode of $BW_{3dB_2} = 21$ MHz.

Element	Length [mm]	Height [mm]	Width [mm]
Taper section S_1	1.3	3	7.112
Taper section S_2	1.3	2.5	
Taper section S_3	1.3	2	
Taper section S_4	1	1.5	
Taper section S_5	1	0.9	
Taper section S_6	2	0.1	
Resonant cavity	9.1	3.556	

Table 4.1: Optimized dimensions of the waveguide taper and rectangular cavity used in the simulation of the waveguide based design.

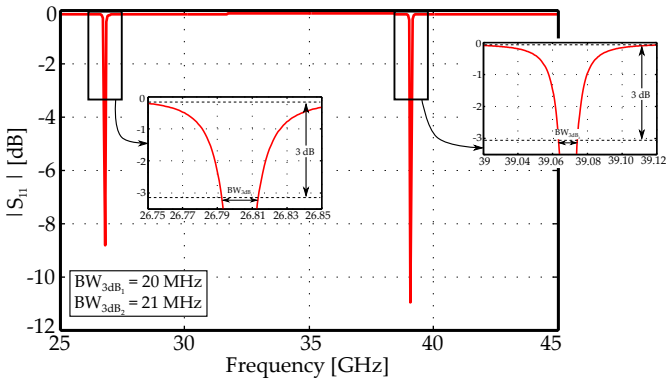

Figure 4.2: Return loss of the waveguide block design.

The electric field distribution at the two resonant frequencies along the analyzed circuit are represented in Figure 4.3. As predicted, the amplitude of the electric field inside the rectangular cavity is almost one order of magnitude bigger than the one existing along the input WR28 waveguide section in both cases considered. Note that even if the first two fundamental cavity modes are noticed along the analyzed input K_a frequency band, the second cavity resonant mode, which has the electric fields vector on the two areas with high input field levels in the cavity in opposite directions, is the mode needed in the analysis herein.

The Q factor of the rectangular cavity is calculated using the formula:

$$Q = \frac{f_r}{BW_{3dB}} \tag{4.2}$$

where f_r is the resonant central frequency and BW_{3dB} is the 3-dB bandwidth.

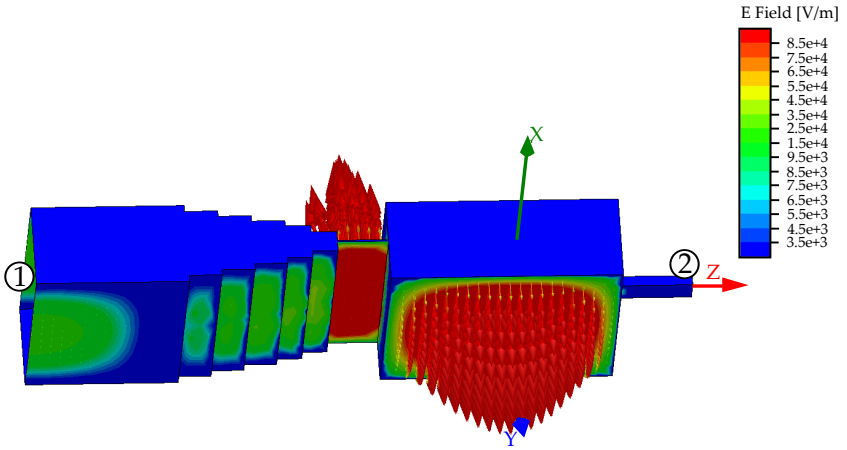

(a) E-field at 26.8 GHz.

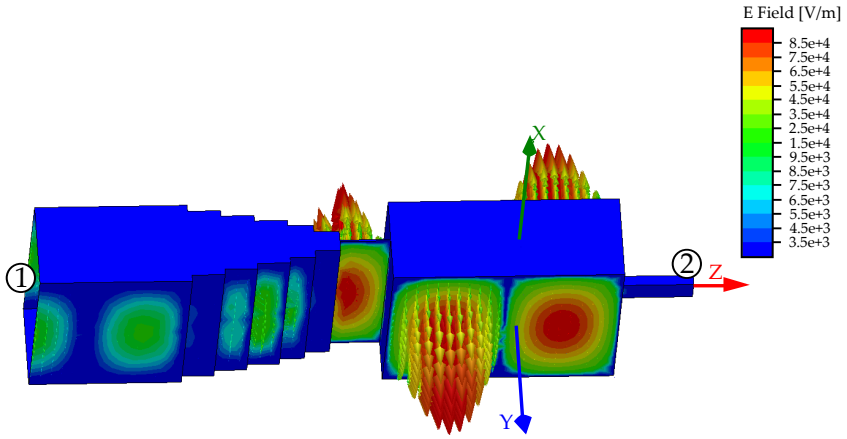

(b) E-field at 39.1 GHz.

Figure 4.3: Electric field distribution along the waveguide block design. Circuit fed through Port 1.

Analyzing the case of the second cavity resonant mode and performing the calculations for the values estimated above, i.e. $f_{r_2} = 39.1$ GHz and $BW_{3dB_2} = 21$ MHz, a Q factor of about 1862 is observed in simulations.

Few-layer graphene component

Next, in order to complete the frequency multiplier structure, a few-layer graphene component is designed. A 25 µm thickness polyimide substrate with dielectric constant $\varepsilon_r = 3.5$ and $\tan\delta = 0.008$ is used as a support for the graphene film. This structure is wrapped in the interior of a 300 µm thickness 3D printed acrylic resin holder with dielectric constant $\varepsilon_r = 3.4$ and $\tan\delta = 0.008$. The whole graphene film

assembly is introduced in the middle of the optimized rectangular cavity, as presented in Figure 4.1. The geometrical arrangement of the graphene layers, mostly the two regions parallel to the E-plane of the waveguide block, must be optimized to take advantage of the areas with high input field levels in the cavity as they provide better harmonic conversion. For this reason, the cavity second resonant mode which has two maximum electric field regions (see Figure 4.3(b)) is used in the excitation of the graphene component with parallel electromagnetic radiation.

In simulations, the graphene film was modeled having the values shown in Table 4.2. These values were given by the graphene sample provider.

Type of graphene	Theoretical thickness [nm]	Conductivity $\sigma_{\parallel}$ [S/m]	Conductivity $\sigma_{\perp}$ [S/m]	Sheet resistance [Ω/sq]
Monolayer	0.345	$6.44 \cdot 10^6$	0	450
Bilayer	0.69	$5.79 \cdot 10^6$	0	250

Table 4.2: Dimensions of the graphene film used in simulations, where $\sigma_{\parallel}$ is the parallel conductivity and $\sigma_{\perp}$ is the perpendicular conductivity to the film plane.

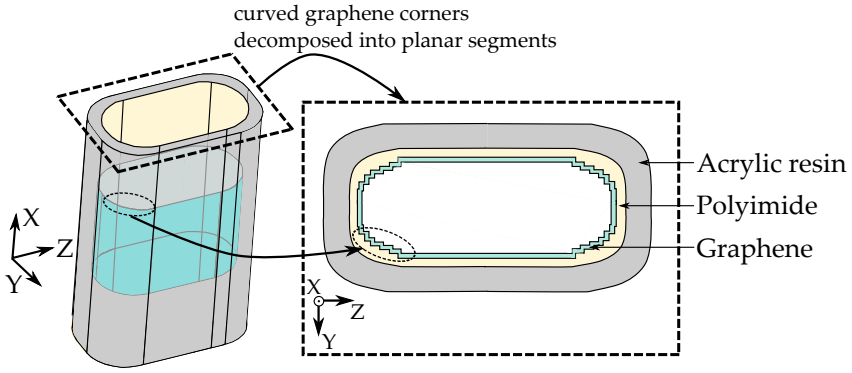

Figure 4.4: Definition of the graphene anisotropic conductivity, where $\sigma_{\perp} = 0$ on the direction perpendicular to each segment length.

The simulation of the complete frequency multiplier design, in the millimeter wave band, is started considering a monolayer graphene film. For this, the waveguide block, optimized in the previous design process, is kept unmodified with one exception, the height of the last waveguide taper section S_6. This height is limited to 0.55 mm due to fabrication restrictions. Further, in order to accurately simulate the curved corners of the graphene film each segment composing these areas is decomposed into planar segments along the two axis of the geometry transverse plane,

as presented in Figure 4.4. By using this approach one can define the anisotropic parallel and perpendicular conductivity of each graphene segment along the corresponding axis of the geometry coordinate system. This approach has been necessary in order to overcome the limitation of the three-dimensional electromagnetic simulator HFSS in terms of anisotropic conductivity assignment to curved surfaces.

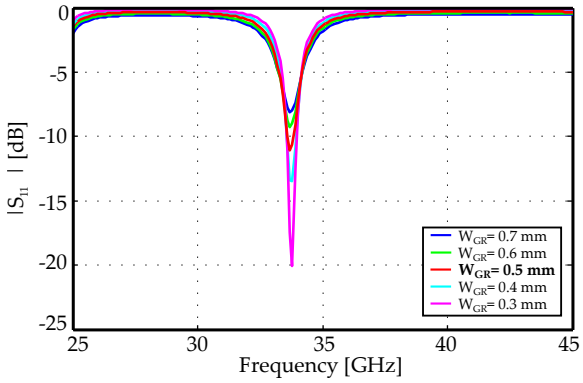

(a) Influence of W_{GR} parameter

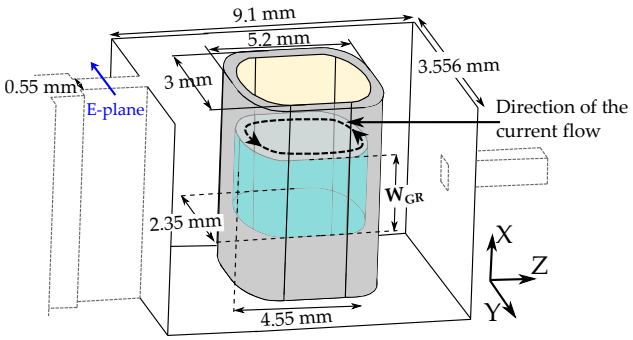

(b) Schematic of the final optimized graphene component

Figure 4.5: Simulated reflection coefficient at Port 1 when varying the width of the graphene component.

A parametric sweep is performed on the width of the graphene film, W_{GR}, in order to study the effect of this parameter on the circuit resonant response. The result of the analysis is presented in Figure 4.5(a). The dimensions of the final optimized graphene component are shown in Figure 4.5(b). As one can notice, decreasing W_{GR} the resonant response of the rectangular cavity is stronger and thus the cavity is less affected by the presence of the graphene film inside it. This means that a narrower graphene layer determines the generation of a lower electric current along the sample and therefore the cavity resonance is less disturbed. The total graphene resistance can be calculated using the formula:

$$R = R_s \cdot \frac{L}{W} \tag{4.3}$$

where $R_s = 450\ \Omega/\text{sq}$ is the sheet resistance, $L = 11.7$ mm is the total length of the graphene component and $W = W_{GR}$ is the width of the graphene layer used in simulations.

Therefore, from Eq. 4.3, one can observe that by decreasing the width of the graphene layer the total resistance increases and ultimately the current generated along the considered sample decreases. A trade-off solution between the resonant response of the rectangular cavity and the electric current induced in the graphene sample should be adopted in order to reach high harmonic conversion. The red line from Figure 4.5(a) corresponds to the final value of the graphene width which was chosen in the optimized structure.

The two resonant frequencies of the rectangular cavity were shifted downwards in frequency as compared to the results from Figure 4.2. For the first resonant mode, its frequency was shifted out of the K_a band while for the second resonant mode, its frequency was shifted 14% downwards to $f_r = 33.7$ GHz. The frequency shift has been the consequence of introducing the polyimide film with graphene and dielectric holder inside the resonant cavity.

Furthermore, the 3-dB bandwidth of the circuit has increased from $BW_{3dB_2} = 21$ MHz (see Figure 4.2) to $BW_{3dB} = 1.3$ GHz and the Q factor has decreased from around 1862 to around 26.

The electric field distribution along the monolayer graphene based frequency multiplier at 33.075 GHz and 33.7 GHz is illustrated in Figure 4.6. The first frequency point, 33.075 GHz, is the lower limit of the 3-dB bandwidth while 33.7 GHz is the circuit central resonant frequency. It can be seen that the electric field levels inside the resonant cavity are higher at the central resonant frequency. This is mainly due to a better circuit resonant response. Nevertheless, in both cases two areas with high input field levels in the cavity were formed. The graphene component was optimized to take advantage of these areas as the electric field there is tangential to its plane surface. According to the analysis discussed in Chapter 1, the irradiation of the graphene film with such an electric field gives rise to odd order harmonic components in the induced current (see Eq. 1.75).

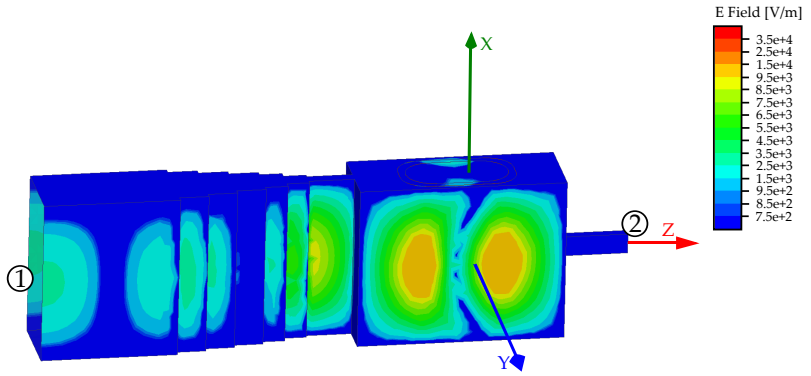

(a) E-field at 33.075 GHz.

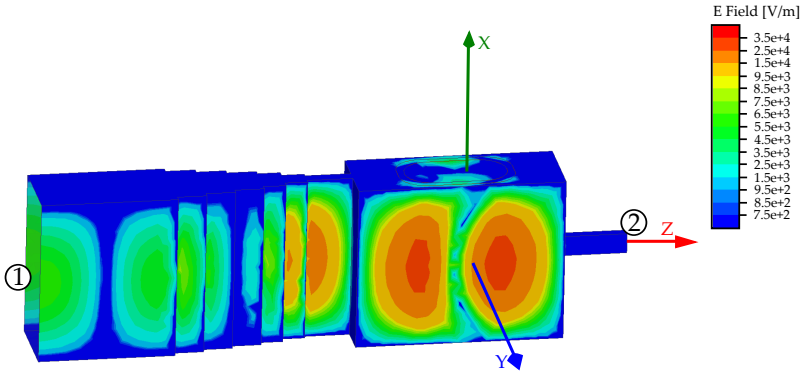

(b) E-field at 33.7 GHz.

Figure 4.6: Electric field distribution in the monolayer graphene based frequency multiplier design.

The linear current density distribution on the monolayer graphene film is calculated using the formula:

$$j_\omega = \sigma^\omega \cdot E_\omega \tag{4.4}$$

where $\sigma^\omega = \sigma_\parallel$ is the anisotropic parallel conductivity of $d = 0.345$ nm thickness monolayer graphene film, and E_ω is the average value of the electric field tangential to the graphene layer. The numeric modeling of the electric field, E_ω, is realized using a Field calculator tool [10, 11] implemented in the three-dimensional electromagnetic simulator HFSS. This tool performs mathematical operations on all saved field data in the modeled geometry. Therefore the field calculator is used to compute the average value of the electric field, at 33.7 GHz, along the graphene layer in the regions parallel to the external electric field excitation (graphene regions parallel to

the Y axis from Figure 4.4). Along the mentioned graphene regions the induced current is composed of odd order harmonic components (according to Eq. 1.75).

Table 4.3 presents the estimated value of the average electric field and the linear current density distribution produced on the monolayer graphene film.

Type of graphene	Conductivity σ^{ω} [S/m]	Average value of E-field E_{ω} [V/m]	Linear current density distribution j_{ω} [A/m^2]
Monolayer	$6.4 \cdot 10^6$	$2.95 \cdot 10^4$	$18.9 \cdot 10^{10}$

Table 4.3: Anisotropic parallel conductivity, average value of the electric field and linear current density distribution on the monolayer graphene film. Input power applied $P_{in} = 1$ Watt.

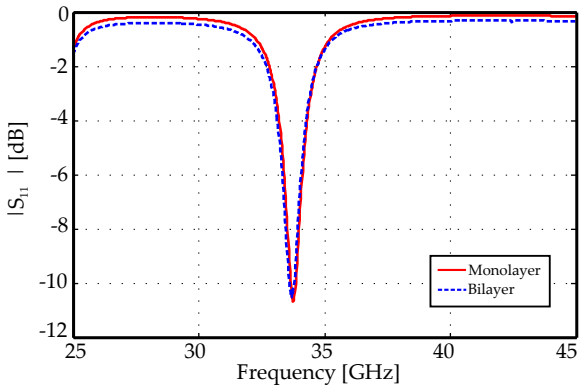

Figure 4.7: Simulated response of the frequency multiplier in the millimeter wave band for a monolayer and bilayer graphene film.

The simulated response of the frequency multiplier in the millimeter wave band for a bilayer graphene film is represented in Figure 4.7. In order to maintain a cavity resonant response with a reflexion coefficient $|S_{11}| < -10$ dB the bilayer graphene width, W_{GR}, is reduced to 0.3 mm. As one can notice, a 3-dB bandwidth of 1.3 GHz has been obtained. This value is similar with the 3-dB bandwidth from the monolayer graphene case. Therefore, the Q factor observed in simulations is maintained around 26.

Furthermore, the linear current density distribution along the bilayer graphene is calculated using the average value of the electric field, computed analogously to the

monolayer graphene case. The obtained data is outlined in Table 4.4. The computed average value of the electric field along the bilayer graphene film is slightly lower than the value obtained in the monolayer case. However, the total linear electric current per cross section area in bilayer graphene is comparable to the obtained value in monolayer graphene as the bilayer cross section area, $S_B = 0.21 \cdot 10^{-12}$ m^2, is bigger than the monolayer cross section area, $S_M = 0.173 \cdot 10^{-12}$ m^2.

Type of graphene	Conductivity σ^{ω} [S/m]	Average value of E-field E_{ω} [V/m]	Current density distribution j_{ω} [A/m^2]
Bilayer	$5.8 \cdot 10^6$	$2.86 \cdot 10^4$	$16.6 \cdot 10^{10}$

Table 4.4: Anisotropic parallel conductivity, average value of the electric field and linear current density distribution on the bilayer graphene film. Input power applied $P_{in} = 1$ Watt.

4.3.1.2 Analysis in the submillimeter wave band

The design of the few-layer graphene based frequency multiplier is continued with the analysis of the circuit in the submillimeter wave band. Note that the multiplication order evaluated to reach the 220-330 GHz band from the input K_a band is $N = 7$. Therefore the circuit excitation in the submillimeter wave band is the current density generated along the graphene film due to the contribution of the 7^{th} order harmonic.

The theoretical estimation of the 7^{th} order current density, as discussed in Chapter 1, for a graphene layer of thickness d has the expression:

$$j_{7\omega-d} = \frac{\sigma^{7\omega}}{d} \cdot (E_{\omega})^7 \tag{4.5}$$

where E_{ω} is the average value of the linear electric field and $\sigma^{7\omega}$ is the 7^{th} order non-linear conductivity computed as follows:

$$\sigma^{7\omega} = \frac{5^2 \cdot 3^2}{2^6} \frac{e^8 v_F}{\pi \hbar^7 (\pi n_s)^2 \sqrt{\pi n_s}} \cdot \frac{-7i}{(7\omega + i/\tau)(6\omega + i/\tau)(5\omega + i/\tau)(4\omega + i/\tau)} \cdot \frac{1}{(3\omega + i/\tau)(2\omega + i/\tau)(\omega + i/\tau)} \tag{4.6}$$

In the above formula, $e = 1.602 \cdot 10^{-19}$ C is the electric charge, $\hbar = 1.05 \cdot 10^{-34}$ J $\cdot$ s is the reduced Planck constant, $v_F = 10^6$ m/s is the Fermi velocity, n_s is the charge carrier density and τ is the electron relaxation time between two collisions. The value of the monolayer and bilayer graphene charge carrier and relaxation time were estimated from the values given by the sample provider. These values together with the calculated 7^{th} order non-linear conductivity are summarized in Table 4.5.

Type of graphene	Charge carrier density n_s [m^{-2}]	Relaxation time τ [s]	7^{th} order non-linear conductivity $\sigma^{7\omega}$ [$S \cdot m^6 \cdot V^{-6}$]
Monolayer	$0.875 \cdot 10^{16}$	$1.77 \cdot 10^{-13}$	$5.9 \cdot 10^{-35}$
Bilayer	$1.56 \cdot 10^{16}$	$2.3 \cdot 10^{-13}$	$11 \cdot 10^{-35}$

Table 4.5: 7^{th} order non-linear conductivity.

The current density of electrons from Eq. 4.5 is valid under the condition $Q_0 < 1$ where the field parameter Q_0 is expressed as:

$$Q_0 = \frac{eE_0 v_F}{\omega \varepsilon_F} < 1. \tag{4.7}$$

Thus, the low-field condition given by Eq. 4.7 is fulfilled for an electric field:

$$E_\omega < \frac{\omega \varepsilon_F}{2ev_F} = \frac{\omega \hbar \sqrt{\pi n_s}}{2e}. \tag{4.8}$$

Figure 4.8 presents the average value of the linear electric field E_ω, estimated along the graphene monolayer and bilayer film from the frequency multiplier, as a function of the applied input power. The values, in each case, are computed at the resonant frequency $f_r = 33.7$ GHz. The low-field limit given by Eq. 4.8 is calculated and it is indicated in the graphics with a dashed line. The field parameter Q_0 is charge carrier-dependent and as a consequence, the low-field condition is fulfilled for a slightly higher electric field value in the bilayer graphene case.

In Figure 4.9, the 7^{th} order current density, calculated according to Eq. 4.5, is represented as a function of the applied input power, P_{in}, in both monolayer and bilayer graphene based frequency multipliers. It can be verified that the estimated value of the 7^{th} order current density in the bilayer graphene film is lower than the

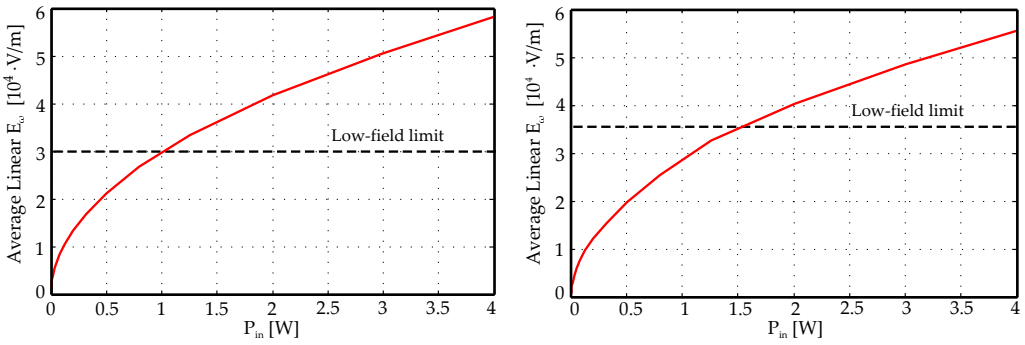

(a) Monolayer graphene (b) Bilayer graphene

Figure 4.8: Representation of the applied input power versus the average linear electric field, E_ω, where the low-field limit is marked with a dashed line.

estimated value in the monolayer film. However, the 7^{th} order electric current per cross section area in bilayer graphene is comparable to the 7^{th} order electric current in monolayer graphene as the bilayer cross section area, $S_B = 0.21 \cdot 10^{-12}$ m^2, is higher than the monolayer cross section area, $S_M = 0.173 \cdot 10^{-12}$ m^2.

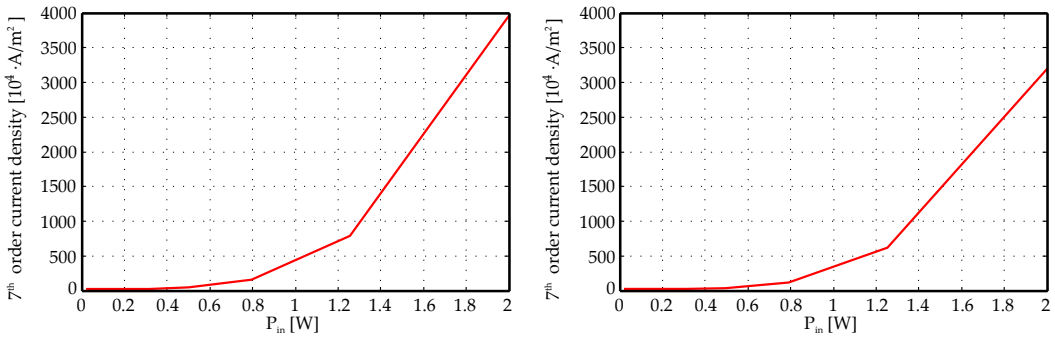

(a) Monolayer graphene (b) Bilayer graphene

Figure 4.9: Representation of the 7^{th} order current density as a function of the applied input power.

One can establish the circuit excitation in the submillimeter wave band by inserting the estimated 7^{th} order current (from Figure 4.9) along the few-layer graphene component for a given input power. Therefore the electric field distribution, for an input power $P_{in} = 1$ W, along the monolayer graphene based frequency multiplier at the output frequency $f_{out} = N \times f_{in}$, with $N = 7$ and $f_{in} = 33.7$ GHz is illustrated in Figure 4.10.

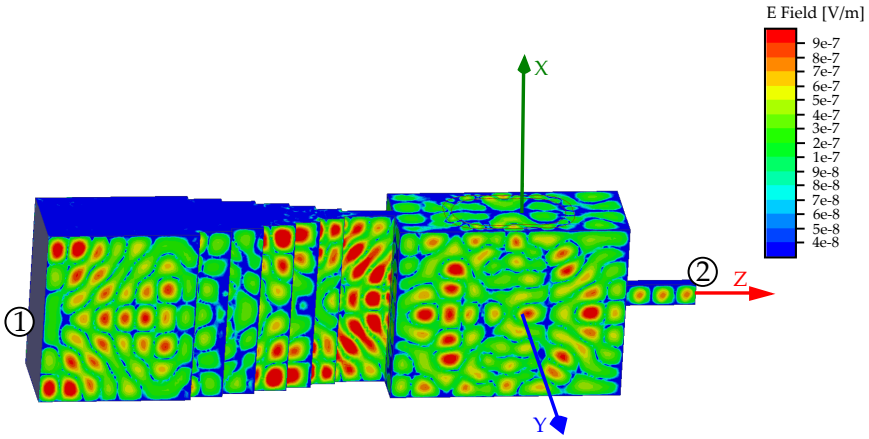

Figure 4.10: Electric field distribution at 236 GHz in the monolayer graphene based frequency multiplier design.

Type of graphene	Input power applied		Output power Port 2		Output power Port 1	
	[W]	[dBm]	[W]	[dBm]	[W]	[dBm]
Monolayer	0.794	29	2.5e-16	-126	2e-18	-146
	1	30	8e-16	-120	5e-18	-140
	1.259	31	6e-15	-112	4e-17	-133
	1.584	32	3e-14	-105	2e-16	-126
	2	33	2e-13	-96	8e-16	-120
Bilayer	1.259	31	3e-15	-115	2e-17	-136
	1.584	32	2e-14	-106	6e-17	-132
	2	33	9.5e-14	-100	4e-16	-123

Table 4.6: Estimated value of the 7^{th} order power, at 236 GHz, received at the output Port 2 and input Port 1.

It is observed that the 7^{th} order signal is radiated from the graphene component in both directions towards the WR3 output waveguide as well as towards the WR28 input waveguide. However, the converted power levels were found substantially higher at the WR3 output waveguide as compared to the power levels reflected at the WR28 input waveguide. Table 4.6 presents the estimated values of the 7^{th} order received power at both output Port 2 and input Port 1 in the monolayer and bilayer graphene based frequency multipliers for different values of the applied input power.

4.3.2 Prototype fabrication and experimental characterization

4.3.2.1 Prototype Implementation

In order to experimentally validate the frequency multiplier design, obtained using the approach that has been described in the previous subsection, a prototype of the complete structure has been manufactured and measured. The waveguide structure was divided into two blocks, resulting from cutting the main structure (as presented in Figure 4.1) throughout its center plane in the direction perpendicular to the geometry width. The two parts are manufactured using a 3-dimensional printer with high precision stereolithography process. In this technique a photopolymer resin is successively cured, layer by layer in a resin tank, as it is exposed to ultraviolet radiation. When the building process is completed, the 3-dimensional object obtained is immersed in isopropyl alcohol in order to eliminate the resin excess, and finally cured in an ultraviolet oven.

This technology is less expensive and decreases significantly the fabrication time of the prototypes as compared to the other technologies used in literature [12, 13]. Moreover, repetitive prototypes with the same fabrication precision can be manufactured at a low cost.

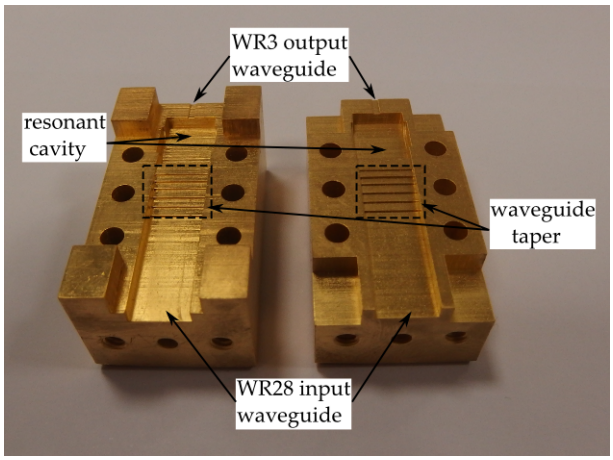

Figure 4.11: Waveguide structure - prototype overview.

The necessary conductivity along the whole waveguide structure was provided through the deposition of a thin gold layer by means of a sputtering process. An image of the final prototype is presented in Figure 4.11.

Next, the graphene structure is prepared in a process including several steps. In a first step the 25 μm polyimide sheet, employed as dielectric substrate of the

graphene layers, is cut to the desired shape with a laser machine. Gold contacts of approximately 1 µm thickness and 1.5 mm length are deposited along the edges of the prepared polyimide sheet in a sputtering process. The monolayer and bilayer graphene films are then transferred on top of the polyimide sheet with gold contacts. The resistance measurement of the two transferred graphene films, from one gold contact to the other, have been performed in order to validate the values used in simulations. As a final step, the two graphene samples were provided with the adequate shape through a second laser ablation process. Figure 4.12 presents the two prepared graphene samples.

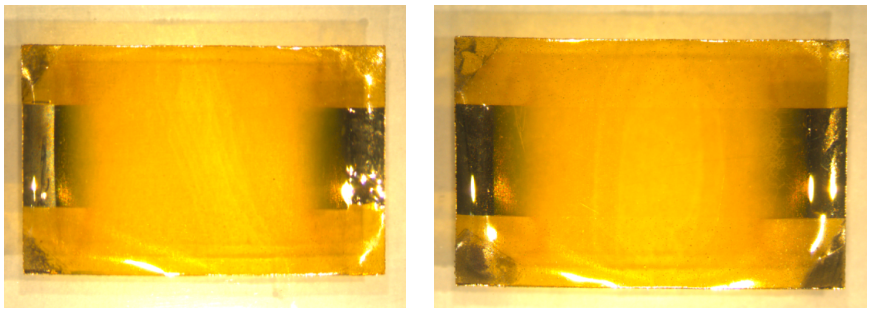

(a) Monolayer graphene sample (b) Bilayer graphene sample

Figure 4.12: Image of the prepared graphene sheets.

The external dielectric holder of the few-layer graphene sheet is manufactured using the aforementioned 3-dimensional printing process. The prepared graphene samples are then introduced into the dielectric holder. The two gold contacts, of each sample, were joined together by applying a thin film of silver painting at their intersection. Figure 4.13 illustrates the assembled version of the monolayer graphene component.

Further, the assembled few-layer graphene component is mounted and secured into the rectangular cavity of the waveguide structure. The two waveguide blocks are then precisely aligned together with several screws of 1 mm diameter and 8 mm length. Standard interface flanges for both WR28 and WR3 waveguides have been directly incorporated into the built waveguide structure. Figure 4.14 presents the assembled version of the monolayer graphene component mounted in its corresponding resonant cavity.

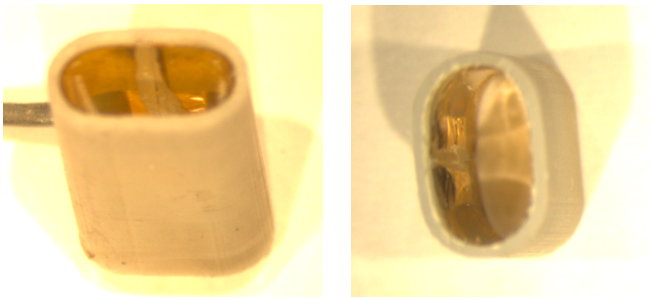

(a) Front view (b) Top view

Figure 4.13: Image of the assembled monolayer graphene component.

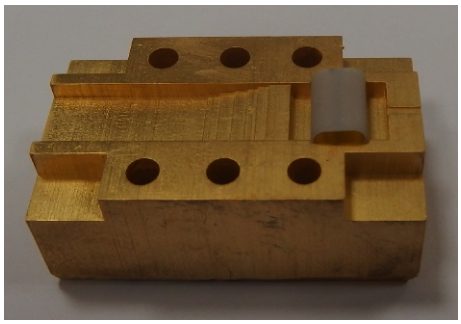

Figure 4.14: Image of the assembled graphene component mounted in its corresponding resonant cavity.

4.3.2.2 Reflection coefficient measurement in the K_a band

The behavior of the few-layer graphene based frequency multiplier prototype is first analyzed in terms of the measured reflection coefficient in the K_a band. For this the WR28 input waveguide port of the frequency multiplier prototype has been connected to the vector network analyzer as presented in the schematic diagram from Figure 4.15. The obtained data is represented together with the simulation results in Figure 4.16 and Figure 4.17. The manufactured prototype with a monolayer graphene component presents two resonant frequencies at 42.2 GHz and at 42.6 GHz which means an almost 25% deviation with respect to the simulation response (33.7 GHz). Moreover the measured 3-dB bandwidth at the two resonant frequencies ($BW_{3dB_{m1}}$ = 3 MHz and $BW_{3dB_{m2}}$ = 5 MHz) is narrower as compared to the simulation response (BW_{3dB_s} = 1.3 GHz).

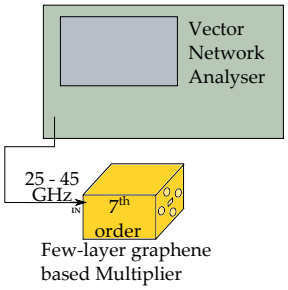

Figure 4.15: Schematic diagram of the reflection coefficient measurement in the K_a band.

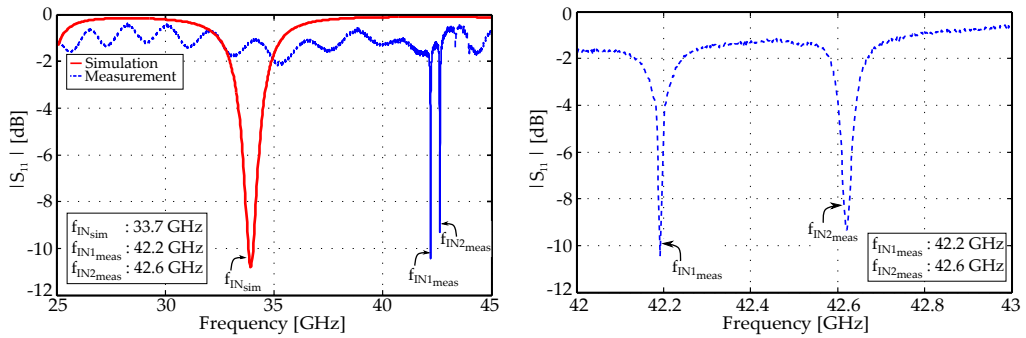

(a) Simulated and measured data (b) Measured data representation

Figure 4.16: Simulated and measured reflexion coefficient of the monolayer graphene based frequency multiplier in the millimeter wave band.

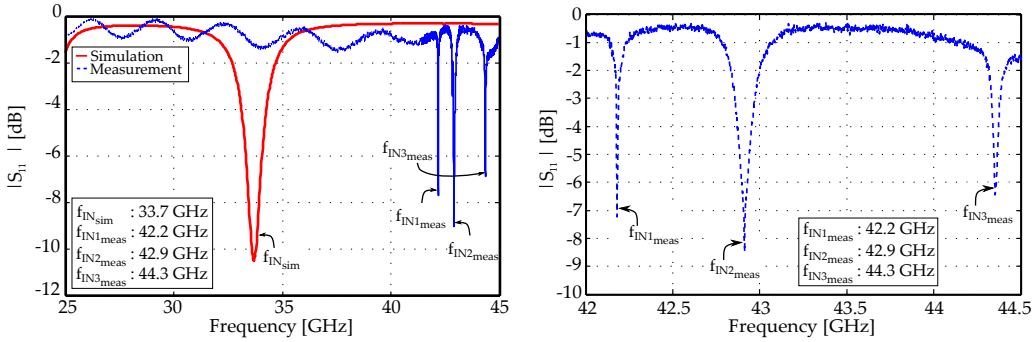

(a) Simulated and measured data (b) Measured data representation

Figure 4.17: Simulated and measured reflexion coefficient of the bilayer graphene based frequency multiplier in the millimeter wave band.

A similar behavior is noticed while analyzing the frequency multiplier prototype integrating a bilayer graphene component. In this case, three resonant frequencies at 42.2 GHz, at 42.9 GHz and at 44.3 GHz were detected. The measured 3-dB bandwidth at each resonant frequency is $BW_{3dB_{m1}} = 2$ MHz, $BW_{3dB_{m2}} = 12$ MHz and $BW_{3dB_{m3}} = 5$ MHz, respectively.

4.3.2.3 Multiplier performance - output power

The schematic of the measurement setup employed for the experimental characterization of the output power generated with the proposed frequency multiplier prototype is presented in Figure 4.18. The input signal, generated by the vector network analyzer, is amplified up to the power level $P_{in} = 33$ dBm with a 30 dB gain power amplifier. This signal is then provided to the WR28 input waveguide section of the frequency multiplier.

The frequency multiplier output signal corresponding to the 7^{th} harmonic component of the input applied signal is measured by the $PNA - X$ vector network analyzer using a *Virginia Diodes* frequency extender (receiver) module operating in the 220 to 330 GHz band.

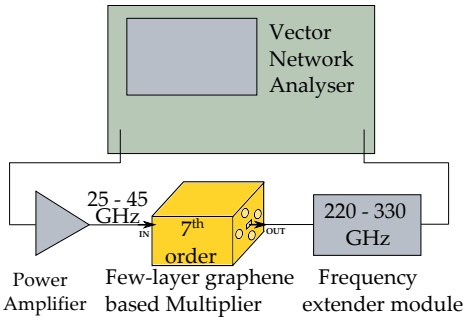

Figure 4.18: Schematic diagram of the measurement setup.

The evolution of the measured output power of the 7^{th} harmonic component for the monolayer and bilayer graphene based frequency multiplier is represented in Figure 4.19 and Figure 4.20 considering different values of the applied input power. In each case, the results have been seen only at specific frequencies within the WR3 output band. The obtained output results correspond to a signal transformation given by $N \times f_{in}$ GHz with N the harmonic order and f_{in} the measured input resonant response of the circuits. These data are represented as shaded areas.

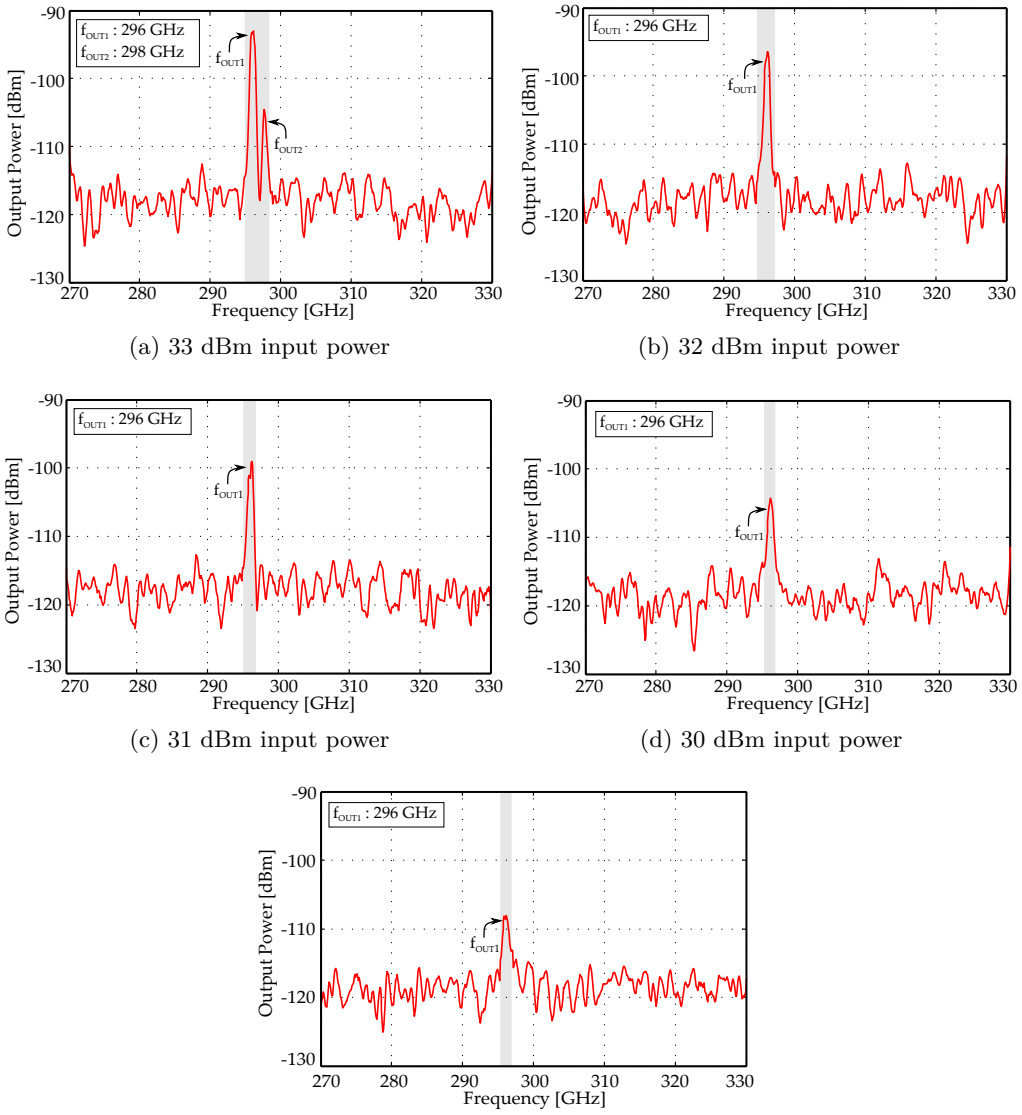

(a) 33 dBm input power

(b) 32 dBm input power

(c) 31 dBm input power

(d) 30 dBm input power

(e) 29 dBm input power

Figure 4.19: Measured output power of the 7^{th} order harmonic monolayer graphene based frequency multiplier for different values of the input power considered.

In the case of a monolayer graphene component, the seventh order transformation of both input measured resonant frequencies was detected at the output of the evaluated prototype. From Figure 4.16 one can notice that the prototype presents a better resonant response at 42.2 GHz than at 42.6 GHz. Therefore, the 7^{th} order output power corresponding to the first resonant frequency, 42.2 GHz ($f_{OUT_1} = 296$

GHz), was observed over the system noise floor for lower values of the input power than the 7^{th} order output power corresponding to the second resonant frequency, 42.6 GHz (f_{OUT2} = 298 GHz). Moreover, the maximum reached output power was around -93.5 dBm which is slightly higher than the estimated value from the simulation process ($P_{out_{SIM}}$ = -96 dBm at P_{in} = 33 dBm). Furthermore, when analyzing the bilayer graphene based frequency multiplier, the maximum measured output power was around -94 dBm. This value is slightly lower than the maximum measured output power from the monolayer graphene case. The measured data of both monolayer and bilayer graphene based frequency multipliers present a relatively slower decreasing trend as compared to the estimated values from Table 4.6.

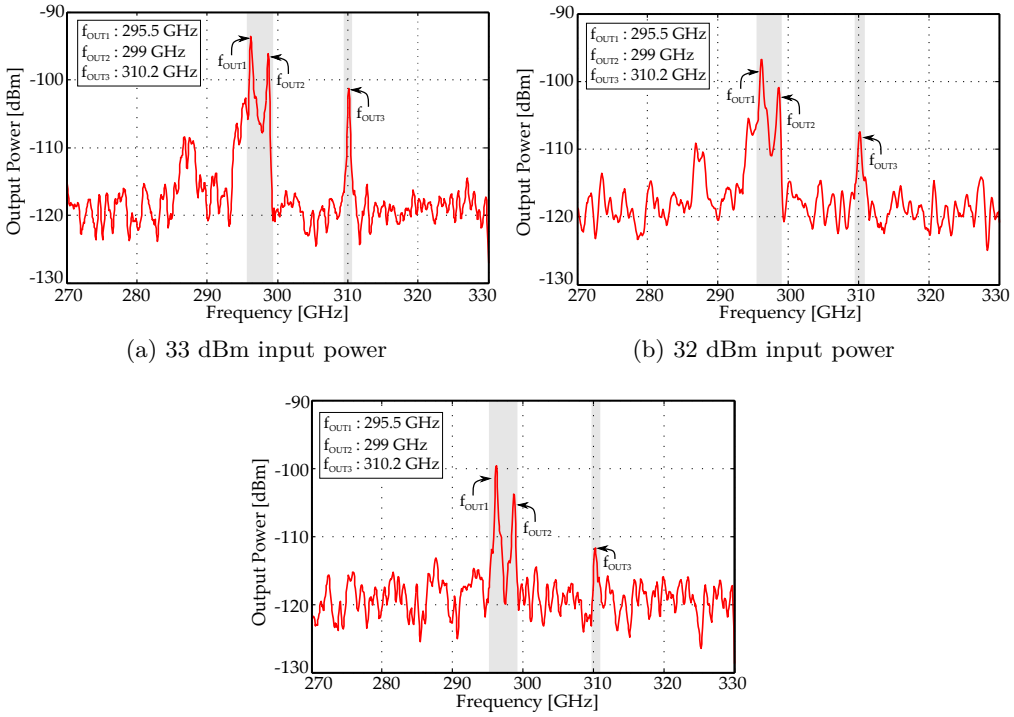

(a) 33 dBm input power

(b) 32 dBm input power

(c) 31 dBm input power

Figure 4.20: Measured output power of the 7^{th} order harmonic bilayer graphene based frequency multiplier for different values of the input power considered.

4.4 Multi-layer graphene based frequency multiplier

The proposed multi-layer graphene based frequency multiplier integrates the same waveguide block structure as the previously described few-layer graphene based

frequency multiplier. The multi-layer graphene component employed for the generation of the high harmonic output content has been initially designed analogous to the few-layer graphene component. This structure is step by step modified as a result of constructively combining several effects, induced along the resonant cavity, as electromagnetic coupling effects and radiation effects of the generated high harmonic content in the direction towards the WR3 output waveguide. Each configuration is individually treated in the upcoming subsections.

The multi-layer graphene film, integrated in the frequency multiplier structure, is obtained by mechanical exfoliation of Highly Ordered Pyrolytic Graphite (HOPG). The values given by the HOPG sample provider, used in the simulations, are summarized in Table 4.7.

Type of graphene	Conductivity $\sigma_{\parallel}$ [S/m]	Conductivity $\sigma_{\perp}$ [S/m]	Layer thickness used in simulations [μm]
Multi-layer (graphite)	$2.1 \cdot 10^6$	500	1

Table 4.7: Dimensions of the multi-layer graphene sheet used in simulations, where $\sigma_{\parallel}$ is the parallel conductivity and $\sigma_{\perp}$ is the perpendicular conductivity to the layer surface.

4.4.1 First multi-layer graphene configuration

4.4.1.1 Design and optimization of the frequency multiplier

The first multi-layer graphene component consists in a 25 μm thickness polyimide substrate with a multi-layer graphene film wrapped in a 300 μm thickness 3D printed dielectric holder. The multi-layer graphene film is initially simulated having an isotropic conductivity $\sigma = 2.1 \cdot 10^6$ S/m. Secondly, the curved corners of the multi-layer graphene sheet, which were produced by wrapping it inside the dielectric holder, were decomposed into planar segments, analogous to the approach presented in Figure 4.4. On each created segment the anisotropic parallel and perpendicular conductivity is defined according to the corresponding axis of the geometry coordinate system (in the direction of the current flow $\sigma_{\parallel} = 2.1 \cdot 10^6$ S/m while in the perpendicular direction, along the thickness axis, $\sigma_{\perp} = 500$ S/m). The result of this comparison is shown in Figure 4.21 for a multi-layer graphene film of 0.5 mm width. In the case of an isotropic graphene model three resonant frequencies can be appreciated along the input K_a band and shortly above 40 GHz. This behavior

is a direct consequence of the increase in the real perpendicular graphene conductivity, $\sigma_{\perp} = 500$ S/m, which allows a higher transport of electrons in the direction perpendicular to the layer surface.

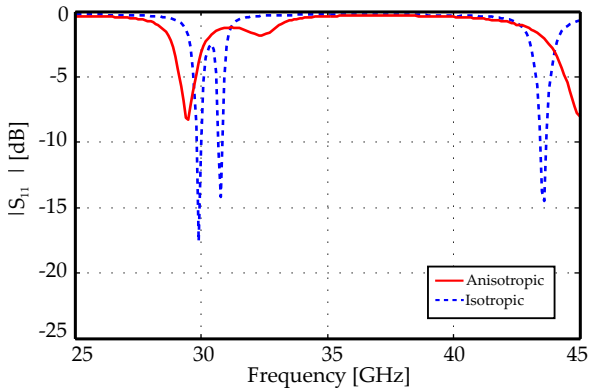

Figure 4.21: Simulated response of the frequency multiplier in the millimeter wave band for a 0.5 mm width multi-layer graphene film.

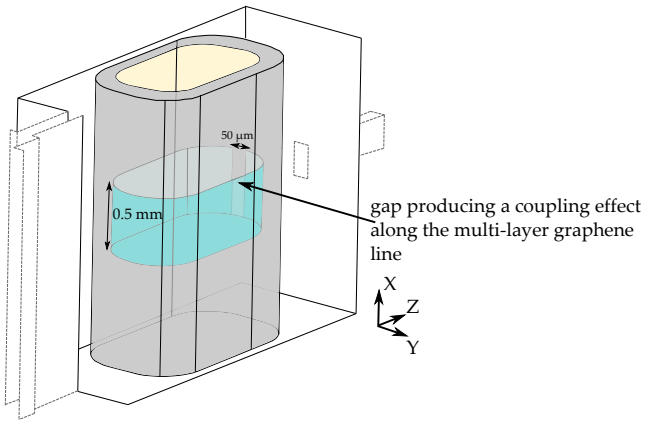

Figure 4.22: Topology of the multi-layer graphene component with the position and dimensions of the introduced coupling section.

Further, as presented in Figure 4.22 a coupling section consisting in a line gap is introduced in the multi-layer graphene component design. The geometrical arrangement of this section is carefully chosen so that the coupling induced resonant frequency is constructively combined with the resonant response of the rectangular cavity which will ensure a higher harmonic conversion. The circuit response in terms of the reflection coefficient at the input port is illustrated in Figure 4.23.

As one can notice, the resonant response of the rectangular cavity is shifted

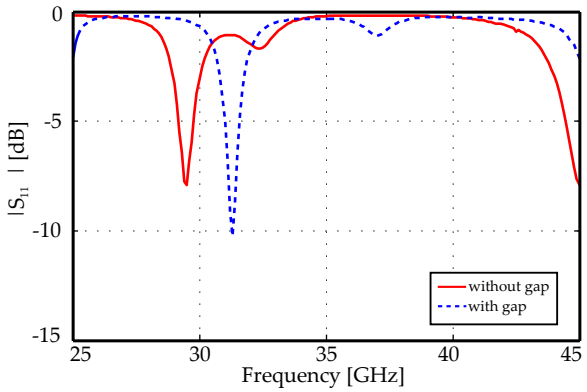

Figure 4.23: Simulated response of the frequency multiplier in the millimeter wave band.

upwards in frequency from $f_{noGap} = 29.5$ GHz to $f_{withGap} = 31.4$ GHz when the coupling section is introduced along the graphene component. Moreover, the circuit frequency response in terms of the reflexion coefficient has been improved, $|S_{11}| < -10$ dB, which determines higher electric field levels in the cavity and ultimately better harmonic excitation. The 3-dB bandwidth at the central frequency 31.4 GHz is $BW_{3dB} = 0.9$ GHz.

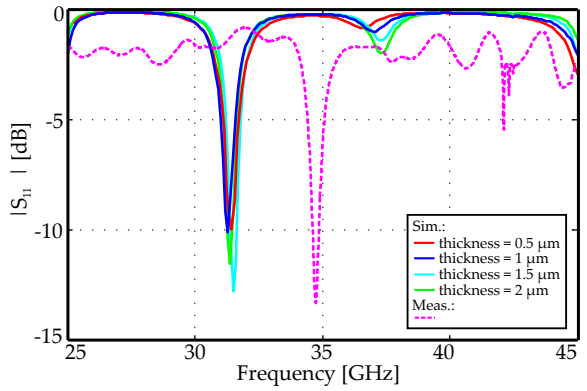

Figure 4.24: Input response of the frequency multiplier - influence of the multi-layer graphene thickness.

Next, an analysis is conducted with the purpose of assessing the effect of the multi-layer graphene thickness on the input response of the frequency multiplier. As presented in Figure 4.24, the multi-layer graphene thickness has been swept between 0.5 µm and 2 µm. The resonant response of the circuit is maintained with a reflexion coefficient $|S_{11}| < -10$ dB for each value of the evaluated thickness. It

can thus be concluded that this parameter should not come as a circuit limitation considering its high harmonic conversion.

Analysis in the submillimeter wave band

The simulation process of the multi-layer graphene based frequency multiplier is continued with the evaluation of the circuit behavior in the submillimeter, WR3 standard, frequency band. As in the previous case (Section 4.3) the harmonic order analyzed to reach the 220-330 GHz output band from the input K_a band is N =7.

The approach used in this section is similar with the approach from Subsubsection 4.3.1.2 and consists in defining a current excitation along the multi-layer graphene film for the generation of the high harmonic output content. The generated 7^{th} order output signal is examined in terms of its electric field distribution inside the circuit. For any value of the current excitation the 7^{th} harmonic power received at the WR3 output waveguide must always be higher than the power transmitted at the WR28 input waveguide for a proper circuit behavior.

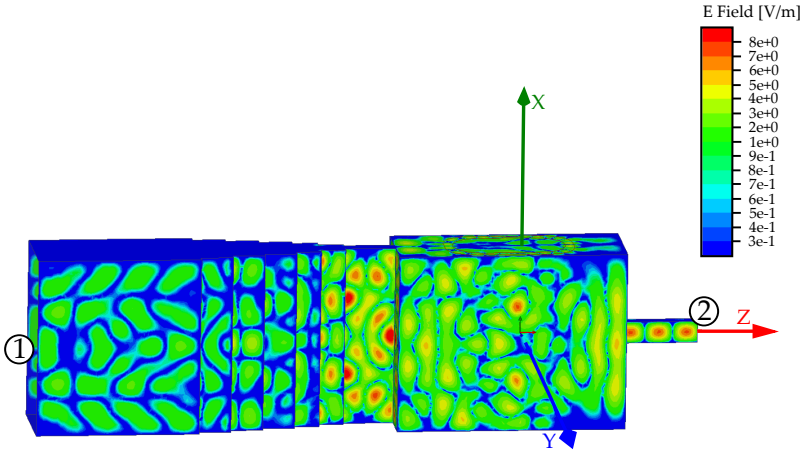

Figure 4.25: Electric field distribution at 220 GHz in the frequency multiplier design.

Figure 4.25 presents the electric field distribution inside the frequency multiplier at the output frequency $f_{out} = 7 \times 32.4 = 220$ GHz. The circuit excitation is a current source of 1 A defined along the multi-layer graphene film. High values of the electric field can be appreciated along the WR3 output waveguide and at some points along the WR28 waveguide taper. However the intensity of the electric field decreases as the electromagnetic wave approaches the WR28 input port. Therefore the 7^{th} order received power at the output port 2 was found around one order of

magnitude higher than the 7^{th} order received power at the input port 1.

4.4.1.2 Prototype fabrication and experimental characterization

For the experimental validation of the frequency multiplier design a prototype of the optimized multi-layer graphene component has been manufactured and it has been assembled into the waveguide block structure from Figure 4.11.

The multi-layer graphene film, integrated in the frequency multiplier structure, is obtained through mechantical exfoliation of a HOPG block. Next, the exfoliated multi-layer graphene film is transferred onto a 25 μm thickness polyimide substrate. Through a laser ablation process, both the polyimide substrate and the multi-layer graphene film are provided with the desired shape. The final obtained multi-layer graphene sample is illustrated in Figure 4.26. Further, the prepared sample is introduced into an external dielectric holder. The sample ends are connected by applying a thin film of silver painting at their intersection (similar to the prototype from Figure 4.13).

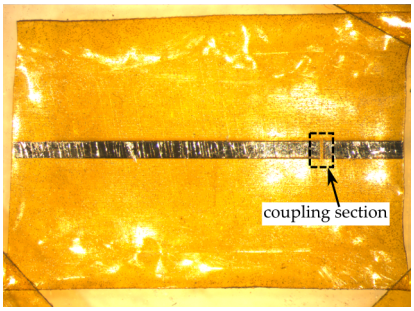

Figure 4.26: Image of the obtained multi-layer graphene sample.

Multiplier performance

All the frequency multipliers presented in this chapter share the same topology of the waveguide block structure. Therefore, the measurement procedure employed for the experimental characterization of the manufactured prototypes is similar with the procedure described in Subsection 4.3.2.3 and with the schematic diagram presented in Figure 4.18.

The behavior of the proposed frequency multiplier has been studied in terms of the power levels received at its output, in the 220-330 GHz frequency range. The obtained data is represented in Figure 4.27 for different values of the input power. From the measured frequency response in Figure 4.24, it can be seen that the circuit

3-dB bandwidth is $BW_{3dB} = 0.85$ GHz and it has the central resonant frequency at $f_{IN} = 34.8$ GHz. This means that the operational output bandwidth of the frequency multiplier prototype for the 7^{th} harmonic order is limited around 6 GHz ($7 \times BW_{3dB}$) with the central frequency at 243.6 GHz ($7 \times f_{IN}$). The measured output response of the frequency multiplier prototype is presented in Figure 4.27, where the 7^{th} order operational bandwidth has been shaded.

The maximum 7^{th} order output power achieved with the presented frequency multiplier topology has been around -72 dBm.

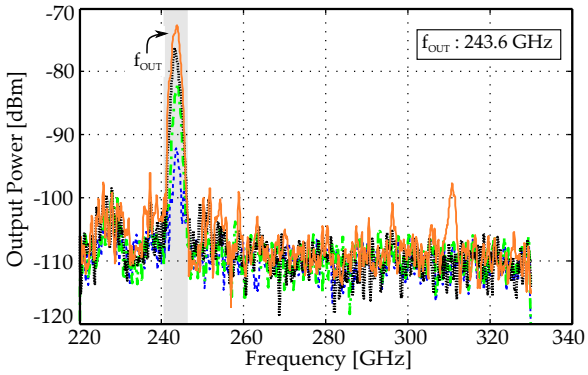

Figure 4.27: Output power of the 7^{th} order harmonic frequency multiplier. Input power considered from 24 to 30 dBm varied in 2 dB steps.

4.4.2 Second multi-layer graphene configuration

4.4.2.1 Design and optimization of the frequency multiplier

The proposed topology of the second multi-layer graphene component is presented in Figure 4.28. The component design differs from the first multi-layer graphene configuration in the way that the location of the coupled lines has been changed to a point with low input field levels in the cavity. Moreover, the geometry of the coupled-line section is chosen so that its response matches the input operation band of the multiplier.

The coupled line sections have been analyzed individually in the K_a band. Figure 4.29 presents the simulated response in terms of the scattering parameters together with the schematic representation of the optimized structure used. As can be seen, the insertion loss between Port 1 and Port 2 in the frequency range from 30 to 32 GHz is below 5 dB ($|S_{21}| > -5$ dB). Outside the mentioned frequency range the attenuation is kept above 10 dB, an exception being the frequency region around 36 GHz, where the value is 6 dB.

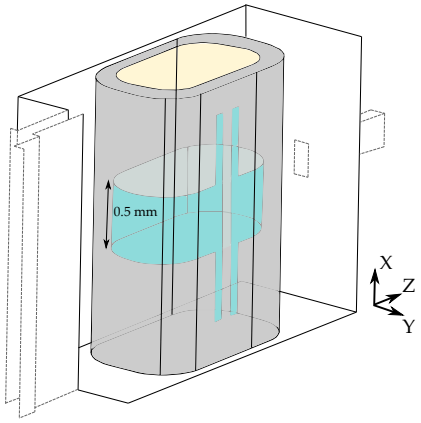

Figure 4.28: Topology of the second multi-layer graphene component.

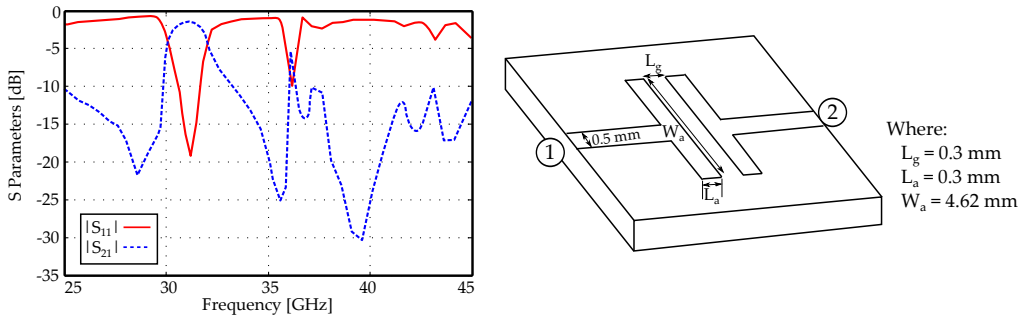

(a) Scattering parameters

(b) Schematic of the coupling section

Figure 4.29: Simulated response of the coupling section.

Furthermore, the coupled line sections wrapped in a dielectric holder were introduced into the design of the frequency multiplier (as presented in Figure 4.28). The whole structure was then simulated in terms of the reflection coefficient at the input port, in the K_a band. The results are represented in Figure 4.30. The circuit presents a frequency response similar with that of the individual coupled line section. It has a resonant frequency response at $f_r = 31.6$ GHz with a 3-dB bandwidth of $BW_{3dB} = 1.22$ GHz. Outside the 3-dB bandwidth the values of the reflexion coefficient are approaching 0 dB, an exception being the frequency region around 26 GHz, where the value is -3.2 dB.

Next, the frequency multiplier design has been analyzed in the submillimeter wave band. The behavior of the circuit is evaluated in terms of the 7^{th} order power received at the output WR3 waveguide and input WR28 waveguide when a current source of an arbitrary value is defined around the graphene film. At the output

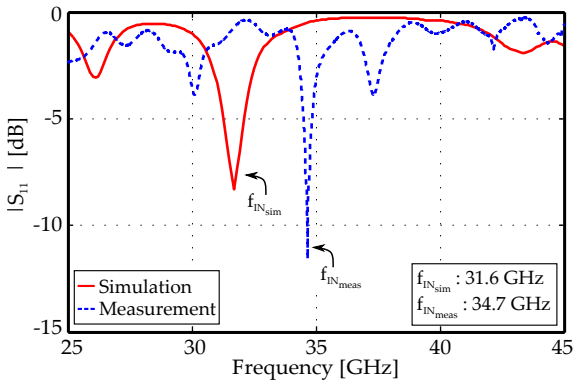

Figure 4.30: Input response of the frequency multiplier.

frequency $f_{out} = 7 \times 31.6$ GHz $= 221$ GHz the 7^{th} order received power at the output port was found around two times higher than the 7^{th} order received power at the input port.

4.4.2.2 Prototype fabrication and experimental characterization

The prototype of the optimized multi-layer graphene component, used to experimentally validate the frequency multiplier design, is presented in Figure 4.31. The multi-layer graphene sample is wrapped in an external dielectric holder and assembled into the waveguide block structure from Figure 4.11 for its measurement.

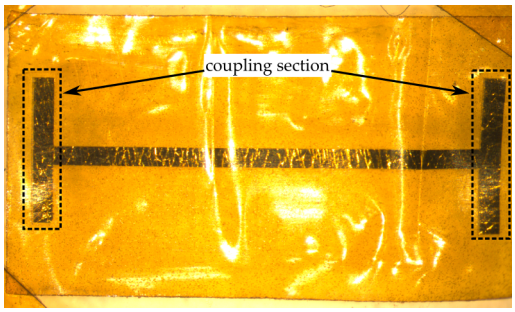

Figure 4.31: Image of the obtained multi-layer graphene sample.

Multiplier performance

The behavior of the proposed multi-layer graphene based frequency multiplier has been analyzed in terms of the converted 7^{th} order power received at the output of the circuit, in the 220-330 GHz band. The measured data, considering different

values of the input power, is represented in Figure 4.32. High levels of the output power have been seen only at specific frequencies within the output band. These frequencies were constrained by the input measured frequency response of the circuit. Therefore a maximum output power around -41 dBm has been achieved at the output frequency f_{out} = 243.2 GHz. The input measured data from Figure 4.30 presents a resonant behavior at f_{INmeas} = 34.7 GHz with values of the return loss greater than 11 dB (f_{out} = 243.2 GHz = 7 × 34.7 GHz). However due to the existence of some parasitic resonances the measured return loss at 30.2 GHz and at 37.3 GHz is greater than 4 dB. As a consequence, the 7^{th} order power levels around 220 GHz respectively around 260 GHz can be observable over the system noise floor in Figure 4.32.

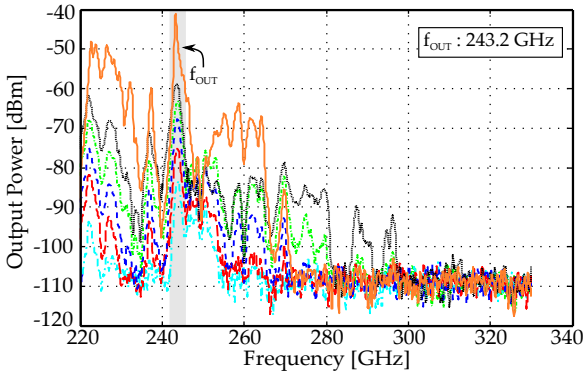

Figure 4.32: Output power of the 7^{th} order harmonic frequency multiplier. Input power considered from 20 to 30 dBm varied in 2 dB steps.

4.4.3 Third multi-layer graphene configuration

4.4.3.1 Design and optimization of the frequency multiplier

The topology of the third multi-layer graphene component proposed in this chapter is presented in Figure 4.33. The component consists of a multi-layer graphene film with two coupling sections. The first coupling section is modeled as a line gap placed along the multi-layer graphene film in an area with high input field levels in the cavity. The second coupling section consist of two parallel conductive plates separated by a 25 μm thickness polyimide substrate. This last section has been designed and analyzed individually in the K_a band. A set of different optimizations were carried out in which the goals were to obtain a wide band and lossless transmission throughout the parallel conductive plates. Figure 4.34 presents the simulated response and the schematic of the final optimized coupler. The circuit presents in-

sertion loss values below 3 dB in the frequency range 25-38 GHz. However, some relatively high value of the insertion loss, $|S_{21}| < -8$ dB, were observed in the upper end of the input analyzed band.

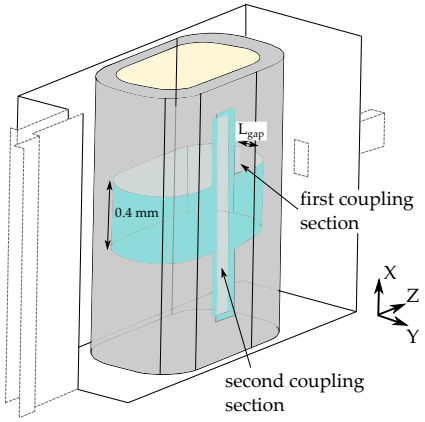

Figure 4.33: Topology of the third multi-layer graphene component.

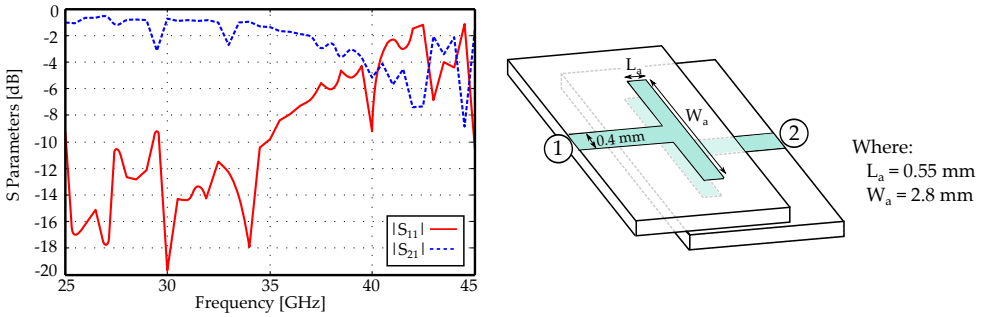

(a) Scattering parameters

(b) Schematic of the coupling section

Figure 4.34: Simulated response of the coupling section.

Next, the complete structure of the frequency multiplier (as presented in Figure 4.33) has been characterized through electromagnetic simulations. The frequency response of the structure for different values of the first coupling lines separation, L_{gap}, has been represented in Figure 4.35. As can be seen, the resonant response of the circuit improves as the separation between the first coupling lines increases. Moreover, a slight upwards frequency shift is also noticed for increased value of L_{gap}. The 3-dB bandwidth at the central resonant frequency of each circuit has been determined from Figure 4.35 (first circuit: $BW_{3dB_{50\mu m}} = 0.9$ GHz at the central frequency 31 GHz, second circuit: $BW_{3dB_{100\mu m}} = 1$ GHz at the central frequency 31.3 GHz, third circuit: $BW_{3dB_{150\mu m}} = 1.05$ GHz at the central frequency 31.4 GHz).

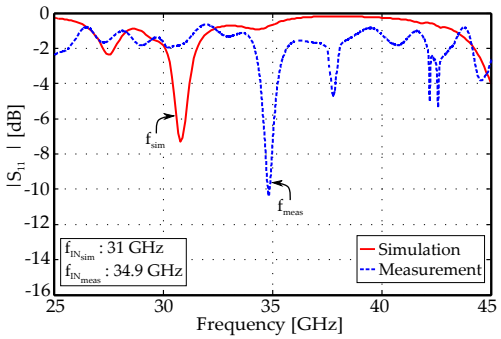

(a) $L_{gap} = 50$ µm

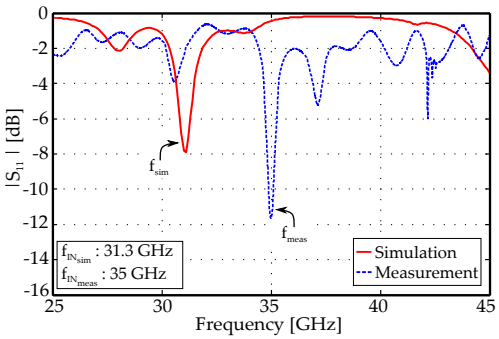

(b) $L_{gap} = 100$ µm

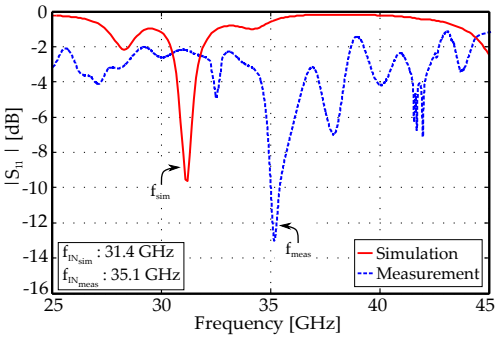

(c) $L_{gap} = 150$ µm

Figure 4.35: Input response of the frequency multiplier.

The characterization of the frequency multiplier behavior is continued with an analysis in the submillimeter wave band. The circuit has been designed to perform the 7^{th} harmonic conversion of an input signal in the K_a band. Towards the goals of constructing a high frequency power efficient multiplier, the 7^{th} order power transmitted at the WR3 output waveguide is simultaneously estimated for all three analyzed circuits in order to determine which configuration best adapts to the need of the circuit. Moreover, in order to test the circuit behavior of high power transmission towards its output, the 7^{th} order power received at the WR3 output waveguide is compared to the power received at the WR28 input waveguide at different frequency points along the 220-330 GHz band. At the output frequency $f_{out} = 7 \times f_{in} = 220$ GHz the relationship between input and output in terms of the 7^{th} order received power was: $P_{7th_{WR3}} = 14 \times P_{7th_{WR28}}$ for the first analyzed circuit, $L_{gap} = 50$ µm, $P_{7th_{WR3}} = 17 \times P_{7th_{WR28}}$ for the second analyzed circuit, $L_{gap} = 100$ µm, and $P_{7th_{WR3}} = 16 \times P_{7th_{WR28}}$ for the third analyzed circuit, $L_{gap} = 150$ µm. The levels of the 7^{th} order received power at the WR3 waveguide were found progressively higher for increased values of L_{gap}. This behavior is expected to be seen

in the measurement process.

4.4.3.2 Prototype fabrication and experimental characterization

For the evaluation of the proposed multi-layer graphene based frequency multiplier, three multi-layer graphene samples, as presented in Figure 4.36, have been manufactured. These samples are assembled into an external dielectric holder and, one at a time, they are mounted into the waveguide block structure from Figure 4.11.

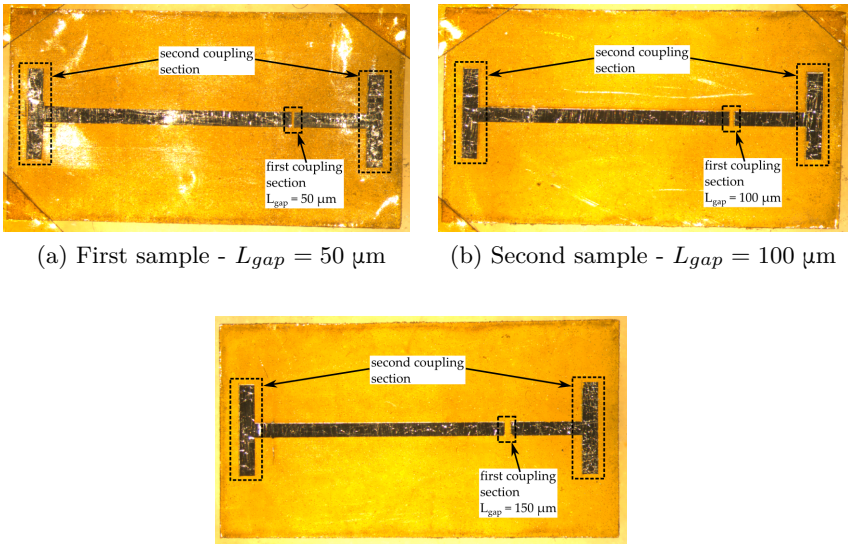

(a) First sample - $L_{gap} = 50$ µm (b) Second sample - $L_{gap} = 100$ µm

(c) Third sample - $L_{gap} = 150$ µm

Figure 4.36: Image of the obtained multi-layer graphene samples.

Multiplier performance

The performance of each 7^{th} order multi-layer graphene based frequency multiplier prototype has been characterized by measuring the output power in the 220-330 GHz frequency band while varying the frequency and the power of the input signal. The measured data is represented in Figure 4.37 for an input power variation from $P_{in} = 18$ to 30 dBm in 2 dB steps. In each case, the input measured frequency response has been represented in Figure 4.35. The slight upwards frequency shift, for increased L_{gap}, seen in simulations has been also observable in measurements. The 3-dB bandwidth at the central resonant frequency of each prototype has been determined (first prototype: $BW_{3dB_{50\mu m}} = 0.9$ GHz at the central frequency 34.9 GHz, second prototype: $BW_{3dB_{100\mu m}} = 0.7$ GHz at the central frequency 35 GHz,

third prototype: $BW_{3dB_{150\mu m}} = 1.75$ GHz at the central frequency 35.1 GHz). The 7^{th} order transformation of each determined input signal, has been shaded in Figure 4.37. The maximum power level achieved with this frequency multiplier topology has been around -68 dBm in the case of the first sample analyzed, -65 dBm in the case of the second sample analyzed and -60 dBm in the case of the third sample analyzed. Seventh order output power has been also noticed in some regions outside the shadowed areas, around 235 GHz and 260 GHz. These transformations were mainly due to some parasitic resonances which can be appreciated at around 33.5 GHz and around 37.1 GHz in the input measured data represented in Figure 4.35.

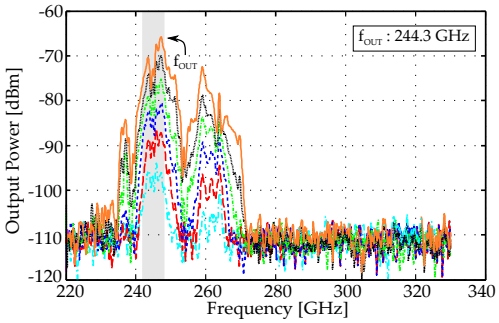

(a) First sample - $L_{gap} = 50$ µm

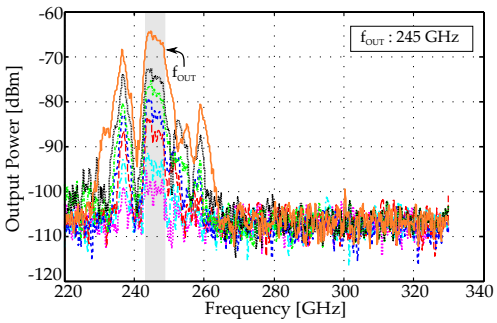

(b) Second sample - $L_{gap} = 100$ µm

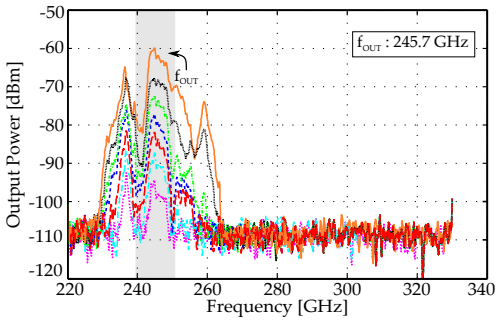

(c) Third sample - $L_{gap} = 150$ µm

Figure 4.37: 7^{th} order output power of the considered frequency multiplier prototypes. Input power varied from 18 to 30 dBm in 2 dB steps.

4.4.4 Fourth multi-layer graphene configuration

4.4.4.1 Design and optimization of the frequency multiplier

The fourth multi-layer graphene component consists in a structure where a multi-layer graphene film is placed on top of a 25 µm thickness polyimide substrate. The

component, as presented in Figure 4.38, is introduced into the resonant cavity of the frequency multiplier. Due to the flexibility of the polyimide substrate, the graphene component takes a semi-elliptical shape inside the cavity. Moreover, it is arranged with the graphene film in direct electrical contact with the narrow rectangular cavity walls and at a distance of 50 μm from the wide cavity wall which is the closest to its curvature. Therefore an electromagnetic coupling effect is produced between the graphene film and the corresponding cavity wall. The total length of the graphene component is 11.7 mm.

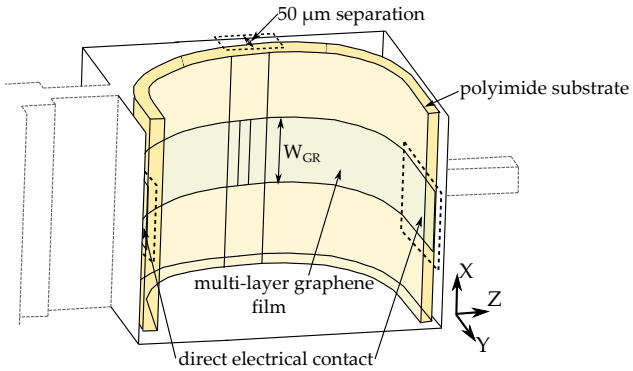

Figure 4.38: Topology of the fourth multi-layer graphene component.

The simulated response of the frequency multiplier in the K_a band is represented in Figure 4.39 for three values of the multi-layer graphene film width, $W_{GR} = 0.2$ mm, $W_{GR} = 0.3$ mm, respectively $W_{GR} = 0.35$ mm. In all three cases, two resonant frequencies with a return loss greater than 10 dB were observed at 27 GHz and around 39.3 GHz. However, as the 7^{th} order conversion of an input signal at $f_r = 27$ GHz results in an output signal out of the 220-330 GHz (WR3 standard) frequency band, $f_{out} = 7 \times f_r = 189$ GHz, this resonance, which actually corresponds to the first resonant cavity mode, will not be considered in the further analysis. Therefore the frequency multiplier behavior is next evaluated considering the frequency response of the second resonant cavity mode (at around $f_r = 39.3$ GHz).

It has been noticed that increasing the width of the multi-layer graphene film, the electromagnetic response of the coupling structure in terms of its resonant frequency response can be shifted upwards in frequency. This effect has been seen in the return loss behavior where the weak resonance obtained at 36.3 GHz in Figure 4.39(a) is shifted to 37.8 GHz in Figure 4.39(b) and ultimately to 38.1 GHz in Figure 4.39(c). Furthermore, due to a constructive interaction between the electromagnetic response of the resonant cavity and that of the coupling structure the 3-dB bandwidth of the frequency multiplier can be enhanced. Therefore, in the case of a multi-layer

graphene film width $W_{GR} = 0.2$ mm the 3-dB bandwidth obtained is $BW_{3dB_{0.2mm}} = 0.5$ GHz. When analyzing the case of a multi-layer graphene film width $W_{GR} = 0.3$ mm the 3-dB bandwidth has increased to $BW_{3dB_{0.3mm}} = 2.4$ GHz. However, for a multi-layer graphene film width $W_{GR} = 0.35$ mm due to a higher upwards frequency shift of the coupler resonant response the total 3-dB bandwidth of the frequency multiplier decreases to $BW_{3dB_{0.35mm}} = 2.2$ GHz.

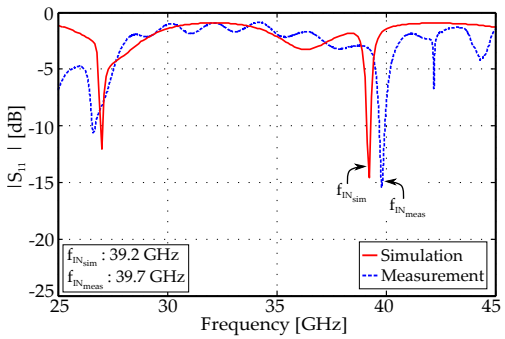

(a) $W_{GR} = 0.2$ mm

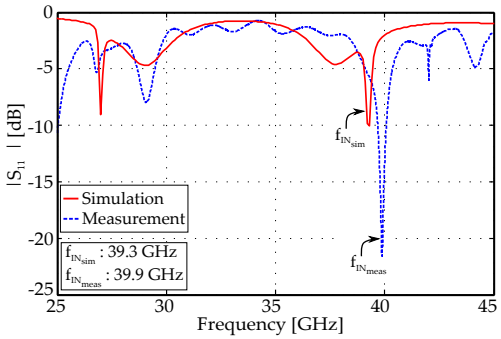

(b) $W_{GR} = 0.3$ mm

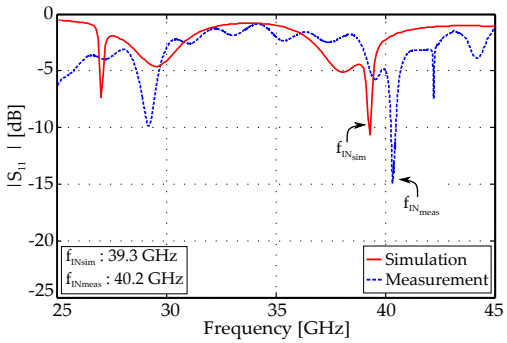

(c) $W_{GR} = 0.35$ mm

Figure 4.39: Input response of the frequency multiplier for different values of the multi-layer graphene film width.

Next, the behavior of the three discussed frequency multiplier configurations has been analyzed in the submillimeter wave band, 220-330 GHz, with regard to the 7^{th} order received power at the circuit output (the WR3 waveguide). For this purpose, a current source has been defined around the multi-layer graphene film for the excitation of the 220-330 GHz signal. The value of the current source is kept constant, 1 A, for all three frequency multiplier configurations. The analysis is conducted at a single output frequency $f_{out} = 7 \times f_{in} = 275$ GHz which corresponds to the 7^{th} order conversion of the circuits central input resonant frequency. Thus,

at the mentioned frequency point, the relationship between the 7^{th} order received power at the output WR3 waveguide and input WR28 waveguide was: $P_{7th_{WR3}} = 6 \times P_{7th_{WR28}}$ for a multi-layer graphene film width $W_{GR} = 0.2$ mm, $P_{7th_{WR3}} = 5 \times P_{7th_{WR28}}$ for a multi-layer graphene film width $W_{GR} = 0.3$ mm, and respectively $P_{7th_{WR3}} = 5.5 \times P_{7th_{WR28}}$ for a multi-layer graphene film width $W_{GR} = 0.35$ mm.

4.4.4.2 Prototype fabrication and experimental characterization

Once the frequency multiplier design has been optimized in the K_a input band and analyzed in the WR3 standard output band, three prototypes of the multi-layer graphene component have been manufactured (Figure 4.40). The components were assembled into the waveguide block (Figure 4.41) for the experimental validation of the proposed topology.

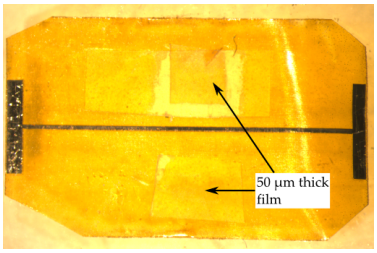

(a) First sample - $W_{GR} = 0.2$ mm

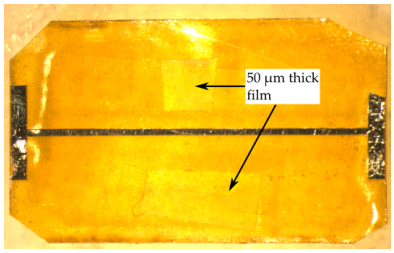

(b) Second sample - $W_{GR} = 0.3$ mm

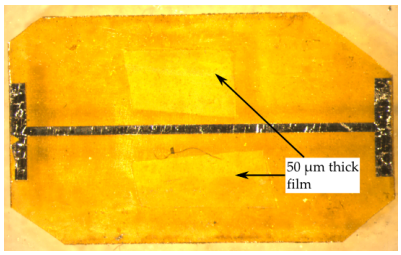

(c) Third sample - $W_{GR} = 0.35$ mm

Figure 4.40: Image of the obtained multi-layer graphene samples.

The two rectangular shaped films which can be appreciated on both side of the multi-layer graphene lines in Figure 4.40 are attached to the 25 µm thickness polyimide substrate in order to control the 50 µm separation of the coupling structure multi-layer graphene - cavity wall. Furthermore, the multi-layer graphene line close to the substrate edges has been widened in order to establish a more reliable electrical contact with the narrow walls of the rectangular cavity in which it is introduced. The four corners of each polyimide substrate were removed as a procedure meant to

ease the assembling process.

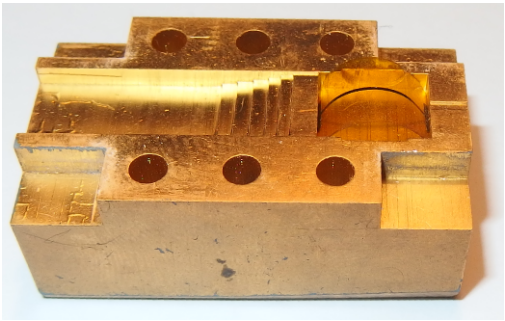

Figure 4.41: Image of a multi-layer graphene sample mounted in its corresponding resonant cavity.

Multiplier performance

The performance of the manufactured prototypes in terms of the generated 7^{th} order power in the 220-330 GHz band is strongly influenced by the input circuit response. In Figure 4.39, the measured input response of each circuit has been represented together with the simulation results. As can be seen, the prototype strongest resonant response has been achieved for a multi-layer graphene film width $W_{GR} = 0.3$ mm where the return loss at the central resonant frequency 39.9 GHz is greater than 21 dB. The 3-dB bandwidth at the central resonant frequency goes from 39 GHz to 40.62 GHz ($BW_{3dB_{0.3mm}} = 1.62$ GHz). The 7^{th} order conversion for that input signal is represented in Figure 4.42(b) where the maximum power level obtained is -34 dBm.

The prototype resonant response of the other two analyzed multi-layer graphene samples, $W_{GR} = 0.2$ mm and $W_{GR} = 0.35$ mm, presents a maximum return loss around 15 dB in both cases. The measured 3-dB bandwidth of the first multi-layer graphene sample, $W_{GR} = 0.2$ mm, at the central frequency 39.7 GHz is $BW_{3dB_{0.2mm}} = 0.9$ GHz while the measured 3-dB bandwidth of the third multi-layer graphene sample, $W_{GR} = 0.35$ mm, at the central frequency 40.2 GHz is $BW_{3dB_{0.35mm}} = 1.62$ GHz. From the 7^{th} order output power represented in Figure 4.42 it can be seen that a wider graphene sample generates a higher output power (maximum output power around -58 dBm in the case of a graphene film width $W_{GR} = 0.2$ mm and around -51 dBm in the case of a graphene film width $W_{GR} = 0.35$ mm).

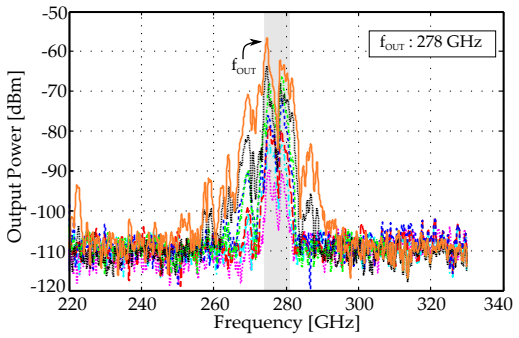

(a) First sample - $W_{GR} = 0.2$ mm

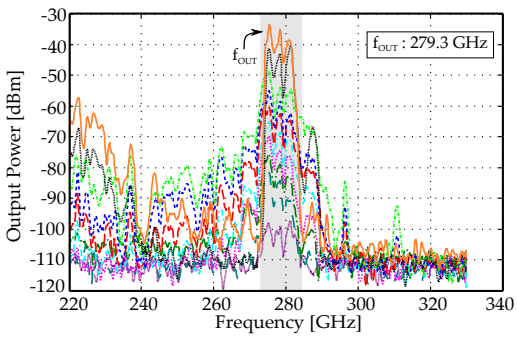

(b) Second sample - $W_{GR} = 0.3$ mm

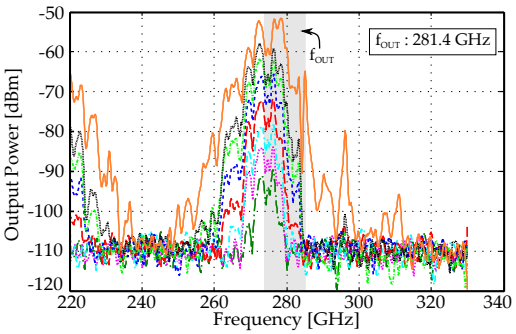

(c) Third sample - $W_{GR} = 0.35$ mm

Figure 4.42: 7^{th} order output power of the considered frequency multiplier prototypes. Input power varied in 2 dB steps with a maximum level of 30 dBm.

4.4.5 Fifth multi-layer graphene configuration

4.4.5.1 Design and optimization of the frequency multiplier

The fifth multi-layer graphene component analyzed in this chapter consists in a 25 μm thickness polyimide substrate with a multi-layer graphene film disposed in a ring shape arrangement. The topology of the frequency multiplier integrating the proposed multi-layer graphene component is illustrated in Figure 4.43.

The geometric pattern of the multi-layer graphene film consists of several rectangular shaped sections connected with a main multi-layer graphene line. The role of the two rectangular shaped sections, which are seen facing one another in the ring shape graphene film arrangement from Figure 4.43, is to establish a solid electrical contact with the cavity side walls. The 150 μm gap present in the middle of one multi-layer graphene line section has been introduced into the design in order to facilitate the fabrication and assembled process of the ring shaped multi-layer

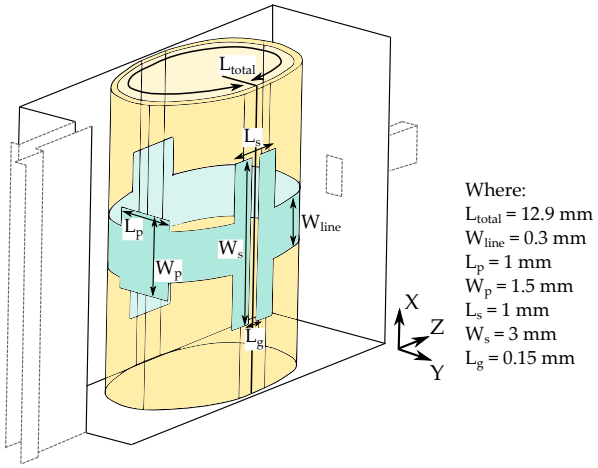

Figure 4.43: Topology of the fifth multi-layer graphene component.

graphene prototype. Furthermore, the third rectangular shaped section has been design to operate as a rectangular patch antenna in terms of high harmonic radiation signal towards the WR3 output waveguide. Different arrangements inside the resonant cavity were tested. One arrangement included the placement of the rectangular patch antenna opposite to its position from Figure 4.43, in the near vicinity of to the WR3 output waveguide. The frequency multiplier design has also been analyzed in a configuration where the rectangular patch antenna is absent. In fact, this configuration is the starting point for the optimization of the proposed frequency multiplier. Therefore, in a first design step, the component position inside the resonant cavity and the geometrical pattern of the multi-layer graphene film, modeled without the rectangular patch antenna, have been determined. Different optimizations were conducted in which circuit features such as a strong input resonant behavior with high input field levels in the cavity were addressed.

The response of the simulated return loss at the input Port 1 is illustrated in Figure 4.44. As can be noticed from the electromagnetic circuit response, a resonant behavior with a return loss greater than 14 dB has been obtained at $f = 43.4$ GHz. The circuit performance in terms of the 3-dB bandwidth is $BW_{3dB_{noPatch}} = 2$ GHz.

Further, the presence of a third rectangular shaped section along the multi-layer graphene film, in the vicinity of the WR28 input waveguide taper, is analyzed in terms of the input circuit resonant response. The simulated return loss in the K_a band is represented in Figure 4.45(a). As can be seen, the circuit resonant frequency is maintained under the same value as in the initial circuit (Figure 4.44). However, the resonant circuit response is stronger (at $f = 43.4$ GHz the return loss is greater

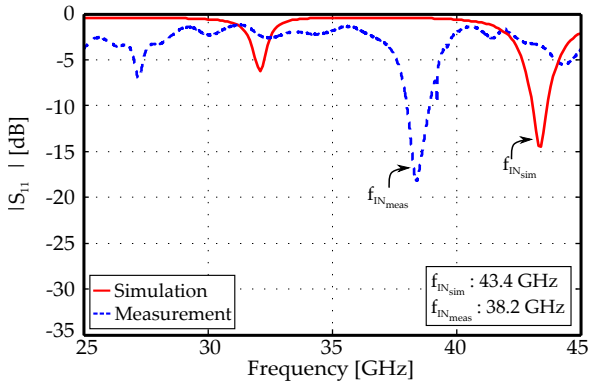

Figure 4.44: Input response of the frequency multiplier - multi-layer graphene line with two rectangular shaped sections.

than 25 dB) while the 3-dB bandwidth is $BW_{3dB_{PatchWR28}} = 2.4$ GHz. As it has been previously mentioned, the rectangular shaped section was designed to operate as a rectangular patch antenna in terms of the 7^{th} order signal radiation towards the WR3 output waveguide. Therefore, the section design has been optimized in the submillimeter wave band. The result of the analysis will be addressed in a further paragraph.

Next, the position of the third rectangular shaped section has been arranged in the near vicinity of the WR3 output waveguide. From the electromagnetic simulation in Figure 4.45(b) it can be seen that the circuit resonant response is analogous to the circuit response from Figure 4.45(a).

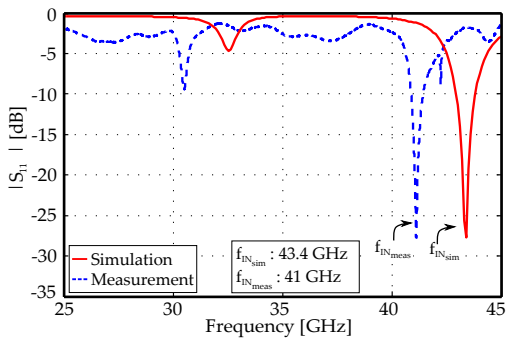

(a) Rectangular patch arranged in the vicinity of WR28 input waveguide

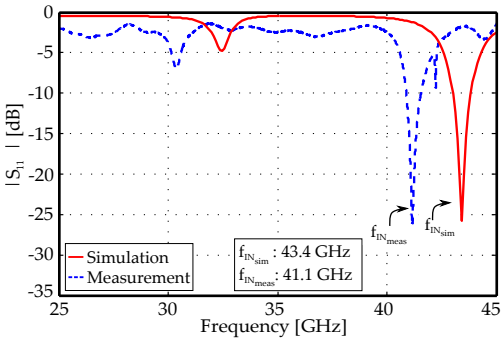

(b) Rectangular patch arranged in the vicinity of WR3 output waveguide

Figure 4.45: Input response of the frequency multiplier - multi-layer graphene line with two rectangular shaped sections and a rectangular patch.

The frequency multiplier design is continued with an optimization of the rectangular patch antenna, the third rectangular shaped graphene section, in the submillimeter wave band. Table 4.8 presents the estimated values of the 7^{th} order received power at the output Port 2, at the termination of the WR3 waveguide, and input Port 1, at the beginning of the WR28 waveguide, when a parametric sweep is launched over the length, L_p, and width, W_p, of the rectangular patch antenna. The multi-layer graphene component studied is arranged in the configuration presented in Figure 4.43. For the excitation of the 7^{th} order signal a current source of 1 A has been defined around the multi-layer graphene film and this value is kept constant during the entire analysis. The output frequency evaluated is $f_{out} = 7 \times f_{in} = 304$ GHz which is the 7^{th} order transformation of the circuit input resonant frequency $f = 43.4$ GHz.

Width W_p [mm]	Length L_p [mm]	Power at Port 2 [W]	Power at Port 1 [W]
1	1.1	1.06e-7	2.08e-7
1	1.3	3e-7	7.4e-7
1	1.5	8e-7	3.6e-7
1	1.7	6.4e-7	4.9e-7
0.8	1.5	6.4e-7	7.7e-7
0.9	1.5	6.6e-7	3.4e-7
1.1	1.5	4.7e-7	2.5e-7

Table 4.8: Estimated values of the 7^{th} order received power at output Port 2 and input Port 1 when sweeping the length and height of the rectangular patch antenna.

According to the results presented in Table 4.8, the longer the rectangular patch length, the higher the transmission of the 7^{th} order power towards the output Port 2. However increasing this parameter over a certain limit, $L_p = 1.7$ mm, has determined a slight reduction of the 7^{th} order transmitted power towards the output Port 2 and it increased the 7^{th} order reflected power at the input Port 1 as compared to the previous analyzed value, $L_p = 1.5$ mm. The optimal values of the rectangular patch antenna are $W_p = 1$ mm and $L_p = 1.5$ mm.

Next, the optimized rectangular patch antenna has been arranged in the vicinity of the WR3 waveguide. For the same output frequency, $f_{out} = 304$ GHz, the levels of the 7^{th} order evaluated power at the circuit output Port 2 were found slightly lower than the values obtained with the previous evaluated design. Finally, the frequency multiplier arrangement with a graphene component consisting of a line with two rectangular shaped sections (rectangular patch antenna absent) is analyzed at the output frequency $f_{out} = 7 \times f_{in} = 304$ GHz. The 7^{th} order received power at the

circuit output Port 2 was found around 2 times higher than the 7^{th} order received power at the circuit input Port 1.

4.4.5.2 Prototype fabrication and experimental characterization

For the experimental validation of the simulated results, prototypes of the two multi-layer graphene components have been manufactured. The multi-layer graphene samples obtained through a laser ablation process are shown in Figure 4.46. These samples have been provided with the desired ring structure by applying a 25 μm thickness polyimide film with adhesive backing at their intersection, in the interior of the created ring. The ring arrangement of the multi-layer graphene component is completed by adding an identical 25 μm thickness polyimide sheet on the bottom side of the multi-layer graphene substrate on the back of the second rectangular shaped graphene section. Figure 4.47 presents an image of the assembled component mounted in the waveguide block.

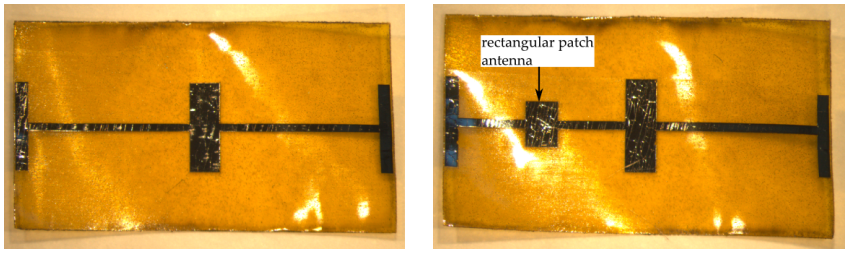

(a) Multi-layer graphene line with two rectangular shaped sections

(b) Complete multi-layer graphene line - rectangular patch antenna included

Figure 4.46: Image of the obtained multi-layer graphene samples.

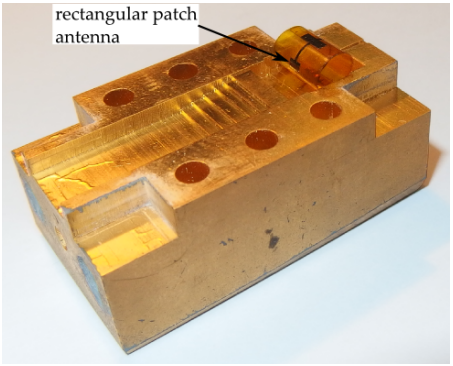

Figure 4.47: Assembled multi-layer graphene component mounted in the waveguide block.

Multiplier performance

In Figure 4.48, the measured results of the frequency multiplier prototype including a multi-layer graphene line sample with two rectangular shaped sections (see Figure 4.46(a)) are represented in terms of the 7^{th} order converted power levels. The shaded area in the frequency range 265.5-267.5 GHz corresponds to a relatively flat output power response with levels around -82 dBm. As can be seen from Figure 4.44, the measured input circuit response in the frequency range 38-38.2 GHz ($38 \times 7 = 265.5$ GHz - $38.2 \times 7 = 267.5$ GHz) presents a return loss greater than 15 dB which indicates a relatively strong circuit resonant behavior.

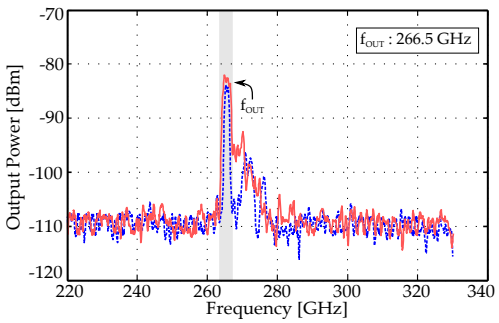

Figure 4.48: 7^{th} order output power of the proposed frequency multiplier prototype including a multi-layer graphene line sample with two rectangular shaped sections. Input power varied from 27 to 28 dBm.

Furthermore, in Figure 4.49, the measured results of the frequency multiplier prototypes which include a multi-layer graphene component with a rectangular patch antenna (see Figure 4.46) are represented in terms of the 7^{th} order converted power levels. The frequency multiplier arrangement where the rectangular patch has been placed in the vicinity of the WR28 waveguide presents a higher input measured resonant response (see Figure 4.45(a)) as compared to the circuit where the rectangular patch has been arranged in the vicinity of the WR3 waveguide (see Figure 4.45(b)). Therefore, the maximum 7^{th} order power achieved with the first circuit arrangement (Figure 4.49(a)) is around -74 dBm while it is about 6 dB lower in the second circuit arrangement (Figure 4.49(b)).

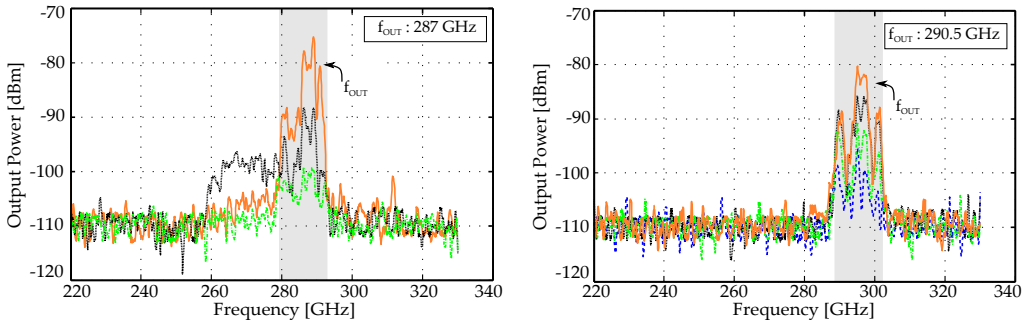

(a) Rectangular patch antenna arranged in the near vicinity of to the WR28 waveguide

(b) Rectangular patch antenna arranged in the near vicinity of to the WR3 waveguide

Figure 4.49: 7^{th} order output power of the proposed frequency multiplier prototype including a multi-layer graphene line sample with two rectangular shaped sections and a patch antenna. Input power varied in 2 dB steps with a maximum level of 30 dBm.

4.4.6 Sixth multi-layer graphene configuration

4.4.6.1 Design and optimization of the frequency multiplier

The topology of the last multi-layer graphene based frequency multiplier proposed in this chapter is presented in Figure 4.50.

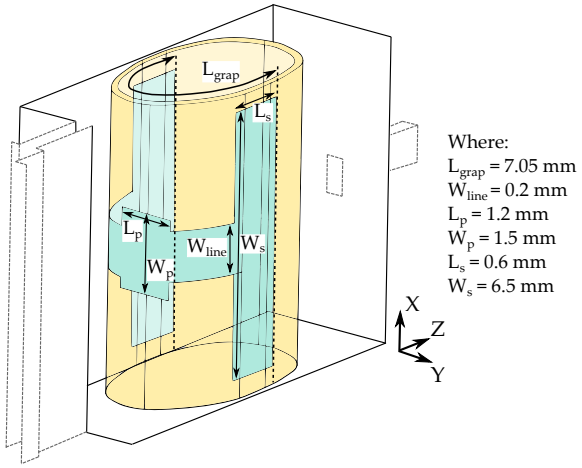

Figure 4.50: Topology of the sixth multi-layer graphene component.

The structure of the multi-layer graphene component is very similar to that described in Subsection 4.4.5. The difference resides in the geometric pattern of the

multi-layer graphene film, designed in this case in a half ring shaped arrangement. The aim of the proposed arrangement is to improve the radiation pattern of the 7^{th} order signal radiated from the multi-layer graphene component by having a more focused beam in the direction towards the WR3 output waveguide.

The frequency multiplier design has been optimized in the input K_a frequency band considering a multi-layer graphene film pattern with two rectangular shaped sections connected with a main multi-layer graphene line. Inside the resonant cavity the multi-layer graphene film is arranged in the vicinity of the WR28 input waveguide taper while having the rectangular shaped sections in contact with the two side walls. Figure 4.51 presents the input simulated response of the frequency multiplier. As can be seen, the circuit presents a resonant response at $f = 41.5$ GHz with a return loss greater than 16 dB. The circuit performance in terms of the 3-dB bandwidth is $BW_{3dB} = 1.8$ GHz.

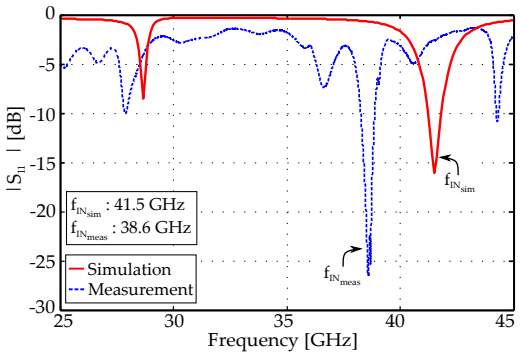

Figure 4.51: Input response of the frequency multiplier - multi-layer graphene line with two rectangular shaped sections arranged in the vicinity of the WR28 waveguide.

Next, a third rectangular shaped section is introduced in the center of the multi-layer graphene film pattern (as presented in Figure 4.50). The electromagnetic behavior of the frequency multiplier has been simulated in the K_a frequency band and the results are represented in Figure 4.52. As can be seen, the circuit resonant frequency is slightly (2.1%) downwards shifted as compared to the previous circuit response while the 3-dB bandwidth is 1.9 GHz. The rectangular shaped section, lately introduced into the multi-layer graphene film pattern, was mainly designed to operate as a rectangular patch antenna in terms of 7^{th} order signal radiation towards the WR3 output waveguide. Thus, the dimensions of the patch antenna have been optimized in the submillimeter wave band (220-330 GHz), in order to achieve an optimal radiation pattern with the main lobe pointing in the direction towards the

output WR3 waveguide while keeping the backwards radiation, towards the input WR28 waveguide, as low as possible.

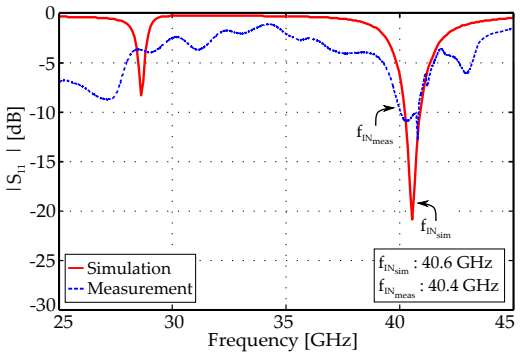

Figure 4.52: Input response of the frequency multiplier - multi-layer graphene line with two rectangular shaped sections and a rectangular patch arranged in the vicinity of the WR28 waveguide.

For the excitation of the frequency multiplier 7^{th} order output signal a current source of 1 A is defined along the multi-layer graphene film. The 7^{th} order power is then evaluated at the output frequency $f_{out} = 7 \times f_{in}$ where f_{in} is the circuit central resonant frequency. The optimized values of the rectangular patch antenna are illustrated in Figure 4.50.

Further, the optimized rectangular patch antenna has been turned around inside the resonant cavity of the frequency multiplier, in the sense that the multi-layer graphene film pattern has been arranged in the vicinity of the WR3 waveguide. The 7^{th} order received power at the WR3 output waveguide was considerably higher in the initial circuit configuration. Figure 4.53 illustrates the electric field patterns concentrated on a drawing plane which has been arranged inside the resonant cavity, at the intersection with the WR3 waveguide. As can be seen, the frequency multiplier configuration presented in Figure 4.53(a) concentrates the radiation beam incoming from the patch antenna in the wanted direction, within the WR3 output waveguide. On the other hand, from the electric field pattern presented in Figure 4.53(b) one can notice a relatively low concentration of the electric field within the WR3 waveguide as the radiation is more confined near the two wide edges of the output waveguide.

Finally, the frequency multiplier arrangement with a multi-layer graphene component consisting of a line with two rectangular shaped sections (rectangular patch antenna absent) is analyzed in the 220-330 GHz frequency band. As in the previous case, a current source of 1 A is defined along the multi-layer graphene film. The multi-layer graphene component inside the frequency multiplier resonant cavity has

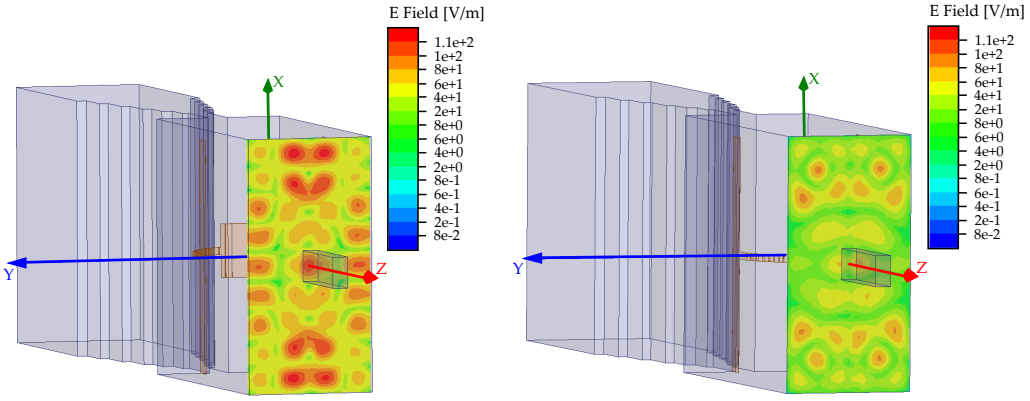

(a) Rectangular patch antenna arranged in the vicinity of the WR28 waveguide

(b) Rectangular patch antenna arranged in the vicinity of the WR3 waveguide

Figure 4.53: Electric field patterns at $f_{out} = 284$ GHz.

been arranged in the vicinity of the WR28 waveguide respectively WR3 waveguide. The 7^{th} order power is then evaluated at the output frequency $f_{out} = 7 \times f_{in}$ (f_{in} is the circuit central resonant frequency taken from the input response). Therefore, the 7^{th} order received power at the frequency multiplier WR3 output waveguide was considerably higher in the configuration with the multi-layer graphene film arranged in the vicinity of the WR28 waveguide. The electric field patterns concentrated on a drawing plane arranged at the intersection between the cavity wall and the WR3 waveguide are illustrated in Figure 4.54. It can be seen that the field patterns are consistent with the field patterns from Figure 4.53.

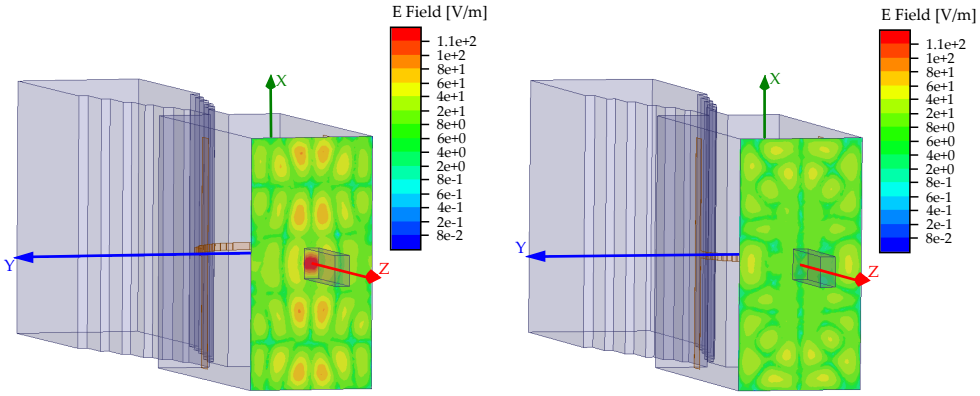

(a) Multi-layer graphene film arranged in the vicinity of the WR28 waveguide

(b) Multi-layer graphene film arranged in the vicinity of the WR3 waveguide

Figure 4.54: Electric field patterns at $f_{out} = 290.5$ GHz.

4.4.6.2 Prototype fabrication and experimental characterization

In order to experimentally validate the proposed frequency multiplier design, prototypes of the two multi-layer graphene components have been manufactured. Figure 4.55 shows an image of the obtained multi-layer graphene samples. The final ring shaped arrangement of these samples has been obtained by applying a 25 μm thickness polyimide film with adhesive backing at their intersection. The assembled multi-layer graphene components are then mounted, one at a time, inside the manufactured waveguide block from Figure 4.11. The arrangement of the multi-layer graphene film inside the resonant cavity has been considered in the vicinity of the WR28 waveguide.

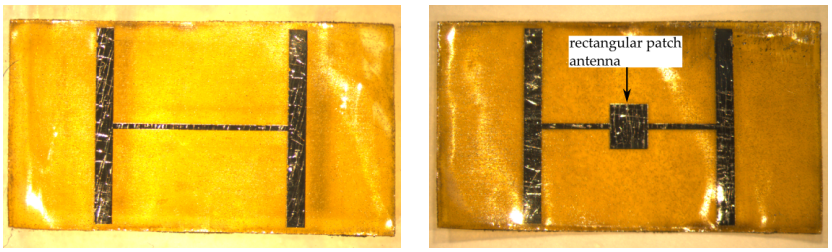

(a) Multi-layer graphene line with two rectangular shaped sections

(b) Complete multi-layer graphene line - rectangular patch antenna included

Figure 4.55: Image of the implemented multi-layer graphene component.

Multiplier performance

In order to experimentally evaluate the behavior of the proposed multi-layer graphene based frequency multiplier, the 7^{th} order received power at the output of the two assembled prototypes has been measured. Figure 4.56 presents the measured output results of the frequency multiplier prototypes including the multi-layer graphene sample shown in Figure 4.55(a). As can be seen from the input measured circuit response represented in Figure 4.51, the prototype presents a strong resonant behavior at 38.6 GHz with a return loss greater than 26 dB. The measured 3-dB bandwidth at the central frequency 38.6 GHz goes from 38 GHz to 39.2 GHz. The 7^{th} order transformation of the input signal is limited between 266 GHz and 274.4 GHz. This frequency range has been shaded in Figure 4.56. However, as the return loss in Figure 4.56 at around 36.5 GHz and around 40.6 GHz is greater than 7.5 dB respectively 5 dB, the 7^{th} order power levels at 255.5 GHz and 284.2 GHz are still observable over the system noise floor. The maximum power level achieved with this

configuration is around -54 dBm.

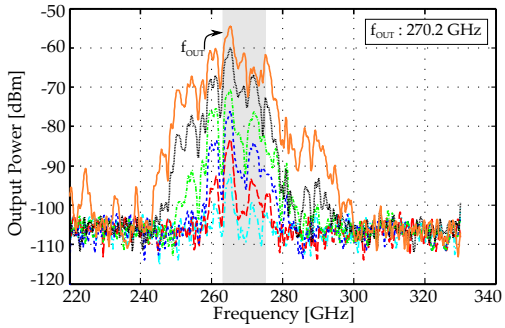

Figure 4.56: 7^{th} order output power of the proposed frequency multiplier prototype including a multi-layer graphene line sample with two rectangular shaped sections. Input power varied from 18 to 28 dBm in 2 dB steps.

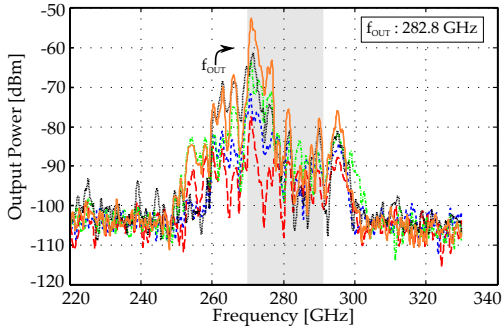

Figure 4.57: 7^{th} order output power of the proposed frequency multiplier prototype including a multi-layer graphene line sample with two rectangular shaped sections and a patch antenna. Input power varied from 20 to 28 dBm in 2 dB steps.

Furthermore, Figure 4.57 presents the measured output results of the frequency multiplier prototype including the multi-layer graphene sample shown in Figure 4.55(b). From the input measured circuit response in Figure 4.52, one can notice that the prototype presents a resonant behavior at 40.4 GHz with a return loss about 11 dB. The measured 3-dB bandwidth at the central frequency 40.4 GHz goes from 38.9 GHz to 41.6 GHz. The 7^{th} order transformation of the input signal in the frequency range $38.9 - 41.6$ GHz has been shaded in Figure 4.57. The maximum power level achieved with this configuration is around -53 dBm which is only 1 dB higher than the maximum output power level achieved with the previous frequency multiplier configuration (see Figure 4.56). Nonetheless, the measured input response of the current configuration was considerably lower (return loss around 11 dB at 40.4

GHz) as compared to the previous configuration (return loss around 26 dB at 38.6 GHz).

4.5 Conclusions

The design of several 7^{th} order Single Stage Frequency Multipliers based on a resonant cavity integrating graphene layers have been presented. The implementation was based on a new frequency multiplier topology in which graphene sheets were placed inside a resonant cavity so that they were exposed to high electric field levels. The proposed topology evaluates the non-linear electromagnetic response of both mono/bilayer graphene films as well as exfoliated HOPG graphite flakes for the generation of output content in the 220-330 GHz frequency band. All proposed graphene based frequency multipliers have been manufactured and experimentally characterized. The 7^{th} order output power as a function of frequency has been analyzed for different values of the applied input power in the K_a band and shortly above 40 GHz.

The monolayer and bilayer graphene based frequency multiplier show a relatively similar behavior in terms of the measured output power levels ($P_{out_{monolayer}} \approx -93.5$ dBm respectively $P_{out_{bilayer}} \approx -94$ dBm when the input power delivered was $P_{in} =$ 33 dBm). However, the measured resonant response of the monolayer prototype was slightly stronger (return loss at 42.2 GHz greater than -11 dB) as compared to the resonant response of the bilayer prototype (return loss at 42.9 GHz greater than -9 dB). Therefore, the monolayer film, inside the resonant cavity, was irradiated with higher electric field levels than the bilayer film which has determined the generation of a slightly comparable 7^{th} order current in the two samples analyzed. The 7^{th} order output content was not measured directly on the graphene component but it was measured at the output of the WR3 waveguide from the frequency multiplier. Therefore, the frequency multiplier configuration had to ensure a good output signal radiation in the direction towards the WR3 output waveguide.

Furthermore, in order to enhance the resonant response of the rectangular cavity as well as the radiation characteristics of the high harmonic multiplied signal towards the frequency multiplier output six multi-layer graphene (graphite) components have been implemented and placed inside the resonant cavity of the frequency multiplier. For an applied input power of $P_{in} = 30$ dBm the maximum 7^{th} order output power reached with the multi-layer graphene based frequency multiplier prototypes has been around $P_{out} \approx -34$ dBm.

Therefore, the groundbreaking single stage frequency multiplier topology has validated the implementation of a high order frequency multiplier, which can be

implemented with mono/bilayer graphene film as well as exfoliated HOPG graphite flakes, for the generation of signals in the submillimeter wave band.

Bibliography

[1] D. A. Hill, "Electromagnetic Fields in Cavities: Deterministic and Statistical Theories," John Wiley & Sons, Inc., Hoboken, New Jersey, 2009.

[2] A. Li, E. Forati and D. Sievenpiper, "Study of the Electric Field Enhancement of High-Impedance Surfaces," 2016 IEEE International Symposium on Antennas and Propagation (APSURSI), October 2016.

[3] P. A. Bernhardt and R. F. Fernsler, "Electric Field Amplification inside a Porous Spherical Cavity Resonator Excited by an External Plane Wave," IEEE Transactions on Antennas and Propagation, Vol. 60, No. 2, pp. 832-839, February 2012.

[4] S. A. Mikhailov, "Non-linear electromagnetic response of graphene, " EPL 79, 27002-pl, 2007.

[5] S. A. Mikhailov and K. Ziegler, "Non-linear electromagnetic response of graphene: Frequency multiplication and the self-conistent-field effects," J. Phys. Condens. Matter 20, 384204, 2008.

[6] S. A. Mikhailov, "Quantum theory of third-harmonic generation in graphene," Phys Rev. B 90, 241301(R), 2014.

[7] A. Hadarig, S. Ver Hoeye, C. Vázquez, R. Camblor, M. Fernández, G. R. Hotopan, L. Alonso and F. Las Heras, "3D Printed Millimeter Wave Receiver Integrating a Graphene Subharmonic Mixer and a Diagonal Horn Antenna, " Global Symposium On Millimeter Waves (GSMM) 2015, Montreal, Quebec, May 2015.

[8] C. Vázquez, A. Hadarig, S. Ver Hoeye, R. Camblor, M. Fernández, G. Hotopan, L. Alonso and F. Las Heras, "Millimetre Wave Receiver Based on a Few-Layer Graphene WR5 Band Subharmonic Mixer," Global Symposium On Millimeter Waves (GSMM) 2015, Montreal, Quebec, May 2015.

[9] C. Vázquez, A. Hadarig, S. Ver Hoeye, R. Camblor, M. Fernández, G. Hotopan, L. Alonso and F. Las Heras, "Millimetre Wave Transmitter Based on a Few-Layer Graphene Frequency Multiplier", 2015 European Microwave Week, Paris, France, September 2015.

[10] Ansoft HFSS Field Calculator Cookbook, 2000 Ansoft Corporation, Pittsburgh, PA, 2000.

[11] Ansoft Field Calculator Cookbook, 2012 SAS IP Inc., Ansys, Canonsburg, PA, 2012.

[12] A. I. Hadarig, C. Vázquez, M. Fernández , S. Ver Hoeye, G. R. Hotopan, R. Camblor, F. Las Heras, "Experimental analysis of the high-order harmonic components generation in few-layer graphene, " Applied Physics A, vol. 118, Issue 1, pp. 82 - 89, January 2015.

[13] C. Vazquez, A. Hadarig, S. Ver Hoeye, M. Garcia, R. Camblor, G. Hotopan, and F. Las Heras, "High Order Subharmonic Millimeter Wave Mixer based on Few Layer Graphene," IEEE Transactions on Microwave Theory and Techniques, Vol. 63, Issue 4, 1361-1369, 2015.

General Conclusions

In this Doctoral Thesis the analysis, optimization and experimental characterization of passive devices with non-linear harmonic content based on mono- and multi-layer graphene operating in the submillimeter wave/THz frequency band have been presented. Moreover, the non-linear electromagnetic behavior of graphene, based on its electronic band structure, for the generation of the high harmonic components that enable the frequency mixing and multiplication effects has been rigorously investigated.

The first topology proposed and analyzed in this Thesis is a Single Stage High Order Submillimeter Wave/THz band Graphene based Frequency Multiplier. Three multiplier devices have been implemented using the discussed topology. The main application of these circuits is the generation of submillimeter wave/low THz band signals for imaging applications, as the fundamental blocks in complete transmission systems. Because the output signal of the circuits is a high harmonic component, $N = 5$ to 17, of the input K_a signal generated in a multi-layer graphene film, the circuits have been designed and optimized to provide a high-amplitude output signal in the frequency band 140-500 GHz. The designs were validated by experimental results obtained through the fabrication and measurement of three prototypes. Both even and odd order harmonic components have been seen at the output of the measured prototypes. The amplitude of the odd order harmonic components was found constantly higher and with a flat frequency response as compared to the even order content generated. For a maximum input power limited to $P_{in} = 24$ dBm a peak output power around -34 dBm has been obtained at 252 GHz considering graphene's 7^{th} order harmonic. This value is nearly comparable with the state of the art, where the implementations with similar harmonic component operate at output frequencies up to 70 GHz.

Starting from the topology of the Single Stage High Order Submillimeter Wave/THz band Graphene based Frequency Multiplier, a mixing topology has been designed and experimentally validated. The circuits have been analyzed considering the up- and downconverted output power obtained for different even harmonic orders,

$M = 6$ to 18. The maximum upconverted power achieved, -44.1 dBm (-56 dBm conversion gain), and the maximum downconverted power achieved, -73.7 dBm (-53 dBm conversion gain), have been both obtained at 347 GHz and they correspond to the 8^{th} harmonic order of the LO signal, the 7^{th} intermodulation product of the two input signals irradiating the multi-layer graphene film. Nonetheless, frequency mixing effect has been seen along the whole analyzed 140 to 500 GHz band where the response for the different harmonic orders was limited by the impedance matching characteristics of the LO signal.

In addition, a complete transmitter-receiver sub-system having the RF signal in the 140-220 GHz band has been assembled and tested. The receiver presented a dynamic range, according to the transmitter-receiver configuration used, between 20 and 45 dB.

The last topology proposed and analyzed in this Thesis is a 7^{th} order Single Stage Frequency Multiplier based on a Resonant Cavity integrating Graphene Layers. The influence of several graphene components on the high harmonic signal generation and signal radiation towards the frequency multiplier output has been analyzed through electromagnetic simulations, and experimentally demonstrated, through the measurement of the prototypes. The analysis revealed that starting from the first design of a frequency multiplier containing a monolayer graphene film component, the multi-layer graphene components which presented stronger input resonant response and harmonic conversion on multiple graphene layers have helped increasing the output power levels measured at the output of the multiplier device. Therefore, the maximum output power conceived with the monolayer graphene frequency multiplier has been $P_{out} = -93.5$ dBm (maximum input power applied $P_{in} = 33$ dBm) while it was around 60 dB higher ($P_{out} = -34$ dBm - maximum input power applied $P_{in} = 30$ dBm) in a multi-layer graphene frequency multiplier.

Therefore, the developed assemblies present a proof of concept which confirm that mono-/multi-layer graphene can be used by itself as a signal generator and/or detector, based on multiplication or mixing, in the submillimeter/low THz band.

List of Publications

Publications Directly Originated by the Doctoral Thesis

International Journal Papers

[1] **A.I. Hadarig**, C. Vazquez, M. Fernandez, S. Ver-Hoeye, G.R. Hotopan, R. Camblor and F. Las Heras: "Experimental analysis of the high order harmonic components generation in few-later graphene," Appl. Phys. A (2015) 118: 83. doi:10.1007/s00339-014-8739-y.

[2] C.V. Antuña, **A.I. Hadarig**, S. Ver Hoeye, M.F. Garcia, R.C. Diaz, G.R. Hotopan and F. Las Heras: "High-Order Subharmonic Millimeter-Wave Mixer Based on Few-Layer Graphene," IEEE Transactions on Microwave Theory and Techniques 63 (4), 1361-1369, 2015.

[3] G.R. Hotopan, S. Ver-Hoeye, C. Vazquez-Antuna, **A. Hadarig**, R. Camblor-Diaz, M. Fernandez-Garcia, and F. Las Heras Andres: "Millimeter wave subharmonic mixer implementation using graphene film coating," Progress In Electromagnetics Research 140, 781-794, 2013.

International Conference Papers

[1] C. Vazquez, **A. Hadarig**, S. Ver Hoeye, , R. Camblor, M. Fernandez, G. Hotopan, L. Alonso and F. Las Heras, "Millimetre Wave Transmitter Based on a Few-Layer Graphene Frequency Multiplier", European Microwave Week, Paris, France, September 6-11, 2015

[2] **A. Hadarig**, S. Ver Hoeye, C. Vazquez, R. Camblor, M. Fernandez, G. Hotopan, L. Alonso and F. Las Heras, "3D Printed Millimeter Wave Receiver Integrating a Graphene Subharmonic Mixer and a Diagonal Horn Antenna", Global Symposium on Millimeter-Wave, GSMM, Montreal, Quebec, Canada, May 25-27, 2015

[3] C. Vazquez, **A. Hadarig**, S. Ver Hoeye, R. Camblor, M. Fernandez, G. Hotopan, L. Alonso and F. Las Heras, "Millimetre Wave Receiver

Based on a Few-Layer Graphene WR5 Band Subharmonic Mixer", Global Symposium on Millimeter-Wave, GSMM, Montreal, Quebec, Canada, May 25-27, 2015

[4] **A. Hadarig**, S. Ver Hoeye, C. Vazquez, M. Fernandez, G. Hotopan, R. Camblor and F. Las Heras: "7th Order Sub-Millimeter Wave Frequency Multiplier Based On Graphene Implemented Using a Microstrip Transition Between Two Rectangular Waveguides," International Conference on Electromagnetics in Advanced Applications, ICEAA, Palm Beach, Aruba, August 3-9, 2014.

[5] C. Vazquez, R. Camblor, S. Ver Hoeye, **A. Hadarig**, G. Hotopan, M. Fernandez and F. Las Heras, "Millimetre Wave Imaging System for the Detection of Hidden Elements in Artwork", International Conference on Electromagnetics in Advanced Applications, ICEAA, Palm Beach, Aruba, August 3-9, 2014.

[6] **A. Hadarig**, S. Ver Hoeye, C. Vazquez, M. Fernandez, G. Hotopan, R. Camblor and F. Las Heras: "High Order Harmonic Frequency Multiplier Based in Graphene," "10 years from the discovery of graphene" Summer School, Patras, Greece, July 14-18, 2014.

[7] C. Vazquez, **A. Hadarig**, S. Ver Hoeye, M. Fernandez, R. Camblor, G. Hotopan and F. Las-Heras,"Millimeter Wave Subharmonic Mixer Based on Graphene," 2014 International Telecommunications Symposium, ITS, São Paulo, Brasil, August 17-20, 2014.

National Conference Papers

[1] **A. Hadarig**, S. Ver Hoeye, C. Vazquez, M. Fernandez, G. Hotopan, R. Camblor and F. Las Heras: "Multiplicador de Frecuencia Submilimetrico de Orden 7 Basado en Grafeno," XXIX Simposium Nacional de la Union Cientifica Internacional de Radio, URSI, Valencia, September 3-5, 2014.

Other Publications

International Journal Papers

[1] Y. Alvarez, R. Camblor, C. Garcia, J. Laviada, C. Vazquez, S. Ver-Hoeye, G. Hotopan, M. Fernandez, **A. Hadarig**, A. Arboleya, F. Las-Heras: "Submillimeter-wave frequency scanning system for imaging applications, " IEEE Transactions on Antennas and Propagation 61 (11), 5689-5696, 2013.

International Conference Papers

[1] L. Alonso, S. Ver Hoeye, M. Fernandez, C. Vazquez, R. Camblor, G. Hotopan, **A. Hadarig**, and F. Las Heras, "Millimetre Wave Textile Integrated Waveguide Beamforming Antenna for Radar Applications", Global Symposium on Millimeter-Wave, GSMM, Montreal, Quebec, Canada, May 25-27, 2015

[2] R. Camblor, S. Ver Hoeye, C. Vazquez, G. Hotopan, M. Fernandez, **A. Hadarig** and F. Las-Heras, "Frequency scanning slotted waveguide in the sub-millimeter wave band", International Conference on Electromagnetics in Advanced Applications, ICEAA, Palm Beach, Aruba, August 3-9, 2014.

[3] R. Camblor, S. Ver Hoeye, C. Vazquez, G. Hotopan, M. Fernandez, **A. Hadarig** and F. Las-Heras, "Sub-millimeter wave imaging system based on frequency scanning antenna", International Conference on Electromagnetics in Advanced Applications, ICEAA, Palm Beach, Aruba, August 3-9, 2014.

[4] R. Camblor, S. Ver Hoeye, C. Vazquez, G.R. Hotopan, M. Fernandez, **A. Hadarig** and F. Las-Heras: "Submillimeter Wave 8×1 Antenna Array With Dielectric Rods to Improve the Radiation Pattern," European Microwave Week, Nuremberg, Germany, October 9-11, 2013.

[5] N. Campos, A. Perez-Mas, P. Alvarez, A. Menendez, D. Gomez, C. Vazquez, **A. Hadarig**, S. Ver Hoeye, A.L. Elias, M. Terrones, M. Fernandez, R. Camblor, G. Hotopan, F. Las Heras, R. Menendez: "A comparison of the performance of micro- and nanosecond laser in micropattering of grapheme films," Graphene Week 2013, Chemnitz, Germany, June 2-7, 2013.

[6] N. Campos, A. Perez-Mas, P. Alvarez, D. Gomez, C. Vazquez, **A. Hadarig**, S. Ver Hoeye, A.L. Elias, M. Terrones, M. Fernandez, R. Camblor, G. Hotopan, F. Las Heras, R. Menendez: "Selective removal of graphene by means of micro- and nanosecond laser irradiation," Imaginenano 2013, Bilbao, Spain, April 23-26, 2013.

National Conference Papers

[1] L. Alonso, S. Ver Hoeye, C. Vazquez, M. Fernandez, **A. Hadarig**, and F. Las Heras, "Textile Integrated Waveguide Cavity-Backed Slot Antenna for 5G Wearable Applications," XXXI Simposium Nacional de la Union Cientifica Internacional de Radio, URSI, Madrid, September 5-7, 2016.

Appendix A

Dispersion relation. Transfer matrix H.

The expression of the Hamiltonian H_{AB} will be calculated for small variations of the wave vector $\overrightarrow{k}$ thus:

$$h(k) = h(K+q) = h(K'+q) = -i\gamma_0 \cdot \sum_j e^{-iK\overrightarrow{b_j}} q\overrightarrow{b_j} \tag{A.1}$$

Inserting the values of the vector points b_j (see Eq. 1.3) in the above equation one obtains:

$$\begin{aligned}
h(k) =& -i\gamma_0 \left[e^{-i\frac{a}{\sqrt{3}}K_y} \cdot \frac{a}{\sqrt{3}} q_y + e^{-i\left(\frac{a}{2}K_x - \frac{a}{2\sqrt{3}}K_y\right)} \left(\frac{a}{2}q_x - \frac{a}{2\sqrt{3}}q_y\right) \right. \\
& \left. + e^{-i\left(-\frac{a}{2}K_x - \frac{a}{2\sqrt{3}}K_y\right)} \left(-\frac{a}{2}q_x - \frac{a}{2\sqrt{3}}q_y\right) \right] \\
=& -i\gamma_0 \left[\frac{a}{\sqrt{3}} q_y \cdot e^{-i\frac{a}{\sqrt{3}}K_y} + \frac{a}{2}q_x \cdot e^{i\frac{a}{2\sqrt{3}}K_y} \left(e^{-i\frac{a}{2}K_x} - e^{i\frac{a}{2}K_x}\right) \right. \\
& \left. - \frac{a}{2\sqrt{3}} q_y e^{i\frac{a}{2\sqrt{3}}K_y} \left(e^{-i\frac{a}{2}K_x} + e^{i\frac{a}{2}K_x}\right) \right] \\
=& -i\gamma_0 \left[\frac{a}{\sqrt{3}} q_y e^{-i\frac{a}{\sqrt{3}}K_y} - 2i \sin\left(\frac{a}{2}K_x\right) \frac{a}{2} q_x e^{i\frac{a}{2\sqrt{3}}K_y} \right. \\
& \left. - 2\cos\left(\frac{a}{2}K_x\right) \frac{a}{2\sqrt{3}} q_y e^{i\frac{a}{2\sqrt{3}}K_y} \right]
\end{aligned} \tag{A.2}$$

At the Dirac point K of value $(k_x, k_y) = \left(-\frac{4\pi}{3a}, 0\right)$ the above expression of the

Hamiltonian becomes:

$$\begin{aligned} h(k) = h\left(K+q\right) =& -i\gamma_0\left[\frac{a}{\sqrt{3}}q_y + 2i\sin\left(\frac{2\pi}{3}\right)\frac{a}{2}q_x - 2\cos\left(\frac{2\pi}{3}\right)\frac{a}{2\sqrt{3}}q_y\right] \\ =& -\frac{a\sqrt{3}}{2}\gamma_0\left(-q_x + iq_y\right) \end{aligned} \tag{A.3}$$

Moreover, at the Dirac point K' of value $(k_x, k_y) = \left(\frac{4\pi}{3a}, 0\right)$ the expression of the Hamiltonian becomes:

$$\begin{aligned} h(k) = h\left(K'+q\right) =& -i\gamma_0\left[\frac{a}{\sqrt{3}}q_y - 2i\sin\left(\frac{2\pi}{3}\right)\frac{a}{2}q_x - 2\cos\left(\frac{2\pi}{3}\right)\frac{a}{2\sqrt{3}}q_y\right] \\ =& -\frac{a\sqrt{3}}{2}\gamma_0\left(q_x + iq_y\right) \end{aligned} \tag{A.4}$$

Appendix B

Charge carrier density

The expression of the graphene charge carrier density as presented in Subsection 1.4 is:

$$n_s = \frac{g_s g_v}{S} \cdot \frac{S}{(2\pi\hbar)^2} \iint dp_x dp_y f_p(t) \tag{B.1}$$

The momentum distribution function of electrons $f_p(t)$ at absolute zero temperature becomes the Heaviside Step Function $\theta\left[p_F^2 - (p_x - p_0(t))^2 - p_y^2\right]$ therefore the limits of the above charge carrier density when working with polar coordinates (for ease of understanding see Figure B.1) are:

$$\begin{aligned} p_F^2 - (p_x - p_0(t))^2 - p_y^2 = 0 \Rightarrow & p_x = p_0(t) \pm \sqrt{p_F^2 - p_y^2} \\ & p_y = \pm p_F \end{aligned} \tag{B.2}$$

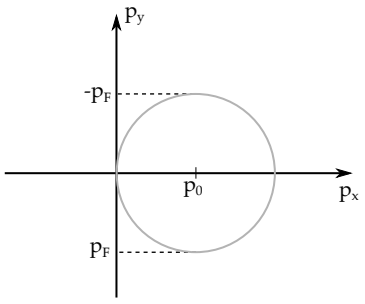

Figure B.1: The Heaviside Step Function $\theta\left[p_F^2 - (p_x - p_0(t))^2 - p_y^2\right]$ in polar coordinates.

Thus, the charge carrier density can be rewritten as:

$$\begin{aligned} n_s =& \frac{g_s g_v}{(2\pi\hbar)^2} \int_{-p_F}^{p_F} dp_y \int_{p_0(t)-\sqrt{p_F^2-p_y^2}}^{p_0(t)+\sqrt{p_F^2-p_y^2}} dp_x \\ =& \frac{g_s g_v}{(2\pi\hbar)^2} \int_{-p_F}^{p_F} dp_y \left[p_0(t) + \sqrt{p_F^2-p_y^2} - p_0(t) + \sqrt{p_F^2-p_y^2}\right] \\ =& \frac{2g_s g_v}{(2\pi\hbar)^2} \int_{0}^{p_F} 2\sqrt{p_F^2-p_y^2} dp_y \end{aligned} \tag{B.3}$$

Make the change of variable:

$$p_y = p_F \sin x \Rightarrow dp_y = p_F \cos x dx. \tag{B.4}$$

In this extend:

$$\sqrt{p_F^2-p_y^2} = \sqrt{p_F^2 - p_F^2 \sin^2 x} = p_F \cos x. \tag{B.5}$$

With these assumptions the charge carrier density becomes:

$$\begin{aligned} n_s =& \frac{2g_s g_v}{(2\pi\hbar)^2} \int_{0}^{\pi\backslash 2} p_F \cos x \cdot 2p_F \cos x dx \\ =& \frac{4g_s g_v p_F^2}{(2\pi\hbar)^2} \int_{0}^{\pi\backslash 2} \cos^2 x dx \\ =& \frac{g_s g_v p_F^2}{4\pi\hbar^2} \end{aligned} \tag{B.6}$$

Appendix C

Current density of electrons

The expression of the current density of electrons which takes into account the Fermi distribution of charge carriers over the quantum states in the energy band structure of graphene, as presented in Section 1.5, is:

$$\begin{aligned} j_x(t) =& -e\frac{g_s g_v v_F}{(2\pi\hbar)^2}\int_{-p_F}^{p_F} dp_y \int_{p_0(t)-\sqrt{p_F^2-p_y^2}}^{p_0(t)+\sqrt{p_F^2-p_y^2}} dp_x \frac{p_x}{\sqrt{p_x^2+p_y^2}} \\ =& -e\frac{g_s g_v v_F}{(2\pi\hbar)^2}\int_{-p_F}^{p_F} dp_y \left[\sqrt{\left(p_0(t)+\sqrt{p_F^2-p_y^2}\right)^2+p_y^2}\right. \\ & \left. -\sqrt{\left(p_0(t)-\sqrt{p_F^2-p_y^2}\right)^2+p_y^2}\right] \end{aligned} \tag{C.1}$$

Likewise in Appendix B, make the change of variable:

$$p_y = p_F \sin x \Rightarrow dp_y = p_F \cos x dx. \tag{C.2}$$

So that:

$$\sqrt{p_F^2-p_y^2} = p_F \cos x. \tag{C.3}$$

Now with the new variable defined, the current density can be written as:

$$
\begin{aligned}
j_x(t) =& -e\frac{g_s g_v v_F}{(2\pi\hbar)^2}\cdot 2\int_0^{\pi\backslash 2} p_F\cos x dx\left[\sqrt{\left(p_0(t)+p_F\cos x\right)^2+\left(p_F\sin x\right)^2}\right.\\
&\left.-\sqrt{\left(p_0(t)-p_F\cos x\right)^2+\left(p_F\sin x\right)^2}\right]\\
=& -e\frac{g_s g_v v_F}{(2\pi\hbar)^2}\cdot 2\int_0^{\pi\backslash 2} p_F\cos x dx\left[\sqrt{p_0^2(t)+2p_0(t)p_F\cos x+p_F^2}\right.\\
&\left.-\sqrt{p_0^2(t)-2p_0(t)p_F\cos x+p_F^2}\right]\\
=& -e\frac{g_s g_v v_F}{(2\pi\hbar)^2}\cdot 2\int_0^{\pi\backslash 2} p_F\cos x dx\left[p_F\sqrt{\frac{p_0^2(t)}{p_F}+2\frac{p_0(t)}{p_F}\cos x+1}\right.\\
&\left.-p_F\sqrt{\frac{p_0^2(t)}{p_F^2}-2\frac{p_0(t)}{p_F}\cos x+1}\right]
\end{aligned}
\tag{C.4}
$$

Denote $-\frac{p_0(t)}{p_F}=Q=\frac{eE_0v_F}{\omega\varepsilon_F}\sin\omega t=Q_0\sin\omega t$ where Q_0 is a field parameter proportional to E_0.

So, under the above assumption, the current density becomes:

$$
\begin{aligned}
j_x(t) =& -e\frac{g_s g_v v_F}{(2\pi\hbar)^2}\cdot 2\int_0^{\pi\backslash 2} p_F^2\cos x dx\left(\sqrt{Q^2-2Q\cos x+1}-\sqrt{Q^2+2Q\cos x+1}\right)\\
=& -e\frac{g_s g_v v_F}{(2\pi\hbar)^2}\cdot 2\int_0^{\pi\backslash 2} p_F^2\cos x dx\cdot\sqrt{Q^2+1}\left(\sqrt{1-\frac{2Q}{Q^2+1}\cos x}\right.\\
&\left.-\sqrt{1+\frac{2Q}{Q^2+1}\cos x}\right)
\end{aligned}
\tag{C.5}
$$

where $\left|\frac{2Q}{Q^2+1}\right|<1,\ \forall Q$.

The series expansion of $\sqrt{1\pm x}$ when $|x|<1$ is:

$$
\begin{aligned}
\sqrt{1+x} &= 1+\frac{1}{2}x-\frac{1}{2^3}x^2+\frac{1}{2^4}x^3-\frac{5}{2^7}x^4+\frac{7}{2^8}x^5-\frac{21}{2^{10}}x^6+\frac{33}{2^{11}}x^7+...\\
\sqrt{1-x} &= 1-\frac{1}{2}x-\frac{1}{2^3}x^2-\frac{1}{2^4}x^3-\frac{5}{2^7}x^4-\frac{7}{2^8}x^5-\frac{21}{2^{10}}x^6-\frac{33}{2^{11}}x^7+...
\end{aligned}
\tag{C.6}
$$

For the ease of calculations denote $\frac{2Q}{Q^2+1} = P$ thus:

$$\sqrt{1-P\cos x}-\sqrt{1+P\cos x} = -\left(P\cos x+\frac{2}{2^4}P^3\cos^3 x+\frac{14}{2^8}P^5\cos^5 x + \frac{66}{2^{11}}P^7\cos^7 x+...\right) \tag{C.7}$$

Therefore the expression of the current density can be rewritten like :

$$j_x(t) = \frac{en_s v_F}{\pi}\cdot 2\sqrt{Q^2+1}\int_0^{\pi\backslash 2}\cos x\left(P\cos x+\frac{2}{2^4}P^3\cos^3 x+\frac{14}{2^8}P^5\cos^5 x + \frac{66}{2^{11}}P^7\cos^7 x\right)dx \tag{C.8}$$

where the charge carrier density n_s is $\frac{g_s g_v p_F^2}{4\pi\hbar^2}$.

The integration of the cosine function in the limits $[0, \frac{\pi}{2}]$ at the second, fourth, sixth and eighth power is:

$$\begin{aligned}\int_0^{\pi\backslash 2}\cos^2 xdx &= \frac{\pi}{4}, \quad \int_0^{\pi\backslash 2}\cos^4 xdx = \frac{3\pi}{2^4}\\ \int_0^{\pi\backslash 2}\cos^6 xdx &= \frac{5\pi}{2^5}, \quad \int_0^{\pi\backslash 2}\cos^8 xdx = \frac{35\pi}{2^8}\end{aligned} \tag{C.9}$$

So the current density can be written in the form:

$$\begin{aligned}j_x(t) =& en_s v_F\frac{1}{2}\sqrt{Q^2+1}\left(P+\frac{3}{2^5}P^3+\frac{35}{2^{10}}P^5+\frac{1155}{2^{16}}P^7\right)\\ =& en_s v_F\frac{1}{2}\sqrt{Q^2+1}\left[\frac{2Q}{Q^2+1}+\frac{3}{2^5}\frac{2^3Q^3}{(Q^2+1)^3}+\frac{35}{2^{10}}\frac{2^5Q^5}{(Q^2+1)^5}\right.\\ &\left.+\frac{1155}{2^{16}}\frac{2^7Q^7}{(Q^2+1)^7}\right]\end{aligned} \tag{C.10}$$

$$j_x(t) = en_s v_F \frac{1}{\sqrt{Q^2+1}} \left(Q + \frac{3}{2^5} \frac{2^2 Q^3}{(Q^2+1)^2} + \frac{35}{2^{10}} \frac{2^4 Q^5}{(Q^2+1)^4} + \frac{1155}{2^{16}} \frac{2^6 Q^7}{(Q^2+1)^6} \right) \tag{C.11}$$

Performing the series expansion of $(Q^2+1)^n$, $Q<1$ where $n=-\frac{1}{2},-2,-4$ and -6, the formula of the current density becomes:

$$\begin{aligned} j_x(t) =& en_s v_F \left(1 - \frac{1}{2}Q^2 + \frac{3}{8}Q^4 - \frac{5}{16}Q^6\right) \left[Q + \frac{3}{2^5} \cdot 2^2 Q^3 \left(1 - 2Q^2 + 3Q^4\right) \right. \\ &\left. + \frac{35}{2^{10}} \cdot 2^4 Q^5 \left(1 - 4Q^2\right) + \frac{1155}{2^{16}} \cdot 2^6 Q^7 \cdot 1 \right] \\ =& en_s v_F \left(1 - \frac{1}{2}Q^2 + \frac{3}{8}Q^4 - \frac{5}{16}Q^6\right) \left[Q + \frac{3}{2^5} \cdot 2^2 Q^3 - \frac{13}{2^6} Q^5 + \frac{67}{2^{10}} Q^7 \right] \\ =& en_s v_F \left(Q - \frac{2^2}{2^5} Q^3 - \frac{1}{2^6} Q^5 - \frac{5}{2^{10}} Q^7 \right) \end{aligned} \tag{C.12}$$

Q was assumed proportional to the electric field so $Q = Q_0 \sin \omega t \sim E_0 \sin \omega t$ therefore for $Q_0 < 1$:

$$j_x(t) = en_s v_F \left(Q_0 \sin \omega t - \frac{2^2}{2^5} Q_0^3 \sin^3 \omega t - \frac{1}{2^6} Q_0^5 \sin^5 \omega t - \frac{5}{2^{10}} Q_0^7 \sin^7 \omega t \right) \tag{C.13}$$

The following trigonometric identities were calculated using De Moivre's formula and the binomial theorem:

$$\begin{aligned} \sin^3 x &= \frac{1}{4} (3 \sin x - \sin 3x) \\ \sin^5 x &= \frac{1}{16} (\sin 5x - 5 \sin 3x + 10 \sin x) \\ \sin^7 x &= \frac{1}{64} (35 \sin x - 21 \sin 3x + 7 \sin 5x - \sin 7x) \end{aligned} \tag{C.14}$$

Finally, after the trigonometric identities from Eq. C.14 were introduced into Eq. C.13 the graphene current density of electrons due to the contribution of the 1^{st}, 3^{rd}, 5^{th} and 7^{th} was determined:

$$
\begin{aligned}
j_x(t) =& e n_s v_F \left[\sin \omega t \left(Q_0 - \frac{3}{2^5} Q_0^3 - \frac{10}{2^{10}} Q_0^5 - \frac{175}{2^{16}} Q_0^7 \right) \right. \\
&+ \sin 3\omega t \left(\frac{1}{2^5} Q_0^3 + \frac{5}{2^{10}} Q_0^5 + \frac{105}{2^{16}} Q_0^7 \right) \\
&+ \sin 5\omega t \left(-\frac{1}{2^{10}} Q_0^5 - \frac{35}{2^{16}} Q_0^7 \right) \\
&\left. + \sin 7\omega t \frac{5}{2^{16}} Q_0^7 \right] \qquad \text{(C.15)}
\end{aligned}
$$